

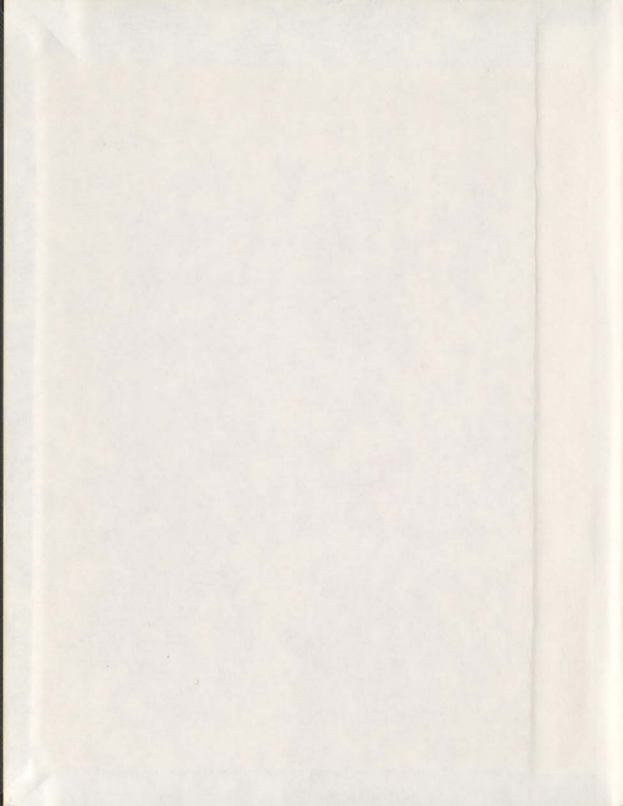
ICE FORCES ON A FACETED CONE  
DUE TO THE PASSAGE OF A LEVEL ICE FIELD

CENTRE FOR NEWFOUNDLAND STUDIES

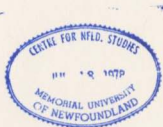
TOTAL OF 10 PAGES ONLY  
MAY BE XEROXED

(Without Author's Permission)

MICHAEL LAU



001311





## **INFORMATION TO USERS**

This manuscript has been reproduced from the microfilm master. UMI films the text directly from the original or copy submitted. Thus, some thesis and dissertation copies are in typewriter face, while others may be from any type of computer printer.

The quality of this reproduction is dependent upon the quality of the copy submitted. Broken or indistinct print, colored or poor quality illustrations and photographs, print bleedthrough, substandard margins, and improper alignment can adversely affect reproduction.

In the unlikely event that the author did not send UMI a complete manuscript and there are missing pages, these will be noted. Also, if unauthorized copyright material had to be removed, a note will indicate the deletion.

Oversize materials (e.g., maps, drawings, charts) are reproduced by sectioning the original, beginning at the upper left-hand corner and continuing from left to right in equal sections with small overlaps.

Photographs included in the original manuscript have been reproduced xerographically in this copy. Higher quality 6" x 9" black and white photographic prints are available for any photographs or illustrations appearing in this copy for an additional charge. Contact UMI directly to order.

Bell & Howell Information and Learning  
300 North Zeeb Road, Ann Arbor, MI 48106-1346 USA  
800-521-0600

**UMI<sup>®</sup>**





National Library  
of Canada

Acquisitions and  
Bibliographic Services

395 Wellington Street  
Ottawa ON K1A 0N4  
Canada

Bibliothèque nationale  
du Canada

Acquisitions et  
services bibliographiques

395, rue Wellington  
Ottawa ON K1A 0N4  
Canada

Your file Votre référence

Our file Notre référence

The author has granted a non-exclusive licence allowing the National Library of Canada to reproduce, loan, distribute or sell copies of this thesis in microform, paper or electronic formats.

L'auteur a accordé une licence non exclusive permettant à la Bibliothèque nationale du Canada de reproduire, prêter, distribuer ou vendre des copies de cette thèse sous la forme de microfiche/film, de reproduction sur papier ou sur format électronique.

The author retains ownership of the copyright in this thesis. Neither the thesis nor substantial extracts from it may be printed or otherwise reproduced without the author's permission.

L'auteur conserve la propriété du droit d'auteur qui protège cette thèse. Ni la thèse ni des extraits substantiels de celle-ci ne doivent être imprimés ou autrement reproduits sans son autorisation.

0-612-54848-1

Canada



**ICE FORCES ON A FACETED CONE**

**DUE TO THE PASSAGE OF A LEVEL ICE FIELD**

by

©Michael Lau, B.A., B.Sc., B.Eng., M.Eng.

A thesis submitted to the  
School of Graduate Studies  
in partial fulfilment of the  
requirements for the degree of  
PhD in Engineering

Faculty of Engineering and Applied Science

Memorial University of Newfoundland

May 1999

St. John's

Newfoundland

## **ABSTRACT**

Faceted conical structures have been proposed as an alternative to the true conical form to ease the fabrication and to lower the construction costs. In considering ice forces on these structures, there was a concern with the validity of existing theories. The main objectives of this study are to improve the understanding of the interaction processes and the failure mechanisms of a level ice field against a faceted cone during continuous ice breaking, and to provide engineers with a set of easy-to-apply formulae for ice load calculation. In this thesis, the results of a three-part study, consisting of experimental and theoretical investigations, are documented. In Part I, a pilot series of physical model tests were conducted to provide a clear insight into the interaction processes. Some important interaction features were identified from analysis of the test data which provided a framework vital to further model development. In Part II, the unique rubble piling process was further examined with the aid of existing particulate mechanics and a comprehensive numerical analysis. A new rubble model was developed to predict the geometry of the rubble and the forces exerted on the structure and the base support. In Part III, an appropriate ice breaking model was selected from the existing theories for the adaptation of the new rubble model. The new model, which considers the salient aspects of the rubble piling process, agrees well with the experimental data.

The above developments and results are significant, because, for the first time, to the knowledge of the author, an ice load model has been established to account for the effect of rubble in ice loading on a multifaceted cone based on essential features of the interaction.

The results provide a useful framework for further model development. The state-of-the-art is such that it is now possible to incorporate rubble load in the force calculation with higher degree of confidence. The methodology for doing so has been developed and presented herein, and constitutes the main contribution of this work to the state-of-the-art.

## **ACKNOWLEDGEMENTS**

I wish to express my deepest gratitude to my supervisor, Dr. J. Molgaard, my co-supervisor, Dr. F.M. Williams, and member of the supervising committee, Dr. A.S.J. Swamidas. They provided much-needed advice and guidance during the course of this research. Their interest and encouragement, as well as many stimulating discussions and helpful suggestion, played a major role in the progress of this work.

I also wish to extend my gratitude to Dr. D.B. Muggeridge who first introduced me to the exciting field of ice research, and has financially and academically support in my formative years. He was also instrumental in organizing and securing funding for the "MUN/ERCL/NRC Multi-Faceted Cone Study" from Natural Sciences and Engineering Research Council (NSERC). Dr. S.J. Jones and Dr. G.W. Timco of the National Research Council of Canada (NRC), Dr. K.R. Croasdale of Esso Resources Canada Limited (ERCL), and Dr. A.S.J. Swamidas of the Memorial University of Newfoundland (MUN) also participated in the grant application. Without their efforts, this research would not have been possible.

Many people have contributed to the experimental program. The experiments described in this thesis was conducted with the help of Mr. J.R. Tucker and Mr. B. Roche of MUN and the technical staff of the Institute for Marine Dynamics' (IMD) ice tank (especially Mr. Spence Butt and Mr. Brian Hill). The Faculty of Engineering's technical services division constructed the model and the load measuring system used in the experiments. Dr. D.B. Muggeridge of MUN, Dr. S.J. Jones and Dr. G.W. Timco of NRC,

Dr. K.R. Croasdale of ERCL, Dr. M. Metge of Canatec Consultants Ltd., Mr. K.C. Chao of Exxon, and Dr. A. Prodanovic of Mobile gave valuable suggestions for improvement of the test program. Their contributions are acknowledged with appreciation.

The generous contribution and continuous support of the National Research Council's Institute for Marine Dynamics in this research is gratefully acknowledged - in particular my former supervisor, Dr. S.J. Jones, who availed me the opportunity to conduct the model test program during my stay in the institute.

IMD has also provided vital support to this research by allowing me to access its computer facility after I left the institute to pursue the graduate research on a full time basis. In particular, I am most grateful to Dr. S.J. Jones and Dr. D. Molyneux, who sponsored my computer work in the institute. My thanks also go to Mr. B. Schooley, system manager of IMD's computer system, and Mr. D. Spencer, a DECICE expert, for their assistance and help in using the software and facility.

Funding for the IMD's test series was partly provided by NSERC through their University Industry Programs (CDR 661-199/88). NRC provided in kinds personnel and test facility. Subsequent analysis of the experimental data was carried out under IMD project PJXAQ94-00115-(022)/A supported by the Panel for Energy Research and Development (PERD). The author acknowledges their sponsorship, together with the guidance and encouragement provided by Dr. S.J. Jones, Dr. F.M. Williams and Dr. R. McKenna.

Academic funding was provided by many source during this work, including: Atlantic Awards Career Development Fellowship made available under the Canada Newfoundland

Offshore Agreement, the Memorial University of Newfoundland, and the Center for Cold Oceans Resources Engineering. Their generosity is gratefully acknowledged.

Finally, I would like to thank my wife, Oi-Hing, and my four children, Grace, Gabriel, Joshua and Rebecca, for their support and patience over such a long period of time, of which any description would be grossly understated.

## TABLE OF CONTENTS

	Page
<b>Abstract</b> .....	ii
<b>Acknowledgements</b> .....	iv
<b>Contents</b> .....	vii
<b>List of Tables</b> .....	xv
<b>List of Figures</b> .....	xviii
<b>Nomenclature</b> .....	xxxii
<b>Chapter 1      Introduction</b> .....	<b>1</b>
1.1     Background .....	1
1.2     Scope and Objectives .....	4
1.3     Approaches and Methodologies .....	5
1.4     Organization of the Thesis .....	7
<b>Chapter 2      Literature Review</b> .....	<b>10</b>
2.1     Ice-Structure Interaction Processes .....	11
2.1.1     Conical Structures .....	11
2.1.2     Sloping Planes .....	14
2.2     Models for Ice Force Predictions .....	15
2.2.1     Analytical Formulations .....	16
2.2.1.1     Croasdale's Approach .....	16

	Page
2.2.1.2 Nevel's Approach .....	19
2.2.1.3 Ralston's Approach .....	22
2.2.1.4 Maattanen's Approach .....	24
2.2.2 Empirical Formulae .....	25
2.3 MUN/ERCL/NRC Multi-Faceted Cone Tests .....	28
2.3.1 Test Program .....	29
2.3.2 Analysis of IME's Test Results .....	32
2.3.3 Analytical Models .....	34
2.4 Comparison of Models and Discussions .....	36
 <b><u>Part I: The Experiment</u></b>	
<b>Chapter 3 Test Program .....</b>	<b>48</b>
3.1 Test Facility and Structure .....	50
3.2 Instrumentation and Data Acquisition System .....	51
3.3 Model Ice .....	52
3.4 Test Matrix and Presentation of Results .....	53
<b>Chapter 4 Analysis of Tests .....</b>	<b>65</b>
4.1 Ice-Structure Interaction and Failure Processes .....	67
4.2 Ice Breaking Mechanisms .....	70
4.2.1 Breaking Pattern Observed in IMD's Series .....	70

	Page
4.2.1.1 Common Beam Failure Scenarios .....	71
4.2.2 Piece Size Analysis .....	73
4.3 Ice Rubble Formation Process .....	78
4.4 General Characteristics of Ice Load .....	80
4.4.1 Ice Load Distribution and Ratio of Horizontal to Vertical Forces	80
4.4.2 Ratio of Neck to Global Forces .....	82
4.5 Semi-Empirical Formulae .....	82
4.6 Comparison with Theoretical Prediction .....	85
4.7 Summary and Discussions .....	86
4.7.1 The Need for Further Ice Force Modelling .....	87
4.7.2 Conceptual Model for Ice Forces Exerted on an Inclined Plane .	90

## **Part II: Ice Rubble Modelling**

<b>Chapter 5</b>	<b>Ice Rubble Under Load .....</b>	<b>110</b>
5.1	Shear Strength of Ice Rubble .....	112
5.1.1	Phenomenological and Structural Approaches for Material Description .....	113
5.1.2	Phenomenological Descriptions of Cohesionless Granular Materials .....	114
5.1.3	Effect of Initial Void Ratio on Internal Friction .....	116

	Page
5.1.4 Limitations of the Phenomenological Approach .....	119
5.1.5 Laboratory Measurements of Rubble Strength .....	120
5.2 Rubble's Surface Profile Due to Natural Dumping Process .....	125
5.2.1 Variation and Maintenance of Rubble Surface Profile .....	126
5.3 Stress-State of Ice Rubble .....	128
5.3.1 Behaviour of Granular Material Under Stress .....	128
5.3.2 Expected Stress State of a Typical Rubble in Front of a Faceted Cone .....	135
5.4 Analytical Methods for the Computation of Wall Thrust Exerted by Earth Mass at the "At-Rest" State .....	137
5.4.1 Melkote's Method .....	138
5.4.2 Limit Equilibrium Methods .....	138
<b>Chapter 6 Rubble Geometry Idealization .....</b>	<b>153</b>
6.1 General Features and Assumptions of the Interacting System .....	154
6.2 Ideal Geometry and Mass Balance .....	159
6.3 Derivation of Basic Equations for Characteristic Heights of Rubble ..	161
6.3.1 Rubble Height at the Edge of Front Facet, $h_{ef}$ .....	161
6.3.2 Rubble Height at the Side of Cone, $h_n$ .....	167
6.3.3 Derivation of Generalized Equation for Maximum Rubble Height Along the Front Facet Face, $h_m$ .....	168

	Page
6.4 Validation of Ice Rubble Geometry Prediction Model .....	174
<b>Chapter 7 Discrete Element Analysis of Rubble Loads on an Rigid Inclined Wall</b>	
.....	188
7.1 Main Features of the DECICE Computer Code .....	189
7.2 Simulations of Rubble Mass at the "At-Rest" Condition .....	191
7.2.1 Generation of Rubble Ice Samples .....	193
7.2.2 Computations of the Coefficient of Lateral Earth Pressure at Rest, $K_0$ .....	194
7.2.3 Angle of Repose Tests .....	198
7.3 Development of Equations for Rubble Loads in 2-D .....	200
7.3.1 Form of Earth Pressure Equation and Relevant Functions .....	201
7.3.2 Overview of DECICE Simulations and Analyses .....	206
7.3.3 Validation of Linear Dependency of Thrust Force on Rubble Height Squared, $h^2$ .....	208
7.3.4 Validation of Linear Dependency of Thrust Force on the Function, $1 - \frac{2\pi}{180^\circ}$ .....	209
7.3.5 Validity of Equation 7.18 for Vertical Walls .....	210
7.3.6 Validity of Equation 7.17 for Inclined Walls .....	212
7.3.7 Derivation of Effective Wall Friction, $\phi'_w$ .....	214
7.3.8 Summary of the Formulae Derived from Best Fit of DECICE Data	

	Page
.....	217
7.4    Load Components Distributed on the Wall and the Supporting Ice Sheet	218
7.5    Application of the New Formula for Walls with Multiple Slopes .....	219
7.6    Application of the New Formula for Other Loading Conditions .....	221
7.6.1  Maximum Slope of Rubble with Basal Sliding at the Rubble/Ice Interfaces .....	222
7.6.2  Maximum Rubble Height Limited by Bearing Failure of the Supporting Ice Sheet .....	223
 <b><u>Part III: Ice Force Model</u></b>	
<b>Chapter 8    Development of a New Ice Force Model .....</b>	<b>254</b>
8.1    Selection of Base Model for Modelling of Ice Breaking Behaviour of Intact Ice .....	255
8.1.1  Experimental Data and Ice Force Models for Smooth Cones, with Ride-Up Ice, But No Rubble .....	255
8.1.2  3-D Modification of Croasdale's Model .....	257
8.1.3  Result of Model Assessment .....	260
8.2    Formulation of Ice Force Model with Rubble at a Faceted Cone .....	262

	Page
8.2.1 General Features and Simplifications of the Ice-Structure Interaction	263
8.2.1.1 Characteristic Ice Breaking Pattern .....	263
8.2.1.2 Heights, Width and Weights of Rubble in Front of the Front Facet .....	264
8.2.1.3 Weights of Ride-Up Ice on Individual Sections on the Front Facet .....	265
8.2.1.4 Heights, Width, and Weights of Rubble in Front of the Side Facets .....	266
8.2.1.5 Weights of Ride-Up Ice on Individual Sections on the Side Facets .....	268
8.2.1.6 Load Distribution and Failure of Ice Sheet .....	269
8.2.2 Coordinate System and Geometry .....	270
8.2.3 Normal and Frictional Forces on Each Facet .....	271
8.2.4 Overview of Various Force Components .....	273
8.2.5 Force Required to Push Ice Blocks Up the Slope Through Ice Rubble .....	275
8.2.6 Force Acting on the Ice Sheet at Waterline .....	276
8.2.7 Modification of Breaking Load for In-Plane Force .....	278
8.3 Validation of the New Ice Load Model .....	279

	Page
<b>Chapter 9     Conclusions and Recommendations .....</b>	<b>296</b>
9.1    Conclusions From the Experimental Investigation (Part I) .....	297
9.2    Conclusions From the Numerical Investigation (Part II) .....	298
9.3    Conclusions From the Ice Force Modelling (Part III) .....	301
9.4    Contributions of This Work .....	301
9.5    Recommendations for Future Work .....	302
9.5.1    Refinements of the Rubble Model .....	304
9.5.2    Refinements of the Ice Force Model .....	305
<b>References .....</b>	<b>306</b>
<b>Appendices</b>	
Appendix A    Summary of Test Conditions, Configurations, and Results of ERCL's and IMD's Test Series: Level Ice .....	331
Appendix B    Load Time History of Tests Conducted in IMD's Test Series .....	339
Appendix C    Example Calculation to Illustrate the Application of Equations Developed in Chapters 7 to 9 .....	376

## LIST OF TABLES

	Page
Table 2.1 Test conditions of each data set used in model formulation and coefficients of the associated formula .....	41
Table 2.2 Prototype and model geometries: symbols given in Figure 2.1 .....	42
Table 3.1 Test matrix for level ice tests in IMD's series .....	56
Table 3.2 Summary of ice conditions for each test .....	57
Table 3.3 Summary of level ice test results .....	58
Table 4.1 General test conditions of the model test series used in piece size analysis .....	93
Table 4.2 Summary of the horizontal to vertical force ratio for level ice tests measured in the three series on multifaceted cones .....	94
Table 4.3 Summary of total, breaking and clearing ice forces measured in IMD series: 1:25 scale model .....	95
Table 5.1 Summary of failure criteria proposed for granular materials (after Evgin and Sun, 1989) .....	144
Table 5.2 Effect of angularity and grading on peak friction angle (after Terzaghi, 1955) .....	144
Table 5.3 Summary of laboratory shear box tests on ice rubble .....	145
Table 5.4 Different equations for coefficient of pressure of loose soil at rest ...	146
Table 6.1 Comparison of predictions from the new geometry model and the	

	Page
measurements from IMD's tests .....	176
Table 7.1 DECICE parameters for the simulations of rubble mass at the "at-rest" condition .....	224
Table 7.2 Summary of the coefficient of lateral earth pressure at rest, $K_{o,1}$ , estimated by gravity method .....	225
Table 7.3 Summary of the coefficient of lateral earth pressure at rest, $K_{o,2}$ , measured from the oedometer tests .....	226
Table 7.4 Summary of the angle of repose, $\phi_r$ , estimated from the rubble's natural slope after slope failure .....	227
Table 7.5 Matrix of DECICE simulations of the thrust exerted upon a retaining wall by cohesionless granular materials at "at rest" state of stress .....	227
Table 7.6 Summary of DECICE simulations of the thrust exerted upon a retaining wall by cohesionless granular materials at "at rest" state of stress .....	228
Table 7.6 Summary of DECICE simulations of the thrust exerted upon a retaining walls by cohesionless granular materials at "at rest" state of stress (cont'd) .....	229
Table 7.7 Computed values for DECICE Analyses conducted in Sections 7.3.3 to 7.3.6 .....	230
Table 7.7 Computed values for DECICE Analyses conducted in Sections 7.3.3 to 7.3.6 (cont'd) .....	231
Table 7.8 Results of simulation runs to validate the direct proportionality between the	

	Page
rubble height squared, $h^2$ , and the total wall thrust, $P_o$ ( $\iota = 22.5^\circ$ and $\phi = 24.2^\circ$ for all cases) .....	232
Table 7.9 Results of the correlation analysis with the ( $P_o - K''$ ) data pairs .....	233
Table 7.10 Base cases and their variations selected to assess the validity of Equation 7.18 for vertical walls .....	234
Table 7.11 Base cases selected to assess the validity of Equation 7.17 for inclined walls .....	235
Table 7.12 Least squares fit of force components computed from Equations 7.31, 7.32, and 7.34, to values obtained directly from simulation runs assuming $\phi_*$ equal to $0^\circ$ , $11.3^\circ$ and $22.5^\circ$ .....	236
Table 8.1 Summary of test conditions used in the selected test programs .....	281
Table 8.2 Summary of average and standard deviation of the predicted to measured mean peak force ratio, $F_{\text{pred}}/F_{\text{meas}}$ , in each test data set .....	282
Table 8.3 Summary of average and standard deviation of the predicted to measured mean peak force ratio, $F_{\text{pred}}/F_{\text{meas}}$ , of all tests for each ice force models .....	283
Table 8.4 Summary of measured loads from IMD's and ERCL's test data and the forces predicted by the new model .....	283

## LIST OF FIGURES

	Page
Figure 2.1 Test structure geometry. All diameters are corner to corner; and all slopes are of facet centres, given as a ratio of vertical to horizontal. ....	43
Figure 2.2 Rubble field types (after Izumiya et al, 1994) ....	43
Figure 2.3 Rubble types in strength-thickness domain (after Izumiya et al, 1994) ....	44
Figure 2.4 Piece size versus ice breaking length for IME's tests (after Izumiya et al, 1994) ....	44
Figure 2.5 Figure showing the definition of ice piece size, $L_w$ and $L_L$ (after Izumiya et al, 1994) ....	45
Figure 2.6 Increase in total load due to rubble (after Izumiya et al, 1994) ....	45
Figure 2.7 Comparison of Croasdale et al's model with tests in ERCL's series (after Croasdale et al, 1994) ....	46
Figure 2.8 Ice forces treated in Izumiya et al's model (after Izumiya et al, 1993) ....	46
Figure 2.9 Comparison of Izumiya et al's model with tests in IME's series where ice rubble was absent (after Izumiya et al, 1993) ....	47
Figure 2.10 Rubble coefficient as a function of ice thickness and ice strength derived from IME's test data (after Izumiya et al, 1993) ....	47
Figure 3.1 Experimental set-up showing a 1:25 scale large neck model mounted under	

	Page
the main carriage .....	59
Figure 3.2 Dimensions of the 1:25 large neck model. All diameters are corner to corner; all slopes are of the facet centres and given as a ratio of vertical to horizontal. All dimensions in millimetres .....	59
Figure 3.3 Dimensions of the 1:25 small neck model. All diameters are corner to corner; all slopes are of the facet centres and given as a ratio of vertical to horizontal. All dimensions in millimetres .....	60
Figure 3.4 Dimensions of the 1:50 large neck model. All diameters are corner to corner; all slopes are of the facet centres and given as a ratio of vertical to horizontal; All dimensions in millimetres .....	60
Figure 3.5 Global load measurement assembly .....	61
Figure 3.6 Orientation of global coordinate axes with respect to the model structure .....	61
Figure 3.7 Neck load cell arrangement for the 1:25 large neck model .....	62
Figure 3.8 Neck load cell arrangement for the 1:50 large neck and 1:25 small neck models .....	62
Figure 3.9 Schematic of the data acquisition system .....	63
Figure 3.10 Matrix showing IMD's, IME's and ERCL's level ice tests in thickness-strength domain (full scale); face-on orientation only .....	64
Figure 3.11 Comparison of mean peak force and mean force plus one and a half times	

	Page
standard deviation (IMD's 1:25 scale model tests) .....	64
Figure 4.1 Photos showing a typical ice breaking, ride-up and rubble piling sequence (Test MUNCONE4_001): (a) initial contact, (b) ice ride-up, (c) rubble accumulation, and (d) fully developed rubble pile .....	96
Figure 4.2 Photo from IMD's series showing the ride-up of ice and the rubble pile (Test MUNCONE6_003) .....	97
Figure 4.3 Profile of crack patterns associated with the (a) edge-on and (b) face-on orientations .....	97
Figure 4.4 Load trace showing typical cyclical ice loading (MUNCONE4_003) ..	98
Figure 4.5 Time history showing high frequency cyclical loading (MUNCONE7_006)	99
Figure 4.6 Bearing failure of unbroken ice sheet in strength-thickness domain, IMD's and IME's series .....	100
Figure 4.7 Ice piece size, $L_L$ , versus breaking length, $L_b$ , with curve fitting for ice thickness larger than 0.045 m. Tatinclaux's equation for urea ice is also given. ....	100
Figure 4.8 Ratio of ice piece size to characteristic length, $L_L/l_c$ , versus ice thickness, $t$ , for seven sets of model test data with sloping structures .....	101
Figure 4.9 Model/Full scale icebreaker test results showing the effect of ice thickness, $t$ , on the ratio of ice piece size to characteristic length, $L_L/l_c$ . Data include low	

	Page
speed test with urea and sea ice .....	101
Figure 4.10 Model/Full scale wedge breaking tests taken from Keinonen et al (1993) showing the effect of ice thickness, $t$ , on the ratio of piece size to characteristic length, $L_c/l_c$ , with loading velocity, $V = 5$ cm/s .....	102
Figure 4.11 Rubble types associated with IME's and IMD's model tests shown in the strength-thickness domain .....	102
Figure 4.12 Non-dimensional resolution factor, $\xi_{\text{meas}}/\xi$ , versus non-dimensional waterline width, $D/l_c$ , for smooth cone tests .....	103
Figure 4.13 Non-dimensional horizontal neck force versus non-dimensional free-board, $z/t$ .....	103
Figure 4.14 Figure showing the definitions of $F_t$ , $F_b$ and $F_c$ ( $\lambda$ is the scale factor)	104
Figure 4.15 Comparison of horizontal breaking force measured in IMD's series to the breaking force predicted by Equation 4.4 .....	104
Figure 4.16 Comparison of horizontal clearing force measured in IMD's series to clearing force predicted by Equation 4.4 .....	105
Figure 4.17 Comparison of total measured horizontal force with prediction from Equation 4.4 for the three test series .....	105
Figure 4.18 Comparison of prediction from Nevel's model with measurements from the three test series: horizontal force .....	106
Figure 4.19 Comparison of prediction from Nevel's model with measurements from the	

	Page
three test series: vertical force .....	106
Figure 4.20 Comparison of horizontal breaking force measured in IMD's series to prediction from Nevel's model .....	107
Figure 4.21 Comparison of horizontal clearing force measured in IMD's series to prediction from Nevel's model .....	107
Figure 4.22 Geometry of the conceptual model for ice forces exerted on an inclined plane .....	108
Figure 4.23 The loads exerted on supporting ice sheet .....	108
Figure 4.24 The loads exerted on pile-up ice .....	109
Figure 5.1 Example of interlocking: (a) slightly interlocked surfaces in loosely packed rubble, (b) highly interlocked surfaces in densely packed rubble .....	147
Figure 5.2 Typical stress-strain curves for loose and dense samples .....	147
Figure 5.3 Internal friction angle versus initial void ratio for medium fine sand. $\phi$ , $\phi_{cv}$ , and $\phi_p$ , are internal friction angle, constant volume strength, and particle contact friction angle, respectively. (after Rowe, 1962) .....	148
Figure 5.4 Three characteristic types of earth pressure .....	148
Figure 5.5 Observed relationship between $K_o$ and $\sin \phi$ for cohesive and cohesionless soils: the solid symbols denote cohesionless soils and the hollow symbols denote cohesive soils (after Mayne et al, 1982) .....	149
Figure 5.6 Graphical illustration of $\Omega$ used in Equation 5.9 .....	149

	Page
Figure 5.7 Rubble geometry showing the two rigid blocks and the potential failure planes .....	150
Figure 5.8 Free body diagram of sliding blocks .....	150
Figure 5.9 Safety factor as a function of $\phi_s/\phi$ for wall angle, $\alpha = 50^\circ$ , angle of repose, $\phi = 30^\circ$ , and ice friction angle, $\phi_\mu = 11.3^\circ$ and $21.8^\circ$ . .....	151
Figure 5.10 Limiting rubble slope as a function of $\phi_s/\phi$ for wall angle, $\alpha = 50^\circ$ , angle of repose, $\phi = 30^\circ$ , and ice friction angle, $\phi_\mu = 11.3^\circ$ and $21.8^\circ$ .....	151
Figure 5.11 Horizontal thrust on the wall as a function of $\phi_s/\phi$ for wall angle, $\alpha = 50^\circ$ , angle of repose, $\phi = 30^\circ$ , and ice friction angle, $\phi_\mu = 11.3^\circ$ and $21.8^\circ$ ..	152
Figure 6.1 Ice breaking pattern showing the location of the accumulation and clearing zones (arrows indicate direction of ice movement) .....	177
Figure 6.2 Ride-up pattern of ice generated from the accumulation and clearing zones (arrows indicate direction of ice movement) .....	177
Figure 6.3 Geometry of a typical rubble showing the location of the accumulation and clearing zones (arrows indicate direction of ice movement) .....	178
Figure 6.4 Geometry of a typical rubble at times $t_1$ , $t_2$ and $t_3$ as it grows in size ( $t_1 < t_2 < t_3$ , and arrows indicate direction of ice movement) .....	178
Figure 6.5 Geometry of an idealized rubble surrounding a faceted cone (only the front right quarter is shown) .....	179

	Page
Figure 6.6 Rubble system selected for mass balance calculation (arrows indicate directions of ice movement and only the front right quarter is shown)	179
Figure 6.7 Geometry of a rubble pile formed by dropping ice blocks from a line source. Note: Half cones formed at the two ends .....	180
Figure 6.8 Rubble geometry in front of an inclined plane formed by end dumping from a line source .....	180
Figure 6.9 Rubble system selected in the calculation of $h_n$ (only the front right quarter of the rubble is shown) .....	181
Figure 6.10 Geometry of $A_n$ corresponding to the Cross-Section A-A as defined in Figure 6.9: (a) front view; (b) top view .....	182
Figure 6.11 Rubble system selected for the calculation of rubble height at the side of the cone, $h_n$ .....	183
Figure 6.12 Cross-sectional view B-B as defined in Figure 6.11 showing the geometry of $A_n$ .....	183
Figure 6.13 Formation of two-dimensional rubble pile from a line source: (a) to (c) lateral slope formed by depositing materials at both ends; (d) lateral slope is not formed due to lateral restraints at both ends .....	184
Figure 6.14 Rubble formation by two consecutive processes: (a) heap formation with lateral restraints (no end effect); (b) lateral slope formation by releasing the	

	Page
lateral restraints .....	184
Figure 6.15 Figure showing the dimensions of a two-dimensional heap formed by the process depicted in Figure 6.14, when: (a) $w \leq 0.5w_r$ , and (b) $w=0.5 w_r$	185
Figure 6.16 Rubble mass formed in front of a sloping plane by a line source with lateral movements of ice blocks restrained .....	186
Figure 6.17 Final shape of the rubble with the lateral restraint on the left hand side removed .....	186
Figure 6.18 Base of the lateral portion of the rubble: coordinates a, b, and j corresponding to those in Figure 6.17, and coordinate o 's the vertical projection (on to the base) of coordinate c in Figure 6.17 .....	187
Figure 6.19 Figure showing the decrease of rubble heights with the decrease of rubble angle. Rubble heights have been non-dimensionalized with heights computed at $t = \phi_r = 35^\circ$ .....	187
Figure 7.1 Figure showing the interaction of ice blocks, cone and ice sheet from a typical DECICE simulation (after Lau, 1994a) .....	237
Figure 7.2 Simulated versus measured horizontal peak forces for a 60 degrees cone in level ice (after Lau, 1994a) (Axis scaling is not given due to data propriety)	237
Figure 7.3 Snap-shots showing generation process of rubble sample: (a) random generation of ice blocks; (b) free falling of ice blocks; and (c) final	

	Page
configuration of rubble sample .....	238
Figure 7.4 Final configuration of rubble samples after initial compaction: ice piece size:(a) 16 m x 16 m; (b) 16 m x 32 m and (c) 16 m x 48 m .....	238
Figure 7.5 Comparison of initial void ratio, $e_o$ , and the associated contact friction, $\mu$ , with aspect ratios, AR = 1, 2 and 3 .....	239
Figure 7.6 Pressure distributions of rubble sample assumed in the gravity test ..	239
Figure 7.7 Comparison of earth pressure coefficient at-rest, $K_{o,1}$ , and the associated aspect ratio, AR, for contact friction, $\mu = 0, 0.2$ and $0.4$ : gravity method .....	240
Figure 7.8 Comparison of earth pressure coefficient at rest, $K_{o,1}$ , and the associated contact friction, $\mu$ , for aspect ratio, AR = 1, 2 and 3: gravity method ..	240
Figure 7.9 Comparison of internal friction angle, $\phi_i$ , and the associated contact friction, $\mu$ , for aspect ratio, AR = 1, 2 and 3: gravity method .....	241
Figure 7.10 Configuration of oedometer tests: side and bottom plates fixed while the top plate moves downward at $V = 0.4$ m/s .....	241
Figure 7.11 Figure showing the increase of horizontal stress, $p_{sh}$ , with the increase of vertical stress, $p_{hv}$ , in a typical simulated oedometer test (Run Q12) ..	242
Figure 7.12 Comparison of the at-rest earth pressure coefficient, $K_{o,2}$ , in simulated oedometer tests and the corresponding coefficient, $K_{o,1}$ , estimated from	

	Page
gravity test simulations .....	242
Figure 7.13 Comparison of the internal friction angle, $\phi_2$ , estimated from oedometer test simulations and the corresponding internal friction angle, $\phi_1$ , from gravity test simulations .....	243
Figure 7.14 Snap shots of Run S12 at (a) $t = 0$ s, (b) $t = 15.3$ s and (c) $t = 30.6$ s showing a typical angle of repose tests .....	243
Figure 7.15a Final configuration of rubbles in the angle of repose tests: (i) Test S12; (ii) Test S13; and (iii) Test S22 .....	244
Figure 7.15b Final configuration of rubbles in the angle of repose tests: (iv) Test S23; (v) Test S32; and (vi) Test S33 .....	245
Figure 7.16 Comparison of the angle of repose, $\phi_r$ , and the associated internal friction angle, $\phi_1$ , obtained from gravity test simulations .....	246
Figure 7.17 Definition of variables commonly used in various earth equations: (a) Coulomb's equation; and (b) Reimbert and Reimbert's equation. (The direction of total wall thrust as defined in Coulomb's equation and Reimbert and Reimbert's equation are different.) .....	246
Figure 7.18 Test configuration and sample geometry for each test simulation conducted for the thrust equation formulation. The results are given in Table 7.6 .....	247
Figure 7.19 Definition of variables used in Table 7.6 .....	248

	Page
Figure 7.20 Comparison of the predictions from Equation 7.18 and the total thrust measured on the wall for the three values of wall friction, $\phi_w = 0^\circ, 11.3^\circ$ , and $21.8^\circ$ , used in the DECICE simulations . . . . .	248
Figure 7.21 Comparison of the predictions from Equation 7.17 and the total thrust measured on the wall for the two values of wall friction, $\phi_w = 11.3^\circ$ and $21.8^\circ$ , in the DECICE simulations . . . . .	249
Figure 7.22 Effects of the wall angle on wall thrust for a combination of internal friction angle, $\phi$ , and rubble angle, $t$ (wall friction, $\phi_w = 21.8^\circ$ ) . . . . .	249
Figure 7.23 Comparison of the predictions from Equation 7.21 and the thrust on the wall in the DECICE simulation . . . . .	250
Figure 7.24 Computed effective friction angle at wall, $\phi'_{\infty}$ , versus wall angle, $\alpha$ , for wall friction angle, $\phi_w = 11.3^\circ$ . The broken line corresponds to $\phi'_{\infty} = \phi_w = 11.3^\circ$ , and the regression line fits data with $\alpha$ between $60^\circ$ to $90^\circ$ . . . . .	250
Figure 7.25 Computed effective friction angle at wall, $\phi'_{\infty}$ , versus wall angle, $\alpha$ , for wall friction angle $\phi_w = 21.8^\circ$ . The broken line corresponds to $\phi'_{\infty} = \phi_w = 21.8^\circ$ , and the regression line fits data with $\alpha$ between $60^\circ$ to $90^\circ$ . . . . .	251
Figure 7.26 Snap-shot of Run R12W3_2 showing the whole rubble mass sliding down along the wall and the supporting ice surfaces . . . . .	251
Figure 7.27 Force equilibrium of the rubble body . . . . .	252

	Page	
Figure 7.28	Figure of a rubble retained by a multi-sloped wall showing the wall thrust and the wall angle of each section .....	252
Figure 7.29	Data for sample calculation showing the use of the derived equations .....	253
Figure 8.1	Breaking and ride-up patterns assumed in Lau-Croasdale's model (only the front right quarter of the cone is shown) .....	284
Figure 8.2	Comparison of Lau-Croasdale's model with existing test data for smooth cones: horizontal mean peak force .....	285
Figure 8.3	Comparison of Lau-Croasdale's model with existing test data for smooth cones: vertical mean peak force .....	285
Figure 8.4	Comparison of Croasdale's model with existing test data for smooth cones: horizontal mean peak force .....	286
Figure 8.5	Comparison of Croasdale's model with existing test data for smooth cones: vertical mean peak force .....	286
Figure 8.6	Comparison of Nevel's model with existing test data for smooth cones: horizontal mean peak force .....	287
Figure 8.7	Comparison of Nevel's model with existing test data for smooth cones: vertical mean peak force .....	287
Figure 8.8	Comparison of Ralston's model with existing test data for smooth cones: horizontal mean peak force .....	288

	Page
Figure 8.9 Comparison of Ralston's model with existing test data for smooth cones: vertical mean peak force .....	288
Figure 8.10 Comparison of predicted to measured values for each test series: horizontal mean peak force .....	289
Figure 8.11 Comparison of predicted to measured values for each test series: vertical mean peak force .....	289
Figure 8.12 Average predicted to measured peak force values for each ice force model .....	290
Figure 8.13 Schematic of crack pattern in front of a faceted cone .....	290
Figure 8.14 Coverage of ride-up ice on an arbitrary section i .....	291
Figure 8.15 Geometry of rubble mass in front of the side facet showing the idealized volumes, $V_i$ and $V_{II}$ .....	291
Figure 8.16 Geometry of ice rode-up the side facet (only the front right quarter of the cone is shown) .....	292
Figure 8.17 Coordinates and geometry (only the front right quarter of the cone is shown) .....	292
Figure 8.18 General interaction between ice and sloping structure showing ice forces on ride-up ice and the ice sheet .....	293
Figure 8.19 Forces acting at the tip of the ice wedge .....	293
Figure 8.20 Forces acting on a layer of ride-up ice at an arbitrary cone section ...	294

Page

Figure 8.21 Comparison of model prediction and ERCL's test data .....	294
Figure 8.22 Comparison of model prediction and IMD's test data .....	295

## NOMENCLATURE

- $A_{nh}$  The projection of cone obstructing ice movement as defined in Figure 6.10 associated with  $A_{rf}$ , or in Figure 6.12 associated with  $A_n$
- $A_{rf}$  Cross-section of rubble as defined in Figure 6.9
- $A_n$  Cross-section of rubble as defined in Figure 6.11
- AR Aspect ratio defined as the ratio of ice thickness to piece size
- $B_{nh}$  Length defined in Figures 6.9 and 6.11 for  $h_{rf}$  and  $h_n$  computations, respectively.
- $B_{rf}$  Length defined in Figure 6.9 for  $h_{rf}$  computations
- $B_n$  Length defined in Figure 6.11 for  $h_n$  computations
- $C_{ob}$  Length defined in Figures 6.9 and 6.11 for  $h_{rf}$  and  $h_n$  computations, respectively.
- D Width of structure
- E Effective elastic modulus of ice sheet
- $F_h$  Breaking component of ice force
- $F_c$  Clearing component of ice force
- $F_m$  Maximum force
- $F_{meas}$  Measured force
- $F_{mp}$  Mean peak force
- $F_s$  Factor of safety
- $F_{x,y,z}$  Force components along the respective Cartesian axes
- $F_x$  Horizontal component along  $x'$  axis
- $H_s$  Horizontal force acting on cone surface as defined in Figure 8.19

$H_T$	Horizontal force acting on top tip of wedge beam as defined in Figure 8.19
$H_{TOT}$	Total horizontal force as defined by Equation 8.43
$H_w$	Horizontal force acting on bottom tip of wedge beam as defined in Figure 8.19
$K$	Earth pressure coefficient function
$K_a$	Earth pressure coefficient function: active state
$K_o$	Earth pressure coefficient function: at-rest condition
$K_p$	Earth pressure coefficient function: passive state
$K'$ , $K''$ , $K'''$ and $K''''$	Various coefficient functions as defined by Equation 7.12
$L_c$	Circumferential crack length
$L_t$	Broken piece size as defined in Figure 2.5 (see Equations 4.1 - 4.5)
$L_w$	Broken piece size as defined in Figure 2.5
$L_b$	Broken length, $(\sigma_t l / \gamma_w)^{1/2}$ (see page 71)
$N$	Normal force
$P$	Earth pressure associated with earth pressure equations; or, Ride-up force tangential to cone surface as defined by Equation 8.47
$P_a$	Force exerted by rubble: active thrust
$P_{bh}$	Force exerted by rubble: horizontal force acting on bottom support
$P_{bv}$	Force exerted by rubble: vertical force acting on bottom support
$P_o$	Force exerted by rubble: total wall thrust (at-rest condition)
$P_p$	Force exerted by rubble: passive resistance

$P_{\text{pred}}$	Force exerted by rubble: predicted
$P_{\text{simul}}$	Force exerted by rubble: simulated
$P_{\text{wh}}$	Force exerted by rubble: horizontal force acting on wall
$P_{\text{wv}}$	Force exerted by rubble: vertical force acting on wall
$R$	Rubble force defined in Izumiya et al's model (Equation 2.23)
$R_s$	Rate of ice supply into the system
$R_c$	Rate of ice clearing from the system
$R_a$	Rate of ice accumulation in the system
RMS	Root-mean-squared value
$V$	Ice velocity
$V_s$	Vertical force acting on cone surface as defined in Figure 8.19
$V_t$	Vertical force acting on top tip of wedge beam as defined in Figure 8.19
$V_{\text{tot}}$	Total vertical force as defined by Equation 8.44
$V_w$	Vertical force acting on bottom tip of wedge beam as defined in Figure 8.19
$V_b$	Beam breaking load under transverse load
$V'_b$	Effective beam breaking load under bending and inplane compression as defined by Equation 8.5
$V_c$	Velocity of ice passing through a cross-section
$W_r$	Weight of rubble ice
$W_{rc}$	Weight of rubble ice displaced by front facet surface of a six faceted cone as defined by Equation 8.14

- $W_{rs}$  Weight of rubble ice displaced by side facet surface of a six faceted cone as defined by Equation 8.22
- $W_{ru}$  Weight of ride-up ice
- $W_{rue}$  Weight of ride-up ice displaced by front facet surface of a six faceted cone as defined by Equation 8.17
- $W_{rus}$  Weight of ride-up ice displaced by side facet surface of a six faceted cone as defined by Equation 8.24
- X,Y,Z Cartesian axes as defined in Figure 8.17
- $X'$  Axis with direction perpendicular to side facet at waterline as shown in Figure 8.17
- $d_{cr}$  Breaking width of ice beam as defined in Figure 8.13
- $d_s$  Projected width of side facet as defined in Figure 8.16
- c Cohesion
- $e_o$  Initial void ratio
- h or  $h_r$  Rubble height
- $h_b$  Vertical distance of bottom level of a wall section from maximum height of rubble as defined in Figure 7.28
- $h_n$  Height of neck section from waterline
- $h_{rc}$  Equivalent rubble height at front facet as defined by Equation 8.13
- $h_{rs}$  Equivalent rubble height at side facet as defined by Equation 8.18
- $h_{rf}$  Rubble height at edge of front facet as defined by Equation 6.18

$h_{rm}$	Maximum rubble height at front facet as defined by Equation 6.35
$h_r$	Rubble height at the side as defined by Equation 6.22
$h_{ru}$	Ride-up height
$h_{ru,c}$	Equivalent ride-up height at front facet as defined by Equations 8.15 or 8.16
$h_t$	Vertical distance of top level of a wall section from maximum height of rubble as defined in Figure 7.28
$l_c$	Characteristic length of ice sheet as defined by Equation 2.8
$p$	Pressure
$p$	Porosity
$t$	Thickness of ice
$w$	Horizontal distance from $h_r$ to $h_{rm}$ as defined in Figure 6.17
$w_f$	Width of facet at waterline
$w_{r,c}$	Average width of rubble at front facet (assumed equal to $w_{ru,c}$ )
$w_{r,s}$	Equivalent width of rubble at side facet as defined in Figure 8.23
$w_{ru,c}$	Average width of ride-up at front facet as defined in Figure 8.12
$x_F$	Direction cosine of frictional force in x-direction as defined by Equation 6.28
$x_N$	Direction cosine of normal force in x-direction as defined by Equation 8.26
$z$	Free-board of structure
$z_F$	Direction cosine of frictional force in z-direction as defined by Equation 6.29
$z_N$	Direction cosine of normal force in z-direction as defined by Equation 8.27
$\alpha$	Cone angle

$\alpha_{ave}$	Average cone angle
$\alpha_p$	Inclination of total wall thrust, $P_o$ , from the horizontal
$\alpha_s$	Cone angle at side of cone
$\gamma$	Weight density of ice
$\gamma_b$	Bulk weight density of granular material
$\gamma_w$	Weight density of water
$\theta$	Angle between plane bcd and plane abd as defined in Figure 8.17
$\theta_{cr}$	Angle between radial crack and x-axis
$\iota$	Angle of inclination of rubble surface
$\mu$	Ice-structure friction
$\mu'$	Effective ice-structure friction
$\nu$	Poisson's ratio
$\xi$	Resolution factor for 2-D interaction as defined by Equation 2.2
$\xi_1$	Resolution factor as defined by Equation 2.5
$\xi_2$	Resolution factor as defined by Equation 2.6
$\xi_{3D}$	Resolution factor for 3-D interaction with smooth cone as defined by Equation 2.25
$\xi_{3D,f}$	Resolution factor for 3-D interaction with faceted cone as defined by Equation 4.6

$\rho$	Density of ice
$\sigma_f$	Flexural strength of ice
$\sigma'_f$	Effective flexural strength of ice, including effect of in-plane compression, as defined by Equation 8.53
$\sigma_h$	Horizontal stress
$\sigma_n$	Normal stress
$\sigma_v$	Vertical stress
$\tau$	Shear stress
$\phi$	Angle of internal friction
$\phi_b$	Angle of base friction
$\phi'_{bh}$	Angle of effective base friction
$\phi_{cv}$	Angle of internal friction corresponding to constant volume strength
$\phi_d$	Angle of inter-block friction as defined in Figure 5.8
$\phi_p$	Angle of internal friction corresponding to peak strength
$\phi_r$	Angle of repose
$\phi_w$	Angle of wall friction
$\phi'_{w}$	Angle of effective wall friction
$\phi_i$	Angle of ice friction
$\psi$	Angle of friction force with respect to the x-axis as defined in Figure 8.17

# **Chapter 1 Introduction**

## **1.1 Background**

Ice mechanics and ice engineering research in Canada have assumed increased importance due to the growing interest in exploration of natural resources and industrial developments in its Arctic offshore regions. A major driving force behind the heightened interest has been hydrocarbon developments in the continental shelf in the Arctic and sub-Arctic seas. Canada has a vast infrastructure dependent on oil and gas and there are no competing fuels on the horizon. Oil and gas are predicted to continue to make up about 60% of Canada's energy consumption for the next two decades, as predicted by Canadian government for the year 2020 (Natural Resources Canada, 1993). The total recoverable reserves for the Frontiers was conservatively estimated at 22 Billion Bbls of oil and 275 Trillion Cfs of gas, with the largest reserves being located at the Grand Banks and the Beaufort Sea (Natural Resources Canada, 1993). Such vast quantities of petroleum reserves ensure a secure source of future supply for Canada in place of the rapidly depleting oil reserves in Western Canada. This has heightened the need for improving current technology to lower the costs of oil production from ice covered areas, and stimulated significant activity in the development of novel offshore structures during the past two decades.

The development of new concepts and designs for engineering structures in ice infested waters poses many challenging problems related to determination of ice loads and assessment of the overall safety of such structures. Conical form at the water line has been

considered to be better than vertical surfaces in protecting vulnerable structures operating in these regions and helping them to withstand severe ice forces, since this configuration reduces ice loads by causing ice features to break in bending. Conical structures also provide a natural and smooth transition from a wide-base to a narrow deck supporting the superstructure.

Although great efforts have been put into both theoretical and experimental investigations concerning ice forces on conical structures [see Wessels and Kato (1989)], serious problems still remain unsolved. A review of the ice load prediction methods for conical structures by Chao (1992) reveals a high degree of uncertainty in ice force prediction, mainly due to the lack of full scale measurements and the absence of proper analytical tools to model the complex three dimensional ice-structure interaction problem. It results in "over-designing" to compensate for current lack of knowledge. Such overdesign leads to excessive construction costs and reduces a project's feasibility. Furthermore, early experimental and theoretical work on ice-cone interaction were entirely devoted to smooth cones which had narrower necks relative to the water line diameter. However, by mid-1980's it had become apparent that new designs, incorporating sloping flat faces (facets) and wide necks above the ice waterline, may be more cost effective and practical, i.e., ODECO AMDP (Chabot, 1985). Such a structure is presently considered for operation in Russian waters off Sakhalin Island. These structural concepts can also be implemented in structures located in less severe ice environments, i.e., bridge piers and lighthouses.

No prior study related to ice forces on faceted cones existed before 1988 (Croasdale

and Muggeridge, 1993). The fundamental interaction processes were not fully understood. Since the flat facet and its sharp corners were unique to a faceted cone, it was suspected that such features would lead to an ice breaking and clearing process substantially different from that of a smooth cone. In considering ice forces on these structures, there was a concern with the validity of existing theories in predicting ice forces knowing that their geometry was significantly different from the true conical form. The anticipation of rubble accumulation in front of the structure also led to a concern that the ice clearing forces would be greater than the predicted values, obtained using current theories. In order to enhance the understanding of how ice would fail and clear around such structures, and to develop a proper ice load estimation formulae, model testing and better theoretical formulation of the interaction were proposed.

In 1988 the Memorial University of Newfoundland (MUN) collaborated with the Institute for Marine Dynamics (IMD) and the Institute of Mechanical Engineering (IME) of the National Research Council of Canada (NRC), Esso Resources Canada Limited (ERCL), Exxon and Mobil in a university-industry program to perform an extensive series of physical model tests in order to better understand how ice floes and ridges would fail and clear around such structures, and how well existing theories predicted the global loads. The results of the various components of the program are described by Croasdale and Muggeridge (1993). While results of each series of tests have been separately documented [Metge and Weiss (1989), and Metge and Tucker (1990) for ERCL's test series; Irani et al (1992) for IME's series, and Lau et al (1993b) for IMD's series], and published [Irani and Timco (1993);

Timco et al (1993); Lau et al (1993a); Izumiya et al (1993, 1994) and Wang et al, (1997)], only very simple analyses were performed and they were fragmented in nature. Many aspects of the interaction processes and the effects of various factors on ice loads were not fully addressed.

I conducted the model test program in IMD with the assistance of Mr. J.R. Tucker of MUN during my stay in the institute. Analysis of the results from the IMD series, supplemented by additional data analysis of the accompanying series, and subsequent ice force modelling form the bulk of the research effort for this thesis. Focus is devoted to level ice tests only.

## **1.2 Scope and Objectives**

The main objectives of this study are:

- (i) To improve the understanding of the interaction processes and failure mechanisms of a level ice field against a faceted cone during continuous ice breaking, and
- (ii) To provide engineers with a set of easy-to-apply formulae for ice load calculations.

In this work, the major issues addressed are:

- (i) Whether the existing theories, proposed based on earlier experiences with smooth cones, were accurate enough for predicting ice forces on comparable faceted cones; and,

- (ii) If the existing theories did not adequately predict ice forces on faceted cones, what modifications were necessary to correct the deficiencies.

From a more practical point of view a load prediction model, applicable to the faceted cone shape, was to be developed for design purposes. The model should reflect accurately the dominant interaction processes generated by this unique shape.

While an improved ice force prediction model is proposed here to suit the practical need of designers, the theoretical modelling effort is kept to a minimum. Existing analyses of ice force on smooth cone were used when deemed appropriate. The improved model represents the most comprehensive attempt to incorporate fundamental processes in its problem treatment and forms a new conceptual framework for future model refinements.

### **1.3 Approaches and Methodologies**

This research investigation consists of experimental, numerical, and theoretical studies described here in three parts. The approach promises the most versatile and relevant procedure for improving our understanding of the ice-structure interaction problem for the multifaceted cone.

In part one, the pilot series of physical model tests are reported. The physical model tests were planned to provide a clear insight into the interaction processes by combining relevant observations and interpretation of results. The ice forces corresponding to peak load events were identified for each test, along with the associated interaction processes. The observed unique interaction processes helped to formulate a conceptual model, which would

provide a focus and outline of the phenomena to be investigated, and the methods to be used to investigate these phenomena.

The model tests also provided a unique set of experimental data to assess the validity of existing formulae for predicting ice loads on a faceted cone. Comparisons were made of the experimental results with the predictions of a leading theoretical model developed for computing ice forces on smooth cones. The comparison further underlined the deficiency of existing theories in predicting ice forces on faceted cones.

It became evident during the early part of the model tests that the ice pile-up induced by the flat facet was a typical behaviour of ice around the faceted cones as opposed to the smooth cones. A proper understanding of the particulate mechanics and the formation process of ice rubble held the key to further studies in this area; this forms the focus of part two of this research. Theories in the field of particulate mechanics were examined, and a new rubble model was developed from appropriate theories to predict the geometry of a fully developed rubble and the load it exerted on the structure. The geometry of the rubble was deduced based on a simple interaction geometry and mass balance considerations; whereas the equations for calculating the boundary forces exerted by the rubble at its interfaces with the wall and the base support were empirically formulated from a rigorous interpretation of a series of numerical simulations of earth pressure on a retaining wall. The numerical simulations were carried over a broad spectrum of interaction conditions using the discrete element method (DEM), implemented in a 2-D version of the computer code DECICE.

Part three was devoted to the development of a new ice force model which took into

account the main features of the interaction processes associated with faceted cones. In view of the existence of many ice breaking models, detailed modelling of the phenomenon of ice breaking under load was not carried out in this work; instead, the existing analytical models of ice forces on sloping structures were critically assessed through an extensive comparison with experimental data, and a base model of ice breaking was selected. This base model was further incorporated into the new rubble model developed in part two, resulting in a set of mathematical formulae which were established based on experimental observations and basic mechanics of ice. These formulae represent in a concise and general fashion the description of ice breaking and clearing phenomena, the observed relationship between the processes, the basic mechanisms that underlie such relationships, and the relationships among relevant ice and structure parameters.

#### **1.4 Organization of the Thesis**

This thesis consists of a total of nine chapters. The first two chapters form the introductory study to the thesis. Chapter 1 discusses the issues addressed in this work. The relevant background, approaches and methodologies are briefly described. Chapter 2 consists of a literature review, which focuses on previous studies and modelling of ice loads on sloping structures. The existing theoretical models and the associated ice-structure interaction processes observed in relevant model tests are summarized, with the limitations and shortcomings of the previous studies discussed. The subsequent seven chapters, viz., Chapters 3 to 8, are divided into three parts, corresponding to the three stages of this study

already mentioned above.

Part I documents the results of the experimental investigation, which consists of two chapters, Chapters 3 to 4. Chapter 3 describes the tests and summarizes the results. Chapter 4 identifies the salient aspects of the ice cone interaction processes, and presents the analysis of peak ice loads. The last section of Chapter 4 serves as a conclusion of this part, where the findings are summarized and a conceptual model is presented, which forms the framework for further model development.

The unique pile-up process of ice around a faceted cone forms the focus of Part II. This part consists of three chapters: Chapters 5 to 7, which document the results of a subsequent rubble modelling. Chapter 5 summarises the constitutive behaviour of a rubble under load. The deformation characteristics of a rubble in front of an inclined wall are identified, and the existing techniques for load calculation are examined. Chapter 6 presents a rubble model for predicting the geometry of an ice rubble in front of a multi-faceted cone. Chapter 7 consists of two parts which summarize the results of a series of numerical simulations using a discrete element code. The first part examines the shear strength of the rubble via a series of shear test simulations; whereas, the second part presents a set of empirical equations to compute the load exerted on an inclined wall and the base support by the rubble.

Chapter 8 constitutes Part III of this thesis. This part is dedicated to the presentation of a new ice force model. In the first half of Chapter 8, a base model for ice breaking is selected for incorporation into new rubble model developed in Part II of this thesis. In the

latter part of Chapter 8, the new ice force model is developed, documented, and validated.

The final chapter summarizes the research efforts and contributions made throughout this study. Conclusions arising out of this study and recommendations for future work in this area are given in this chapter.

## **Chapter 2   Literature Review**

The faceted cone is a structure proposed for future oil and gas developments in the Arctic and sub-Arctic regions; consequently, there is no theoretical and/or experimental studies on such structures available in open literature. Since the faceted cone possesses a basic conical form with inclined surfaces, a review of studies carried out on inclined structures, i.e., conical structures and inclined planes, could be helpful to the present research. Thus, the literature available on ice interaction with an inclined structure is reviewed and discussed in this chapter. Emphasis is laid on the available theoretical modelling of ice loads on the structure and the observed ice-structure interaction processes; the physical modelling of ice load is only briefly discussed.

Over the last two decades, significant progress has been made in developing models to predict ice loads on inclined structures (including conical structures and sloping planes). Extensive reviews of the existing analytical and empirical methods were given by Sodhi (1987), Marcellus et al (1988), Cammaert and Muggeridge (1988), and Sanderson (1988). Wessels and Kato (1989) reviewed the ice failure modes around conical structures, and summarized the available model scale and full scale measurements. Evaluations of the performance of several methods were given by Croasdale (1980), Timco (1984a), Marcellus et al (1988), and Chao (1992).

Section 2.1 gives an overview of the dominant interaction processes as observed in model tests. The subsequent theoretical models are summarized in Section 2.2. The work

described in this thesis was conceived as part of a larger project with collaboration among many participants. A general overview of the whole test program is given in Section 2.3. The major findings reported by other participants are also summarized in the section. Section 2.4 compares various modelling approaches and gives a state-of-the-art assessment of the present available expertise on ice force predictions on conical structures.

## **2.1 Ice-Structure Interaction Processes**

### **2.1.1 Conical Structures**

The following description of the interaction between a conical structure and a level ice sheet is based on the studies reported by Croasdale (1980), Sodhi (1987), Wessels and Kato (1989), and others. Additional details of the failure processes and ice forces encountered by sloping structures have been obtained from experiments carried out by Haynes et al (1983), Wessels (1984), Kato (1986), Hirayama and Obara (1986), Clough and Vinson (1986), Maattanen (1986), Lau et al (1988), and Lau and Williams (1991).

As an ice sheet advances toward a conical structure, local crushing of ice occurs at the ice-structure interface. The local crushing creates an interaction force normal to the structure surface. In addition, because the ice is sliding upwards relative to the surface, a frictional force is also generated. These forces create in-plane and out-of-plane forces, and an edge moment; and a complex three dimensional stress state is induced in the ice. As the ice sheet continues to advance, the stresses increase until failure of the advancing ice sheet occurs in either one or a combination of the following failure modes: bending, crushing,

shear, buckling, and splitting. Observations show that the bending failure is more dominant than the other modes of failure under interaction conditions such as low inclination angle ( $10^\circ$  to  $60^\circ$ ), low ice-cone friction coefficient, small ice thickness, and low speeds of ice movement.

For a bending failure of ice sheet, the failure mechanism is governed by the flexural stresses induced in the ice in both radial and circumferential directions. If the cone is small compared to the ice thickness, radial cracks radiating at  $60^\circ$  intervals initiate the failure. The peak load, however, occurs when circumferential cracks develop and wedges of ice break off. With increasing cone diameter the curvature of the cone surface at the waterline decreases, and the maximum tensile stresses of the ice cover change from circumferential direction to the radial direction. This process causes the ice sheet to fail first circumferentially and thereafter radially.

Failure modes other than bending can dominate under specific loading conditions. With increasing steepness and roughness of the cone surface, or ice thickness, the failure mode also changes gradually from bending to shear or crushing. At higher speeds, the failure mode changes abruptly from bending to shear or crushing due to dynamic effects (Wessels, 1984; and Haynes et al. 1983). The speed at which the transition of failure modes takes place was found to increase with the increase in the inclination angle (Haynes et al. 1983).

The influence of shear stresses on determining failure modes becomes more important with increasing ice thickness and is finally predominant for thick ice fields (Maattanen, 1986). Observation of actual fracture patterns in thin ice reveals that pure

bending occurs when circumferential cracks form at distances slightly higher than the characteristic lengths; and with increase in thickness, the average length of broken pieces decreases which may indicate a combination of bending and shear failures (Wessels, 1984; and Lau et al., 1988).

Michel (1978) has described the condition where ice sheets interact with inclined structures having an inclination to the horizontal of greater than 75°. For structures in this category, crushing will generally take place before bending.

After the local failure of an ice sheet the broken ice pieces, pushed by the approaching ice sheet, rotate until they are parallel to the inclined surface, and begin to ride up the face of the structure (which has been termed ride-up); then the ice clears around and slides down the back side of the cone. As the ice pieces rotate, water drag and inertia forces are developed on the structure. The broken ice pieces sliding up the inclined surface also develop frictional and gravity forces on the surface.

The geometry of structure above the waterline has a significant influence on the way the broken ice clears around the structure. On a cone with relatively narrow superstructure, the ice can clear around the structure easily; however, for a wide conical structure or a sloping plane, the ice may reach the superstructure and roll back onto itself, creating additional ice on the slope of the structure, which may lead to an ice rubble pile in front of the structure, interfering with the ice breaking process.

If the ice is weak, the load applied to the unbroken ice sheet by the broken ice pieces, as they are being pushed up the cone surface, may cause the ice sheet to fail in bending with

the broken ice pieces sliding down the front of the cone.

### 2.1.2 Sloping Planes

Many experiments have been conducted to study the features of ice failure processes and the associated ice loads on narrow and wide sloping planes (Zabilansky et al., 1975; Sorensen, 1978; Haynes et al, 1983; Timco, 1984b; Frederking and Timco, 1985; Michel and Picard, 1989; Valanto, 1989; and Finn, 1991). The observed failure modes and the interactions are similar to those described in the previous section. The features of ice failure processes, particular to ice interaction with sloping planes, were summarized as follows (Sorensen, 1978; and Timco, 1984b):

As the ice sheet is lifted upwards by a narrow plane, two radial cracks extend outward from the corners of the plate at an angle of about  $30^\circ$  according to Michel and Picard (1989) and Frederking and Timco (1985), and  $45^\circ$  according to Finn (1991), to the sides of the plate, forming a cantilever beam with the width slightly wider than the structure. Occasionally, a radial crack also emanates from the centre of the plate (Finn, 1991; and Michel and Picard, 1989). When the flexural stress in the ice sheet exceeds the strength of the ice, a circumferential crack forms at a finite distance from the structure, and the peak load is attained. Under some circumstances, the peak force could occur during the radial cracking (Frederking and Timco, 1985).

Upon further advance, the broken ice slabs slide up the front face reaching the top of the structure. The ice which overhangs the sides of the inclined plane usually breaks off due

to its own weight. In comparing with conical structures, the ice clearing around a sloping plane is less efficient. The broken ice slabs usually reach the top of the structure. If they are not cleared off, they may roll back onto themselves, leading to an ice rubble pile in front of the structure, which interferes with the ice breaking process.

## 2.2 Models for Ice Force Predictions

The development of computational methods for ice loads on sloping structures has been limited because of the lack of knowledge about the dynamic nature of interactions, and the complex rheological behaviour of ice and boundary conditions during the interaction. In order to meet the practical needs of designing structures with conical forms, various computational methods have been developed by making assumptions that would permit analysis of the problem using available theoretical procedures. The simplest method to treat the interaction is to assume that the structure is rigid and that only the deformation and failure of ice sheet are considered. It should be noticed that all the analytical formulae were derived based on observations from small-scale model tests with gentle sloped cones (i.e., ~45° to the horizontal), thin ice, low friction coefficient and low ice speed, in which bending failure is dominant.

In the following sections, several approaches for predicting sheet ice loads on inclined structures are reviewed, which cover essentially all the important known models, and are representative of the available approaches. These approaches generally fall into two basic types:

- (i) Analytical formulations based on elastic or plastic analysis, and
- (ii) Semi-empirical formulae based on experimental data.

### **2.2.1 Analytical Formulations**

Classical analytical procedures have been adopted to investigate the effects of an ice sheet impinging on a single conical structure. The forces depend on the mechanisms of failure and the geometry of the structure. Usually dynamics, creep and other effects are completely neglected with some justification.

#### **2.2.1.1 Croasdale's Approach**

Croasdale (1980) proposed a simple two-dimensional theory for wide structures based on the theory for beams on elastic foundations (Hetenyi, 1946). The ice sheet was treated as a semi-infinite elastic beam on elastic foundation subjected to a horizontal force,  $F_x$ , and vertical force,  $F_z$ , at one end. At the instant of first contact, the relationship between  $F_x$  and  $F_z$  can be derived by resolving the forces, viz.,

$$F_x = F_z \xi \quad (2-1)$$

where  $\xi$  is called resolution factor defined as:

$$\xi = \frac{\sin\alpha + \mu_r \cos\alpha}{\cos\alpha - \mu_r \sin\alpha} = \tan(\alpha + \tan^{-1}\mu_r) \quad (2-2)$$

with  $\alpha$  being the angle of the slope from the horizontal and  $\mu_s$  the friction coefficient.

The maximum value of  $F_x$  is limited by the flexural (tensile) strength of the ice sheet with an vertical edge loading supported by an elastic foundation. The horizontal force per unit width of the structure, generated at the instant of first failure of ice, is given by:

$$\frac{F_x}{D} = 0.68\sigma_f \left( \frac{\gamma_w t^5}{E} \right)^{\frac{1}{4}} \xi \quad (2-3)$$

where D is width of the structure;  $\sigma_f$ , bending strength;  $\gamma_w$ , weight density of water;  $t$ , ice thickness; and E is elastic modulus of ice. For subsequent interaction, an extra force is required to push the ice up the slope. The corresponding total force experienced by the structure is

$$\frac{F_x}{D} = \xi_1 \sigma_f \left( \frac{\gamma_w t^5}{E} \right)^{\frac{1}{4}} + zr\gamma\xi_2 \quad (2-4)$$

where:

$$\xi_1 = 0.68\xi \quad (2-5)$$

$$\xi_2 = \xi(\sin\alpha + \mu_s \cos\alpha) + \frac{\sin\alpha + \mu_s \cos\alpha}{\tan\alpha} \quad (2-6)$$

with  $z$  being the free-board, and  $\gamma$  the weight density of ice.

In the above relationship (Equation 2.4), the first term (on right hand side) can be considered as the force necessary to break the ice, and the second term can be considered as the force necessary to push the ice pieces up the sloping structure. It could be a simplified 2-D relationship for a wide structure, but as the structure width decreases relative to the characteristic length of ice, the zone of ice failure will be wider than the structure itself, and most of the ice pieces will not necessarily ride-up the structure but clear around it. For narrow structures, Croasdale suggested a simple correction to adjust the two dimensional force by the ratio of the length of the circumferential crack divided by the structure width, i.e., multiplying the ice breaking component by

$$1 + \frac{\pi^2 l_c}{4D} \quad (2-7)$$

where  $l_c$  is the characteristic length for the plate given as

$$l_c = \left( \frac{Et^3}{12\gamma_w} \right)^{\frac{1}{4}} \quad (2-8)$$

However, other investigators (Ralston, 1977; and Nevel, 1980 and 1992) have given more rigorous analyses of the three-dimensional problem.

In 1994, Croasdale et al extended their three-dimensional analysis to incorporate adjustments for in-plane compression as well as effects of ice rubble build-up in front of the structure. The in-plane compression creates a compressive stress in the ice sheet increasing its effective flexural strength. The increase in load was computed through an iterative process. The modifications for the presence of ice rubble include: the force necessary to push the advancing ice sheet through the ice rubble; the additional force necessary to push the ice blocks up the slope through the ice rubble; and, the additional force necessary to lift and shear the ice rubble on top of the ice sheet. Croasdale pointed out that the model was simple to use and could be easily incorporated into a probabilistic methodology. He further asserted that the model gave results similar to more complex models, i.e., Nevel's model (1992) although simplistic assumptions had been made.

His model is based on simple mechanics and provides a good appreciation of the important roles various parameters and processes play on ice force development. It can be a useful starting point for the development of more complex approaches, and will be examined in a greater detail in Chapter 9.

### **2.2.1.2 Nevel's Approach**

In a three dimensional case when the zone of failure extends wider than the structure, the failure occurs after the formation of radial cracks when a circumferential crack takes place. Therefore, the simple beam theory has to be replaced by a more complicated plate theory, and the ice force problem is reduced to the prediction of the forces necessary to:

- (i) Initiate radial or circumferential cracks in a semi-infinite floating ice sheet,  
and
- (ii) Fail a series of truncated ice wedges, formed by radial cracking of the ice, as  
it advances against the cone.

Nevel (1965) performed numerical integration to determine the bending moment required to initiate failure of an semi-infinite floating ice plate. He treated the problem as a semi-infinite plate on an elastic foundation with a load applied near the ice edge. The maximum deflection which occurred at the edge under load, the moment which caused the initial radial cracking of the plate, the distance from the edge at which a circumferential crack would occur, and the moment that caused the circumferential crack were calculated and given in graphical and tabulated forms.

If the failure was initiated by radial cracking, a series of truncated ice wedges would form, and the subsequent failure was reduced to the prediction of forces necessary to fail these wedges. Nevel (1972) gave the failure force  $P$  on the tip of a truncated wedge to be:

$$\frac{6P}{b_o \sigma f^2} = 1.05 + 2.0\left(\frac{a}{l_c}\right) - 0.5\left(\frac{a}{l_c}\right)^3 \quad (2-9)$$

where  $a$  is the distance from the tip of the wedge over which it is loaded, and  $b_o$  is a constant defining the width of the wedge,  $b$ , in the equation

$$b = b_o x \quad (2-10)$$

with  $x$  being the distance along the wedge. His analysis compares favourably with published data on the ultimate load carrying capacity of ice sheets.

Nevel (1980) further analysed the wedge on an elastic foundation subjected to an in plane force and edge moment and he considered the buckling and bending of this wedge. An exact solution was obtained by means of a contour integral in a complex plane. In general, the solution shows that this additional moment is small because the deflection of the ice wedge is small when failure of the wedge occurs. However, the effect of in-plane compression becomes increasingly important for steeper cones and thicker ice.

Recently, Nevel (1992) refined the existing analytical theories and presented a rigorous treatment of ice forces and moments on conical structures from ice floe. The new theory included either simultaneous or sequential breaking forces and the ride-up forces. The ice cover was treated as an idealized truncated wedge based on his earlier work (1980). Of particular significance is the development of forces from ice sliding on the surface of the cone. The analysis identified where the forces acted on the cone, and hence allowed the determination of moments. Furthermore, the in-plane compression and edge moment were incorporated in the solution.

In general, the cone could be multi-sloped, composed of a number of conical sections with the vertical neck of the cone being the smallest section. For each broken ice piece, the forces which act on the cone were determined along with those which were transmitted to the broken ice piece below. The analysis proceeded from the neck section to the waterline with a resultant ice load from the broken ice pieces acting on the floating ice wedges.

To calculate the wedge failure load, Nevel used his solution for the deflection of a wedge on an elastic foundation (Nevel, 1980) by considering the bending of a wedge beam, with its free end being acted on by a shear force, a bending moment, and a compressive horizontal force. For sequential breaking, it was assumed that the maximum load on the cone occurred when the centre wedge failed. Hence, the maximum force was the sum of force from the wedge nearest the centre which failed and all other wedges that did not fail. In simultaneous breaking, the breaking loads for all the wedges were summed.

A computer program was written which allowed sufficient variations of the input parameters permitting the simulation of realistic ice condition. His solution was rather complicated and too lengthy to be reproduced here and the reader is referred to the original paper for full details (Nevel, 1992).

#### **2.2.1.3 Ralston's Approach**

Croasdale's and Nevel's approaches were based on the theory of elastic plate or beam on elastic foundation. An analysis by Ralston (1977), was based on an elastic-plastic representation of the ice failure. He used three-dimensional plate theory, and plastic limit state analysis, where the work done by external forces was equated to the rate of energy dissipation. The use of an upper-bound procedure of plastic limit analysis led to a mathematical model for both sheet ice failure and ride-up on a conical structure. The derived formulae for the horizontal  $F_x$  and the vertical forces  $F_z$  were expressed as follows:

$$F_x = A_4[A_1\sigma_f t^2 + A_2\gamma_w t(D^2 + A_3\gamma_w t(D^2 - D_n^2))] \quad (2-11)$$

$$F_z = B_1 F_x + B_2 \gamma_w t(D^2 - D_n^2) \quad (2-12)$$

where  $D_n$  and  $D$  were top and waterline diameters of the cone, respectively;  $A_1$  and  $A_2$ , coefficients dependent on:

$$\frac{\gamma_w D^2}{\sigma_f t} \quad (2-13)$$

and  $A_3$ ,  $A_4$ ,  $B_1$  and  $B_2$  were coefficients dependent on the cone angle and ice friction. Values for the coefficients were given in his paper.

In both the equations given above (Equations 2.11 and 2.12), the last term (on the right hand side) is due to ice pieces sliding over the cone surface, and the other terms result from ice breaking. According to observations, radial cracks occur before circumferential cracks and not simultaneously. These circumferential cracks give the maximum assumed ice loading condition. The elastic analyses of failure follow closely each stage of crack development, while the simultaneous formation of the circumferential and radial cracks assumed in Ralston's model is not realistic. Therefore, Ralston's plastic approach tends to overestimate the bending resistance of ice. Maattanen and Hoikkanen (1990) modified Ralston's solution to omit the contribution of energy dissipation due to radial cracking. This result gave a better fit to their model test data and field measurements. Nevertheless,

Ralston's theory has been regarded widely to be satisfactory in predicting ice forces after extensive comparisons with experimental data.

#### **2.2.1.4 Maattanen's Approach**

Full-scale measurements (Maattanen and Mustamaki, 1985; Hoikkanen, 1985) have indicated that a rubble pile is likely to form in front of a conical structure. Previous scale model tests and theoretical models do not consider the effects of pile-up.

Maattanen (1986) refined the analytical models by taking into account the effect of the ice rubble pile on the bending moment distribution in the ice sheet in front of the structure. The model is formulated using finite element methods capable of both bending and buckling analysis. A constant thickness ice sheet is moving laterally and breaking against an inclined wall under a triangular shaped ice rubble pile. The rubble pile is treated by using classical Coulomb's soil mechanics. The two dimensional model is based on the bending theory of a beam on elastic foundation. The loading consists of horizontal and vertical edge reaction loads and distributed vertical and horizontal rubble loads. Different ice failure modes are considered.

An example calculation shows that the ice rubble pile loading enhances edge crushing and shearing, changes the location of the maximum bending moment, and results in smaller broken floes than predicted by previous models. With the same bending moment level the ice load could increase by about 50% due to the ice rubble.

In a subsequent work, Maattanen and Hoikkanen (1990) extend the analysis to a three

dimensional case. The beam theory is replaced by a more complicated wedge plate theory. The new ice force calculation procedure is compared with results of full scale measurement and scale model tests. The correspondence between the calculations and measurements appears to be good.

### 2.2.2 Empirical Formulae

Empirical and semi-empirical formulae have been proposed based on small scale model tests (Afanas'ev et al, 1971; Edward and Croasdale, 1976; Pearce and Strickland, 1979; Brooke, 1981; Hirayama and Obara, 1986; and Kato, 1986). The total force was customarily split into two components:

- (i) The force essential for breaking the ice, and
- (ii) The force necessary to cause the broken ice to slide up the surface.

Dimensional analysis has been the main tool in finding the form of equations. The coefficients in each formula are then determined by linear regression analysis of data from respective experiments. The empirical formulae are summarized in this section. The test variables for each test data sets, and the coefficients of the respective formula are listed in Table 2.1.

Afanas'ev et al (1971) proposed the following empirical relationship based on elastic plate theory:

$$F_x = a_0 \sigma f^2 \tan \alpha \quad (2-14)$$

where

$$a_o = \frac{S_x}{1.93l_c} \quad (2-15)$$

with  $S_x$  being the length of the circumferential crack given as

$$S_x = 1.76 \left( \frac{D}{2} + \frac{\pi l_c}{4} \right) \quad (2-16)$$

Their results give only the breaking component of the force exerted by the ice sheet. Although this formula underestimates the force, the effects of ice strength, ice thickness, and cone angle are clearly included and the trends seem reasonable.

Edwards and Croasdale (1976) performed a series of model tests on 45° cones with a friction coefficient of 0.05. They dimensionally argued that the horizontal force  $F_x$  on the cone should be

$$F_x = a_o \sigma f^2 + a_1 \gamma D t^2 \quad (2-17)$$

where  $a_o$  and  $a_1$  are constants. The first term is the ice force caused by ice breaking, and the second term is the force generated due to ice riding up the structure slope. The ride-up force component is a function of  $D$  and  $t^2$ , while the breaking component is independent of the width of the cone at waterline. The form of the empirical expression is similar to Ralston's plasticity model except that the ice ride-up component contains  $Dt^2$  rather than  $D^2t$ . Ralston

(1977) commented that if the ice clearing term was re-written in terms of  $D^2t$ , the coefficients would also be approximately those computed by his analysis for the test conditions. Data from model tests showed reasonable agreement.

Pearce and Strickland (1979) claimed that the equation

$$F_t = a_0 \sigma f^2 + a_1 \gamma D^2 t \quad (2-18)$$

fitted their experimental data.

Brooks (1981) adapted the general form of ice resistance equation for an ice breaking ship to fixed, upward-breaking, conical structures as:

$$F_t = a_0 \sigma f^2 + a_1 \gamma D^{1.3} t^{1.7} + a_2 \gamma D^2 V^2 \quad (2-19)$$

where  $V$  is the velocity of the ice. The first term is the ice breaking component, the second term is the ice ride-up component, and the third term accounts for the inertia effects of the moving ice sheet. Dimensional analysis yields relationships between the exponents in each term of the equation. The coefficients,  $a_0$ ,  $a_1$ ,  $a_2$ , and the exponents were determined from a limited data set derived from model tests with a 45° cone. The test variables included waterline diameter, ice flexural strength, ice thickness, and ice velocity.

Based on their model tests and several other published test data sets, and dimensional analysis, Hirayama and Obara (1986) proposed the following formula:

$$F_x = a_0 \sigma_f t^2 \left( \frac{D}{l_c} \right)^{0.34} + a_1 \gamma \xi D^2 t \left( \frac{z}{D} \right) \left( \frac{1 - \frac{z \tan \alpha}{D}}{\sin \alpha} \right) \quad (2-20)$$

Their results agreed well with other published test data and with the theoretical results of Ralston (1977). However, the data showed a slight dependency of ice breaking component on  $(D/l_c)$ , and such dependency was not observed in previous tests. Ralston explained that the apparent discrepancy was due to the small values of  $(D/l_c)$  tested by other investigators, which was typically limited to a range of less than 0.5. When  $(D/l_c) \ll 1$ , there will be no dependence on the cone diameter.

Kato (1986) published the following empirical formula:

$$F_x = a_0 \sigma_f t^2 + a_1 (D^2 - D_a^2) \gamma t \quad (2-21)$$

where the coefficients  $a_0$  and  $a_1$  were functions of cone configuration, coefficient of friction, and relative velocity between ice and structure. Kato kept the friction coefficient between ice and the structure at 0.09 in his model tests. Since the coefficients in the analytical expression were also dependent on the friction coefficient, he commented that it was necessary to investigate the dependency of these coefficients on the coefficient of friction.

### 2.3 MUN/ERCL/NRC Multi-Faceted Cone Tests

The experimental work conducted by the author was carried out as part of a larger project, entitled "MUN/ERCL/NRC Multi-Faceted Cone Study", a collaboration between

Memorial University of Newfoundland (MUN), the National Research Council Canada (NRC), Esso Resources Canada Limited (ERCL), Exxon and Mobil. As the major focus of the collaborative program was on ridges, only limited amount of data were obtained for level ice. Nevertheless, sufficient data on level ice were obtained from which valuable insights were gained and further mathematical modelling was made possible. In Section 2.3.1, the test program is briefly summarized, followed by a review of the findings contributed by other participants of the program. Emphasis is given to the level ice tests as they form the focus of the present study.

### **2.3.1 Test Program**

The principal objectives of the collaborative program were:

- (i) To understand how multi-year ice floes and ridges would interact with a multifaceted cone; and
- (ii) To investigate the effects of ice-structure interaction and the forces developed on faceted conical structures having the diameter of the above-water vertical "neck" to be almost as large as the waterline diameter.

Under the cooperative agreement, ERCL was responsible for the testing of two large scale models (1:10 and 1:20) in their outdoor basin in Calgary. The test program for MUN and NRC involved testing of small and a medium size models at NRC's indoor facilities -- a 1:50 scale model at the Institute for Mechanical Engineering (IME) in Ottawa and 1:25 and

1:50 scale models at the Institute for Marine Dynamics (IMD) in St. John's. With model tests conducted in four different scales, the results of this program could be used to determine the influence of any scaling effects on modelling ice-structure interaction as well as to provide a good comparison of model ice results with those where "naturally grown" saline ice was used, i.e., ERCL's series.

The principal dimensions of the prototype and model structures are shown in Figure 2.1 and summarized in Table 2.2; the circumscribed diameters are given for base, waterline, collar and neck dimensions. The dimensions are based on the geometry of several large exploration drilling structures designed for the Beaufort Sea. These concepts incorporate sloping flat faces (facets) and wide necks above the ice waterline. The structure is a six-faceted multi-angle cone having a circumscribed diameter of 115.5 m at the base, 30.0 m at the waterline and 23.1 m at the neck. A similar structure with a 11.6 m wide neck was also modelled to study ice interaction with cones having a smaller neck to waterline diameter ratio. The number of sides was chosen to emphasize the effect of using a multifaceted structure as distinct from a smooth cone. The slope of the sides, 5:6 or about 40°, was close to that proposed for several exploration drilling structures. The steep 2:1 slope section between the neck and the larger lower section was designed to prevent thick ice pieces from jamming against the neck.

During the IME test, the model was elevated to give a larger waterline diameter to increase the loads on the structure for reasonable accuracy of the measurement. This resulted in a scale of approximately 1:30 at the waterline for IME's tests. IME's tests were carried out

only with small-neck model, whereas both IMD's and ERCL's tests used both small and large neck models.

The ice sheet used in the IME and IMD test series was made of EG/AD/S model ice developed by Timco (1986), whereas saline ice was used in ERCL's test series. Flexural strength of the ice sheet was measured using several *insitu* beams. In most of the tests, the beam loads were measured by applying the load, both in the upward and downward directions. The elastic modulus, ice density and friction coefficient were also measured during all the tests except the IME series. Several measurements for the compressive and shear strength were also carried out for IMD's tests.

The models in IMD's and ERCL's facility were tested in a face-on orientation in which a facet was facing the approaching ice. Two additional orientations, edge-on and intermediate, were also tested in IME's series to examine the effect of orientation.

ERCL's series primarily focussed on ridge loads on structure. Data from the level ice tests were limited in nature which prevented detailed parametric evaluation. Nevertheless, ERCL's tests were performed in a much larger scale than the existing tank experiments, and natural grown ice were used, which provided valuable data for ice force model validation. On the other hand, IMD's and IME's test series provided a substantial amount of data in level ice under various highly controlled test conditions; hence they provided valuable data for detailed parametric evaluation and process identification.

The measured ice properties along with the configuration of the test condition in each test for ERCL's and IME's series are extracted from respective data report and reproduced

in Appendix A for quick reference.

### 2.3.2 Analysis of IME's Test Results

Rubble building is an essential part of the ice clearing process. Large amounts of rubble accumulate in front of the cone, and impose substantial loading on the structure and the intact ice sheet.

Izumiya et al (1994) analysed the model test data obtained in NRC-IME's facility, and provided quantitative information on the formation of the rubble field and its effects on the ice forces. They identified four types of rubble formed in front of the faceted cone with face-on orientation. A schematic of each rubble type is shown in Figure 2.2 with the following description given after Izumiya et al (1994):

(i) **A-Type:**

When the ice was strong, the ice pieces were very large compared to its thickness. The broken ice pieces would ride-up the model and fall off the side of the facet readily. The rubble field that formed was small.

(ii) **B-Type:**

This type of rubble field was commonly observed. To form this type of rubble field, the ice pieces which fell from the top of the cone would roll back down the front of the cone, and form a single-thickness rubble field as a steady-state condition.

(iii) **C-Type:**

This type of rubble field was also quite common. It was similar to the B-Type, except that the ice pieces broke up into many small pieces as they rolled down the front of the model, when the ice strength was low. This created a rubble field consisting of small ice blocks and crushed, mushy ice.

(iv) **D-Type:**

This type of rubble field was not common. It generally occurred when the ice was both thick and strong, and large pieces of ice would pile up in front of the cone.

The occurrence of various types of rubble was found to be a function of ice strength and ice thickness. Figure 2.3 shows the occurrence of the different types of rubble in strength-thickness domain.

The size of broken ice pieces played an important role in the rubble formation process and the ice force exerted on the model. Izumiya et al also performed a piece size analysis with data from the IME series. They reported the average sizes of ice pieces at the neck,  $L_w$  and  $L_l$ , were directly proportional to the parameter,  $L = (\sigma_i/\gamma_w)^{1/3}$ , as shown in Figure 2.4. The  $L_w$  and  $L_l$  are defined in Figure 2.5.

Izumiya et al also showed the ratio of the maximum ice force on the model,  $F_T$ , to that in the no rubble condition,  $F_{T0}$ , as a function of  $L/D$ , where  $D$  is the maximum waterline diameter of the model (Figure 2.6). The effects of the rubble field on the ice force were shown to be a function of ice piece size, ice strength and ice thickness. Based on their

tests, the rubble can increase the ice load by a factor of 1.5 to 2.5.

### 2.3.3 Analytical Models

Croasdale et al (1994) and Izumiya et al (1993) have developed ice force models concurrently based on observations from the multi-faceted cone experiments.

Croasdale et al (1994) compared his model with the experiments conducted in ERCL's outdoor test basin where ice rubble was present as shown in Figure 2.7. Their model is reviewed in Section 2.2.1.1. The size of the rubble was estimated from photographs. It should be noted that Croasdale et al only developed a theory for single slope cone structures, while the test structures were multi-sloped. The procedure by which he adapted his theory to the multi-sloped cone was not provided. Despite a large scattering of data at the lower measured load levels, his predictions agreed quite well with the experimental data, and provided an upper-bound to the measurements.

Izumiya et al (1993) extended Frederking and Timco's work (1985) on ice forces on inclined panels, and developed a model for ice force exerted on a face-on oriented cone with rubble present. By considering various force components on the ice sheet contacting the facet at the waterline as shown in Figure 2.8, they identified the following component for ice force:

$$F_z = V_B + V_R + R + (P + R)\sin\alpha \quad (2-22)$$

where  $F_z$  is the total vertical force;  $V_B$ , the vertical force required to break ice;  $V_R$ , the force

due to rotation of ice; R, the force due to the weight of ice rubble; and P is the force due to the weight and friction of ice pieces on the facet. For further details about each individual force components, please refer to their paper.

Izumiya et al established the validity of their model under no rubble condition by comparing their model predictions with the peak force in the initial portion of force time series, where ice rubble was absent, as shown in Figure 2.9. The figure shows good agreement between model prediction and measurements. Furthermore, the comparison shows that the existing model treatment of the ice force on conical structures is applicable to a faceted cone for the prediction of the ice breaking and ride-up forces, if the unique geometry of the faceted cone is properly considered.

Izumiya et al's model requires the vertical force R due to the weight of rubble to be known. To estimate the values of R, Izumiya et al introduced a rubble coefficient,  $C_R$ , where:

$$R = C_R \gamma \gamma_w w f_b l \quad (2-23)$$

with  $w$ , being the width of facet at waterline;  $\gamma$ , weight density of ice;  $\gamma_w$ , weight density of water; and  $f_b$ , the breaking length taken as half of the characteristic length. This rubble coefficient gave the relative index to the volume of rubble ice field. They established the relationship of the rubble coefficient as a function of ice thickness and strength by back-calculating the coefficient of each test using their model (Figure 2.10). Izumiya et al pointed out the complexity of rubble modelling, and the various factors affecting its

formation. Although, a functional relationship was observed between the rubble coefficient and the ice thickness and strength, the large scattering of data testifies to the complexity of rubble piling, and further study and accumulation of data are needed.

Izumiya et al's and Croasdale et al's models were formulated based on a limited set of test data. The functional relationships of the rubble geometry, ice mechanics, and clearing process to the basic ice and structure parameters had not been adequately established. The lack of such relationships from models severely limited their applicability to a wider range of ice and structure conditions. Despite the over-simplification of the interaction process, both models have clearly identified the interaction between the important force components, which may form the basis for future model developments.

#### 2.4 Comparison of Models and Discussions

Many of the empirical formulae reviewed so far take a common form:

$$F_x = a_0 \sigma_f t^2 + a_1 \gamma D^2 t \quad (2-24)$$

where the coefficients  $a_0$  and  $a_1$  are functions of structural shape, coefficient of friction and relative velocity. Since it is considered that the breaking component is due to bending which relates to a factor of  $\sigma_f t^2$ , and the ride-up component relates to a weight of ice mounted on the structure, the form is reasonable.

The fundamental limitation of the empirical formulae has been that they have modelled only a particular situation and hence cannot be extended to other situations. This

limitation leads to a wide range of values obtained for the respective coefficients. As shown by Croasdale (1980) and Chao (1992), a substantial variation of force prediction still exists, and a conclusive confirmation of the empirical approaches has not been reached.

Most analytical models for forces on a conical structure have calculated either  $F_x$  or  $F_z$ , and used the resolution factor,  $\xi$ , to calculate the other force component, i.e., Equation 2.1. The resolution factor is theoretically derived for a sloping plane; and, therefore, it would hold for forces on an inclined plane only. For a cone local ice failure and deflection of the sheet distributes the force around the circumference. Bercha and Danys (1975) have shown that if  $F_z$  is uniformly distributed around the front half of the circumference, then the ratio of the net forces obtained by integrating the respective force distributions around the circumference is given by

$$\xi_{3D} = \frac{2}{\pi} \xi \quad (2-25)$$

Thus, the value of the resolution factor depends on the distribution of the forces around the cone. Lau and Williams (1991) have shown that such consideration is vital in the interpretation of experimental data.

All analytical models and empirical formulae reviewed so far essentially describe quasi-static behaviour in which the inertial loads are low enough to be neglected. Results from many model tests (Haynes et al, 1983; Wessels, 1984; Maattanen, 1986; and Lau and Williams, 1991) have shown a speed effect on failure mode and ice force, and it is widely recognized that a static analysis may not suffice to explain the dynamic effect.

The influence of shear stresses on determining failure modes becomes more important with increasing ice thickness. Since the existing theories are formulated by assuming pure bending failure using classical theories of thin beam or plate on elastic foundation with the shear stress across ice thickness being ignored, the validity of these formulae in predicting failure of thick ice may be questionable. Furthermore, failure modes other than bending may dominate under certain indentation conditions.

Limited field measurements of ice loads on conical shaped bridge piers and lighthouses have been made and reported in the literature (Danys and Bercha, 1975; Alberta Research Council, 1980; Oshima et al., 1980; Hoikkanen, 1985; Frederking et al. 1985; Maattanen and Mustamaki, 1985; Frederking et al. 1992; Maattanen, 1994; Cheung, 1997; Brown et al. 1998). The ice failure mode observed was usually different from existing theoretical and experimental models. It was also observed that a rubble pile is likely to form in front of a conical structure (Maattanen and Mustamaki, 1985; Hoikkanen, 1985). This large amount of rubble, accumulated in front of the cone, imposes substantial loading on the structure and the intact ice sheet. An ice clearing component as much as 80% of the total load on the structure has been measured in the work described in this thesis. Previous model tests and theoretical models do not consider the effects of pile-up. Omission of such factors in those analytical and empirical formulations might have severely underestimated the ice forces.

The foregoing review of past research shows that the most general and advanced analytical theories available at present have the theoretical weakness of application limited

to thin ice, small resolution factor and low interaction speed in which pure bending failure is dominant. They are also limited to the initial stage of the interaction before any significant rubble piles up around the cone. However, the prevailing practice of component delineation according to the two dominant interaction phenomena, i.e., ice breaking and ice clearing, is consistent with the currently available experience of ice loads on conical structures.

Preliminary analysis of results has been reported (Croasdale and Muggeridge, 1993) in which reasonably good agreement has been found between forces measured from the faceted cone tests and those computed using the existing theories for smooth cones. It now appears that this agreement is accidental since the ice clearing pattern is totally different from that postulated in the smooth cone models.

The present state of rubble modelling as exhibited by the two models formulated concurrent to this research, i.e., Izumiya et al (1993) and Croasdale et al (1994), shows two weaknesses:

- (i) The rubble geometry was highly uncertain. The existing models select rubble height on the basis of limited observations from tank tests. The dependency of rubble geometry in ice and structure parameters has not been formulated which limits use of the models to a narrow range of ice and structure conditions.
- (ii) The stress-state of the rubble is highly uncertain. The assumptions and simplifications with regard to the state of the rubble may not be valid which can cast doubt on the validity of the treatment. Information on the stress-state

of the rubble is fundamental to rubble modelling.

In the subsequent analysis of the experimental data and the numerical analyses developed for ice load computation, an effort is made to improve the modelling procedure and thus remove those limitations.

Table 2.1 Test conditions of each data set used in model formulation and coefficients of the associated formula

Test	Cone Angle $\alpha$ ( $^{\circ}$ )	Cone Waterline D (cm)	Neck Waterline D <sub>n</sub> (cm)	Ice Thickness t (cm)	Flexural Strength $\sigma_f$ (kPa)	Ice Modulus E (MPa)	Friction Coeff. $\mu_s$ ( )	Ice Velocity V (cm/sec)	$a_0$ , $a_1$ and $a_2$
Afanas'ev et al (1971)	30,45, 60	12 - 18	9.7	3.0 - 3.5	37 - 40	29.4	n.a.	n.a.	$a_0$ ; Eq. 2.15
Edward & Croasdale (1976)	45	25 - 100	0	1.7 - 6.8	1 - 41	n.a.	0.05	n.a.	$a_0 = 1.6$ $a_1 = 6.0$
Pearce & Strickland (1979)	45, 60	73.7	48.9	1.3 - 9.9	13.8	6.9	n.a.	1.27	n.a.
Brooks (1981)	45	63.5 - 102.6	n.a.	3.56 - 5.92	10.3 - 22.3	-7.5	n.a.	.18 - 1.09	$a_0 = 0.285$ $a_1 = 5.47$ $a_2 = 797$
Hirayama & Obara (1986)	50 - 80	10.4 - 37.5	4.0 - 30.5	0.65 - 3.1	27 - 710	35 - 2000	n.a.	n.a.	$a_0 = 2.43$ $a_1 = 0.7$
Kato (1986)	45 - 80	34.2 - 34.9	14 - 29	2.0 - 5.0	10 - 40	n.a.	0.09	n.a.	n.a.

Table 2.2 Prototype and model geometries: symbols given in Figure 2.1

	Prototype	ERCL-Ess Basins			NRC-IMD			NRC-IME
Dimension	1:1 large neck (m)	1:10 large neck (m)	1:10 small neck (m)	1:20 large neck (m)	1:25 large neck (m)	1:25 small neck (m)	1:50 large neck (m)	1:50 small neck (m)
Base*, a	115.5	7.75	7.75	7.75	3.418	3.418	3.418	1.84
Waterline**, b	34.65	3.465	3.465	1.74	1.386	1.386	0.693	1.15
Collar, c	30.0	3.0	3.0	1.50	1.201	0.739	0.601	0.60
Neck, d	23.1	2.31	1.155	1.155	0.924	0.462	0.462	0.23
Height 1, e	29.2	1.667	2.083	1.708	0.800	0.966	1.016	0.58
Height 2, f	1.67	0.167	0.583	0.084	0.067	0.233	0.033	0.333
Height 3, g	6	0.6	0.6	0.30	0.240	0.240	0.120	0.134
Height 4, h	20	1.4	1.0	1.00	0.800	0.400	0.400	0.197

Note: \*The base width was not modelled in model scale

\*\*The waterline of NRC-IME's model was modelled in 1:30 scale

All diameters are corner to corner

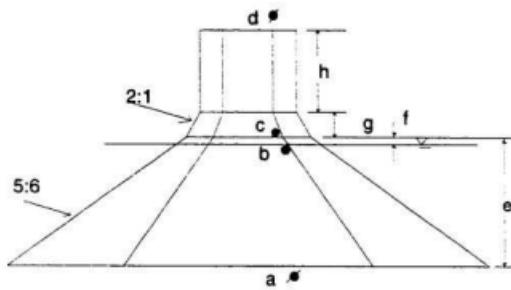


Figure 2.1 Test structure geometry. All diameters are corner to corner; and all slopes are of facet centres, given as a ratio of vertical to horizontal.

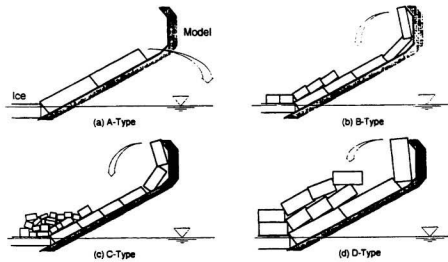


Figure 2.2 Rubble field types (after Izumiya et al., 1994)

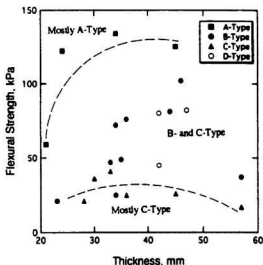


Figure 2.3 Rubble types in strength-thickness domain (after Izumiyama et al., 1994)

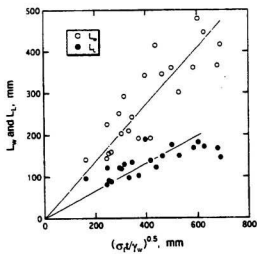


Figure 2.4 Piece size,  $L_w$  and  $L_L$ , versus the parameter,  $(\sigma_i l / \gamma_u)^{0.5}$ , for IME's tests (after Izumiyama et al., 1994)

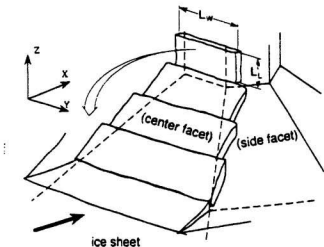


Figure 2.5

Figure showing the definition of ice piece size,  $L_w$  and  $L_L$  (after Izumiya et al, 1994)

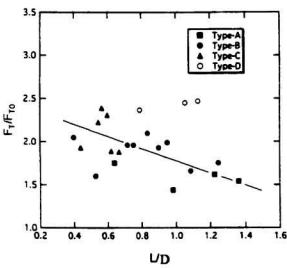


Figure 2.6

Increase in total load due to rubble (after Izumiya et al, 1994)

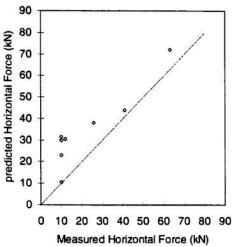


Figure 2.7 Comparison of Croasdale et al's model with tests in ERCL's series (after Croasdale et al, 1994)

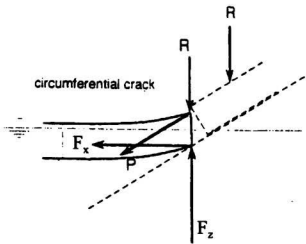


Figure 2.8 Ice forces treated in Izumiya et al's model (after Izumiya et al, 1993)

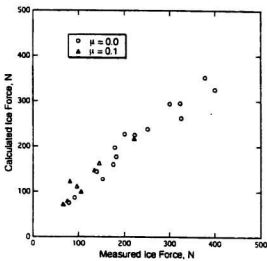


Figure 2.9 Comparison of Izumiyama et al's model with tests in IME's series where ice rubble was absent (after Izumiyama et al, 1993)

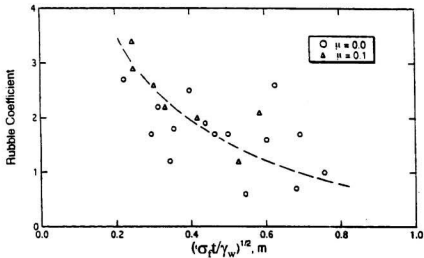


Figure 2.10 Rubble coefficient as a function of ice thickness and ice strength derived from IME's test data (after Izumiyama et al, 1993)

## **Part I The Experiment**

### **Chapter 3 Test Program**

Part I documents the results of the experimental investigation conducted in IMD's test basin and the additional data analyses. As a part of this task, the results from all three test series were consolidated and analyzed. The test results were put into a spread-sheet containing relevant ice and structure conditions, ice forces and the associate failure processes. The available video recording made for each test was examined to identify the interaction processes and the corresponding failure mechanisms associated with each test condition. The influence of various parameters on ice loads and the associated failure processes were assessed through the parametric evaluation. The parameters considered include ice advancing speed, structure orientation, ice strength and thickness. The loads measured in the three test series were compared with predictions from a leading force prediction algorithm. The discrepancies found indicated a necessity for further model development.

Through detailed analysis of the dominant interaction processes and the associated force levels under a wide range of test conditions, answers to the following three questions were sought:

- (i) Was there any similarity or otherwise between the faceted and smooth cones, in terms of interaction processes and the associated force levels?

- (ii) Do the existing models provide satisfactory predictions of the model test measurements?
- (iii) What additional underlying processes are generated due to the new cone form that would be needed to improve the model prediction?

The test program conducted in IMD has been documented in Lau et al (1993b). In this chapter, the test program is briefly described. It should be pointed out from the start that the test program conducted in IMD is unique. It ventured into two new areas: Structural shape and ice thickness regime. Firstly, the inclined facet obstructed the clearing of broken ice, leading to rubble pile-up (rubble pile up was not observed in previous model tests with smooth cones). Secondly, the advance in ice modelling techniques and the increase of model basin size permitted testing in ice up to 0.16 m thickness without compromising scaling, adequate run distance and boundary conditions. The ice thickness of 0.16 m targeted in these tests increased the ice thickness regime to about two times beyond those previously attempted with cones. Tests in thick ice led to ice breaking patterns different from those observed from previous tests conducted in thinner ice. The above two characteristics are new for such tests, and will be examined in detail in the following chapters.

A brief description of the test facility, test structure, instrumentation, data acquisition system, and the model ice is given in Section 3.1 to 3.3. The test matrix and results are documented in Sections 3.4. Emphasis is given to level ice tests only.

### **3.1 Test Facility and Structure**

The model tests were carried out in the ice tank at the Institute for Marine Dynamics (IMD), St. John's, Newfoundland (Jones, 1993). The ice testing basin was 96 m long, 12 m wide and 3 m deep with a useable ice sheet length of 76 m. The main towing carriage, weighing 80,000 kg, had a speed range of 0.001 m/s to 4.000 m/s with an accuracy of 0.1%. The computer for the drive control and the data acquisition system were housed in the thermally insulated control room on the carriage.

The experimental set-up is shown in Figure 3.1. The structure was tested at two scales, 1:25 and 1:50, with a large neck, and additional tests were performed in 1:25 scale with the smaller neck. Dimensions of the three model configurations are shown in Figures 3.2 to 3.4. The model was designed in modules to allow the scales and neck sizes to be easily changed. The main component of the model is the lower cone structure to which various necks and collars could be attached to facilitate these changes. The model was constructed of 1/4" thick marine grade aluminum plates welded to a rigid frame of 2" x 4" aluminum channels. The model surface was finished to a friction coefficient,  $\mu_s$ , of 0.09.

The model was rigidly mounted to the underside of the ice tank carriage through a specially designed towing post constructed from 12" x 12" x ½" steel box beam. The cone and the neck sections were instrumented separately to measure the forces and moments about the three major axes.

For each cone, an *insitu* dynamic test was performed to measure its natural frequency. Analysis of the force signals showed two dominant frequencies of the set-up at

about 3 and 11 Hz (Lau et al, 1993b).

### **3.2 Instrumentation and Data Acquisition System**

The global load measuring system consisted of a series of 3 six-component load cells placed between two steel plates as shown in Figure 3.5. The upper plate was attached to the tow post and the model was rigidly secured to the lower plate. To enhance the system, the load cells were rigidly fixed to one plate by hemispherical bearings while the other plate was secured by a bolted connection. The installation of these bearings resulted in a significant reduction of residual moments on the transducers and the system was capable of measuring the loads to within an acceptable error range (2% and 5% for forces and moments, respectively).

One AMTI model SRMC8-6-20000 and two AMTI model SRMC8-6-10000 six component load cells were used in this configuration. The forces and moments were resolved to a global X, Y, Z coordinate system shown in Figure 3.6. The origin of the global coordinate system was located along the centerline of the cone at the water level. The X-axis was positive in the direction of ice motion, the positive Z-axis was directed vertically upwards, and the direction of the Y-axis was such that X, Y, Z formed a right handed coordinate system.

The loads on the neck were measured by one or two AMTI model SRMC6-6-4000 six-component load cells rigidly mounted between the lower cone and the neck. The 1:25 large neck model was equipped with two dynamometers; while, both the 1:25 small neck

and 1:50 large neck models were fitted with only one of the dynamometers. The load cell configuration for these models are shown in Figures 3.7 and 3.8. Using the known geometry of the system, the forces experienced by the neck were resolved to the global origin of the model.

Accelerations of the model in the three principle axis were measured using three Systron Donner accelerometers and the deflection of the tow post and the model were measured by two Schaevitz linear voltage displacement transducer during tests.

A schematic arrangement of the data acquisition system is given in Figure 3.9. Excitation for the transducers was provided by the NEFF System 620 Series 300 signal conditioner. The transducer outputs from the load cells and the LVDT's were filtered by a 10 Hz analog low pass filter and digitized at a rate of 50 Hz whereas the accelerometer outputs were filtered by 100 Hz and digitized at a rate of 200 Hz by a NEFF System 620 Series 100 amplifier/multi-plexer and stored in a Vax 11/750 computer for analysis. The analog outputs of the transducer were recorded by a KYOWA RTP-600B 14 channel tape recorder, to allow examination of the high frequency components of the signals.

Video recordings were made of all tests using four colour video cameras which provided overhead, sides, and underwater coverage. The video recordings were synchronized with the data acquisition system, with an accuracy of 0.5 second. Significant ice events were also documented in the form of 35 mm colour prints by a number of still cameras.

### 3.3 Model Ice

The experiments were carried out using EG/AD/S model ice. The structure and

properties of this ice are described in Timco (1986). The ice growth process and the ice formation modelled that of full scale sea ice, giving a realistic vertical distribution of mechanical properties. The percentage concentrations of EG/AD/S for the present test series were 0.39/0.036/0.04. Density of the ice,  $\rho$ , was 920 kg/m<sup>3</sup>. For each ice sheet, flexural strength,  $\sigma_p$ , was measured frequently throughout the test period. The values reported at test time were interpolated from the strength versus time curve for the ice sheet. Both downward and upward breaking flexural strengths were measured. Typically, the upward breaking flexural strength,  $\sigma_{u0}$ , was about one half of the downward breaking strength,  $\sigma_{d0}$ . The effective elastic modulus, E, was determined from deflections of ice plate under a given load (Sodhi et al. 1982). The ratio of elastic modulus to upward breaking flexural strength, E/ $\sigma_{u0}$ , ranged from 4000 to 12000. The reported ice thickness, t, was the average over approximately 30 measurements for the ice sheet with a standard deviation of 2.5%. Other properties, including compressive strength,  $\sigma_c$ , shear strength,  $\sigma_s$ , ice-cone friction and ice density, were also measured. The procedures for producing and characterizing level ice sheets are described in detail in Lau et al (1993b).

### 3.4 Test Matrix and Presentation of Results

The test matrix with details of the test program are given in Table 3.1. It was developed to accommodate the testing of two scales (1:25 and 1:50) of model, two sizes of neck at one scale (1:25), and a variety of sheet ice strengths and thicknesses over a five week period. The models were tested in the face-on orientation.

A total of 18 tests were conducted in 5 ice sheets. In each ice sheet, level ice tests were performed at model velocities of 0.01 m/s, 0.04 m/s and 0.06 m/s to assess the effect of different interaction rates. The ice conditions for each test run are summarized in Table 3.2. A number of tests (MUNCONE3, MUNCONE4 and MUNCONE7) were conducted over a period of two days to obtain variation of ice strengths.

For the first run of each test, the ice pile in front of the structure was cleared away to permit the ice to come into full contact with the front perimeter of the cone at waterline. A run distance of 3 m was required for the test to reach a quasi-steady state. To speed up this process in subsequent runs, the rubble built up from the prior run was not cleared from the model prior to the start of the run.

In Figure 3.10 the test matrix is plotted together in full scale with the matrices of ERCL's and IME's test series to facilitate cross comparison among tests performed in the three tanks. Only the tests with a face-on orientation were plotted together, since they were the only orientation tested in all three tanks. In IME, the model was built at 1:50 scale but tested in the scale of approximately 1:30 at waterline. Since the effective waterline width of the structure is an important parameter affecting the ice loads, the data were scaled up by a factor of 1:30 according to the cone's waterline. It should be noted that the neck diameter must also be scaled accordingly, i.e., inscribed neck diameter is equal to 6 m in full scale.

The test data were analysed and plotted in the form of time-traces for the following parameters:

- (i) three global force components; and
- (ii) three neck force components.

The plots for the individual tests are presented in Appendix B.

The time series for the tests MUNCONE3 to MUNCONE6 were digitally filtered with an upper cut-off frequency of 2.75 Hz before plotting. During test MUNCONE7, the intact ice sheet rode up onto the collar resulting in failure of the ice in high frequency. Hence, the time series were not digitally filtered in order to retain the high frequency interaction data.

The sheet ice test results are summarized in Tables 3.3. Basic statistical analyses were performed on the time series of the measured forces. Only the steady state portion of the force records was analysed and plotted.

The mean peak forces were determined by finding up-crossings of the time trace above a reference level equal to the mean of the data plus one standard deviation. The maximum value between this point and the next down-crossing of the same level was designated a peak. The mean peak force was the mean of the above peaks. In Figure 3.11 the mean peak horizontal and vertical forces are plotted against mean force plus one and a half times standard deviation. The correlation is good except for the tests where the shear type failure occurred (not included in Figure 3.11). Thus, the peak forces for this test series can be estimated as one and a half times the standard deviation above the mean of the force record.

Table 3.1 Test matrix for level ice tests in IMD's series

Test	V (cm/s)	t (cm)	$\sigma_{fu}$ (kPa)	E (MPa)
<b>TEST MUNCONE3; MODEL: 1:25S; SHEET NO. 1</b>				
001	1	15.8	44.4	383
002	6	15.8	44.1	383
003	4	15.8	43.6	383
005	4	14.8	29.4	164
<b>TEST MUNCONE4; MODEL: 1:25L; SHEET NO. 2</b>				
001	1	16.0	41.1	389
002	6	16.0	40.6	389
003	4	16.0	40.4	389
006	4	16.4	19.7	188
<b>TEST MUNCONE5; MODEL: 1:25L; SHEET NO. 3</b>				
001	1	9.5	30.7	156
002	6	9.5	30.2	156
003	4	9.5	29.9	156
<b>TEST MUNCONE6; MODEL: 1:25L; SHEET NO. 4</b>				
002	4	12.4	22.5	120
003	1	12.4	22.5	120
004	6	12.4	22.5	120
<b>TEST MUNCONE7 ; MODEL: 1:50L; SHEET NO. 5</b>				
001	1	16.0	33.7	524
002	6	16.0	33.2	524
003	4	16.0	32.8	524
006	4	16.3	18.7	236

Table 3.2 Summary of ice conditions for each test

Test	t (cm)	$\sigma_{fu}^1$ (kPa)	$\sigma_u^1$ (kPa)	E/ $\sigma_{fu}$	$\sigma_c/\sigma_{fu}$	$\sigma_e/\sigma_{fu}$	$\rho$ (kg/m <sup>3</sup> )	$\mu_e$
MODEL: 1:25S; SHEET NO. 1								
MUNCONE3_001	15.8	44.4	79.8	4810	NA	NA	916	0.11
MUNCONE3_002	15.8	44.1	79.4	4810	NA	NA	916	0.11
MUNCONE3_003	15.8	43.6	78.7	4810	NA	NA	916	0.11
MUNCONE3_005	14.8	29.4	42.4	3796	NA	NA	921	0.09
MODEL: 1:25L; SHEET NO. 2								
MUNCONE4_001	16.0	41.1	74.7	5212	5.2	1.5	914	0.09
MUNCONE4_002	16.0	40.6	73.5	5212	5.2	1.5	914	0.09
MUNCONE4_003	16.0	40.4	72.9	5212	5.2	1.5	914	0.09
MUNCONE4_006	16.4	19.7	39.0	4615	5.2	1.8	923	0.09
MODEL: 1:25L; SHEET NO. 3								
MUNCONE5_001	9.5	30.7	43.4	3002	4.9	2.1	928	0.09
MUNCONE5_002	9.5	30.2	41.6	3002	4.9	2.1	928	0.09
MUNCONE5_003	9.5	29.9	40.8	3002	4.9	2.1	928	0.09
MODEL: 1:25L; SHEET NO. 4								
MUNCONE6_002	12.4	22.5	36.0	3213	5.4	1.9	919	0.08
MUNCONE6_003	12.4	22.5	35.4	3213	5.4	1.9	919	0.08
MUNCONE6_004	12.4	22.5	35.1	3213	5.4	1.9	919	0.08
MODEL: 1:50L; SHEET NO. 5								
MUNCONE7_001	16.0	33.7	70.2	8494	3.8	1.7	918	0.08
MUNCONE7_002	16.0	33.2	69.7	8484	3.8	1.7	918	0.08
MUNCONE7_003	16.0	32.8	69.3	8494	3.8	1.7	918	0.08
MUNCONE7_006	16.3	18.7	42.8	5383	4.7	1.5	920	0.08

Note: <sup>1</sup>  $\sigma_{fu}$  - bottom in tension;  $\sigma_{fu}$  - top in tension

All tests run in face-on orientation.

Table 3.3 Summary of level ice test results

Test	GLOBAL HORIZONTAL FORCE (kN)				GLOBAL VERTICAL FORCE (kN)				NECK HORIZONTAL FORCE (kN)			
	Max	Mean	StDev	Mean Peak	Max	Mean	StDev	Mean Peak	Max	Mean	StDev	Mean Peak
MUNCONE3_001	4.52	3.78	0.35	4.29	5.46	4.70	0.41	5.30	0.60	0.23	0.12	0.47
MUNCONE3_002	5.18	4.18	0.52	4.94	6.06	4.97	0.55	5.72	0.49	0.21	0.09	0.39
MUNCONE3_003	5.32	4.33	0.50	5.05	6.65	5.67	0.51	6.37	0.51	0.20	0.09	0.38
MUNCONE3_005	3.42	2.93	0.25	3.23	4.22	3.87	0.22	4.18	0.36	0.19	0.05	0.29
MUNCONE4_001	5.25	4.31	0.45	5.01	5.37	4.33	0.39	4.72	0.33	0.19	0.05	0.29
MUNCONE4_002	6.27	5.02	0.58	5.91	6.57	5.49	0.59	6.33	0.40	0.27	0.05	0.37
MUNCONE4_003	6.54	5.09	0.61	6.01	6.94	5.81	0.60	6.74	0.48	0.33	0.04	0.41
MUNCONE4_006	5.08	4.17	0.45	4.96	5.07	4.50	0.31	4.86	0.31	0.16	0.01	0.26
MUNCONE5_001	2.16	1.78	0.13	1.95	2.17	1.82	0.15	1.98	0.10	0.05	0.02	0.09
MUNCONE5_002	2.38	1.85	0.23	2.27	3.35	1.89	0.24	2.49	0.21	0.12	0.05	0.15
MUNCONE5_003	2.25	1.77	0.18	2.04	2.26	1.83	0.18	2.15	0.21	0.14	0.01	0.16
MUNCONE6_002	3.08	2.65	0.21	2.95	3.28	2.82	0.19	3.14	0.25	0.18	0.02	0.22
MUNCONE6_003	2.96	2.56	0.17	2.81	3.16	2.85	0.13	3.06	0.21	0.12	0.02	0.16
MUNCONE6_004	3.26	2.74	0.19	3.06	3.46	3.02	0.14	3.27	0.19	0.13	0.02	0.17
MUNCONE7_001	8.86	6.87	1.41	8.51	4.10	2.43	0.46	3.40	0.98	0.54	0.14	0.82
MUNCONE7_002	9.99	5.92	1.34	8.43	5.80	3.43	0.78	4.86	1.01	0.50	0.15	0.80
MUNCONE7_003	10.40	6.78	1.44	9.05	5.56	3.41	0.76	4.79	0.98	0.54	0.14	0.82
MUNCONE7_006	6.34	4.03	0.65	5.45	3.66	2.57	0.36	3.16	0.97	0.42	0.12	0.66

Note: Horizontal - (+) toward the model; Vertical - (+) downward



Figure 3.1 Experimental set-up showing a 1:25 scale large neck model mounted under the main carriage

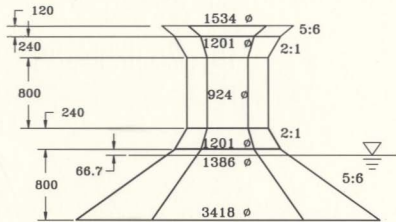


Figure 3.2 Dimensions of the 1:25 large neck model. All diameters are corner to corner; all slopes are of the facet centres and given as a ratio of vertical to horizontal. All dimensions in millimetres.

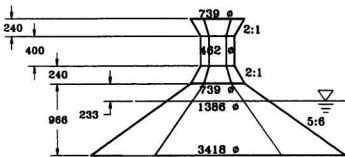


Figure 3.3 Dimensions of the 1:25 small neck model. All diameters are corner to corner; all slopes are of the facet centres and given as a ratio of vertical to horizontal. All dimensions in millimetres.

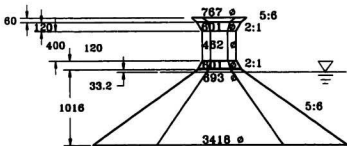


Figure 3.4 Dimensions of the 1:50 large neck model. All diameters are corner to corner; all slopes are of the facet centres and given as a ratio of vertical to horizontal. All dimensions in millimetres.

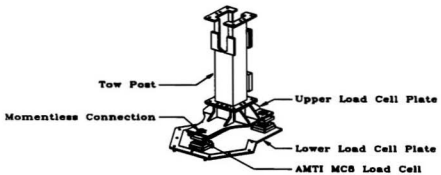


Figure 3.5 Global load measurement assembly

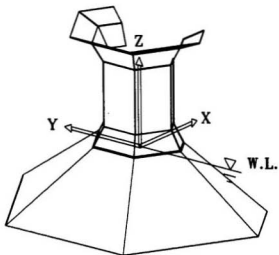


Figure 3.6 Orientation of global coordinate axes with respect to the model structure

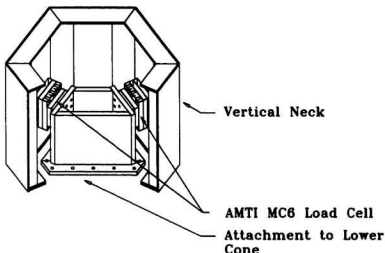


Figure 3.7 Neck load cell arrangement for the 1:25 large neck model

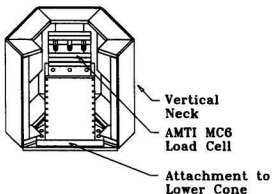


Figure 3.8 Neck load cell arrangement for the 1:50 large neck and 1:25 small neck models

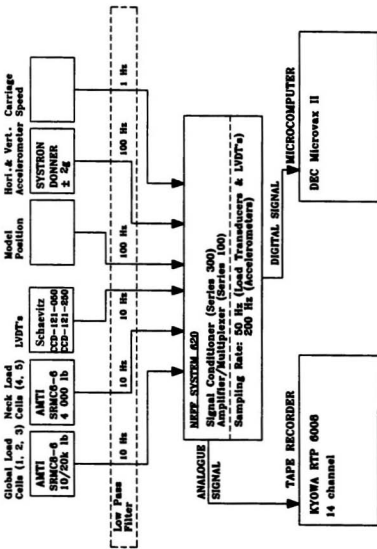
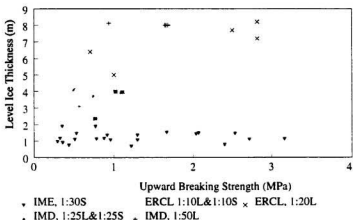


Figure 3.9 Schematic of the data acquisition system



## **Chapter 4 Analysis of Tests**

The ice failure and clearing processes around a faceted cone, in a quasi-steady-state ice breaking, have been identified for each test for the IMD's and IME's tests. Most tests in ERCL's series were performed with an ice sheet typically shorter than two characteristic lengths in the direction of ice motion, resulting in a significant end effect. Ice pieces were typically very large, and most of the runs were stopped before a quasi-steady-state interaction was achieved. The breaking and the subsequent clearing of ice were complex. Nevertheless, the breaking and clearing patterns were similar to those observed in the early stage of the ice-cone interaction observed in tests from other tanks.

Information on the ice breaking patterns, i.e., crack imprint and piece size, is of vital importance in the interpretation of the test results. The dominant failure modes, which are generally difficult to discern, can be inferred from the crack imprint and the resulting broken ice piece size. The crack pattern and piece sizes are also important in determining the subsequent interaction process, i.e., the manner in which the ice rides up the structure and the subsequent nature of the rubble pile-up, and the ice force on the model. In this work, piece size analyses were conducted using video recording of the multi-faceted cone experiments. The factors influencing the piece sizes were examined, and the relationship between ice piece size and the ice thickness and strength was established. The results were compared with previous model test data and the findings of Izumiya et al (1994).

An important aspect of the model tests is the observation of a rubble pileup in front

of the faceted cone models. The influence of a rubble buildup in the MUN/ERCL/NRC multi-faceted cone experiments is addressed with emphasis on tests conducted in IMD's tank. The analysis provides further insights into the formation process of ice rubble, and the effects of important ice-structure interaction parameters on rubble geometry during steady-state ice rubble clearing.

The latter part of this chapter documents the results of ice force analysis carried out on the three test series with the focus given to the IMD's test data. The steady-state portion of the load trace of each test was analysed, and the ice breaking and clearing components of the total ice force were identified. The consistency of data among the three test series was assessed using a semi-empirical formula developed from IMD's series. Measurements from all tests were then compared with predictions from a leading theoretical ice force model, developed for smooth cones, to assess the validity of existing models for predicting ice loads on a faceted cone.

Section 4.1 gives a summary of the dominant features of ice structure interaction and the various failure processes observed from tests conducted in the three model basins. The process consists of three major components: namely the ice breaking mechanism, the ride-up process and the ice rubble formation process. Main features associated with ice breaking mechanism and rubble formation process are further analysed and discussed in Sections 4.2 and 4.3, respectively. Section 4.4 presents the general aspects of the ice load, including the load distribution and the ratio of horizontal to vertical forces, and the ratio of neck to global forces. Section 4.5 presents the semi-empirical formula, and examines the data consistence

among the three test series. A comparison of the test results with Nevel's model is given in Section 4.6. Section 4.7 summarizes the results obtained from Part I of this investigation. A conceptual model is proposed, which forms the framework for Parts II and Part III of this study.

#### **4.1 Ice-Structure Interaction and Failure Processes**

The interaction process with faceted cones was similar to that observed from previous tests with sloping structures as shown in a series of snapshots during a typical test run (Figure 4.1). The failure mechanism was typically governed by the flexural stresses induced in ice in both radial and circumferential directions due to bending of the ice sheet. For a faceted cone with a face-on orientation, a pair of radial cracks initiated from the two edges of the front facet, forming a series of three truncated wedges upon initial contact. The two side wedges forced against the facets on the two respective sides, and a central wedge pushed against the front facet. A radial crack also started from the centre of the front facet in most of the IMD tests

Upon further advance of the ice sheet, circumferential cracks developed and wedges of ice broke off. The front wedge slid up the front facet, over the collar and neck, reaching the top of the structure, and fell back onto the advancing ice sheet resulting in a rubble pile-up in front of the cone, interfering with the ice-breaking process. On the other hand, the side wedges slid up the side facets and cleared around the cone without difficulty.

In the case of thinner and weaker ice used in IME's series, in sliding up the front

facet, the ice which was overhanging the sides of the inclined plane usually broke off due to its own weight, and slid around the side facets. In IMD's tests, such secondary breaking did not occur due to the stronger and thicker ice used. Instead, the ride-up ice formed a shielding wall effectively increasing the width of the front facet to a width slightly wider than the facet width at the waterline (Figure 4.2). This increase substantially facilitated rubble piling. The build up of rubble pile continued until a quasi-steady ice clearing process was achieved with a constant number of ice pieces accumulated in front of the cone.

If the cone was oriented in an edge-on mode, the rubble pileup did not occur due to the absence of a flat face perpendicular to the oncoming ice movement. Typically, a radial crack initiated from the frontal cone edge and propagated along the centerline. This resulted in two truncated wedges, with the two wedges forcing themselves against the facets on the two respective sides. With the advance of the ice sheet, the truncated wedges failed, rode up the front facets, over the collar and neck, and cleared around the cone without difficulty. A quasi-steady ice clearing process was achieved with a constant breaking and clearing of ice.

The profile of the crack patterns associated with the two orientations is shown in Figure 4.3. The circumferential cracks run at a distance from the cone perimeter with a given characteristic length resulting in cyclical ice loading (Figure 4.4).

For the cone with a small freeboard, i.e., IMD's 1:50 scale model tests, the intact ice sheet rode up onto the collar and was caught by the transition of the collar and the cone before any circumferential crack could form. The loading geometry resulted in the failure of ice in shear mode, with failure occurring along the grain boundaries of the columnar

model ice. Small chips of ice broke off from the intact ice sheet and extruded from the cone resulting in high frequency cyclical loading (Figure 4.5).<sup>1</sup> The channel formed by the model's passage appeared very regular at the approximate width of the collar diameter. Piles of extruded ice were formed on either side of the channel. The ice chips cleared around the neck with only a small pileup.

Occurrence of the shear mode of failure was determined by whether the ice sheet reached the cone-collar transition before it failed in bending; hence the failure mode was very sensitive to the ratio of the effective modulus to the flexural strength,  $E/\sigma_f$ , of ice. The extrapolation of the results to full scale should be cautioned since the  $E/\sigma_f$  ratio of the model ice typically may vary from as low as 500 to 2000, much smaller than the full scale values measured in the field (which are of the order of 5000); hence the maximum deflection at failure in the field as predicted from model tests is correspondingly higher than expected. For example, Keinonen et al (1993) compared the properties and behaviour of field ice and EG/AD/S model ice by performing field and model wedge breaking tests and found the deflection of ice predicted from model tests to be between 3 and 10 times higher than basic elastic deflection measured in the field for the test velocity of 5 cm/s due to the excess plasticity of the EG/AD/S ice at low loading rates.

Other failure modes of the ice sheet were also observed. For example, for thin and

---

<sup>1</sup>Tests MUNCONE4\_003 and MUNCONE7\_006 were tested with the same ice speeds and run distances.

weak ice used in the IME's test series, bearing failure of the ice sheet occurred before a significant amount of ice piled up in front of the cone, due to the weight exerted on the unbroken ice sheet by the broken ice pieces, as they were being pushed up the cone surface. Once a bearing failure occurred, ice pieces got jammed between the structure and the oncoming ice sheet, leading to complex contact geometry. After that, the cone experienced a short period of non-steady state loading. The occurrence of this failure mode as a function of ice strength and thickness is shown in Figure 4.6. This type of bearing failure did not occur for test conditions targeted in IMD's test series.

## 4.2 Ice Breaking Mechanisms

Different model geometries and ice regimes result in a variety of failure patterns as discussed in the preceding section. In Section 4.2.1, the breaking patterns observed in the IMD's 1:25 scale model tests are further examined. Special attention will be given to the cracking mechanism during steady-state interaction process for obvious reasons. Section 4.2.2 gives a comprehensive analysis of the broken pieces as observed in the present test series as well as the previous tests. The analysis points to the need for further studies in this area.

### 4.2.1 Breaking Pattern Observed in IMD's Series

The broken ice pattern could be inferred and reconstructed from the video recording by considering the shape of each broken piece as sketched in Figure 4.3b. A pair of radial

cracks first propagated to a short distance comparable to the ice thickness, and then converged toward each other to form a circumferential crack. The two radial cracks made an angle of up to 30° from the direction of the ice advance. Another crack started from the centerline in between the other two cracks.

This observation was contrary to the failure mechanism routinely assumed in previous treatments of the problem as discussed in the following section. The radial cracks did not propagate into the ice far enough to form wedges which behaved as infinite wedges; instead, the failure mechanism observed from IMD's test series was associated with the ultimate failure of finite cantilever beams.

The history of crack development determined the boundary condition and loading at ultimate failure, i.e., how far the radial cracks propagated into the intact ice sheet at the onset of the circumferential cracking, which effectively determined the length of the wedge to be bent. In the following section, three common beam bending scenarios associated with flexural failure are further discussed.

#### **4.2.1.1 Common Beam Failure Scenarios**

If we follow the mode of crack development from the first impact, three failure scenarios could be identified, depending on beam length:

- (i) Formation of a cusp by circumferential cracking with limited radial cracking;
- (ii) Formation of circumferential cracks by cantilever beam failure. The radial crack length was substantially less than 3 times the ice characteristic length.

As a result, the wedge failed as a finite cantilever wedge, having a circumferential crack at its root; and

- (iii) Formation of circumferential cracks after extensive radial cracking. The radial cracks propagated at least 3 times the characteristic length of ice dissecting the ice into wedges before ultimate failure occurred. The wedge could be assumed to fail as a semi-infinite wedge.

Nevel has pioneered the theoretical analysis of ice breaking due to interaction with a cone. He assumed that the radial cracks propagated to such an extent that the wedges behaved as independent infinite wedges (Case 3). Early experience from small scale model tests conducted in thin ice tended to confirm his theory. Since then, most of the subsequent ice cone modeling investigations assumed this failure scenario. Only recently has this assumption been called into question, based on the increasing understanding of fracturing mechanisms and recent experiments in thicker ice.

With increasing ice thicknesses, Bazant and Li (1993) showed the onset of ice failure changed from radial cracking to circumferential cracking. Hence, the loading geometry was changed from a semi-infinite wedge beam (Case 3) to a cantilever beam (Case 2) and eventually to a plate (Case 1). Numerical analysis (Valanto, 1992; Jebaraj et al, 1992; Bazant and Li, 1993; and Derradji-Aouat, 1994) and test data (see next section) tend to support this observation.

#### 4.2.2 Piece Size Analysis

Generally the ice breaking process produced a variety of piece sizes. Ettema et al (1991) suggested that it was chaotic in nature. Varsta (1983) showed that the ice cusp size and force on a landing craft bow was dependent on the velocity, and hence the loading rate. Tatinclaux (1986) measured the ice floe distribution in the wake of a simple wedge in urea and synthetic model ice. He found that the average ice piece size,  $L_L$ , was independent of the characteristic length of ice; instead, it was directly proportional to the parameter,  $(\sigma_f t / \gamma_w)^{1/2}$ , as follows:

$$L_L = C \left( \frac{\sigma_f t}{\gamma_w} \right)^{1/2} \quad (4-1)$$

where  $\sigma_f$  was the flexural strength of ice;  $t$ , the ice thickness; and,  $\gamma_w$ , the specific weight of water. The constant  $C$  depended on the kind of ice, with  $C$  being equal to 0.54 and 0.254 for urea doped ice and synthetic ice, respectively. In this report, the parameter,  $(\sigma_f t / \gamma_w)^{1/2}$ , was called the "breaking length"  $L_b$  for convenience.

In this section, the size relationship is further examined using the faceted cone test data obtained from the three tanks. The data sets were supplemented with data from four other test series conducted with similar model structures [Lau et al (1988) and Lau and Williams (1991) with a 45° smooth downward breaking cone; Sodhi et al (1985) with a 45° smooth upward breaking cone; and Timco (1984b) with a 45° upward sloping

plane]. These model tests were performed in urea or EG/AD/S ice, with the exception of ERCL's tests which were conducted in thick naturally grown saline ice. Despite slight differences in model shape, these tests were conducted in ice and structure conditions similar to one another. To further reduce the possible influences of test parameters other than ice thickness and strength, data from tests with comparable cone and interaction conditions, i.e., ice advancing speed, friction coefficient, cone angle and waterline diameter, were chosen for analysis. The range of variations for each parameter is given in Table 4.1.

For IMD's, ERCL's, IME's and Lau et al's tests (1988),  $L_L$ , was estimated from video recordings made of each test by counting the number of circumferential cracks, and the corresponding run duration and velocity. To ensure that the estimated values of  $L_L$  were representative of the primary ice breaking length, the values were compared with those obtained from bow imprints taken after tests, i.e., Lau et al's tests; and in the cases where bow imprints were not available, i.e., IMD's series, comparisons were made with the broken ice pattern inferred and reconstructed from the video recordings (see Section 4.2.1). For the other tests where the piece size was not reported, it was estimated from the ice breaking frequency,  $f$ , and the ice speed,  $V$ , using the following relationship:

$$L_L = \frac{V}{f} \quad (4-2)$$

which gives the average size of the ice blocks during primary failure due to circumferential cracking.

Figure 4.7 shows the ice piece size  $L_L$  versus the length  $L_b$  observed in all seven

model test series. The data were further grouped according to ice thickness either larger or smaller than 0.045 m. The relationship

$$L_L = 0.54L_b \quad (4-3)$$

as developed by Tatinclaux for urea doped ice was also plotted in the same figure. The figure shows a good agreement of Tatinclaux's relationship with data obtained in ice thinner than 0.045 m. For thicker ice, the dependency of  $L_L$  on the factor  $L_b$  is negligible, and the following relationship fitted the test data very well:

$$L_L = 0.15 + 0.039L_b \quad (4-4)$$

Figure 4.8 shows the ratio of piece size to characteristic length,  $L_L/l_c$ , as a function of ice thickness,  $t$ , for the multi-faceted cone and the supplementary test series. The data indicated a clear relationship between the  $L_L/l_c$  and ice thickness despite a large variation of ice strength.

Simple elastic theory predicted a value of 0.78 for the ratio,  $L_L/l_c$  (Afanas'ev et al, 1971), and the value was independent of ice thickness. However, Figure 4.8 shows that this was valid only for a very thin ice, and the ratio decreased with increasing ice thicknesses. The dependency of piece size on ice thickness reflects the complexity of ice-breaking process, and contributes to the scale effect. The data also suggest a lower limit for the ratio,  $L_L/l_c$ , and the tests conducted in IMD's and ERCL's ice tanks with ice sheets thicker than 9 cm clearly reflect a similar viewpoint. The following equation fits the data very well:

$$\frac{L_L}{l_c} = 0.0168t^{-0.942} \quad (4-5)$$

This observed trend is also consistent with the results from field observations. In the case of ship-ice interaction, Keinonen (1983) pointed out:

"In model tests, the ice is broken into large cusps, the typical size of ice blocks being anywhere between 3-6 times the ice thickness. In full scale, the typical blocks are radically smaller being in the range of 0.5-2 times the ice thickness."

This apparent lack of scaling of the broken piece size is of significance for modelling the dynamics of ice and rubble clearing around a structure, and leads to difficulty in model testing of fragmented ice.

Further review of model tests with other sloping structures (both model and full scales) confirmed the previous finding as shown in Figures 4.9 and 4.10.

Figure 4.9 shows the non-dimensional piece size observed in the wake of six ice breaker hulls (both model and full scale) taken from Tatinclaux (1986) with a model wedge, and the Kigoriak in both model and full scale trials, Howard and Abdelnour (1987) with the 1:8 scale R-Class model, and Valanto (1993) with the IB Kapitan Sorokin in full scale.

Figure 4.10 is extracted from the piece size data reported by Keinonen et al (1993) who conducted 28 tests on an inclined indenter moving against a simply supported wedge. The tests were conducted at the ESSO outdoor basin in Calgary using natural saline ice with

thickness varying from 0.16 to 0.29 m and a flexural strength of approximately 200 kPa. The indenter angle of 25°, 50° and 75° to the horizontal were tested with two wedge angles of 90° and 120°. All tests were conducted using two indenter speeds: 0.05 m/s and 0.30 m/s. Only data associated with the lower speed are plotted in Figure 4.10.

Both figures indicate a limiting value of 0.2 for  $L_L/l_c$  in full scale. This value is a bit higher than 0.1 associated with the multi-faceted cone tests. It may be due to the different ice breaking processes observed.

One explanation for the discrepancy between the theories and test data is the non-inclusion of shear action across the ice thickness in the existing analytical treatments of failure. The characteristic length of a beam (or plate) on an elastic foundation was derived solving the differential equation of the elastic line using classical theory of an elastic beam (or plate) on elastic foundation (Hetenyi, 1946), i.e., a thin beam (or plate) with small deflection. The classical theory, which neglects the effect of transverse shear (i.e., shear modulus, in effect, is set to infinity), becomes unreliable in the case of beams (or plates) of considerable thickness, especially in the case of the highly concentrated loads experienced in the types of interactions investigated. Furthermore, with a ice piece size to characteristic length ratio of as low as 0.1, the transverse shear would play an important role in ice breaking. Buckling may also occur with increasing thickness and cone angle which lead to smaller piece sizes (Derradji-Aouat, 1994).

Satisfactory modeling of ice failure mechanisms is an essential requisite for the proper computation of ice forces on the structure; however, an adequate examination of the

problem is outside the scope of this work. Nevertheless, it is reasonable to assume the piece sizes encountered in full scale to be 0.1 to 0.2 l, according to the present analysis.

#### **4.3 Ice Rubble Formation Process**

In the present study, the rubble types as observed in the IMD's test series were identified and shown in the strength-thickness domain with IME's test data. The rubble field classification scheme developed by Izumiya et al (1994) was adopted (see Figure 4.11).

For IMD tests, C-Type rubble field was typically formed in front of the 1:25 scale models; however, rubble field was not observed in front of the 1:50 scale model as the small crushed ice pieces cleared around the cone readily. The C-Type rubble field was significantly larger than those of the same type observed in IME's tests due to a larger ice thickness and model neck, and a smaller freeboard. The rubble field tended to accumulate, till it reached the neck section.

The C-type rubble field consisted of small ice blocks and crushed, mushy ice. In IME's tests, these small ice blocks were created when the weak ice pieces fell from the top, breaking and rolling down the front of the model. This secondary ice breaking is important, since the degree of breakage determined which of the three types, designated A-type, B-type and C-type, would occur. Degree of breakage, which was highly dependent on the thickness and shape of the ice pieces and the ice strength, increases from A-type to B-type to C-type. In IMD's tests, a crack extended from the centre of the front facet creating two ice pieces before they rolled down from the top of the cone. Such a mechanism was sufficient to create

small ice pieces even though the ice was relatively thick and strong. The ice pieces at the neck, which were typically cubic in shape, rolled down the front facet resulting in a rubble pile of randomly oriented ice pieces.

The manner in which the rubble evolved and changed shape during the interaction, i.e., its geometry and size, could be explained in terms of ice generation and clearing processes. The ice in front of the cone could be divided into 3 zones: a central accumulation zone and two side clearing zones. Understanding of the main features of these zones is vital to a satisfactory rubble modelling. The ice generation and clearing processes associated with these zones will be examined in detail in Chapter 6.

It is recognized from this study that a unique rubble surface profile is generated during steady-state accumulation by a process similar to dumping process from a line source. In this case, the free-surface of the rubble is governed by a slope stability criterion with the slope angle,  $\iota$ , being equal to the angle of repose,  $\phi_r$ , of the rubble material. This surface profile, together with the rubble height profile around the cone's perimeter, defines the geometry of the rubble mass.

It is also recognized that the rate of ice supply is balanced by the rate of ice clearing during the steady-state portion of the interaction, and the geometry and mass of the rubble can be estimated by geometric considerations and mass balance.

The above-mentioned slope stability and mass balance criteria constitute the two fundamental aspects of the clearing processes which will be examined in detail in Chapters 5 and 6.

## 4.4 General Characteristics of Ice Load

### 4.4.1 Ice Load Distribution and Ratio of Horizontal to Vertical Forces

It can be shown that if the vertical force,  $F_z$ , is uniformly distributed around the front half of a six-faceted cone with a face-on orientation, the ratio of the net horizontal to vertical forces,  $F_x/F_z$ , obtained by integrating the respective force distributions is given by a resolution factor:

$$\xi_{3D,f} = \frac{2}{3}\xi \quad (4-6)$$

where  $\xi$  is the resolution factor for a sloping plane; and the value of this resolution factor is a good measure of the distribution of ice forces around the cone.

Table 4.2 summarizes the experimental values of the horizontal to vertical peak force ratio measured in the three test series, i.e.,  $\xi_{\text{meas}}$ . The theoretical values of the resolution factor for the two limiting cases,  $\xi_{3D,f}$ , and  $\xi$ , and the estimated percentage of ice force distributed on the front facet,  $\%_{\text{front}}$ , are also given.  $\xi_{3D,f}$  corresponds to the case where the vertical force is uniformly distributed around the front half of the cone; whereas,  $\xi$  is calculated assuming all ice forces are acting on the cone section at the front facet.

In general, the experimental values,  $\xi_{\text{meas}} = F_x/F_z$ , were close to the theoretical values,  $\xi$ , for 2-D loading suggesting that the major portion of the load (with more than 70%) was distributed along the front facet during the peak force events. This observation was contrary to the observations obtained from previous model tests with smooth cones where the

resolution was found to be governed by  $\xi_{3D}$ , i.e., Equation 2.25.

Figure 4.12 shows the relationship of the non-dimensional resolution factor,  $\xi_{\text{meas}}/\xi$  and the non-dimensional waterline width,  $D/l_c$ , for existing test data for smooth cones. The data sets contain data from 10 level ice test programs done worldwide on conical structures with a total of ~400 data points (Afanas'ev et al, 1971; Verity, 1975; Edwards et al, 1975; Edwards and Croasdale, 1976; Manders and Abdelnour, 1978; Hirayama and Akamatsu, 1982; Wessels, 1984; Sodhi et al, 1985; Lau et al, 1988; and Izumiya et al, 1991).

The experimental value,  $\xi_{\text{meas}}$ , has been non-dimensionalized by  $\xi$ . The upper limit ( $= 1$ ) corresponds to the 2-D case where all loads are assumed to act on the front edge of the cone. The lower limit ( $= 2/\pi$ ) corresponds to the 3-D case where the forces are uniformly distributed along the front perimeter of the smooth cone.  $\xi_{\text{meas}}/\xi$  is generally lower than the value for the 2D case and in many cases is close to what is expected for a uniform distribution, particularly for  $D/l_c$  greater than 1. It is consistent with the observation that for a very narrow structure, ice-cone contact is concentrated at the front edge of the cone, and with the waterline width increases, the ice-cone contact increases from the front edge toward the side of the cone, and eventually full contact of ice with the front half of the cone occurs with a certain waterline (Hirayama and Obara, 1986).

The values of  $D/l_c$  for the faceted cone series were a lot greater than 1, and a uniform distribution was expected. The reason for this difference between the smooth cones and the faceted cones is not clearly understood, but might be attributed to two reasons. Firstly, the

resolution factor was calculated assuming all load to act on the conical section only. The large amount of rubble pile-up on the collar and the neck section would increase the resolution factor since they have an inclination larger than that of the cone section. The second reason is that the ride-up and pile-up would primarily occur on the front facet, which would distribute most of the clearing loads onto the front facet in a two-dimensional manner.

#### **4.4.2 Ratio of Neck to Global Forces**

Freeboard is the most important parameter influencing the ice loads on the neck. With a large freeboard the broken ice can clear around the cone without a significant amount of ice pieces accumulating on the neck. Figure 4.13 shows the effect of freeboard on the ratio of the neck to global horizontal loads for the level ice tests. The freeboard is non-dimensionalized by the ice thickness. The ratio of the neck to global force increases with the decrease of non-dimensional freeboard. The non-dimensional neck force is below 0.16 for all tests except the two runs tested in a very strong ice with a small freeboard to thickness ratio, i.e., ERCL's Tests 2 and 4.

### **4.5 Semi-Empirical Formulae**

In this study, the ice breaking and clearing components of the total ice force, during steady-state ice loading, were analysed. The ice breaking component is the force needed to break the ice. The ice clearing component is the load imposed by the broken ice pieces as they slide up the cone surface. These two components are attributed to completely different

mechanisms, and they were isolated and treated separately for deeper understanding of the interaction. A semi-empirical formula, based on experimental measurements and basic mechanics of ice, was developed as a way to compare the results obtained from the three ice tanks.

Table 4.3 gives a summary of the mean peak force,  $F_{mp}$ , and the associated ice breaking and clearing force components, i.e.,  $F_b$  and  $F_c$ , measured in IMD's 1:25 scale model test series. The ice clearing force,  $F_c$ , is assumed equal to the mean trough force. The ice breaking force,  $F_b$ , is obtained from subtracting the ice clearing force from the mean peak force as shown in Figure 4.14. In the present test series, a major portion of the total load in the structure was observed to be due to ice clearing, with the ice breaking force sometimes contributing to as little as 20% of the total ice forces.

The mean peak and trough forces were determined by the up-crossing method as described in Section 3.4. Since there was a concern with the dynamic effects during the unloading phase after the ice failed which tended to affect the trough force, the time-history records were filtered through a 1.5 Hz low pass filter before analysis.

The semi-empirical formula was developed from IMD's 1:25 scale model tests.<sup>2</sup> Predictions from this formula are then compared with the measurements from the other two tanks to assess the consistence of results among the three tanks. As noted above a review of existing empirical and analytical formulae for ice load computation on cones suggested the

---

<sup>2</sup>The experimental results with the 1:50 scale model were excluded due to the shearing/crushing failure observed during tests.

following common form for the horizontal ice force:

$$F_x = a_0 \sigma_f^2 + a_1 \gamma D^2 t \quad (4-7)$$

where the coefficients,  $a_0$  and  $a_1$ , are functions of structural shape and coefficient of friction. The first term is the ice force caused by ice breaking, and the second term is the ice force due to ice riding up the structure slope. Experimental data also indicated that the vertical force was relatively independent of cone angle and friction coefficient, and the horizontal force could be related to the vertical force through a resolution factor,  $\xi$ , which depended on the inclination angle and the ice-structure friction coefficient. Therefore, the following form was used in the present analysis:

$$F_x = \xi(a_0 \sigma_f^2(\sigma_f^{k_0} t^{k_1}) + a_1 \gamma D^2 t(\sigma_f^{k_2} t^{k_3})) \quad (4-8)$$

where  $\sigma_f^{k_0} t^{k_1}$  and  $\sigma_f^{k_2} t^{k_3}$  are empirical functions, which take into account the influence of pile-up on the breaking and clearing forces;  $k_0$ ,  $k_1$ ,  $k_2$ ,  $k_3$ ,  $a_0$  and  $a_1$  are empirical coefficients which are optimized to fit the experimental data.

The ice breaking and ice clearing components of the general expression were derived individually from the IMD's data resulting in the following expression for the horizontal force:

$$F_x = \xi(711 \sigma_f^2(\sigma_f^{-0.56} t^{0.02}) + 1.05 \gamma D^2 t(\sigma_f^{0.08} t^{0.42})) \quad (4-9)$$

In Figures 4.15 and 4.16, the ice breaking and the ice clearing forces predicted by Equation 4.9 are compared to the experimental data. In the above comparisons, the scatter in data may be partly due to the effects of neck size and velocity which are not included in the above formulation.

In Figure 4.17, the total force predicted from Equation 4.9 is compared with the experimental data from the three tanks. In general, Equation 4.9 predicts the model test results well, indicating a good agreement among the results obtained from the three model basins, with loads measured extending more than three orders of magnitude.

#### 4.6 Comparison with Theoretical Prediction

Theoretical loads corresponding to the level ice experiments were calculated by applying the elastic model due to Nevel (1992). This model is shown to be satisfactory in predicting ice forces after extensive comparison with the existing experimental data. (See Chapter 8.1). The mean features of the model have been reviewed in Section 2.2.1.2.

Figures 4.18 and 4.19 show a comparison of the total horizontal and vertical peak loads measured from the three tanks with the loads calculated from Nevel's theory.<sup>3</sup> The agreement between the theoretical predictions and measured forces is remarkably good for the ERCL and IME series; however, this theoretical model consistently under-predicts the

---

<sup>3</sup>Again, the experimental results with the IMD's 1:50 scale model were excluded from the comparison due to the shear/crushing failure observed during tests which was mentioned in Section 4.2.

ice loads measured in IMD's tests by an average of 46%. Two points should be noted here. Firstly, a majority of tests conducted in IME's and ERCL's series do not have a substantial amount of rubble piling in front of the structure. Furthermore, ERCL's ice thickness was less uniform than the ice from other two tanks, resulting in non-simultaneous ice breaking, and most tests were stopped before any significant amount of ice could accumulate on the cone. Hence, the theory might possibly overestimate the ice breaking components while underestimate the ice clearing component of the total ice force.

To show this, the model predictions were compared with the results from the IMD's test series to assess the accuracy of the model to predict the individual force components. Only components of the horizontal force were compared. Figures 4.20 and 4.21 give the results of comparison for the ice breaking and ice clearing components, respectively. The model predicts well the breaking component of the lower forces measured in thinner ice, but underpredicts those of the higher forces measured in thicker ice; whereas the model consistently under-predicts the ice clearing component by about 30%, and again, the higher the force the higher the error. Since ice rubble tends to increase the ice clearing components of ice force due to its dead weight, the model is expected to under-estimate the clearing component. This weight could also increase the breaking load somewhat by imposing an in-plane compression at the tip of the supporting ice sheet as discussed in Chapter 8.

#### 4.7 Summary and Discussions

Based on observations from model tests, a conceptual model is formulated to describe

qualitatively the primary interaction processes. The conceptual model provides a conceptual basis for the mathematical modelling outlined hereafter. In Section 4.7.1 the major findings of the test program are summarized, and the need for further ice force modelling discussed. In Section 4.7.2 the general features of the interaction behaviour under investigation are briefly described, and a method to incorporate the effect of rubble in the existing ice load models is presented.

#### **4.7.1 The Need for Further Ice Force Modelling**

The validity of the existing theories for predicting global loads on a faceted cone is one of the principal concerns from industry's point of view. The analysis of ice sheet loads with a leading ice force predictor developed for smooth cones indicates that the theory would likely under-predict the clearing component of ice loads. Particularly, the error in ice load estimation might be quite large when a large rubble field piles in front of the structure, justifying further studies to develop some new formulae for the estimation of ice loads on such structures.

Important insights have been obtained from a closer analysis of the model test results. The process of ice failure and clearing during its interaction with the faceted structure has indicated the presence of many new features. This process is substantially different from that of a smooth cone and a two-dimensional sloping plane. The facet corners, acting as stress concentration points, seem to play important roles because two cracks propagate from the corners in many of the tests. In addition, the flat facet and large neck tend to prevent

efficient ice clearing and initiate rubble piling in front of the structure.

Failures other than that due to bending modes have been observed from the tests. These may be due to the complex three-dimensional stress state induced in the ice sheet. Piece size measurements significantly diverge from those predicted by existing theories which are formulated using classical theories of thin beam or plate on elastic foundation with the non-inclusion of shear action across the ice thickness. Previous studies have shown that the failure mode could gradually alter from bending to shear with increasing ice thickness. Incorporating the three-dimensional nature of ice behaviour into the investigation of the problem is essential to advance our present understanding of the interaction process.

Rubble building is an essential part of the ice clearing process. The large amount of rubble, accumulated in front of the cone, imposes a substantial loading on the structure and the intact ice sheet. An ice clearing component as much as 80% of the total load on the structure has been measured (see Table 4.3). The factors which contribute to the amount of ride-up and rubble formation, and their subsequent effects on the interaction process were poorly understood. Omission of these factors may lead to a severe underestimation of ice forces.

Although a considerable amount of data was obtained from model tests mentioned in the previous section, a number of important ice-structure parameters, i.e., number of facets, cone angle, ice-ice and ice-cone friction coefficients, etc., were not varied in the test program, and the results were valid only for the conditions and geometries of the experiments. Due to the limited numbers of parameters examined, these model tests were

more useful in confirming and calibrating algorithms for ice loads rather than in directly providing equations for design ice loads. It is therefore considered likely that it would be helpful to perform mathematical modelling in order to extend the observed relationships to more general interaction conditions and geometry. The modelling is supplemented by a series of numerical simulations to be presented in Chapter 7. The simulations provide information on the complex stress conditions and load distributions, and how the loads were transmitted and distributed along the ice sheet and on the surface of the structure, which is helpful to a better understanding of the basic mechanical processes that take place during the interaction.

On faceting a cone and enlarging the size of the neck, the interaction and failure mechanisms were significantly altered. Existing theories of ice loads on a cone could not explain this change. Since there are obvious economical advantages in incorporating flat facets and large necks in the design of conical structures, an ice force model that allows for the effects of cone facets, neck size, and the rubble pile, would be an asset to the industry. Obviously, many issues associated with the three basic processes of ice breaking, ice ride-up, and the ice piling should be addressed in a comprehensive study. However, the time constraint imposed on this research prevented a comprehensive examination of the problem. Instead, a decision was made to focus further efforts on the formation of ice rubble in front of the structure and its effect on ice loads, as no previous model has adequately accounted for its effects.

In the following, a conceptual model is presented which provides a method for

considering the dominant processes, and a framework to incorporate a rubble model into the existing ice force models. Attention is given to the better characterization of rubble pile-up phenomenon and the associated ice load. Since the issues related to ice breaking and ice ride-up have been studied previously in greater detail, the knowledge gained from these studies is used in the present work.

#### **4.7.2 Conceptual Model for Ice Forces Exerted on an Inclined Plane**

The model is proposed to explain the interaction processes between a faceted cone and a level ice sheet during a continuous ice breaking mode. It provides an outline of the phenomena to be investigated, and a framework for incorporating rubble load theory into existing ice force models. The model is detailed enough to describe the interaction processes as well as to obtain the form of equations for individual force components.

The geometry of the problem is presented for a two-dimensional case in Figure 4.22. For simplicity, the model is given in 2-D, and a constant thickness ice sheet is moving horizontally and breaking against a faceted cone under an ice rubble pile, the shape of which is yet to be determined. From a modelling point of view, it is convenient to divide the interaction process into three major simultaneous phenomena, i.e., (1) ice breaking, (2) ride-up, and (3) rubble pile-up, where different features dominate. The first phenomenon is the failure of ice under contact forces imposed by the cone, the ride-up ice and the rubble surcharge. The second phenomenon is the pushing of a layer of broken ice up the cone surface. The third phenomenon is the clearing of a rubble surcharge around the cone due to

the continuous movement of the level ice past the cone. The three phenomena are mutually dependent. The constitutive properties of the rubble and ride-up ice depend on the geometrical and mechanical properties of the constituent ice pieces which are generated by the breaking of the ice sheet, and the size of ice pieces generated during ice breaking is in turn affected by the additional loading imposed by the rubble and ride-up ice. The ice breaking and ride-up processes have been extensively studied and many models are available to predict the total load due to their effects. However, the rubble pile-up process is less well understood. For each process, some of the aspects regarded as important and/or unique to the present investigation are briefly described below.

Figures 4.23 and 4.24 summarize the loads exerted on the ice sheet, the ride-up and the pile-up which should be taken into account. The weight of the pile-up,  $W_p = W_c + W_r$ , is partly supported by the ride-up ice and partly by sheet ice, i.e., distributed loads  $q_c$  and  $q_r$ . The force,  $N$ , required to lift the rubble surcharge and break the ice sheet, acts at the bottom edge of the ice sheet. As the ice moves and rides up along the cone, frictional forces,  $q_i\mu_{ii}$ ,  $N_i$ , and  $q_c\mu_{ci}$ , are also developed at the ice-rubble, ice-cone, and rubble-cone interfaces respectively, where  $\mu_i$  and  $\mu_{ci}$  are the ice-ice and ice-cone friction coefficients at the respective interfaces. A component,  $P$ , acting at the top edge of the ice sheet is also required to push the ice up the slope. The failure of the ice sheet can take place either by bending, shearing, crushing, buckling, or a combination of them. The velocity of ice is assumed to be high enough that brittle ice failure mode is predominant. During a quasi-steady state ice

interaction, some constant amounts of rubble ice pile up in front of the structure, when the rate of ice supply is equal to the rate of ice clearing. The underlying ice sheet may fail before this quasi-steady state is reached.

The rubble is under constant shearing due to constant deformation of the rubble. To take into account the effects of this rubble ice in ice force prediction, the amount and distribution of the rubble and associated forces exerted at the inclined boundary (with the ride-up ice) and the base (on the supporting ice sheet) must be known. The rubble pile formation mechanism is a complicated process involving the dynamic balance between the supply of ice pieces due to continuous ice breaking, and the clearing process of ice as the rubble pile moves past the cone. Understanding these two processes is the key to modelling the mechanism of rubble formation: besides, other factors such as the size and distribution of rubble ice, and the dynamic interactions between the individual ice pieces must also be considered.

Table 4.1 General test conditions of the model test series used in piece size analysis

PARA-METER	Sloping Plane	Smooth Cone			Faceted Cone (face-on orientation only)		
	Timco, 1984	Lau & Williams, 1991	Lau et al, 1988	Sodhi et al, 1985	IMD 1:25	IME 1:50	ERCL 1:20
Cone Angle, ( $^{\circ}$ )	45	45	45	45	40	40	40
Breaking Direction	Up	Down	Down	Up	Up	Up	Up
Waterline Diameter, (m)	1.0	1.28	1.28	1.5	1.38	1.24	1.72
Friction	0.02	0.15	0.15	0.1	0.09	0.01	0.08
Velocity, (m/s)	< 0.06	0.01/0.05	0.01/0.05	0.02/0.06	0.01/0.04/0.06	0.06	0.06

Table 4.2 Summary of the horizontal to vertical force ratio for level ice tests measured in the three series on multifaceted cones: face-on orientation only

Test Series	Friction Coefficient, $\mu$	$\xi_{\text{meas}} = F_x/F_z$	$\xi$	$\xi_{\text{M.F.}}$	$\%_{\text{front}}^3$	No. of Data Points
<sup>1</sup> IME	0	$0.791 \pm 0.046$	0.833	0.555	0.899	15
	0.1	$1.162 \pm 0.085$	1.018	0.679	1.283	7
<sup>2</sup> IMD	0.09	$0.913 \pm 0.08$	0.998	0.665	0.830	14
ERC	0.1	$0.87 \pm 0.177$	1.018	0.679	0.709	10

Note: 1 A friction coefficient of 0 is associated with runs 1 to 38, and a friction coefficient of 0.1 is associated with runs 39 to 66.

2 1/25th scale model tests only

3 % force distribution on front facet calculated by the following equation:

$$\%_{\text{front}} = \frac{\frac{\xi_{\text{meas}}}{\xi} - \cos(60^\circ)}{1 - \cos(60^\circ)}$$

Table 4.3 Summary of total, breaking and clearing ice forces measured in IMD series:  
1:25 scale model

Test (#)	V (m/s)	$F_{tot}$ (N)	$F_c$ (N)	$F_b$ (N)	$F_b / F_{tot}$	$\sigma_{fu}$ (kPa)	t (m)
Test Set: Small neck model with neck size: 0.231 m							
3.1	0.01	4287	2890	1397	0.309	44.4	0.158
3.2	0.06	4942	3200	1742	0.337	44.1	0.158
3.3	0.04	5049	3100	1949	0.366	43.6	0.158
3.5	0.04	3232	2400	832	0.243	29.4	0.148
Test Set: Large neck model with neck size: 0.462 m							
4.1	0.01	5005	2950	2055	0.391	41.1	0.160
4.2	0.06	5907	3800	2107	0.336	40.6	0.160
4.3	0.04	6006	3500	2506	0.383	40.4	0.160
4.6	0.04	4963	3150	1813	0.357	19.7	0.164
5.1	0.01	1953	1520	433	0.200	30.7	0.095
5.2	0.06	2274	1450	824	0.346	30.2	0.095
5.3	0.04	2035	1440	595	0.264	29.9	0.095
6.2	0.04	2950	2150	800	0.260	22.5	0.124
6.3	0.01	2810	2050	760	0.257	22.5	0.124
6.4	0.06	3060	2250	810	0.249	22.5	0.124

Note: Waterline diameter: 1.386 m; friction coefficient: 0.09; and ice density: 930 kg/m.

Figure 4.1

Photos showing a typical ice breaking, ride-up and rubble piling sequence (Test MUNCONE4\_001): (a) initial contact, (b) ice ride-up, (c) rubble accumulation, and (d) fully developed rubble pile



(a)



(b)



(c)



(d)



Figure 4.2 Photo from IMD's series showing the ride-up of ice and the rubble pile (Test MUNCONE6\_003)

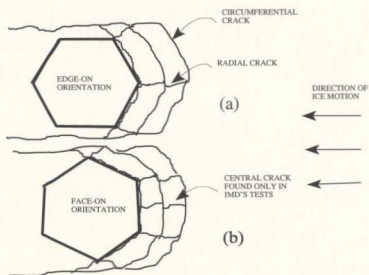


Figure 4.3 Profile of crack patterns associated with the (a) edge-on and (b) face-on orientations

## FORCE ON STRUCTURE IN X, Y, Z DIRECTIONS

MUNCONE7\_006

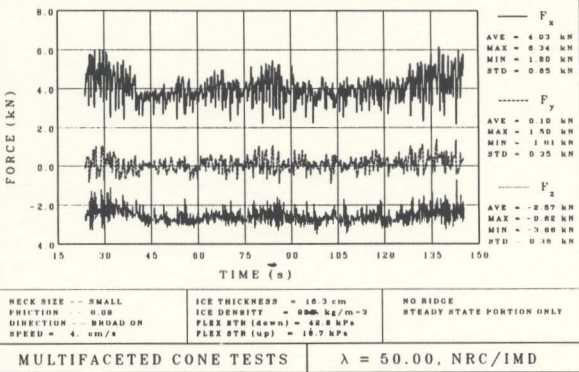


Figure 4.5 Time history showing high frequency cyclical loading (MUNCONE7\_006)

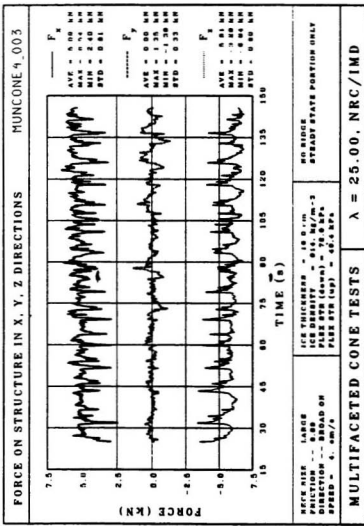


Figure 4.4 Load trace showing typical cyclical ice loading (MUNCONE4\_003)

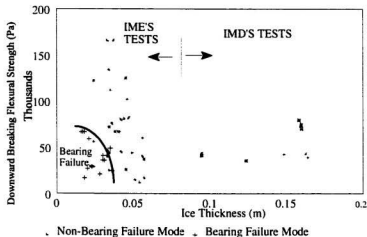


Figure 4.6 Bearing failure of unbroken ice sheet in strength-thickness domain, IMD's and IME's series

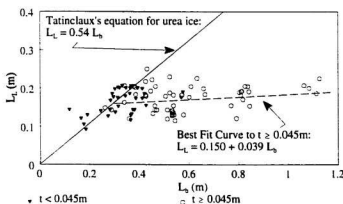


Figure 4.7 Ice piece size,  $L_L$ , versus breaking length,  $L_b$ , with curve fitting for ice thickness larger than 0.045 m. Tatinclaux's equation for urea ice is also given.

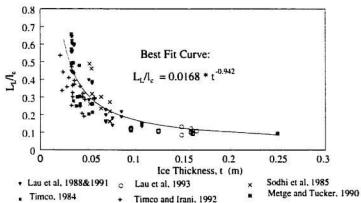


Figure 4.8 Ratio of ice piece size to characteristic length,  $L_L/l_c$ , versus ice thickness,  $t$ , for seven sets of model test data with sloping structures

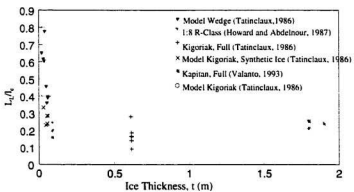


Figure 4.9 Model/Full scale icebreaker test results showing the effect of ice thickness,  $t$ , on the ratio of ice piece size to characteristic length,  $L_L/l_c$ . Data include low speed test with urea and sea ice.

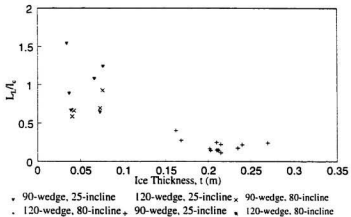


Figure 4.10 Model/Full scale wedge breaking tests taken from Keinonen et al (1993) showing the effect of ice thickness,  $t$ , on the ratio of piece size to characteristic length,  $L_L/L_c$ , with loading velocity,  $V = 5$  cm/s

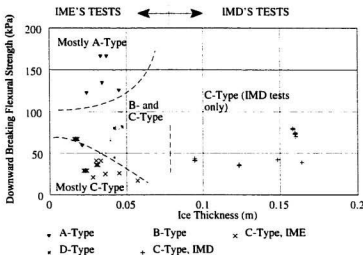


Figure 4.11 Rubble types associated with IME's and IMD's model tests shown in the strength-thickness domain

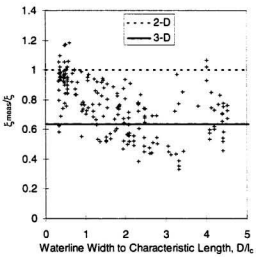


Figure 4.12 Non-dimensional resolution factor,  $\xi_{\text{meas}}/\xi_s$ , versus non-dimensional waterline width,  $D/l_c$ , for smooth cone tests

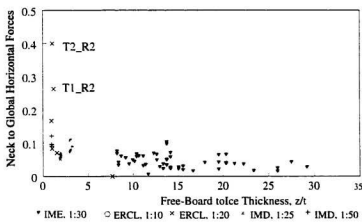


Figure 4.13 Non-dimensional horizontal neck force versus non-dimensional free-board,  $z/t$

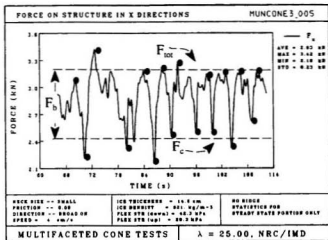


Figure 4.14    Figure showing the definitions of  $F_a$ ,  $F_b$  and  $F_c$  ( $\lambda$  is the scale factor)

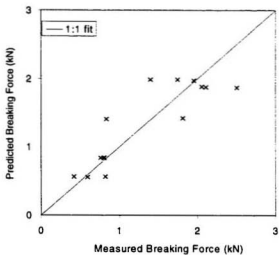


Figure 4.15    Comparison of horizontal breaking force measured in IMD's series to breaking force predicted by Equation 4.9

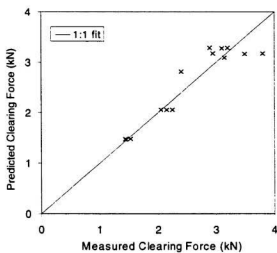


Figure 4.16 Comparison of horizontal clearing force measured in IMD's series to clearing force predicted by Equation 4.9

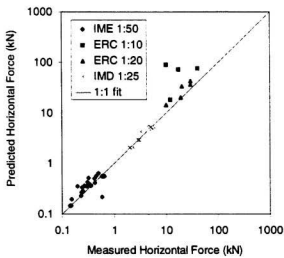


Figure 4.17 Comparison of total measured horizontal force with prediction from Equation 4.9 for the three test series

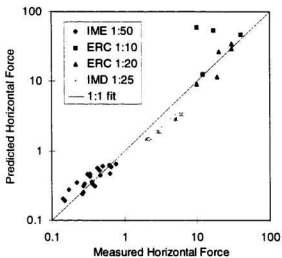


Figure 4.18 Comparison of prediction from Nevel's model with measurements from the three test series: horizontal force

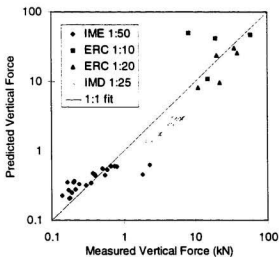


Figure 4.19 Comparison of prediction from Nevel's model with measurements from the three test series: vertical force

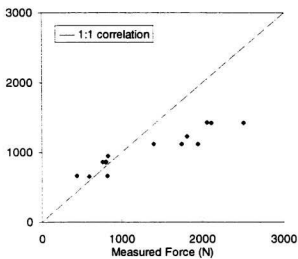


Figure 4.20 Comparison of horizontal breaking force measured in IMD's series to prediction from Nevel's model

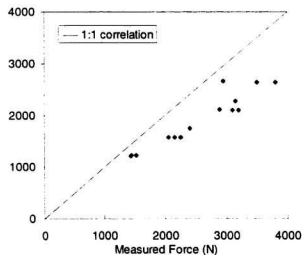


Figure 4.21 Comparison of horizontal clearing forces measured in IMD's series to prediction from Nevel's model

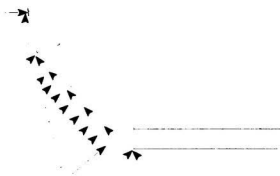


Figure 4.22 Geometry of the conceptual model for ice forces exerted on an inclined plane

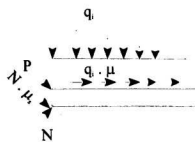


Figure 4.23 The loads exerted on supporting ice sheet

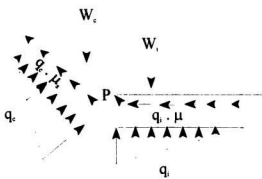


Figure 4.24 The loads exerted on pile-up ice

## **Part II Ice Rubble Modelling**

### **Chapter 5 Ice Rubble Under Load**

The process of ice rubble pile-up around a conical structure has been poorly understood. When a rubble mass clears around a structure, the load that can be imposed on the structure is influenced by a number of parameters, including: structure form, speed, porosity, roughness, lateral confinement of the rubble, and the size-shape-strength-and-roughness of ice fragments comprising the ice rubble. Furthermore, geometry of the rubble field and loading conditions at its boundaries would give rise to a complex state of stress distribution.

In order to understand and to quantify the influence that a rubble field has on ice-cone interaction behaviour, it is necessary to examine both the kinematic and the dynamic aspects of the rubble clearing processes. The manner in which ice blocks are generated and cleared around the structure determines the size and shape of the rubble formation. This rubble mass, in turn, being pushed against the structure, exerts forces on the ride-up ice and the supporting ice sheet. Until now there has been very few research studies dedicated specially to this subject. However, the problems encountered in the studies of rubble load on structures are quite similar to those found in soil mechanics; while the constitutive material differs, the similar particulate nature of the materials provides the common ground.

In this and the following two chapters, a rubble model is developed to model ice

rubble behaviour in front of a faceted conical structure. Basic theories of soil mechanics are explored, and the geometry of the rubble and the associated forces are modelled with the aid of numerical simulations. This chapter focuses on the basic mechanical behaviour and the failure processes of ice rubble under loading conditions typical of the ice-cone interaction process. Chapter 6 presents a simple method to characterize and compute the geometry of a fully developed rubble from known ice and structure conditions. The predictions agree well with the experimental data. In Chapter 7, a set of empirical equations are developed to calculate forces exerted by a cohesionless granular mass, i.e., ice rubble, on a retaining wall using a series of discrete element analysis. These equations are further incorporated into an ice force model which will be presented in Chapter 8.

The model developed in this work involves three important phenomenological parameters: the angle of internal friction, the angle of repose, and the earth coefficient function. The first parameter is a constitutive property of granular materials with Coulomb-type shear behaviour. The second parameter characterizes the natural slope of granular materials being dumped. The third parameter describes the stress state of a rubble mass under various loading conditions. The second and the third parameters are functions of loading conditions, and are closely related to the first parameter. In Section 5.1, the shear strength of granular materials is discussed, followed by a brief review of laboratory measurements of ice rubble shear properties. In Section 5.2, the surface profile of a rubble pile due to the natural dumping process is explored. The angle of repose, an important geometrical parameter of this profile, is discussed in detail. In Section 5.3, the behaviour of

granular materials under stresses is examined. The characteristic stress states of the granular materials under arbitrary loads, as described by various earth coefficients, are identified and further explored. Based on basic theories of soil mechanics, it is concluded that the cohesionless rubble is in an elastic state throughout its mass during the typical ice-cone interaction process under investigation. Finally, two existing methods for the computation of wall thrust exerted by an earth mass at-rest are assessed in Chapter 5.4.

### **5.1 Shear Strength of Ice Rubble**

Mostly, ice rubble studies were carried out due to the concerns expressed for the integrity of the structure encountered by ice ridges. In most of the instances, the ridges fail in shear with the maximum loads experienced by the structure are limited by the shear strength of the rubble materials. Therefore, measurements of rubble mechanical properties were mainly focussed on shear strength. The shear strength of an ice rubble under isothermal conditions is basically made up of:

- (i) The structural resistance to displacement of the ice blocks because of the interlocking of the ice blocks,
- (ii) The frictional resistance to translation between the individual ice blocks at their contact points, and
- (iii) The cohesion (adhesion) between the surfaces of the ice blocks.

For a cohesionless material, cohesion is negligible, while the resistance to deformation is influenced strongly by its frictional resistance at the contact surface and the

interlocking between ice blocks. A knowledge of the possible magnitude of this shear resistance and the factors that influence it are essential to a rational design.

### **5.1.1 Phenomenological and Structural Approaches for Material Description**

The mechanical behaviour of rubble is a complex reflection of its structure. Like other particulate materials, the deformation is brought about by mutual sliding and rotation of the ice blocks. The existence of mutual contacts restricts the freedom of motion of the individual block resulting in strength and rigidity of the ice rubble. The number and strength of the contact bonds are to a large extent determined by the size, shape, roughness and strength of the discrete blocks, the nature of the interaction between the various phases, the state of the ice rubble in question (e.g., its density and void ratio), and its texture.

The mechanical behaviour of ice rubble material can be studied using two different approaches: the phenomenological approach and the structural approach. In the phenomenological approach the laws governing the processes are deduced from the correlation between the input and the output data of a system whose dimensions greatly exceed those of their constitutive units; and hence, the real substances are replaced by mathematical models of structureless continua. The structural approach, on the other hand, analyses the mechanical behaviour based on the interaction between the fundamental constitutive units of the system. Phenomenological conclusions are then made possible through statistical synthesis.

Since the phenomenological characteristics are a result of rubble structure, a

structural definition is the fundamental one. A formulation of the phenomenological relations as a statistical synthesis of structural analysis would be ideal solution. This is the only way in which one can correctly understand and pay due regard to their specific structural characteristics which lead to constitutive relations of particulate materials. However, a complete structural analysis is frequently unsuccessful even in the case of the simplest deterministic systems, such as mono-crystals (Macmillan, 1972). For instance, in the statistical characterization of particulate materials, it has been often found to be incapable of describing the complete behaviour. In the present work, phenomenologically formulated mechanical laws useful in simple engineering computation are adopted.

### 5.1.2 Phenomenological Descriptions of Cohesionless Granular Materials

A classical foundation for the entire phenomenological approach was laid by Coulomb (1773). For the shear strength of soils, Coulomb derived a simple expression using "the law of friction and cohesion" proposed for soil substances by Amontons (1699):

$$\tau = c + \sigma_n \tan\phi \quad (5-1)$$

where  $\tau$  and  $\sigma_n$  are the shear and normal stresses on the failure surface, respectively;  $c$  is the cohesion; and  $\phi$  is the effective angle of internal friction. This definition of strength was further refined by Mohr (1882), who proposed the idea of representing graphically the combination of stresses by a circle. In the Mohr-Coulomb failure criterion, the strength of

a granular soil can be represented by the Mohr failure envelope, which is a line drawn tangent to the Mohr circles representing the state-of stress at the peak points of the stress-strain curves under various confining stresses. For cohesionless materials, the cohesion is negligible, i.e., the internal friction dominates the deformation characteristics and becomes the principal mechanical parameter of the materials.

Rubble is neither a solid nor a liquid, but it has some of the characteristics of both of these states of matter. It differentiates itself from fluids as described by Delanges (1788): "when poured, retain their shape, when excavated, do not fill the depression, after being shaken or otherwise disturbed, settle rapidly as soon as the external impulse no longer acts". However, on the other hand, it is similar to fluids in its tendency to exert a lateral pressure against an object with which it comes in contact due to the Poisson's ratio effect. This characteristic can be measured by the coefficient of lateral pressure, K, i.e., the reciprocal of the ratio between the vertical stress and the horizontal stress which tends to resist lateral deformation of the material. As we shall see, this K-coefficient is closely related to the internal friction of the material.

An important implication of the Mohr-Coulomb theory is that in a general three dimensional stress state, the intermediate principal stress has no influence on the failure criterion. This is approximately true. The behaviour of granular materials may be influenced by many factors, such as void ratio, gradation of grain sizes, loading path, temperature, time, and stress history. In recent years, an increasing number of other failure criteria have been proposed to give a better modelling of the most significant aspects of granular material

behaviour, including non-linearity, inelasticity, shear dilatancy, and path dependency (see Table 5.1). An overview of failure criteria for engineering materials, especially geological materials, was given by Desai and Siriwardane (1984), including elasticity model, classical plasticity models and other more recently developed models.

In the light of recent research, the linear Mohr-Coulomb model does certainly not mean the last word in strength theory, and in some problems it has proved inadequate in describing the true behaviour of unconsolidated ice rubble (Ettema and Urroz-Aguirre, 1991; Sayed et al, 1992; and Løset and Sayed, 1993). Yet, for engineering purposes, it has become a very useful and dependable tool for judging, by strength computations, the danger of failure in solid bodies under general stress conditions.

### 5.1.3 Effect of Initial Void Ratio on Internal Friction

The internal friction of a granular material in a given state is the result of a number of factors and influences, i.e., the void ratio of the material, the confining stresses, the rate of loading, etc.. which act upon the material at the moment of its shear failure. Of these factors, void ratio<sup>1</sup> is by far the most important. This ratio, which is a function of block shape and size distribution, can have a profound influence upon the rubble's internal friction.

The internal friction angle,  $\phi$ , of a cohesionless Coulomb material is made up of two

---

<sup>1</sup>The ratio of the volume of the pores to the volume of the solids in a rubble sample is called "void ratio"; while porosity is defined as the volume of the pores to the total volume of the rubble sample.

components: firstly, the frictional resistance arising from the sliding between particles; secondly, the structural resistance due to the interlocking of the particles. The former is solely a property of the material; whereas, the latter is purely geometric. The effect of particle interlocking is illustrated in Figure 5.1. In loosely packed materials, to start shear it is only necessary to make the particles slide upon one another. In a dense pack, the particles are interlocked with its neighbours, and have to move upwards and slip along the shear plane during shear. This tendency to dilate during shear was first observed by Reynolds (1885), and is known as the Reynolds dilatancy. The denser the packing, the greater is the tendency to dilate.

The influence of the dilatancy on the behaviour of granular materials has been studied by Rowe (1962), Been and Jefferies (1985), Bolton (1986), Goddard and Bashir (1990), Bashir and Goddard (1991); Goddard (1992), Balandran and Nemat-Nasser (1993), Pouliquen and Renaut (1996), and Schanz and Vermeer (1996). Housby (1991) gave an excellent review on the relationships between the friction angle, dilation angle, density and pressure in a granular material.

In a typical tri-axial strength test, the shear stress-strain behaviour of granular materials at a given normal load depends on the initial packing density (Lambe and Whitman, 1979). Figure 5.2 shows schematically two types of characteristic stress-strain curves. For densely packed samples, the shear stress increases with the strain, reaching a peak,  $\phi_p$ , and then gradually decreasing to some constant value,  $\phi_{cv}$ . Over this range of strains, there is usually an initial reduction in the volume of the sample due to compression

followed by an increase due to dilatancy. The maximum shear strength,  $\tau_p$ , is referred to as peak strength,  $\phi_p$ .<sup>2</sup> The denser the sample, the more the stress-strain curve shows a pronounced peak and the subsequent stress decreases following this peak. On the other hand, in case of loosely packed samples, the stress-strain curve does not show a pronounced peak, and instead the stress increases asymptotically to the critical value while the volume decreases. At very large strain both dense and loose samples achieve the same void ratio,  $e_{cv}$ , exhibit little or no tendency to further volume change; and the deviatoric stress for both curves becomes essentially constant. The strength for this state is referred to as constant volume strength,  $\phi_{cv}$ .<sup>3</sup> At this state, the sample can deform without volume change.

Figure 5.3 further shows the relationship between the internal friction angle,  $\phi$ , and the initial void ratio,  $e_o$  (Rowe, 1962). This trend of higher  $\phi$  for denser soil is always the same regardless of the type of granular materials. And, hence, this internal friction angle,  $\phi$ , is not a material property but depends strongly on the void ratio which reflects the degree of interlocking between blocks.

Since the strength at the ultimate condition for a particular sample is the same regardless of its initial void ratio,  $\phi_{cv}$  may be thought of as a material property. The value of  $\phi_{cv}$  can be approximated with reasonable accuracy by the angle of repose,  $\phi_r$ , i.e.,  $\phi_{cv} = \phi_r$  (see

---

<sup>2</sup>  $\phi$  and its variants, i.e.,  $\phi_p$  and  $\phi_{cv}$ , are actually internal friction angles; however, they are commonly referred to as the strength of cohesionless materials in soil mechanics.

<sup>3</sup>The angle is sometime referred to as ultimate, critical or residual angle (Lambe and Whitman, 1979).

Section 5.2).

Beside the void ratio, the internal friction is also dependent on the rubble composition, stress state, stress history, temperature, stress and strain rates, and the structure of the rubble. From Figure 5.1, it is clear that the angle of internal friction is also influenced by the grain size distribution and grain shape (Holtz and Gibbs, 1956) (see Table 5.2). The interlocking is particularly important as the angular ice blocks tend to interlock more thoroughly than round blocks. The general influence of the other variables outlined above with respect to soils has been detailed by Mitchell (1976).

#### **5.1.4 Limitations of the Phenomenological Approach**

The forces and movements induced by rubble-cone interaction processes are analysed primarily from a macroscopic point of view, which means that the rubble mass is assumed to be a continuum rather than composed of individual material parts, and the ice blocks are uniformly distributed throughout the body. Such an assumption will be sufficiently valid as long as voids are small and irregularities are present only on a scale small enough in comparison to the size of the structure under consideration.

In a typical ice-rubble interaction situation there are transients. Even after steady-state is reached, sizeable fluctuation of ice load can be observed which is superimposed on the constant base line. Although this fluctuation can be attributed to the nature of ice breaking and ride-up cycles, it may also be partly attributed to the pulsating clearance of rubble ice due to the discrete nature of broken ice pieces and the local variation of geometric

and mechanical properties.

In a typical rubble/structure system, a quantitative answer can only be given from case to case based on detailed statistical considerations that are beyond the scope of this research. Qualitatively, however, one can imagine that with decreasing size of the ice pieces, with respect to the structure dimensions, the discrete nature of the rubble becomes of lesser significance increasing the accuracy of a continuum macroscopic description. Observations from the present model tests, in terms of the geometry of the rubble and the associated loads on the models, suggest that the size effect is not significant even with the structure width to piece size ratio as low as 4.

If, however, the dimensions of the ice pieces became comparable to the structure width, the pulsating nature of ice clearance may become significant. In such situations, methods which account for the discrete nature of the interaction, i.e., discrete element modelling, should be employed and the fluctuation phenomena taken into account.

### **5.1.5 Laboratory Measurements of Rubble Strength**

Knowledge of the mechanical properties of bulk rubble is a prerequisite for analysis of rubble mass behaviour. The mechanical properties, such as internal friction and cohesion, can be determined through shear strength tests. These tests also allow the influence of strain rate and other variables such as block size and distribution, temperature, etc., to be investigated.

Most of the studies to date have been carried out in the laboratory, many of which

have been performed on artificially generated ice rubble using some form of the direct shear box or the simple shear apparatus. From these empirical test results, constitutive relationships have been derived. The type of apparatus used in published shear box experiments and the general results obtained are reviewed by Ettema and Urroz-Aguirre (1989 and 1991). The main features of these properties are briefly reviewed here. More detailed information can be found in the cited references.

The first comprehensive study into the properties of rubble ice was conducted by Prodanovic (1979) who performed direct shear tests on submerged samples. His results indicated that the bulk rubble obeys the Mohr-Coulomb criterion, under a certain range of stresses and displacement rates, i.e., Equation 5.1.

Other experiments by Keinonen and Nyman (1978), Weiss et al (1981), Hellman (1984), Gale et al (1985), Wong et al (1987), Sayed (1987), Urroz-Aguirre and Ettema (1987) and Case (1991) are in agreement with this conclusion, but there is an enormous spread in the reported values of friction angle and cohesion. For example, angles of internal friction have been reported from 11° to 65°, while cohesion has usually been reported to be negligible, but has also been reported to be up to 20 kPa by Sayed (1987). The shear box test results are summarized in Table 5.3.

The extreme variation in reported experimental results for the shear strength of ice rubble testifies to the complexity of what may seem a simple measure of resistance to shear. This variation may be attributed in part to the different testing methods used. Early tests used direct shear boxes (Prodanovic, 1979; Weiss et al, 1981; Hellman, 1984; and Fransson

and Sandkvist, 1985). Other tests were done using simple shear box (Urroz-Aguirre and Ettema, 1987), a plane-strain box (Sayed, 1987; and Sayed et al, 1992), and a small tri-axial cell (Wong et al, 1987). The direct shear boxes do not give a well defined failure plane within the sample; consequently, the stress and strain measurements cannot be properly quantified. The set-up used by Urroz-Aguirre and Ettema (1987), Sayed et al (1992), and Wong et al (1987) overcame this problem by producing uniform deformation in the sample. Different sample preparation methods, range of stresses, strain rates, sample temperature, melting or freezing of the samples, and the difficulty in proper scaling of the bulk material further complicate the problem as well.

Bruneau (1997) collected laboratory ice rubble shear data from the literature and compared them with the theoretical behaviour of a loose and dense sand. He concluded that the lower bound strength of ice rubble undergoing shear was similar to that of loose sand. He conjectured that the higher strength is attributed to various degrees of interblock bonding. Chao (1993) developed regression equations for estimating apparent cohesion and effective internal friction angle for unconsolidated ice rubble using four sets of ice rubble shear strength measurements (Prodanovic, 1979; and Weiss et al, 1981; Fransson and Sandkvist, 1985; and Case, 1991). It was found that the thickness and flexural strength of the ice pieces are the most important factors in determining the cohesion of the ice rubble. For the internal friction of the ice rubble, void ratio appears to be the most important parameter. Although the regression analysis was based on limited measurements of 10 - 15 data points, his findings regarding the internal friction are in agreement with other granular materials.

Recent studies on ice rubble mechanics indicated the importance of micro-mechanical interaction between constituent ice pieces in determining the overall mechanical properties of the ice rubble. Hopkins and Hibler (1991) conducted a series of discrete element simulation with a two-dimensional shear box filled with blocks which have a length to thickness distribution characteristic of pressure ridges. Particle shape, angularity, uniformity, mixture anisotropy, and compactness were modelled rigorously within the limits of the two-dimensional simulation. The results showed clearly that variations in the coefficient of friction have a great effect on the shear strength of angular rubble. They also demonstrated that local rearrangement of block and breakage are competing mechanisms for the relief of local forces on the nominal failure plane. Breakage which depended primarily on load produced a load dependence in the shear strength. Their results demonstrated the need to take account the micro-mechanical properties and interactions between the constituent ice blocks in rubble research, and also the versatility of Discrete Element Method, as these factors could be readily incorporated into the problem.

In interpreting the available laboratory measurements, two characteristics of rubble ice must be kept in mind. The first is the breakage of constituent ice blocks under confining pressures, which varies widely from test to test. Unlike other granular material, i.e., soils, the strength of ice is relatively weak, and considerable breakage of ice blocks may occur under even a moderate pressure. This breakage substantially affects the interlocking of the sample which is reflected in a lower internal friction at higher pressure. The second is the size of the sample. Unlike testing of real soils, rubble samples used in previous tests are

made from various sources, ranging from large size field ice to small size manufactured ice cubes. Early tests used relatively small test chambers, which might have led to size effects. Furthermore, all data on mechanical properties are from small scale laboratory tests, and uncertainties remain regarding the extrapolation of small scale data to field conditions.

Recently, comprehensive field experiments were carried out near Borden, Prince Edward Island adjacent to the Confederation Bridge to develop reliable and practical methods for characterizing the *in situ* strength of ice rubble in first-year ridges and rubble fields (Bruneau et al, 1998). Two *in situ* shear strength testing methods were attempted. The first, referred to as the direct shear approach, involved the horizontal displacement of a pre-cut ridge core slab. Forcing the solid ice layer sideways resulted in the shearing of bonds with the underlying ice rubble keel. The second approach, referred to as the downward punch technique, involved the vertical displacement of a pre-cut block of the ridge's refrozen layer. The technique provided a vertical failure of the underlying keel. Ancillary measurements were made of level ice thickness, ridge depths, ridge profiles, refrozen layer core samples, water salinities, sail heights, block size dimensions and weather conditions. Careful analysis of the data set will provide significant information on the deformation properties of ice rubble.

The measurement of the strength properties of ice rubble have been focussed on its plastic failure state under high to medium pressure. Only a few have been performed at the low pressure regime. Whereas, the rubble in front of a cone is expected to be in a loose state, i.e., cohesionless and under low confining pressure, and hence the test conditions may not

model the stress state that exists in the rubble under a typical interaction. At the rubble's free surface, the rubble is at the limit plastic state characterized by the internal friction angle at its loose state,  $\phi_{cv}$ . (See Section 5.2) Inside the rubble mass, the rubble is at its elastic state, which can also be related to  $\phi_{cv}$  (see Section 5.3). This  $\phi_{cv}$  is essential to model the rubble behaviour associated with the problem under investigation; yet, such measurements associated with ice rubble are scanty.

## 5.2 Rubble's Surface Profile Due to Natural Dumping Process

If a dry granular cohesionless material, i.e., dry, clean sand, is poured slowly from a not very high level onto a smooth horizontal plane, it will form a cone with its free surface inclined at a definite angle to the plane due to the internal friction of the material. The limiting slope formed by this process is called the angle of repose,  $\phi_r$ , and it presents the maximum inclination at which the material will just begin to move down the slope. Since the poured material generally finds itself in a loose state, the maximum stable slope angle,  $\phi_r$ , is about equal to the angle of internal friction for the loose state,  $\phi_{cv}$ . The existence of this angle of repose has been shown in various text books on soil mechanics, i.e., Lambe and Whitman (1979).

Observations from experiments indicate that a similar slope failure process constantly takes place at the free surface of the rubble as a result of constant dumping of ice blocks onto its surface; and hence the rubble's free surface profile may be conveniently assessed by the

simple, empirical measurement of its angle of repose assuming the scale of the ice pieces is small.

### **5.2.1 Variation and Maintenance of Rubble Surface Profile**

When rubble clears around the cone, three processes may arise:

- (i) Continuous dumping of ice blocks from the top to the rubble's free surface;
- (ii) Removal of ice blocks at the foot of the rubble as they move and clear from the side, and
- (iii) Increase of the free surface inclination of the rubble as it slides up the cone.

All three processes tend to increase the surface slope of the rubble, and hence ensure a unique surface profile of the rubble to be maintained at its angle of repose by continuous failure of its free surface. The third process happens only when the rubble is allowed to slide up the wall with the underlying ice, when the static friction is high enough to prevent sliding between the rubble and the underlying ice. When this condition occurs, it also accentuates the effects of the other two processes.

During steady-state rubble accumulation, the rubble slope fluctuates between two limiting values. Initially, the slope angle is less than the angle of repose. The slope increases through the aforementioned three processes until the slope is larger than the angle of repose for the rubble material, and progressive slope failure occurs. Up to this point, the motion of

ice pieces is slow and static equilibrium is maintained at each time instant. However, after the on-set of the slope failure, the motion of the toppling ice pieces is large and substantial kinetic energy is acquired by the toppling ice and the subsequent failure is dynamic. The slope after failure is substantially less than the angle of repose.

Cantelaube-Lebec et al (1995) reported an 8 degree difference between the angle of repose just after an avalanche, and the angle of maximum stability just before the avalanche in their experiment on the equilibrium conditions at the surface of a flowing 2-dimensional granular medium. The pre-avalanche slope angle represents the limiting condition which corresponds to the maximum amount of rubble loading on the cone.

Various aspects of gravity driven granular flows of particles down inclined surfaces, similar to the avalanche process, have also been studied by Savage and Nohguchi (1988), Jan et al (1992), Abu-Zaid and Ahmadi (1993), Chou (1994) and Pouliquen and Renault (1996).

Another process was also observed during tests which could limit the maximum rubble slope. Before the limiting angle of repose can be reached, all of the rubble mass can slide down the facet, thus decreasing the slope. This is expected to happen when the cone angle is steep or the ice-ice friction is low. Again, the pre-failure condition is static.

The angle of repose is affected by measuring methods and many parameters. Three methods commonly used to measure the angle of repose are described by Linoya (1993), viz., injection method, discharge method and tilting method. Brown and Richard (1990) have described each of these methods and discussed the various parameters affecting the angle of repose. Linoya et al (1990) have identified the various factors influencing the angle of repose

for granular materials, such as: particle size, size distribution, void fraction, injection rate, falling distance and size of heap.

### 5.3 Stress-State of Ice Rubble

#### 5.3.1 Behaviour of Granular Material Under Stress

Stresses within a granular mass are caused by the external loads applied to the granular mass and by its own weight. Since rubble mass is made up of blocks, it is essential to understand how a mosaic of granular material behaves under stress. Classical theories governing the earth pressure on a retaining wall form the logical starting point due to the well explored nature of the subject and the similarity of the interaction processes under investigation.

The stress state of a granular mass, under various loading conditions, can be described using the concept of earth pressure ratio function. In soil mechanics, this function is commonly expressed by a ratio called the coefficient of lateral stress, and is denoted by the symbol K:

$$K = \frac{\sigma_h}{\sigma_v} \quad (5-2)$$

where  $\sigma_h$  and  $\sigma_v$  are the horizontal and the vertical stresses, respectively. The value of K can vary over a wide range depending on the magnitude of the lateral (horizontal) pressure which can develop in the rubble mass. This lateral pressure can be related to the strength and

stress-strain properties of the material and deformations which occur within the mass as a result of lateral movements. There are three distinct kinds of lateral pressure, and a clear understanding of the nature of each is essential. In the special case, where there has been no lateral strain within the soil, the coefficient of lateral stress is said to be in the "at-rest" condition, and is denoted by the coefficient of elastic equilibrium at rest,  $K_0$ .  $K_0$  describes the geostatic stress condition. Coefficients for the two plastic limit equilibria,  $K_p$  and  $K_s$ , can also be identified.  $K_p$  and  $K_s$  describe the two plastic limits at which rigid plastic material yields plastically.

To illustrate the material behaviour at these three states, consider a level soil mass of semi-infinite extent retained by a smooth, rigid, wall as shown in Figure 5.4 which summarizes the general relationships between lateral deformation and pressure. For simplicity, the soil is assumed to be homogeneous, isotropic and cohesionless. The granular material tends to slip laterally and seek its natural slope. This tendency results in a push against the wall.

The vertical stress  $\sigma_z$  is controlled by gravity, and can be estimated from a profile of overburden stress with depth. For the condition where the soil deposit is normally consolidated<sup>4</sup>, the total vertical stress in the homogeneous soil at any depth of  $z$  is equal to the weight of the overburden:

---

<sup>4</sup>A condition in which the existing overburden pressure represents the maximum vertical pressure the soil mass has been subjected in its history.

$$\sigma_v = z\gamma_s \quad (5-3)$$

where  $\gamma_s$  is the total unit weight of the soil. There are no shear stresses upon vertical and horizontal planes within the soil; and hence, in the case of a horizontal ground surface, the vertical and horizontal components of the overburden stress are also principal stresses. If these stresses are associated with zero lateral deformations of the soil, i.e., the unyielding wall depicted in Figure 5.4b, they are referred to as the lateral stress at rest and the earth pressure coefficient is designated  $K_0$ .

The horizontal stress,  $\sigma_h$ , and hence the earth coefficient,  $K$ , are highly influenced by the current soil state. If the wall of Figure 5.4 is allowed to move away from the retained soil mass, the soil starts to expand in the horizontal direction, following the wall movement. (See Figure 5.4a) The lateral expansion of the soil against a smooth wall does not affect the vertical stress within the soil, but leads to a decrease in the lateral stress. Any element of soil will then behave just like a specimen of a tri-axial test in which the confining stress is decreasing while the axial stress remains constant. The soil's shear strength acts opposite to the direction of the expansion resulting in shearing resistance developed within the soil mass, and hence the lateral soil pressure on the wall decreases. When the soil develops its maximum shearing resistance with increasing lateral expansion, a sliding surface is formed in the soil behind the retaining wall, and the horizontal stress exerted on the wall decreases to a certain minimum, and no further decrease in the horizontal stress is possible. The horizontal stress for this condition is called the active stress, and the ratio of horizontal to

vertical stress is called the coefficient of active stress and is denoted by the symbol  $K_a$ .

If the same wall moves into the retained soil mass, the soil is compressed in the horizontal direction, with the soil shearing resistance acting to oppose the lateral compression (see Figure 5.4c). Any element of the soil is now in just the condition of a tri-axial specimen being failed by increasing the confining pressure while holding the vertical stress constant. When sufficient lateral movement occurs, the shearing strength of the soil is fully mobilized and the reaction of the resulting lateral earth pressure reaches its maximum value. The horizontal stress condition is called the passive stress, and the ratio of horizontal to vertical stress is called the coefficient of passive stress,  $K_p$ .

Figure 5.4 illustrates the important fact that lateral pressures change gradually in accordance with wall movement, and reach the fully active or passive conditions only when adequate movement has occurred. Until such movement is achieved, the lateral pressure acting on the wall is intermediate between the two limiting values, and the soil is said to be in a state of elastic equilibrium. Results of large scale model tests are reported by Tschebotarioff (1951).

The active and passive earth pressures constitute the ultimate case. The state of stress at this two extreme situations are called Rankine states, after the British engineer Rankine (1858) who noted the relationship between the active and passive conditions. For a simple case of a level cohesionless fill behind a frictionless vertical wall, the magnitudes of  $K_a$  and  $K_p$  are given by:

$$K_a = \frac{1 - \sin\phi}{1 + \sin\phi} \quad (5-4)$$

$$K_p = \frac{1 + \sin\phi}{1 - \sin\phi} \quad (5-5)$$

The range of K values can be large. For  $\phi = 35^\circ$ , the possible range of earth pressures is as follows:

Earth pressure	Symbol	Computed as	K coefficient
Active	$K_a$	Eq. 5.4	0.27
At Rest	$K_o$	Eq. 5.7	0.43
Passive	$K_p$	Eq. 5.5	3.69

The two limiting values  $K_p$  and  $K_o$  vary by factor of 13.7. Thus, it is important to identify the appropriate values for K to match a particular deformation and failure process.

The at-rest stress state is of practical and theoretical significance to the present investigation, since stress state is established when the backfill is placed behind a rigid wall without allowing any lateral strain, i.e., soil deposited behind a rigid unyielding wall, a process similar to the disposition of ice rubble in front of a rigid cone wall through end dumping process. This process results in a cohesionless granular pile in loose state, and, thus, the initial state of the rubble can be characterized by  $K_o$ .

When the soil is in a state of elastic equilibrium, the stresses in the lateral direction

can be computed from the stress-strain relationships of the soil assuming a linear isotropic material behaviour. The isotropic linear elastic body is characterized by two parameters: the Young's modulus of elasticity, E, and the Poisson's ratio, v, or with the use of another set of elastic constants -- the modulus of rigidity, G, and the Lamé's constant,  $\lambda$ .

The relationship between lateral and vertical strains is described by Poisson's ratio<sup>5</sup>, v; and for the condition of zero lateral strain the relationship between the principle stress (horizontal stress and vertical stress) are related by the ratio:

$$K_n = \frac{\sigma_h}{\sigma_v} = \frac{v}{1 - v} \quad (5-6)$$

Matsuo et al (1978) compared the measured earth pressure at rest on a retaining wall with the results from finite element computation, and showed that the elastic theory is applicable to evaluate earth pressure at rest if the Poisson's ratio can be properly given. The classical model of linear elasticity has been modified for use with dry cohesionless granular materials to account for the non-linearity of the stress-strain relationships of particulate structures. Even with these major modifications, accurate predictions of loads due to small deformations are very difficult to make due to a lack of knowledge of the stiffness moduli and strains as

---

<sup>5</sup>While the concept of Poisson's ratio used in continuum mechanics is still valid for a granular mass, it should be noted that, the Poisson's ratio is used here to describe the behaviour of the whole granular mass, i.e., not the individual discrete ice block. As the stress-state of the rubble depends on its load history, the Poisson's ratio of the rubble is not a material property and varies with the stress-state.

they change from point to point within the granular body.

Several theoretical and empirical relationships for  $K_o$  have been postulated for loose sands as summarized in Table 5.4 [Jáky, 1944 and 1948; De Wet, 1961; Brooker and Ireland, 1965; Wierzbickzky (see Rymsza (1979)); Feda, 1982; Matsuoka and Sakakibara, 1987; and Szepesházi, 1994]. However, experimental values of  $K_o$  are best represented by a simple expression given by Jáky (1948):

$$K_o = 1 - \sin\phi \quad (5-7)$$

The validity of this formula has been established by Szepesházi (1994) and Mayne and Kulhawy (1982). After giving a detailed examination of Jáky's equation, Szepesházi found the Jáky's equation and its variations compared well with 152 measurements from a variety of soils. Mayne and Kulhawy (1982) conducted an extensive review of laboratory data from over 170 different soils as shown in Figure 5.5 (Mayne and Kulhawy, 1982). Statistical analysis conducted on  $K_o$  for all available data indicated:

$$K_o = 1 - 1.003\sin\phi \quad (5-8)$$

having a sample correlation coefficient,  $r = 0.802$ . The scattering of data may be due to the variations of the other index properties of the soil, i.e., liquid limit, plasticity index, clay fraction, uniformity coefficient, void ratio, etc.

Many other investigators have also corroborated the results, i.e., Simons (1958); Brooker and Ireland (1965); Bishop (1971); Pruska (1972); Wroth (1972); Myslivec

(1972); Andrawes and El-Sohby (1973); Lambe and Whitman (1979); Fukagawa and Ohta (1988); Mesri and Hayat (1993); and Feda et al (1995).

### 5.3.2 Expected Stress State of a Typical Rubble in Front of a Faceted Cone

When the rubble is formed by a natural dumping process, the clearing of the rubble from the structure is analogous to the bulk material transport on an inclined belt conveyor as the supporting ice sheet and the ride-up ice act as the belt conveyor. And hence the rubble in front of the cone may constantly be subjected to two simultaneous processes:

- (i) The deposition of granular material in loose state in front of the structure during the initial formation; and
- (ii) The ride-up of rubble onto the facet in which the rubble is forced to conform to the underlying support when the rubble is conveyed up the facet.

The first process results in a rubble with stress associated with the at-rest state. The second process may affect the stress state within the rubble, with the stress-state deviating from the at-rest condition and moving toward the two plastic limits, depending on the type of deformation in question, i.e., compression or extension

The real interaction process may be a good deal more complicated than the simple picture presented above, but the essential process is nevertheless clear. It is expected that the maximum force that is exerted by the rubble on the wall would correspond to the elastic equilibrium state with a  $K$  value somewhat close to  $K_o$ , and it can diverge from  $K_o$  depending

on the effect of the second process. In all likelihood, such a change is negligible as long as the rubble is allowed to clear from the structure; therefore, in the present study, the effect of the second process on ice load is assumed to be negligible, and is not studied.

Possible extra load due to horizontal compression may be of concern, if the rubble is prevented from riding-up the structure; however, it should be noted that the rubble will not attain the passive state, even in this case. It is illustrated as follows:

General equations for passive earth pressure coefficients,  $K_p$ , can be established graphically through Poncelet's constructions (1840) for various wall angles,  $\alpha$ , rubble angle,  $t^6$ , wall friction angle,  $\phi_w$ , and the internal friction angle,  $\phi$ , of the rubble material (Jumikis, 1962). The expected rupture angle,  $\Omega$ , as defined in Figure 5.6 is given as follows (Jumikis, 1962):

$$\tan \Omega = \frac{\tan(\phi - \alpha) + \sqrt{\tan(\phi - \alpha)[\tan(\phi - \alpha) + \cot(\phi + (90^\circ + t))]}}{1 + \tan(-\phi_w - (90^\circ + t))[\tan(\phi - \alpha) + \cot(\phi + (90^\circ + t))]} \quad (5.9)$$

It should be noted that when the rubble angle,  $t$ , is equal to the angle of repose,  $\phi$ , the rupture angle,  $\Omega$ , is equal to zero and the actual rupture line would make an angle  $\phi$  below the horizontal level.

The above formula suggests that for an discrete rubble mass accumulated in front of

---

<sup>6</sup> In this thesis, the rubble angle,  $t$ , is reckoned as negative above and positive below the horizontal plane which is different from the common convention used in the field of soil mechanics. In the case under investigation, the angle is always positive.

an inclined wall, passive shear failure within the rubble will not occur during a typical interaction process, due to the large positive inclination of the free surface of the rubble. Any shearing failure (if there is any) will take place at the bottom of the rubble, where a weak shearing plane already exists, way before the shear strength of the rubble is fully mobilized.

#### **5.4 Analytical Methods for the Computation of Wall Thrust Exerted by Earth Mass at the At-Rest State**

The problem of the earth pressure within rubble at the 'at-rest' state or near it corresponds to one of the calculation of the earth pressure at rest for triangular fills.

The calculation methods of earth pressure at the ultimate Coulomb's and Rankine's equilibrium states have been studied and examined by many researchers and engineers (Coulomb, 1773; Caquot and Kerisel, 1948; Terzaghi and Peck, 1967; Packshaw, 1969; James and Bransby, 1971; and Shields and Tolunay, 1973); but there is no satisfactory method to compute the lateral pressure on walls due to fill at the at-rest state. Technical literature for the calculation of lateral pressures on a rigid wall due to a triangular fill, as in the present case, is limited.

In this section, two existing methods for the calculation of lateral pressures on a rigid wall due to a triangular fill are described: Melkote's elastic analysis (Melkote, 1977) and limit equilibrium methods. The discussion focuses on the limit equilibrium methods, while Melkote's method is only briefly described.

#### **5.4.1 Melkote's Method**

Melkote has developed a set of equations to compute earth pressures exerted on retaining walls by triangular fills as in the case of wrap-around for transition blocks, between earth dams and concrete spillways. His method consists of two steps by recognizing two important features of the problem, i.e., the fill is triangular in shape and the pressure is exerted in an 'at rest' condition. His derivations are based on Jürgenson's work (1934) on strip loads on semi-infinite masses. In this method, the vertical wall pressures due to the triangular fill are first estimated by calculating the vertical pressures due to a quarter infinite fill against the retaining wall on the basis of integration of Boussinesq's Equation (1885) for a single concentrated load acting on a semi-infinite medium; and then unloading the fill in strips beyond the actual embankment section. The horizontal pressures are then obtained by multiplying the vertical pressures with the coefficient of earth pressure at rest. His method is also applicable to a wall inclined at any angle, and a fill consisting of any number of layers with different densities and compaction characteristics. Due to the complexity of the derivation, the equations are not presented here.

Melkote's method has rarely been used as designers favour simpler methods.

#### **5.4.2 Limit Equilibrium Methods**

A simpler and widely used method, which may be applicable to the problem under investigation, is the limit equilibrium method commonly used in slope stability analysis (Huang, 1983). This method is based upon states of limit equilibrium which have dominated

earth pressure problems for over two hundred years. The analysis essentially applies the principles of static equilibrium to a relatively simple geometry in which slip on discontinuities is governed by a specified shear strength model. It involves making an estimate of the weights to be resisted, the geometry and the shear strength of the failure surface, and the amount of shear mobilized within the granular mass. The stability of individual slopes is expressed as a factor of safety,  $F_s$ , which is the ratio of forces resisting movement to the forces tending to induce sliding. When the mass is stable, the factor of safety is higher than unity; and when the factor of safety is equal to unity, the slope will be unstable, i.e., at limiting equilibrium. A factor of safety smaller than unity implies an impossibly steep slope.

Most problems in slope stability are statically indeterminate, and hence various levels of simplification are used in order to arrive at a unique solution. This leads to a variety of methods (Fellenius, 1936; Bishop, 1955; Morgenstern and Price, 1965; Seed and Sultan, 1967; Spencer, 1967; Wang et al, 1972; and Janbu, 1973), ranging from the simple wedge method (Seed and Sultan, 1967) to the very sophisticated finite-element method (Wang et al, 1972). In this section, the simple wedge method is presented to illustrate the general computational procedures of the limit equilibrium methods.

As we have already shown in the previous section, any sliding will occur at the pre-existing sliding plane, and the principle underlying stability calculation of the triangular rubble mass is the failure in shear along the sliding planes, when the driving forces exceed the resisting forces. The forces on the ice contact surfaces, due to the rubble, can be

reasonably estimated by assuming that the rubble is made up of a number of hypothesized rigid blocks piled up against the inclined surface and considering the equilibrium of forces for each of these blocks. By considering the rubble blocks as rigid bodies, it is possible to predict rubble forces on the cone with the aid of rigid body mechanics. The simplest analysis consists of two rigid blocks moving along the contact surfaces: the support and the incline, as shown in Figure 5.7.<sup>7</sup> The lower block has a weight,  $W_1$ ; and the upper block has a weight,  $W_2$ , resting on the incline with an angle,  $\alpha$ . The dimensions of  $W_1$  and  $W_2$  are given. The rubble is assumed to be cohesionless, and have a natural slope,  $t = \phi$ . The contact surfaces between the rigid blocks, support, and wall as well as each other form potential failure planes. The sliding resistance of the rubble at the wall and the support is governed by ice friction angle,  $\phi_r$ .

The distribution of forces on each plane depends on the interaction force between the two sliding blocks and can be determined by considering the two blocks jointly. Figure 5.8 shows the free-body diagram for each block. The angle of the inter-block force,  $\phi_d$ , is required for solution, and may be assumed equal to the developed friction angle, i.e.,  $\tan\phi_d = \tan\phi/F_s$ ,<sup>8</sup> with  $F_s$  being the factor of safety commonly used in limit equilibrium analysis.

---

<sup>7</sup>The mechanism in Figure 5.7 is not strictly kinematically feasible for the rigid blocks analysis, because any downward vertical movement of the upper block will cause the block to lock up at point A. This difficulty can be overcome by assuming that sufficient localised deformation occurs in the region around point A to allow the mechanism to operate.

<sup>8</sup>At the verge of failure, the friction at the sliding planes, along the support and the incline, is fully mobilized, i.e., equal to  $\tan\phi_d$ ; however, the friction between the two rigid blocks

By assuming that the factor of safety,  $F_s$ , is everywhere the same, applying equally to  $\tan\phi$  for the rubble material between blocks, and to  $\tan\phi_u$  at the wall and the support, there are a total of four unknowns,  $P$ ,  $F_s$ ,  $N_1$  and  $N_2$ ; where  $P$  is the force acting between the two blocks, and  $N_1$  and  $N_2$  are the forces normal to the failure planes. The problem is statically determinate with four unknowns and four equations, two from each block.

For the lower block, summing all forces in the vertical direction and the horizontal directions, and solving for  $N_1$  and  $P$ :

$$N_1 = \frac{W_1 \cos\phi_d}{\cos\phi_d - \left(\frac{\tan\phi_u}{F_s}\right) \sin\phi_d} \quad (5-10)$$

$$P = \frac{N_1 \tan\phi_u}{F_s \cos\phi_d} \quad (5-11)$$

or  $P$ , in term of the unknown  $F_s$  only:

$$P = \frac{W_1 \tan\phi_u}{F_s \cos\phi_d - \tan\phi_u \sin\phi_d} \quad (5-12)$$

For the upper block,

may not be fully mobilized, i.e., the angle of the inter-block force is less than or equal to  $\tan\phi$ , depending on the value of  $F_s$ .

$$N_2 = \frac{W_2 \cos \phi_d}{\cos(\phi_d - \alpha) - \left( \frac{\tan \phi_u}{F_s} \right) \sin(\phi_d - \alpha)} \quad (5-13)$$

$$P = \frac{N_2 \left[ \sin \alpha - \left( \frac{\tan \phi_u}{F_s} \right) \cos \alpha \right]}{\cos \phi_d} \quad (5-14)$$

or P, in term of the unknown  $F_s$  only:

$$P = \frac{W_2 \left[ \sin \alpha - \left( \frac{\tan \phi_u}{F_s} \right) \cos \alpha \right]}{\cos(\phi_d - \alpha) - \left( \frac{\tan \phi_u}{F_s} \right) \sin(\phi_d - \alpha)} \quad (5-15)$$

The equation for the factor of safety  $F_s$  as a function of input parameters  $\phi_d$ ,  $\phi_u$ ,  $\alpha$ ,  $W_1$  and  $W_2$  can be determined by equating Equations 5.12 and 5.15. Once  $F_s$  is obtained,  $N_1$ ,  $N_2$  and P can be computed from Equations 5.10, 5.13 and 5.15. A computed value of  $F_s$  greater than unity means sliding at the potential failure plane does not take place; while, a values of  $F_s$  smaller than unity means that the sliding failure will occur with a given rubble angle. In such cases, the rubble angle should be reduced and a new  $F_s$  computed until a value of unity for  $F_s$  is obtained. The corresponding rubble angle is the maximum angle which can satisfy the static equilibrium condition.

By assuming the rubble as rigid blocks, the limit equilibrium methods ignore the flexibility of the rubble mass. Furthermore, the assumed value of  $\phi_s$  highly influences the

stress distribution on the potential sliding plane, and the associated factor of safety. For example, Figures 5.9 to 5.11 show the safety factor, the limiting rubble angle, and the horizontal wall thrust, calculated from the fore-mentioned method, as a function of  $\phi_s/\phi$  for  $h = 1$  m,  $\alpha = 50^\circ$ ,  $\phi = 30^\circ$  and  $\phi_s = 11.3^\circ$  and  $21.8^\circ$ . A commonly accepted way to estimate  $\phi_s$  has yet to be developed.

In Chapter 7, empirical equations to calculate wall thrust due to a triangular fill at the at-rest state will be formulated from a series of numerical simulations. The equations are simple to use and yet account fully for the discrete nature of the fill materials.

Table 5.1 Summary of failure criteria proposed for granular materials (after Evgin and Sun, 1989)

Isotropic Criteria	Anisotropic Criteria
1. Mohr-Coulomb 2. Drucker-Prager (1952) a. Bishop (1971)	1. Hill (1950) (for orthotropic materials) 2. Generalization of Mohr Coulomb's Criteria a. Baker and Krizek (1970) b. Boehler and Sawzuck (1970) c. Nova and Sacchi (1979) 3. Tsai-Wu a. Tsai and Wu (1971) b. Wu (1974) c. Saada et al. (1983)

Table 5.2 Effect of angularity and grading on peak friction angle (after Terzaghi, 1955)

Shape and Grading	Loose	Dense
Rounded, uniform	30°	37°
Rounded, well graded	34°	40°
Angular, uniform	35°	43°
Angular, well graded	39°	45°

Table 5.3 Summary of laboratory shear box tests on ice rubble

Author	Test Performed	Material Tested	Shearing Rate (mm/s)	Initial Void Ratio, $e_v$	Normal Pressure (kPa)	Test Temp. (°C)	Cohesion c (kPa)	Friction Angle, $\phi$ (°)
Keinonen & Nyman (1978)	Direct shear	Block 3.21, saline ice ( $t=b$ block thickness)	n.a.	0.54 - 0.59	0.5 - 1.5	n.a.	0.11	47
Prodanovic (1979)	Vertical shear	Max. block size: 81, saline ice	19 - 38	n.a.	0.0 - 2.7	n.a.	0.26 - 0.58	47 - 53
Weiss et al (1981)	Vertical shear	Similar to above, max. block size: 41	3 - 25	0.23 - 1.00	0.0 - 28.0	-4.0 - -20.0	1.7 - 3.4	11 - 34
Helman (1984)	Vertical shear	ice chip, commercial ice (mean diameter 30 mm), and urea-doped ice	1.6 - 92.0	n.a.	0.0 - 4.0	0	0.0 - 5.8	43 - 65
Gale et al (1985)	Direct shear	Max. cube size: 9.5 mm, fresh water ice	n.a.	0.67 - 1.00	51 - 140	-1	n.a.	n.a.
Uroz-Aguirre & Eitema (1987)	Simple shear	Parallelipped blocks, max. dimension from 16 to 95 mm, fresh water and polyethylene ice	2	n.a.	0.6	0	n.a.	35 - 52
Sayed (1987)	Plane strain compression	30 mm cubic blocks, fresh water ice	n.a.	0.67 - 9.85	2.5 - 35.0	-10.0, -22.0	10 - 20	27 - 45
Cuse (1991)	Direct shear	Block size: 1.31, EG/ADS ice	1	n.a.	n.a.	+2.0	0.52 - 0.82	27 - 49

Table 5.4 Different equations for coefficient of pressure of loose soil at rest

Source	Equation
Jáky (1944) - original	$K_o = K_a (1 + \frac{2}{3}\sin\phi)$
Jáky (1948) - simplified	$K_o = 1 - \sin\phi$
De Wet (1961)	$K_o = \frac{1 - \sin^2\phi}{1 + 2\sin^2\phi}$
Brooker and Ireland (1965)	$K_o = 0.95 (1 - \sin\phi)$
Wierzbiczky ((see Rymsha (1979))	$K_o = \tan^2(45^\circ - \frac{\phi}{3})$
Feda (1982)	$K_o = \frac{\tan\phi - \sqrt{2} - \left(\frac{1+2\beta}{2\sqrt{2}(1+\beta)}\right)}{\left(\frac{1+2\beta}{\sqrt{2}(1+\beta)}\right) - 2\tan\phi - \sqrt{2}}$ <p><math>\beta</math> is the ratio of the elastic and plastic axial strains</p>
Matsuoka and Sakakibara (1987)	$K_o = \frac{1}{1 + 2\sin\phi}$
Szepesházi (1994)	$K_o = (1 - \sin\phi) \left( \frac{\sin\phi}{(1 - \sin\phi)(\sin\phi - \sqrt{4.5 + 4\sin\phi} + 3)} \right)$

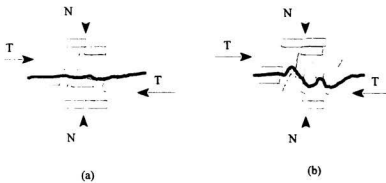


Figure 5.1 Example of interlocking: (a) slightly interlocked surfaces in loosely packed rubble, (b) highly interlocked surfaces in densely packed rubble

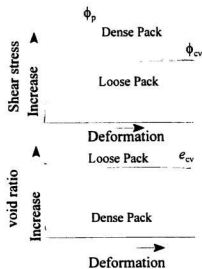


Figure 5.2 Typical stress-strain curves for loose and dense samples

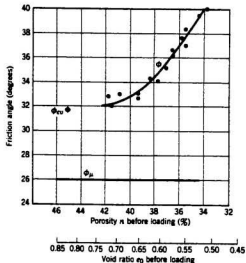


Figure 5.3 Internal friction angle versus initial void ratio for medium fine sand.  $\phi$ ,  $\phi_{cv}$ , and  $\phi_\mu$ , are internal friction angle, constant volume strength, and particle contact friction angle, respectively. (after Rowe, 1962)

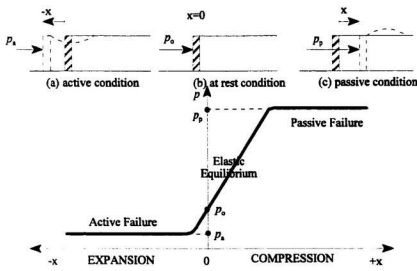


Figure 5.4 Three characteristic types of earth pressure

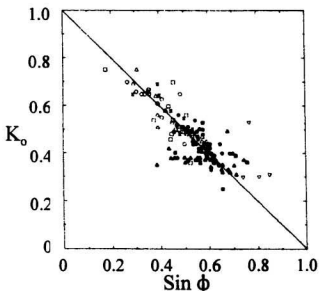


Figure 5.5

Observed relationship between  $K_o$  and  $\sin \phi$  for cohesive and cohesionless soils: the solid symbols denote cohesionless soils and the hollow symbols denote cohesive soils (after Mayne and Kulhawy, 1982)

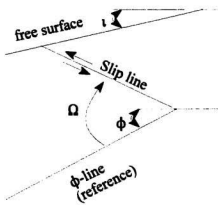


Figure 5.6 Graphical illustration of  $\Omega$  used in Equation 5.9

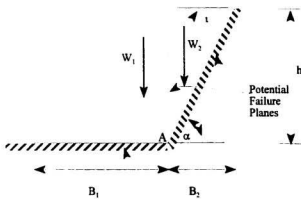


Figure 5.7 Rubble geometry showing the two rigid blocks and the potential failure planes

$$\phi_d = \tan^{-1} (\tan\phi / F_s)$$

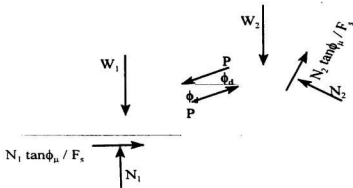


Figure 5.8 Free body diagram of sliding blocks

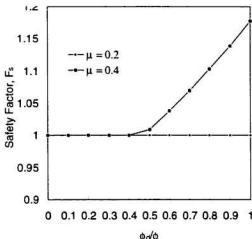


Figure 5.9 Safety factor as a function of  $\phi_d/\phi$  for wall angle,  $\alpha = 50^\circ$ , angle of repose,  $\phi = 30^\circ$ , and ice friction angle,  $\phi_\mu = 11.3^\circ$  and  $21.8^\circ$

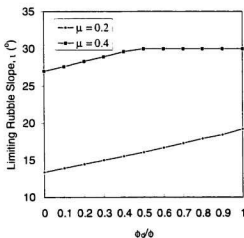


Figure 5.10 Limiting rubble slope as a function of  $\phi_d/\phi$  for wall angle,  $\alpha = 50^\circ$ , angle of repose,  $\phi = 30^\circ$ , and ice friction angle,  $\phi_\mu = 11.3^\circ$  and  $21.8^\circ$

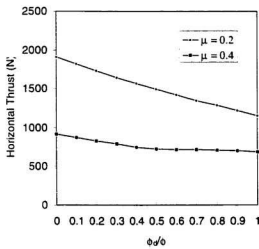


Figure 5.11 Horizontal thrust on the wall as a function of  $\phi_d/\phi$  for wall angle,  $\alpha = 50^\circ$ , angle of repose,  $\phi = 30^\circ$ , and ice friction angle,  $\phi_\mu = 11.3^\circ$  and  $21.8^\circ$

## Chapter 6 Rubble Geometry Idealization

When an ice sheet encounters an obstacle in its path, the amount of ice blocks that can be generated and piled up in front of the structure is influenced by a number of structure and ice parameters. A realistic modelling of the rubble field and the mechanism of its formation is essential to an accurate ice load estimate.

In this Chapter, a new model to predict the shape and size of the rubble is presented based on insights obtained from the earlier experiments (Chapter 4) and the basic soil mechanics theories (Chapter 5). The purpose of this model is to compute the geometry of the rubble based on simple yet essential interaction processes and mechanical principles. Section 6.1 describes the general features of the interacting systems and the assumptions used. The discussion forms the conceptual basis of the rubble geometry idealization. In Section 6.2, an idealized geometry of a fully developed ice rubble is presented. Such a rubble is expected to pile-up in front of a faceted cone during typical rubble generation and clearing processes. The geometry is uniquely defined by the rubble's angle of repose, and the characteristic rubble heights along the cone perimeter. The methodology to predict the amount of ice piled up via mass balance considerations is also described.<sup>1</sup> Section 6.3 presents the detailed derivation of the basic equations for the rubble height calculations. The key heights are the maximum heights of the rubble along the front facet and side of the cone.

---

<sup>1</sup>McKenna and Bruneau (1997) used a very similar mass balance technique to estimate rubble build-up on conical structures during ridge interactions by considering the projected area of the advancing ice and the amount of ice rubble cleared.

The derivations are validated in Section 6.4 by comparing the predicted values of the maximum heights to the corresponding measurements from physical model tests.

### 6.1 General Features and Assumptions of the Interacting System

A considerable simplification of the analysis can be realized by recognizing the principal features of ice generation, ice supply and ice clearing processes associated with the interaction between a relatively thick and strong slow moving ice sheet and a face-on oriented faceted cone. Figure 6.1 describes the typical ice breaking pattern observed in the model tests. The ice sheet in front of the cone can be divided into 3 characteristic zones: an accumulation zone located directly in front of the front facet and a clearing zone located on both sides of the accumulation zone (the ice tends to accumulate in the accumulation zone and clear from the clearing zone). For simplicity, the width of the accumulation zone is equal to the facet width at the waterline<sup>2</sup>,  $w_f$ ; whereas, the width of the clearing zones is almost equal to the projected waterline width of the side facet in the direction of ice movement.

If the ice is thick and strong, the train of ice blocks generated from the accumulation zone will be allowed to ride up the front facet, reaching the neck intact, and form an inclined wall with a constant width,  $w_f$ , as shown in Figure 6.2. This wall forms a barrier preventing any ice clearing through it; and any ice generated from the ice breaking can only clear

---

<sup>2</sup>The width of the accumulation zone is influenced by the ice breaking pattern, and a more precise method to estimate this width is given in Section 8.2.1.1.

beyond the wall at both sides. Hence, analogous to those of the ice sheet, accumulation and clearing zones can also be identified within the rubble, as shown in Figure 6.3.

When the ride-up ice from the accumulation zone reaches the neck, the broken ice blocks fall back onto the accumulation zone following a path parallel to the centerline of the cone. These ice blocks contribute to a constant supply of ice blocks into the rubble. On the other hand, the ice blocks generated from the clearing zone ride up the side facet and clear around the cone without obstruction; and hence, they do not contribute to the supply of the rubble.

Since the rubble is sitting on top of the ride-up ice, it follows the same clearing process of the underlying ice. In most case, the friction between the rubble and the underlying ride-up ice is sufficient to prevent any sliding between the interface. As a result, the rubble is transported up the facets with the underlying ice acting as a conveyer belt. The ice blocks located in the accumulation zone cannot clear around the cone, but instead tumble back onto the accumulation zone due to the obstruction of the neck located directly in their path. These blocks eventually move sideways into the clearing zone. Once the ice blocks are in the clearing zone, they ride up and clear from the side facet with the riding-up ice. The idealized flow pattern around the cone is also given in Figure 6.3.

The rubble surface profile is generated by a process analogous to the process of berm construction by end dumping of granular materials from a line source, i.e., at the end of a belt conveyor. Although the rubble is constantly pushed forward by the front facet, the speed is so slow that it does not seem to affect the process. This process results in a rubble with a

surface profile governed by slope stability criterion where the slope of the rubble is equal to the angle of repose of its constituent material. With this surface profile known, the geometry of the rubble can be uniquely defined with a given height profile around the cone perimeter.

The size and shape of the rubble at any instant during its development depend on the balance between the supply and clearance of ice blocks to the rubble system. At the steady state rubble clearing process, a constant amount of rubble piles up in front of the structure, and its mass can be estimated by geometric consideration and a mass balance calculation.

Neglecting the discrete nature of the ice flow, the rate of ice supply into the rubble depends on the thickness and velocity of the ice sheet and size of the cone; and the rate of ice clearing from the rubble depends on the size of the rubble formation. At the earlier stages of the rubble growth, the rate of ice clearing is low as most ice blocks are situated in the accumulation zone. As the rubble grows, the rate of ice clearing from the sides increases with increasing amount of the ice blocks moving into the clearing zone, until the rate of ice clearing equals to the rate of ice supply. When this condition occurs, the rubble is fully developed. As the rubble grows, the slope tends to be constant, equal to the angle of repose.

Figure 6.4 shows the geometry of the rubble as it grows in size.

To simplify the problem treatment, the following six assumptions are used for the analysis:

(i) Rubble Generation Process:

The rubble pile is generated by end dumping of ice blocks from a line source

located at the neck directly above the front facet.

(ii) Cohesionless Ice Blocks:

The constant deformation of the rubble mass prevents any cohesion being developed within the rubble.

(iii) Full Mobilization of Shear Strength at Rubble's Free Surface:

The shear strength is fully mobilized at the rubble's free surface. It follows from assumptions (i) and (ii) that the free surface of the rubble is equal to the angle of repose of the material.

(iv) Full Rubble Development:

The rubble is allowed to develop fully without the bearing failure of the supporting ice sheet.<sup>3</sup>

(v) Quasi-Static Equilibrium State of Rubble:

The ice velocity is slow enough that the dynamic motion of the ice

---

<sup>3</sup> This condition is valid for relatively strong ice tested in IMD's series; however, this may not always be the case. The maximum amount of rubble may not be developed due to failure of the supporting ice sheet, as observed in several tests conducted in IME. In such cases, the strength of the supporting ice sheet has to be considered (see Section 7.6.2).

blocks can be ignored.<sup>4</sup> The rubble in front of the cone is assumed to maintain a quasi-static equilibrium state at all time. It follows that:

- (a) The shape of the fully developed rubble can be deduced from considering the static stability of the rubble around the structure alone. In other words, the dynamic motion of the individual ice block does not alter this stable shape.
- (b) The inertial impact of ice blocks tumbling down the slope will not destabilize the natural slope of the rubble, i.e., the slope maintains at its angle of repose.

(vi) No Interaction Between the Free Surface and the Rubble-Ice Interface

The existence of the structure does not modify the free surface profile of the rubble, i.e., the rubble is thick enough that there is no interaction between the free surface and the ice-structure interface. The free-surface maintains its angle of repose independent of the ice-structure interface condition. Thus, a unique geometry of the rubble can be obtained by first forming a heap of rubble from a line source and then superimposing it on to the structure.

---

<sup>4</sup>Observation from model tests shows no discernible effects on the piling process or the geometry of the rubble with speed up to 2 m/s full scale.

## 6.2 Ideal Geometry and Mass Balance

Figure 6.5 shows the idealized geometry of the rubble system surrounding a simple faceted cone. Only the front right quarter of the cone is shown. The free surface of the rubble always maintains at its natural angle of repose,  $\phi_r$ , in the radial direction. The profile of rubble height around the front perimeter of the cone is defined by three characteristic heights,  $h_n$ ,  $h_f$ , and  $h_m$ , which are the heights of rubble at the side of the cone, at the edge of the front facet, and the maximum heights along the front facet, respectively. In the present model, the values of  $h_n$ ,  $h_f$ , and  $h_m$  are derived, and the variation of height between these three points along the cone perimeter is assumed to be linear. The increase of height from the edge of the front facet toward its centerline is due to the end effect typical of a three-dimensional heap formation from a line source with finite length (see Section 6.3.3); and the increase of height from the edge of the front facet toward the side of the cone is due to the ride-up of the rubble ice along the side facet. The rubble height profile along the cone's perimeter, together with the known geometry of the cone and the assumed natural angle of repose, uniquely define the geometry of the rubble.

The above idealized geometry is deduced from considering the main features of the rubble generation and clearing processes, and is in agreement with observations from model tests (see Figure 4.1d). Once this geometry is deduced, the size of the rubble, i.e., the values of  $h_n$ ,  $h_f$ , and  $h_m$ , can be obtained through mass balance calculation.

To illustrate this, please refer to the rubble system shown in Figure 6.6. Again, only the front right quarter of the system is shown. The rubble's free surface, the cone surface,

and an imaginary vertical plane form the boundaries of the system under consideration. The ice blocks are supplied into the system at the top of the rubble, and eventually clear through the cross-section of the rubble intersected by the vertical plane, i.e., cross-sectional area, A. The general mass balance equation governing the selected system is given as follows:

$$R_s = R_u + R_c \quad (6-1)$$

where  $R_s$  and  $R_c$  are the rate of ice supply to and clearing from the rubble system, respectively; and  $R_u$  is the rate of ice accumulation in the system.

In the case of a steady flow, there is no mass accumulation within the rubble system. Thus, the rate of mass supply to the rubble system is equal to the rate of mass clearing from the system:

$$R_s = R_c \quad (6-2)$$

Since all the ice mass riding up the front facet must eventually enter into the rubble system as ice supply to the system, the rate of ice supply is equal to the rate of ice displaced by the front facet; and hence:

$$R_s = w_f t V \quad (6-3)$$

where  $w_f$  is the waterline width of the front facet;  $t$ , is the ice thickness; and  $V$  is the ice advancing speed.

The rate of ice clearing through an arbitrary cross-section in the rubble mass is a

function of the area of the cross-section, A, as well as the velocity,  $V_c$ , and the porosity,  $p$ , of ice passing through it:

$$R_c = 2(1 - p)AV_c \quad (6-4)$$

The factor of 2 reflects the fact that same cross-section, A, exists at both sides of the cone.

In the present derivation, two imaginary vertical planes are selected, a front reference plane and a side reference plane which intersect the rubble mass with the cross-sections associated with  $h_f$  and  $h_s$ , respectively. Since the rubble moves with the underlying ice sheet, the speeds of ice clearing through these two reference planes are assumed to be equal to the ice advancing speed V. By equating the ice clearing rate to the ice supply rate, i.e., Equations 6.3 and 6.4, and letting  $V_c$  equal to V:

$$A = \frac{w_f t}{2(1 - p)} \quad (6-5)$$

The geometry of A is defined by the angle of repose at the rubble surface, the cone angle at the ice cone interface, and an unknown height which is determined in the next section.

### 6.3 Derivation of Basic Equations for Characteristic Heights of Rubble

#### 6.3.1 Rubble Height at the Edge of Front Facet, $h_f$

Because of its proximity to the source of ice supply, the geometry of the frontal portion of the rubble is highly affected by the way the ice blocks are supplied into the rubble

system.

Figure 6.7 shows the geometry of a rubble pile formed by dropping ice blocks from a line source. If we ignore the end effect due to the finite width of the line source, the rubble will have a central wedge section with length equal to the width of the line source, and a half cone section formed at each of the two ends. The free surface of the rubble has an angle equal to the angle of repose,  $\phi_r$ , of the dumped material. Suppose that we dump material from a finite line source onto an inclined plane with the same width as the source, the expected geometry of the rubble is illustrated in Figure 6.8. In other words, the geometry of the rubble formed in front of a structure can be obtained by super-imposing the rubble on the structure.

To perform a mass balance calculation for  $h_{rf}$ , only the frontal portion of the rubble is considered. Figure 6.9 defines the rubble system to be considered. The cone in this problem consists of three sections, with the subscript 1 denoting the lowest section and subscript 3 the neck section. The geometry of the cone, in terms of the height,  $h_i$ , and the slope,  $\alpha_i$ , of each section is known. The slope of the rubble is equal to  $\phi_r$ . In this figure, the rubble reaches the vertical neck, but the analysis also applies to rubble with its height at the edge of the ride-up ice below level of the neck. To simplify the calculation, the thickness of the ride-up ice is ignored, and the width of the ride-up ice wall is assumed equal to  $w_r$ . The reference plane intersects the rubble at the side of the ride-up ice on the neck and front facets to form a cross-section  $A_{rf}$ . It is assumed that some ice will be trapped between the side-facet

and the back of the ride-up ice wall, preventing any ice to pass through cross-section  $A_2$ , and the trapped ice is not considered in this analysis. The rest of the rubble system interfaces with the side-facet at area  $A_3$ ; and, hence, the ice, which is supplied from the top of the front facet, must clear from the rubble system through cross-section  $A_{rf}$ .

Figure 6.10 shows the geometry of  $A_{rf}$  corresponding to the Cross-Section A-A as defined in Figure 6.9. The cross-sectional area,  $A_{rf}$ , can be obtained by considering the geometry of the system:

$$A_{rf} = \frac{B_{rf} h_{rf}}{2} - A_{ob} \quad (6-6)$$

where  $A_{ob}$  is the projection of  $A_1$  (see Figure 6.9) onto the reference vertical plane where the ice is directly blocked by the portion of the structure protruding beyond the ride-up ice wall. Since:

$$B_{rf} = \frac{h_{rf}}{\tan\phi_r} \quad (6-7)$$

then:

$$A_{rf} = \frac{h_{rf}^2}{2\tan\phi_r} - A_{ob} \quad (6-8)$$

When the rubble increases in height, the front reference plane moves toward the rear

part of the cone with increasing  $C_{ob}$ , until, and unless, the  $h_n$  is equal to or greater than  $h_2$ , and portion of the cone blocking the ice movement increases with increasing  $B_{ob}$  and  $h_{ob}$ . The shape of  $A_{ob}$  depends on the geometry of the cone, i.e.,  $\alpha_{rf,i}$ ,  $h_i$ , and the height  $h_{ob}$  or length  $B_{ob}$  as defined in Figure 6.10. In Figures 6.9 and 6.10,  $B_{ob}$  and  $h_{ob}$  are shown at their maximum values. The  $\alpha_{rf,i}$  corresponding to each cone section can be obtained by tracing the interaction between the cone and the vertical reference plane. It can be shown that when the plane intersects the cone surface at a particular section, the intersecting line always makes an angle equal to the cone's side angle,  $\alpha_{s,i}$ , with the horizontal, where  $i$  is the corresponding section; and hence  $\alpha_{rf,i} = \alpha_{s,i}$ . It can also be shown that the following relationships hold for a six-faceted cone of any cone inclinations and sections:

$$\frac{B_{ob}}{C_{ob}} = \tan 30^\circ \quad (6-9)$$

and

$$\frac{\tan \alpha_{s,i}}{\tan \alpha_i} = \sin 60^\circ \quad (6-10)$$

where  $\alpha_i$  and  $\alpha_{s,i}$  are the slopes of the centerline and edges of a facet at section  $i$ , respectively.

The distance  $C_{ob}$  is equal to:

$$C_{ob} = \frac{h_{rf} - h_{n-1}}{\tan \alpha_n} + \sum_{i=1, n-1} \frac{h_i - h_{i-1}}{\tan \alpha_i} \quad (6-11)$$

where the subscript, n, is the highest section of the cone the rubble reaches, and  $h_0$  is equal to zero. Substituting Equations 6.10 and 6.11 into Equation 6.9:

$$B_{ob} = \left( \frac{h_{rf} - h_{n-1}}{\tan \alpha_{n,n}} + \sum_{i=1, n-1} \frac{h_i - h_{i-1}}{\tan \alpha_{i,i}} \right) \sin 30^\circ \quad (6-12)$$

The height  $h_{ob}$  can be calculated from  $B_{ob}$ ,  $\alpha_s$  and  $h$ , i.e.,

$$h_{ob} = \left( B_{ob} - \sum_{i=1, m-1} \frac{h_i - h_{i-1}}{\tan \alpha_{i,i}} \right) \tan \alpha_{s,m} + h_{m-1} \quad (6-13)$$

where m is the number of sections blocking the ice clearing. In the above equation, m cannot be calculated a-priori; however, unless the height of the lowest cone,  $h_1$ , is very small, for all intents and purposes, the ice will only be blocked by the lowest section of the cone, i.e.,  $m = 1$ , with  $h_{ob}$  equal to  $(B_{ob} \tan \alpha_{s,1})$ . In this case,  $A_{ob}$  can be calculated from the following equation:

$$A_{ob} = \frac{1}{2} B_{ob} h_{ob} = \frac{1}{2} B_{ob}^2 \tan \alpha_{s,1} \quad (6-14)$$

Combining Equation 6.14 and Equation 6.8 gives:

$$A_{rf} = \frac{1}{2} \left( \frac{h_{rf}^2}{\tan\phi_r} - B_{ob}^2 \tan\alpha_{t,1} \right) \quad (6-15)$$

Letting A from Equation 6.5 equal to  $A_{rf}$  in Equation 6.15,  $h_{rf}$  can be solved:

$$h_{rf} = \sqrt{\left[ \frac{w_f t}{(1-p)} + B_{ob}^2 \tan\alpha_{t,1} \right] \tan\phi_r} \quad (6-16)$$

where  $B_{ob}$  is computed from Equation 6.12.<sup>5</sup>

To compute the value of  $B_{ob}$ , the highest section, n, which the rubble reaches must be known. The value n can be obtained via trial and error method by assuming an arbitrary n, and then the corresponding  $h_{rf}$  is calculated and compared with  $h_n$ , the height of the assumed section. If  $h_{rf}$  is greater than  $h_n$ , then the actual n is greater than the assumed value, and a higher value for n must be assumed until  $h_{rf}$  is smaller than the assumed  $h_n$ .

For an unlikely event that m is greater than 1,  $A_{ob}$  and  $h_{rf}$  can be calculated from the following generalized equations:

$$A_{ob} = \frac{1}{2} \left[ \frac{h_{ob}^2}{\tan\alpha_{s,m}} + \sum_{i=1,m-1} h_i^2 \left( \frac{1}{\tan\alpha_{s,i}} - \frac{1}{\tan\alpha_{s,i+1}} \right) \right] \quad (6-17)$$

<sup>5</sup>Provided the value of n is known, Equations 6.12 and 6.16 form a set of two simultaneous equations with two unknowns,  $B_o$  and  $h_{rf}$ .  $B_o$  and  $h_{rf}$  can be solved by iterative procedure by letting the initial value of  $h_{rf}$  equal  $h_n$ . A few iterations will give a converged value of  $h_{rf}$ .

$$h_n = \sqrt{\left[ \frac{w_f t}{(1 - p_i)} + \frac{h_{ob}^2}{\tan \alpha_{i,m}} + \sum_{i=1,m+1} h_i^2 \left( \frac{1}{\tan \alpha_{i,i}} - \frac{1}{\tan \alpha_{i,i+1}} \right) \right] \tan \phi_r} \quad (6-18)$$

where  $h_{ob}$  is computed from Equation 6.13, and the trial value of  $h_n$  is computed via the above trial and error method by assuming an arbitrary  $m$  (in an ascending order) for each assumed  $n$  value.

### 6.3.2 Rubble Height at the Side of Cone, $h_n$

For the calculation of the characteristic rubble height at the side of the cone,  $h_n$ , consider an imaginary vertical axial plane of symmetry in the cone, B-B, which intersects the rubble at the side of the cone with a cross-section  $A_n$  as shown in Figure 6.11. Again, to maintain a constant amount of ice mass within the rubble system, the rate of ice supply to the rubble system must be equal to the rate of ice clearing through  $A_n$ .

The cross-section,  $A_n$ , is depicted in Figure 6.12. The slope of the rubble is equal to  $\phi_r$ . Again similar to Equation 6.8:

$$A_n = \frac{h_n^2}{2 \tan \phi_r} - A_{ob} \quad (6-19)$$

where  $A_{ob}$ , a function of  $h$ ,  $h_n$ ,  $\alpha_n$  and  $n$ , is given as the following:

$$A_{ob} = \frac{1}{2} \left[ \frac{h_n^2}{\tan \alpha_{i,n}} + \sum_{i=1,n-1} h_i^2 \left( \frac{1}{\tan \alpha_{i,i}} - \frac{1}{\tan \alpha_{i,i+1}} \right) \right] \quad (6-20)$$

where the subscript n denotes the highest section where the rubble reaches (see Figure 6.12).

Substituting Equation 6.20 into Equation 6.19 leads to the following equation for  $A_n$ :

$$A_n = \frac{1}{2} \left[ h_n^2 \left( \frac{1}{\tan \phi_r} - \frac{1}{\tan \alpha_{i,n}} \right) - \sum_{i=1,n-1} h_i^2 \left( \frac{1}{\tan \alpha_{i,i}} - \frac{1}{\tan \alpha_{i,i+1}} \right) \right] \quad (6-21)$$

By substituting Equation 6.5 into Equation 6.21,  $h_n$  can be solved:

$$h_n = \sqrt{\frac{\frac{w_f t}{(1-p)} + \sum_{i=1,n-1} h_i^2 \left( \frac{1}{\tan \alpha_{i,i}} - \frac{1}{\tan \alpha_{i,i+1}} \right)}{\frac{1}{\tan \phi_r} - \frac{1}{\tan \alpha_{i,n}}}} \quad (6-22)$$

To compute the highest section, n, of the cone which the rubble reaches, trial and error procedure similar to those given in the preceding section can be used.

### 6.3.3 Derivation of Generalized Equation for Maximum Rubble Height Along the Front Facet Face, $h_m$

Observations from model tests indicate that the rubble edge along the front facet is not level. The rubble height profile is parabolic with the height decreasing from a maximum value,  $h_m$ , at the centerline of the front facet to  $h_e$  at the edge. This decrease can be

attributed to the end effect during the formation process of a three-dimensional rubble pile from a finite line source with a constant output rate along its length. In this section, this effect is explained and a simplification in regarding the rubble geometry is made in order to arrive at a simple relation between  $h_{m\bar{r}}$  and  $h_r$ . The implication of this approximation and its correction are then addressed. Due to geometric complexity of a multi-sloped cone, only the equations associated with single sloped cones are derived in this section.

The phenomenon of end effect due to dumping from a finite line source is illustrated in Figure 6.13 for a simple two-dimensional case. If there is no lateral restraint, a portion of the dumped material at the two ends will slide down the heap to form a lateral slope; and thus decrease its height at the two ends. Conceptually, the end effect can be illustrated by replacing the heap formation with two steps process as shown in Figure 6.14. The rubble material is first dumped within the two lateral wall restraints, and then, the lateral wall restraints are released to allow materials at both ends to collapse to form the lateral slopes. The profile of the heap can be computed by letting area  $A_1$  equal to area  $A_2$ . The length,  $w$ , can be viewed as the portion of the line source which is subjected to the end effect. Figure 6.15 shows the dimension of a two-dimensional heap formed in front of a facet by the process depicted in Figure 6.14. As material is added to the heap, the length  $w$  will increase with increase of  $B$ ,  $h_r$ , and  $h_{m\bar{r}}$ . If  $w$  is smaller than  $0.5 w_f$ , a trapezoidal profile is formed with:

$$w = 0.5B \quad (6-23)$$

and the maximum height:

$$h_{rm} = B \tan\phi_r = 2h_{rf} \quad (6-24)$$

as shown in Figure 6.15a. The maximum value of  $w$  is limited to  $0.5 w_f$ , when a triangular profile is formed. If the heap is allowed to grow further, the dimensions  $B$ ,  $h_{rf}$  and  $h_{rm}$  will increase while  $w$  is kept constant. The maximum height:

$$h_{rm} = h_{rf} + w \tan\phi_r = h_{rf} + 0.5w_f \tan\phi_r \quad (6-25)$$

as shown in Figure 6.15b.

To extend the analysis to a three-dimensional case analogous to the rubble formation in front of a conical structure, the problem is simplified by assuming the geometry of the rubble in front of the cone to be identical to that formed by dumping materials in front of an inclined plane. Figure 6.16 shows half of the rubble mass formed in front of a sloping plane by a line source with the lateral movement of ice blocks restrained. The right hand side is the plane of symmetry through the centerline of the sloping plane. Figure 6.17 shows the final shape of the rubble after the removal of lateral restraint on the left hand side. The inclined plane is selected in order to simplify the derivation. The plane intersects the rubble over an area, part of which is a triangle,  $e_{gj}$ , with an area  $A_5$ . (See Figure 6.17.) The derivation is only for a single slope structure with the front facet wide enough such that  $w$

is less than  $\frac{1}{2} w_f$ .<sup>6</sup> To further simplify the computation, the curved free surface on the lateral slope is approximated by a plane surface. The width,  $w$ , can be computed by equating the volume,  $V_w$ , of the wedge abcdef in Figure 6.16 to the volume,  $V_p$ , of the pyramid abcj in Figure 6.17 and is given as:

$$w = \frac{B}{3} \quad (6-26)$$

$B$  and  $h_m$  are related to  $B_1$  and  $h_{rf}$ , respectively, by a simple proportionality of 1.5, i.e.:

$$B = \frac{3}{2} B_1 \quad (6-27)$$

and

$$h_m = \frac{3}{2} h_{rf} \quad (6-28)$$

Combining Equations 6.26 and 6.27:

$$w = \frac{B_1}{2} \quad (6-29)$$

These relationships, applicable to cases with  $w$  less than  $\frac{1}{2} w_f$ , are independent of  $\phi$ , and  $\alpha$ .

To compute  $w$  using Equation 6.29,  $B_1$  must be known.  $B_1$  can be estimated by a method similar to those used in the previous section by considering the cross-section  $A_s$  in

<sup>6</sup>For the size of the structures encountered in the field,  $w$  is generally less than  $\frac{1}{2} w_f$ .

Figure 6.17; and  $B_1$  is given as:

$$B_1 = \sqrt{\frac{w_f t}{(1 - p)\sin\phi_r} \cos \left[ \sin^{-1} \left( \frac{\sin\phi}{\sin\alpha} \right) \right]} \quad (6-30)$$

Despite a slight difference between the cross-section used in the derivation of the  $h_{rf}$  in Section 6.3.1 and the one used here, the  $h_{rf}$  computed in Section 6.3.1 can be used to estimate  $h_{rm}$  via Equation 6.28.<sup>7</sup>

In the above derivation,  $V_p$ , i.e., the volume abcj of Figure 6.17, is assumed to be a pyramid. Since the volume abcj is part of a right circular cone bisected by an inclined plane, the surface acj is a curved surface and an exact solution should treat line aj as a circular arc, as shown by a dotted line in the figure. The approximate solutions of w and  $h_{rm}$  always under-estimate the exact values, and the error increases with increasing  $\alpha$ .

To adjust for the error incurred by the assumption, consider the base of the lateral portion of the rubble as shown in Figures 6.18. The area  $A_3$ , i.e., triangle abj, is the approximate base area of the lateral portion of the rubble deposited in front of the inclined plane, whereas the area,  $A_3 + A_4$ , is the true base area. The values of  $A_3$  and  $A_4$  are given in the following relationships:

$$A_3 = \frac{r^2}{2} \sin\alpha_r (1 - \cos\alpha_r) \quad (6-31)$$

---

<sup>7</sup>For a reasonably deep cone, i.e., cone angle,  $\alpha > 45^\circ$  and rubble angle,  $\phi_r = 35^\circ$ , the  $h_{rf}$  derived from the vertical or the inclined reference planes are within 1% of each other.

$$A_4 = \frac{\pi r^2 \alpha_r}{360} - r^2 \sin\left(\frac{\alpha_r}{2}\right) \cos\left(\frac{\alpha_r}{2}\right) \quad (6-32)$$

where,

$$\alpha_r = \cos^{-1}\left(\frac{\tan\phi_r}{\tan\alpha}\right) \quad (6-33)$$

The exact values of  $w$  and  $h_m$  can be obtained by the following relationships:

$$w = \frac{1}{2} B_1 \left( \frac{A_3 + A_4}{A_3} \right) \quad (6-34)$$

$$h_m = \frac{h_{rf}}{1 - \frac{1}{3} \left( \frac{A_3 + A_4}{A_3} \right)} \quad (6-35)$$

For example, for the case of a cone with an angle of  $\alpha$  equal to  $53^\circ$  and a rubble with slope equal to the angle of repose,  $\phi_r = 35^\circ$ ,  $A_3$  and  $A_4$  equal to  $0.201r^2$  and  $0.083r^2$ , respectively, and the ratio,  $(A_3 + A_4)/A_3 = 1.41$ . Therefore, the exact solution for  $w$  and  $h_m$  are equal to  $0.57B_1$  and  $1.887h_{rf}$ , according to Equations 6.34 and 6.35, respectively.

#### 6.4 Validation of Ice Rubble Geometry Prediction Model

The predictions for  $h_n$  and  $h_m$  from the above model are compared to the measurements with the two 1:25 scale models tested in the IMD's series. Only those tested with a velocity of 0.04 m/s were examined.<sup>8</sup> The large necked model was tested in 0.094 m, 0.123 m and 0.160 m thick ice, and the small necked model was tested in 0.158 m thick ice, with a total of four data points. The model predictions and the relevant measurements are given in Table 6.1. An example calculation is given in Appendix C. The angle of repose,  $\phi_r$ , was about 35° estimated from the video recording. This value is used in the model predictions. To use the equation for  $h_m$ , the structure is assumed to have an average slope,  $\alpha_{ave}$ , of 49.8° and 56.9° for the small and the large necked models, respectively. The computed  $h_m$  is only slightly sensitive to the  $\alpha_{ave}$ , i.e., the  $h_m$  is within 5% computed from  $\alpha_{ave}$  ranging from 40° to 60°. The computed  $w$  for all tests is less than 0.5  $w_f$ , indicating a trapezoidal rubble height profile along the front facet.

Despite limited data used, the predictions from the derived equations give excellent agreement with the measurements from the selected tests with the difference between the computed and the measured values for  $h_n$  and  $h_m$  being 2.6% and 1.2% (on the average), respectively. It is expected that such agreement will hold for other faceted cone structures provided that the interaction assumed in this work prevails.

---

<sup>8</sup>There was no discernable effect on ice force or ice clearing process due to ice velocity. The rubble heights measured from the selected tests were considered representative to those associated with tests conducted with different velocities.

The model predicts that the rubble height at the edge of the front facet is lower than the rubble height at the side of the cone. This prediction is consistent with the general observations from model tests in which the rubble is forced to ride-up the side facet with its height increasing gradually toward the side of the cone (see Figure 4.1d).

This model assumes the rubble slope is governed by  $\phi$ , of the rubble material. In the case where the rubble angle,  $t$ , is smaller than  $\phi$ , due to premature sliding failure of the rubble, the actual  $t$  should be used. With the reduction of  $t$ , the rubble heights will be reduced as shown in Figure 6.19.

There is no rubble accumulation for a cone with edge-on orientation since all ice will slide along the side facet and clear around the cone continually. For cones oriented between the face-on and edge-on directions, the ice blocks can slide along the side facet or fall back onto the on-coming ice sheet. The balance of these two tendencies governs the motions of the blocks. No consideration is given to this, and this model is valid for faceted cones with face-on orientation only.

Table 6.1 Comparison of predictions from the new geometry model and the measurements from IMD's tests

Test	Model	Measurements				Predictions		
		t (m)	w/w <sub>f</sub>	h <sub>n</sub> (m)	h <sub>mm</sub> (m)	h <sub>n</sub> (m)	h <sub>r</sub> (m)	h <sub>mm</sub> (m)
MUNCONE3	1:25S	0.158	0.43	0.49	0.68	0.48	0.36	0.67
MUNCONE5	1:25L	0.095	0.35	0.35	0.51	0.33	0.27	0.51
MUNCONE6	1:25L	0.124	0.41	0.37	0.57	0.36	0.30	0.58
MUNCONE4	1:25L	0.160	0.46	0.39	0.65	0.39	0.34	0.66

Common Parameters:

<sup>1</sup> Parameter	Model 1:25S	Model 1:25L
h <sub>1</sub> (m):	0.233	0.067
h <sub>2</sub> (m):	0.466	0.307
w <sub>f</sub> (m):	0.693	0.693
α <sub>1</sub> (°):	39.8	39.8
α <sub>2</sub> (°):	63.4	63.4
α <sub>ave</sub> (°):	49.8	56.9
p ( ):	0.3	0.3
φ <sub>r</sub> (°):	35	35

Note: <sup>1</sup> Subscript: 1 - lower cone, 2 - collar

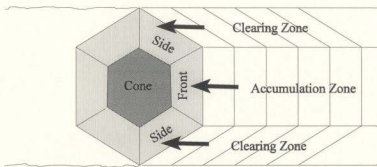


Figure 6.1 Ice breaking pattern showing the location of the accumulation and clearing zones (arrows indicate direction of ice movement)

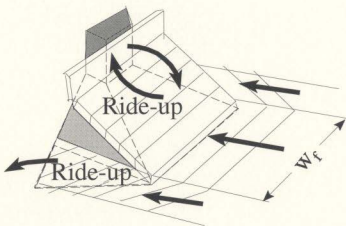


Figure 6.2 Ride-up pattern of ice generated from the accumulation and clearing zones (arrows indicate direction of ice movement)

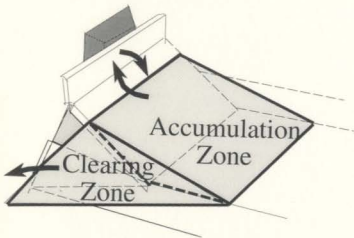


Figure 6.3 Geometry of a typical rubble showing the location of the accumulation and clearing zones (arrows indicate direction of ice movement)

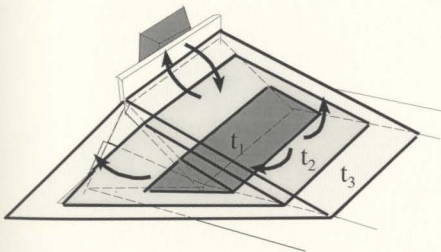


Figure 6.4 Geometry of a typical rubble at times  $t_1$ ,  $t_2$  and  $t_3$  as it grows in size ( $t_1 < t_2 < t_3$  and arrows indicate direction of ice movement)

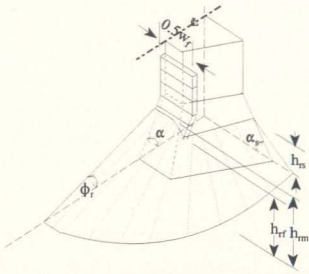


Figure 6.5 Geometry of an idealized rubble surrounding a faceted cone (only the front right quarter is shown)

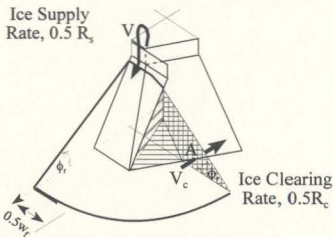


Figure 6.6 Rubble system selected for mass balance calculation (arrows indicate directions of ice movement and only the front right quarter is shown)

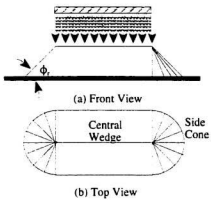


Figure 6.7   Geometry of a rubble pile formed by dropping ice blocks from a line source. Note: Half cones formed at the two ends

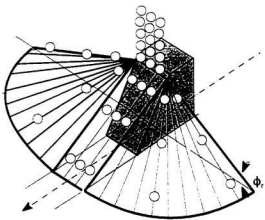


Figure 6.8   Rubble geometry in front of an inclined plane formed by end dumping from a line source

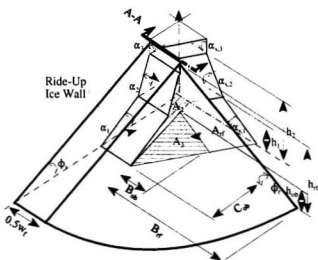


Figure 6.9 Rubble system selected in the calculation of  $h_{rf}$  (only the front right quarter of the rubble is shown)

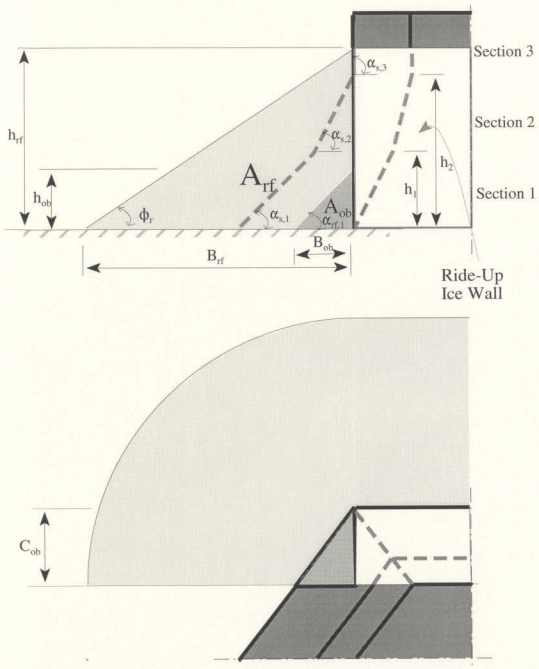


Figure 6.10 Geometry of  $A_{rf}$  corresponding to the Cross-Section A-A as defined in Figure 6.9: (a) front view; (b) top view

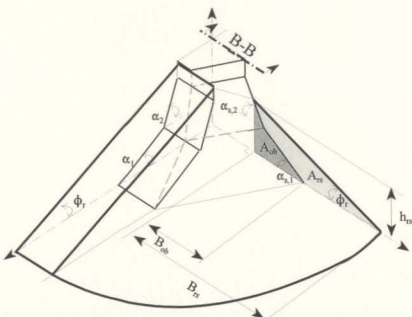


Figure 6.11 Rubble system selected for the calculation of rubble height at the side of the cone,  $h_{ts}$

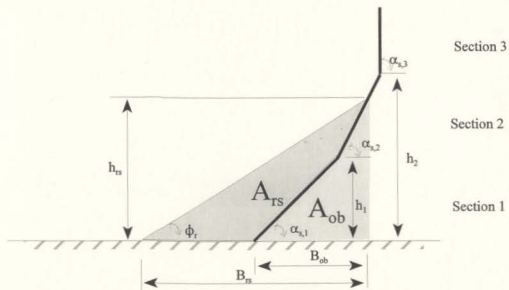


Figure 6.12 Cross-sectional view B-B as defined in Figure 6.11 showing the geometry of  $A_{rs}$

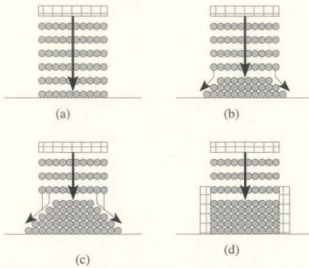


Figure 6.13 Formation of two-dimensional rubble pile from a line source: (a) to (c) lateral slope formed by depositing materials at both ends; (d) lateral slope is not formed due to lateral restraints at both ends

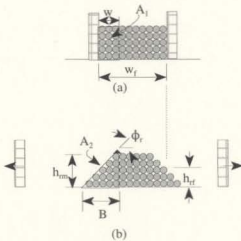


Figure 6.14 Rubble formation by two consecutive processes: (a) heap formation with lateral restraints (no end effect); (b) lateral slope formation by releasing the lateral restraints

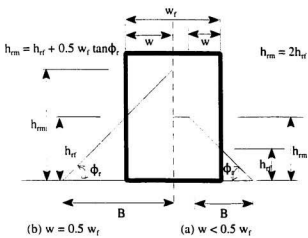


Figure 6.15 Figure showing the dimensions of a two-dimensional heap formed by the process depicted in Figure 6.14, when: (a)  $w < 0.5w_f$ , and (b)  $w = 0.5w_f$

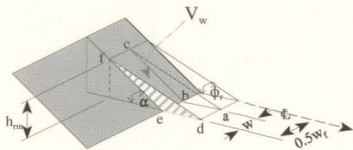


Figure 6.16 Rubble mass formed in front of a sloping plane by a line source with lateral movements of ice blocks restrained

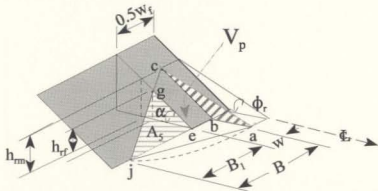


Figure 6.17 Final shape of the rubble with the lateral restraint on the left hand side removed

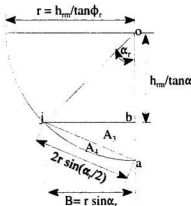


Figure 6.18 Base of the lateral portion of the rubble: coordinates a, b, and j corresponding to those in Figure 6.17, and coordinate o is the vertical projection (on to the base) of coordinate c in Figure 6.17

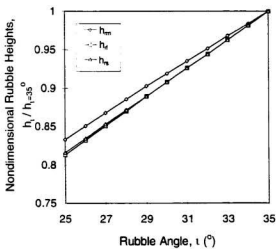


Figure 6.19 Figure showing the decrease of rubble heights with the decrease of rubble angle. Rubble heights have been non-dimensionalized with heights computed at  $t = \phi_r = 35^\circ$ .

## **Chapter 7 Discrete Element Analysis of Rubble Loads on an Rigid Inclined Wall**

Discrete element analysis (DEM) using the computer program DECICE has provided a powerful simulation tool for complementing analytical and experimental work. It is particularly appropriate for cases in which contact behaviour between adjacent ice blocks govern the mechanical properties of the ice rubble. The versatility of DEM in modelling ice related problems has been demonstrated in a number of recent works (Babic et al. 1990; Hopkins and Hibler, 1991; Hopkins, 1992; Evgen et al. 1993; Loset, 1994a and 1994b; Hopkins, 1995; Sepehr et al. 1997; Sayed, 1997; Katsuragi et al. 1997; Wang et al. 1997; and Sayed and Timco, 1998).

In the present study, the problem of rubble loads exerted on the faceted cone is treated as a two-dimensional problem using the DECICE2D, a two-dimensional version of the discrete element code DECICE.<sup>1</sup> The numerical investigation has been divided into two parts. In part one, the geometries of a one-dimensional compression (oedometer) test (Lambe and Whitman, 1979) and a simple gravity test were simulated to evaluate the internal friction parameters for simulated ice rubble blocks, i.e., the internal friction angle,  $\phi$ , the

---

<sup>1</sup> The appropriateness of DECICE in ice related problems has been demonstrated by the author in his previous work, including modelling of rubble shear properties, ice force on a moored buoy (McKenna et al. 1997), ice interactions on a bridge pier (Lau, 1994a), and jamming of floes at bridge piers (Lau, 1994b).

corresponding 'at-rest' earth pressure coefficient,  $K_0$ , and the angle of repose,  $\phi_r$ . The effects of ice shape and friction were investigated. In part two, the loads exerted on an unyielding retaining wall and the base support by a rubble pile were addressed. The effect of rubble height, rubble slope, wall inclination, and the internal friction of the rubble were examined, and a set of equations were formulated from the results of the simulations. These equations are incorporated into the ice force model presented in Chapter 8.

In this chapter the results of the analysis are summarized. Section 7.1 describes briefly the main features of the DECICE computer code. The results of studies on simulations of rubble mass behaviour at the "at-rest" state are presented in Section 7.2. Section 7.3 summarizes the results of the load computation for rubble at the same stress state, from which an equation for the computation of total wall thrust is derived and presented for a variety of simulated ice and structure conditions. Equations for the other components are derived in Section 7.4. The equations are extended to walls with multiple slopes in Section 7.5; and finally, the application of the new formula for other loading conditions is discussed in Sections 7.6.

## 7.1 Main Features of the DECICE Computer Code

DECICE is a two- and three-dimensional discrete element computer program for solving complex solid mechanics problems involving multiple interacting bodies undergoing fracturing. In this method, the problem domain is divided into discrete elements. Each element is considered as a distinct body which interacts with, or disconnects from,

neighbouring elements during loading. The movement of each block is governed by the laws of motion due to unbalanced forces acting on the element. Elements may be rigid or deformable. The deformability, frictional, and damping characteristics of the interfaces between elements are represented by spring-slider-damper systems which are located at contact points between elements. Prescribed force displacement relations for the spring-slider-damper system allow evaluation of normal and shear forces between elements. The algorithmic detail of DECICE is described in the DECICE theoretical manual (Intera Technology, Inc., 1986c).

DECICE has been calibrated against a wide set of experimental and field results, including ice ride-up and pile-up on artificial island side-slopes (Hocking et al., 1985a), dynamic impact of ice on an offshore structure (Hocking et al., 1985b), ice ride-up and ice ridge cone interaction (Hocking et al., 1985c), identification of ice properties (Intera Technology, Inc., 1986a), analysis of spray ice platform (Applied Mechanic, Inc., 1985), and ice ridging loads (Intera Technology, Inc., 1986b).

Recently, the author (1994a) has performed an independent verification of DECICE in ice force prediction and simulation. A series of six runs, which simulate the dynamics of sheet ice interaction with a 60° conical bridge pier, were conducted using DECICE3D, a 3-D version of DECICE. The results were verified with model tests carried out in the tank of the Institute for Marine Dynamics (Spencer et al., 1993) and the available field observations around Finnish Kemi I lighthouse in the Gulf of Bothnia (Hoikkanen, 1985; and Maattanen and Hoikkanen, 1990). Figure 7.1 shows the interaction of the ice blocks, the cone and the

ice sheet from a typical DECICE simulation of ice forces on a 60° cone in ice. A plot of predicted versus measured horizontal peak forces is shown in Figure 7.2. A close agreement between the calculated peak force values with the experimental measurements suggests that DECICE is a promising simulation tool for solving ice cone interaction problems.

## 7.2 Simulations of Rubble Mass at the "At-Rest" Condition

For a cohesionless ice rubble, the most important and commonly used phenomenological descriptor to describe the mechanical behaviour of the rubble is its internal friction angle,  $\phi$ . During a typical rubble piling, the rubble's free surface is at a state of limit plastic equilibrium characterized by the angle of repose,  $\phi_r$ ; while, inside the rubble, it is at elastic state characterized by the lateral coefficient of earth pressure at rest,  $K_0$ . These two parameters can be related to the internal friction angle of the rubble material in a loose state,  $\phi_{cv}$ , and are essential to model the rubble behaviour; yet, measurements associated with ice rubble are not available.

The main objectives of this part of the analysis, using DECICE simulations, are to:

- (i) Obtain the internal friction angle of the bulk rubble which is to be used in the subsequent load simulations; and,
- (ii) Verify the relationship between the internal friction angle, the lateral coefficient of earth pressure at rest, and the angle of repose of the rubble materials in the range of expected field conditions.

Two series of simulations were conducted. In the first series, rubble samples with a wide range of ice piece aspect ratio, AR, and ice friction,  $\mu$ , were prepared and the at-rest earth coefficient was computed via two test set-ups: (i) a simple gravity test, and (ii) the standard oedometer test. From the earth coefficient, the corresponding internal friction angle was computed using Jáky's equation. In the second series, six rubble masses were allowed to form in front of an inclined wall with a process analogous to the material dumping or avalanche, a formation process similar to that taking place in a typical ice/cone interaction. The natural angle of repose,  $\phi_r$ , thus formed and the material's internal friction angle,  $\phi$ , were compared.

The main parameters common to each simulation are summarized in Table 7.1. The analyses were conducted as two-dimensional (plane strain) problems using the explicit time-stepping solution scheme. In this study, the ice blocks were modelled by the simply deformable perfectly elastic solid element. The specimens were tested in a dry condition. Furthermore, element cracking was not allowed. This condition was confirmed during selected preliminary runs, in which the stress within each element was sufficiently low and element fracture was not observed. The stress-strain relationship is linear elastic in each element with an elastic modulus of  $0.2E7$  N/m $^2$  and a contact stiffness of  $0.2E8$  N/m $^2$ , chosen for computation efficiency. The effects of elastic modulus and contact stiffness on the  $K_0$  values were not examined; however, the these values are in line with the values used by Sayed (1995) and Hopkins and Hibler (1991) in their simulations of rubble shear properties.

the results of which compared well with experimental data.<sup>2</sup> For these simulations, the added masses and moments of inertia were not included. The details of the simulations and the results are given in the following sub-sections.

### 7.2.1 Generation of Rubble Ice Samples

Three sets of rubble samples with uniform piece sizes ranging from 0.16 m x 0.16 m, 0.16 m x 0.32 m, and 0.16 m x 0.48 m, were prepared. These corresponded to the aspect ratios, AR, of 1:1, 1:2 and 1:3, respectively. Each set consisted of 3 samples with ice friction,  $\mu$ , set at 0, 0.2, and 0.4. The chosen values of ice friction,  $\mu = 0.2$  and  $0.4$ , reflect the range of values frequently quoted for design purposes. The density of ice was  $900 \text{ kg/m}^3$ . The rubble samples were prepared via a natural dumping process as shown in Figure 7.3. Firstly, a total of 475 pieces of randomly oriented ice blocks with a prescribed piece size and contact friction were generated by normal randomizing method within a rectangular area formed by three frictionless rigid elements representing two side-walls and a bottom plate. The rectangular area had a height,  $h$ , approximately 3.5 times the width,  $b$ , of the base. After the random generation, the blocks were then allowed to fall and compact at the bottom of the box by applying gravitational acceleration to the elements. Vibration of ice blocks due to inter-block collisions was damped by applying a 35% critical mass damping. A semi-

---

<sup>2</sup>Sayed (1995) used a spring constant of  $0.265E7 \text{ N/m}$  between rigid sphere resulting in an effective elastic modulus of the bulk rubble of approximately  $7 \text{ MPa}$  which agreed well with the experimental values reported by Løset and Sayed (1993).

randomly packed form was created through the impacting of blocks on the boundaries and between blocks. After compaction, the sample had a height to width ratio of approximately 2 to 1. The packing condition of the assembly was considered to be loose, and the cohesion was set to zero. Figure 7.4 shows the final configuration of the rubble samples after the initial compaction.

The initial void ratio<sup>3</sup>,  $e_0$ , of the bulk sample was dependent on the ice friction as shown in Figure 7.5. This reflects the fact that the inter-block sliding is easier for a lower contact friction resulting in a much denser configuration during natural deposition process.

### 7.2.2 Computations of the Coefficient of Lateral Earth Pressure at Rest, $K_0$

Two methods of measuring the coefficient of lateral earth pressure at-rest,  $K_0$ , i.e., a simple gravity method and the oedometer test, were simulated.

After all the blocks had settled down, the forces acting on the bottom plate and the side-walls were summed. Since no external load was applied to the rubble sample except its own self-weight, it is dubbed "gravity method". Since there was no friction between the ice blocks and the rigid boundaries, shear stresses upon vertical and horizontal planes within the rubble sample were not allowed to develop; and the principal axes coincided with the horizontal or vertical axis, the ratio of the principal stresses was equal to the coefficient of

---

<sup>3</sup>The void ratio,  $e_0$ , for two dimensional cases is defined as the ratio of the area of void to the area of the solid mass in an arbitrary cross-section. The void ratio for three-dimensional cases can be estimated as  $3.33e$  assuming the sample is made up of an assemblage of spheres.

lateral stress at rest,  $K_0$ . By assuming a linear increase of stresses with depth from the top surface<sup>4</sup>, the horizontal and vertical stresses,  $p_{wh}$  and  $p_{bv}$ , at the bottom surface of the sample were calculated:

$$p_{wh} = 2 \left( \frac{P_{wh}}{h} \right) \quad (7-1)$$

$$p_{bv} = \frac{P_{bv}}{b} \quad (7-2)$$

where  $h$  and  $b$  are the height and width of the sample, respectively; and  $P_{wh}$  and  $P_{bv}$  are the sum of the normal forces exerted on the wall and the base, respectively; and, thus,  $K_0$ :

$$K_0 = \frac{p_{wh}}{p_{bv}} = 2 \left( \frac{P_{wh}}{P_{bv}} \right) \left( \frac{b}{h} \right) \quad (7-3)$$

The geometry and variables used for Equations 7.1 to 7.3 are shown in Figure 7.6.

A summary of the coefficient of lateral earth pressure at rest,  $K_0$ , estimated by this method is given in Table 7.2. The internal friction angle for each sample as calculated from

<sup>4</sup>The assumption implied that the horizontal wall thrust,  $P_{wh}$ , will act at a distance  $L_p$  equal to  $1/3 h$  from the bottom of the sample. To verify this assumption, the point of action of  $P_{wh}$  was computed for each simulation. For all cases,  $P_{wh}$  acted on the side wall within a distance  $0.045h$  from the assumed point of action.

Jáky's equation<sup>5</sup>:

$$K_o = 1 - \sin\phi \quad (7-4)$$

is also given in the table. The subscript I associated with the symbols  $K_o$  and  $\phi$  refers to the gravity tests.

A comparison of the earth pressure coefficient at rest,  $K_o$ , and the associated aspect ratio of the ice pieces, AR, is given in Figure 7.7. The data shows no discernible effects of the ice pieces geometry on the earth pressure coefficient. However, there is a significant dependency of the earth pressure coefficient at rest,  $K_o$ , on the contact friction,  $\mu$ , as shown in Figure 7.8. The coefficient shows a higher sensitivity to ice friction at the lower friction values.

Figure 7.9 shows the same set of data comparing the internal friction angle,  $\phi$ , and the associated ice friction,  $\mu$ . Since the internal friction is a combined function of ice block interlocking and friction, the values corresponding to zero ice friction can be a measure of the effect of the block interlocking, which contribute up to about 10 degrees to the internal friction angle. This angle is analogous to the effective roughness angle used in rock mechanics to explain the higher apparent angle of friction due to visible roughness and other surface irregularities (Patton, 1966; and Hoek and Bray, 1981), and can be referred to as the

---

<sup>5</sup>In practical soil mechanics, Jáky's equation is an approximation. The validity of this formula has been explored in Section 5.3.1.

"interlocking angle". Within the range of ice friction examined, the internal friction angle is roughly equal to the arithmetic sum of this angle and the contact friction angle.

The above simulation is relatively simple to perform and the stress and strain conditions are similar to the field conditions studied. A more popular test, called oedometer test, was also simulated for comparison with the gravity test. In this test, stress is applied to the sample along the vertical axis, while strain in the horizontal direction is prevented. The results of the oedometer test simulation are summarized in Table 7.3. In this table, the subscript 2 associated with the symbols  $K_o$  and  $\phi$  denotes the oedometer tests. Only the samples with contact friction values of 0.2 and 0.4 were tested. Figure 7.10 shows the configuration of the oedometer test simulation. In this case, gravity force was set to zero, and a top plate was added to the problem setup. The rubble, initially in a loose condition, was compressed one dimensionally in strain controlled manner giving no strain in the lateral direction. The top plate moved and compressed the sample with a velocity of 0.4 m/s, while the forces on the side-walls, and the top and bottom plates were monitored continually. The vertical velocity corresponded to axial strain rates ranging from 0.04/s to 0.07/s depending on the height of each sample. Again, assuming a uniform load distribution along the sample's surface, the  $p_{ub}$ ,  $p_{bv}$ ,  $K_{o,2}$ , and  $\phi_2$  can be computed at any instant during the test. Figure 7.11 shows an increase of the horizontal stress with increasing vertical stress during a typical test simulation.

Figure 7.11 exhibits density-dependent assembly characteristics with a slight decrease

of  $K_{o,2}$  with time. This decrease is a manifestation of increasing degree of interlocking as the samples become denser upon compression. In order to compare the  $K_o$  values obtained from these tests to the gravity tests, the  $K_{o,2}$  value corresponding to the moment of first contact between the top plate and the ice was estimated from the data points before comparison, i.e.,  $K_o$  value at the same void ratio. A comparison of the values of  $K_o$  and  $\phi$  estimated from the gravity tests and the oedometer tests are given in Figures 7.12 and 7.13, respectively. Again, the subscript 1 refers to the gravity tests and the subscript 2 denotes the oedometer tests. The figures show good agreement between the values of  $K_o$  and  $\phi$  from the oedometer and gravity tests.

### 7.2.3 Angle of Repose Tests

In this series of simulations, the number of ice blocks in each sample was increased from 475 to 950 pieces to give a better surface profile for the angle of repose computations. The simulations were performed on the three standard rubble samples, with ice friction equal to 0.2 and 0.4. A total of six runs were conducted. The samples were prepared with the same method given in Section 7.2.1. After each rubble sample was prepared, the rigid sidewall at the right side of the box was changed into a movable element, which moved slowly away from the rubble sample with a velocity of 0.22 m/s as shown in Figure 7.14. The surface of the bottom plate had a coefficient of friction equal to 0.2, while the friction at the wall was set to zero. Initially, both sliding of the ice blocks at the bottom surface and the

failure of the rubble surface occurred; however, the bottom sliding ceased at the latter part of the simulation due to the frictional resistance at the bottom, and the final profile of the rubble was determined by slope failure. Damping of ice blocks is not necessary in this case as the friction between ice blocks was sufficient to damp out the slight vibration induced by the ice blocks rolling down the slope. Table 7.4 summarizes the results from this simulation series.

Figure 7.15 shows the configurations of the rubble at the end of each simulation run. The profile of the natural angle varies significantly along the surface of the rubble depending on the local variations of ice block orientation and interlocking which affect the sliding conditions of the surface ice along the free surface. Typically the surface slope at the mid-hill section had lesser variation than those of the top and the bottom sections where the slopes were sub-critical. Therefore, the angle of repose,  $\phi_r$ , was determined by taking the best fit of the slope profile at the mid-section only. In Figure 7.16, this angle is compared with the rubble's internal angle,  $\phi_i$ , obtained from the gravity test simulations. The angles of repose are up to  $4.5^\circ$  smaller than the rubble's internal friction angles.

The above angle of repose was measured after the avalanche condition. The slightly lower values of the angle of repose measured may be due to the specific avalanche condition used. With the constant activity at the free surface due to the rolling down of the rubble blocks, it is expected that the maximum angle will be somewhat lower than the angle of repose of the material.

### **7.3 Development of Equations for Rubble Loads in 2-D**

In this section a set of equations for rubble load computations, i.e., the total thrust force and its angle of attack, are presented for a variety of ice and structure conditions. These equations are formulated by:

- (i) First, deducing the form of the principal equation and identifying the relevant functions from examining the existing earth pressure equations for various loading geometries and conditions; and, then,
- (ii) Performing a series of DECICE simulations, the analysis of which either confirms the selected relationship or gives a better functional relationship between the total thrust force and the relevant variables identified in the principal equation.

The equations provide the best fit to the DECICE results, and are applicable to a cohesionless rubble mass of various heights and internal frictions which is deposited in front of an unyielding wall with single or multi-slopes. The rationale behind the selected form equation and relevant functions is described in Section 7.3.1. The matrix for the DECICE simulations is described in Section 7.3.2; and a detailed analysis is in Sections 7.3.3 to 7.3.6. A general equation for thrust force calculation is formulated and validated. In Section 7.3.7, empirical equations to estimate the amount of friction mobilized at the wall are presented. If this friction is known, the other components of the rubble load, acting on the wall and the supporting ice sheet, can be computed from the wall thrust via a simple force balance calculation. Finally, in Section 7.3.8, the results of the DECICE analysis are summarized.

### 7.3.1 Form of Earth Pressure Equation and Relevant Functions

Research on the pressure exerted by a variety of cohesionless granular materials, i.e., loose sand, on a retaining wall has been a subject of concern to scientists over the last two centuries. In all the various theories used in solving this problem, the expression for the total thrust exerted on a wall takes the following common form:

$$P = \frac{1}{2} \gamma_b h^2 K(\alpha, t, \phi, \phi_w) \quad (7-5)$$

where:

$\gamma_b$  = bulk density of the granular material,

$h$  = vertical height of the backfill,

$\alpha$  = angle of the inclination of the inner face of the wall measured from the horizontal plane,

$t$  = angle of the inclination of the free surface of the backfill in relation to the horizontal plane, reckoned as negative above and as positive below this plane.<sup>6</sup>

$\phi$  = angle of internal friction of the backfill,

$\phi_w$  = angle of wall friction, and

$K$  = earth pressure coefficient function,

and the form of  $K(\alpha, t, \phi, \phi_w)$  depends on the loading geometry and the state of stress in the

---

<sup>6</sup>In this thesis  $t$  is defined as positive below the horizontal which is different from the convention commonly used in soil mechanics.

backfill. For example, Coulomb's equations for computing active thrust,  $P_a$ , and passive resistance,  $P_p$ , exerted on an inclined wall with a sloping backfill are given as (Liu and Evett, 1987):

$$P_a = \frac{1}{2} \gamma_b h^2 \left[ \frac{\sin^2(\alpha + \phi)}{\sin^2 \alpha \sin(\alpha - \phi_w) \left( 1 + \sqrt{\frac{\sin(\phi + \phi_w) \sin(\phi + \iota)}{\sin(\alpha - \phi_w) \sin(\alpha - \iota)}} \right)^2} \right] \quad (7-6)$$

$$P_p = \frac{1}{2} \gamma_b h^2 \left[ \frac{\sin^2(\alpha - \phi)}{\sin^2 \alpha \sin(\alpha + \phi_w) \left( 1 + \sqrt{\frac{\sin(\phi + \phi_w) \sin(\phi - \iota)}{\sin(\alpha + \phi_w) \sin(\alpha - \iota)}} \right)^2} \right] \quad (7-7)$$

In addition, Reimbert and Reimbert's (1974) empirical equations applicable to wall thrust, when the backfill is on the verge of significant plastic deformation in active or passive manners, are given as:

$$P_a = \frac{1}{2} \gamma_b h^2 \left( \frac{180^\circ - 2\phi}{180^\circ + 2\phi} \right)^2 \left( 1 - \frac{2\iota}{180^\circ} \right) \left( \frac{180^\circ - \alpha - \phi}{90^\circ - \phi} \right) \quad (7-8)$$

$$P_p = \frac{1}{2} \gamma_b h^2 \left[ \left( \frac{180^\circ - 2\phi}{180^\circ + 2\phi} \right)^2 \left( \frac{180^\circ + 2\phi}{180^\circ - 2\phi} \right)^n \right] \left( 1 - \frac{2\iota}{180^\circ} \right) \left( \frac{180^\circ - \alpha - \phi}{90^\circ - \phi} \right) \quad (7-9)$$

where  $n$  in Equation 7.9 is equal to 1 in the case of rotational passive resistance and 2 in the

case of translatory passive resistance.

As for the 'at-rest' state, there is not yet a commonly acceptable general equation to compute the wall thrust applicable to inclined wall with sloping backfill, due to the lack of studies in this area. Nevertheless, for the case of a level cohesionless normally consolidated fill behind a frictionless vertical unyielding wall, the wall thrust can be calculated using the following formula where the fill is assumed to be at the geostatic state:

$$P = \frac{1}{2} \gamma_b h^2 K_u \quad (7-10)$$

The variables used in Equations 7.5 to 7.10 are defined in Figure 7.17.<sup>7</sup>

Equation 7.5 is a good starting point for the present analysis, i.e., all previous soil pressure equations are of this form. In this work, Equation 7.5 is assumed, and the form of  $K(\alpha, t, \phi, \phi_u)$  is deduced through a series of DECICE simulations.

Reimbert and Reimbert's equations, i.e., Equations 7.8 and 7.9, are particularly relevant to the present investigation as their equations apply to loading conditions similar to the present case, and were validated by extensive experimentation. They are by far the simplest, and provide a clear delineation of the effects of  $\alpha$ ,  $t$ ,  $\phi$ , and  $\phi_u$  on the  $K$  function. For example, in Reimbert and Reimbert's Equation, the  $K$  function takes the following form:

---

<sup>7</sup>Note that the direction of the thrust as defined in Coulomb's Equation and the Reimbert and Reimbert's Equation are different.

$$K(\alpha, \iota, \phi, \phi_w) = K(\alpha, \iota, \phi) = K'(\phi) \left( 1 - \frac{2\iota}{180^\circ} \right) \left( \frac{180^\circ - \alpha - \phi}{90^\circ - \phi} \right) \quad (7-11)$$

or the following generalized form:

$$K(\alpha, \iota, \phi, \phi_w) = K'(\phi) K''(\iota) K'''(\phi, \alpha) K''''(\phi_w) \quad (7-12)$$

The first term on the right hand side of Equation 7.12 is a function of  $\phi$  only, the form of which depends on the particular stress state of the backfill. (The corresponding functions for other stress states are given in Section 5.3.1.) The second term is a function of  $\iota$  only which accounts for the effect of backfill inclination. The third term is a function of  $\alpha$  and  $\phi$ , which accounts for the effect of wall inclination. The last term is equal to 1 indicating no influence of  $\phi_w$  on the  $K$  function.

Reimbert and Reimbert's  $K$  function serves as a logical starting point for the analysis of the DECICE results. Since the rubble is deposited in front of an unyielding wall, the rubble is expected to be at the 'at rest' state. Therefore,  $K'(\phi)$  is assumed to be a function of  $\phi$  in the form of ' $1 - \sin\phi$ ' via Jaky's equation, i.e.,

$$K'(\phi) = (1 - \sin\phi) \quad (7-13)$$

The theoretical and experimental validities of Equation 7.13 for cases with vertical frictionless wall and level fill have been shown in previous sections. It is also hypothesized

that the Reimbert and Reimbert's (1974) coefficient functions corresponding to  $K''$ ,  $K'''$  and  $K''''$  for the effects of rubble inclination, wall inclination and wall friction are also valid for the 'at rest' state under investigated, since the 'at rest' state is located in between the two states<sup>8</sup> Reimbert and Reimbert studied, i.e.,

$$K''(t) = \left(1 - \frac{2t}{180'}\right) \quad (7-14)$$

$$K'''(\alpha, \phi) = \left( \frac{180' - \alpha - \phi}{90' - \phi} \right) \quad (7-15)$$

$$K''''(\phi_w) = 1 \quad (7-16)$$

These assumptions lead to the following general equation for the thrust applicable to an inclined wall with a sloping backfill:

$$P_o = \frac{1}{2} \gamma_b h^2 (1 - \sin\phi) \left(1 - \frac{2t}{180'}\right) \left( \frac{180' - \alpha - \phi}{90' - \phi} \right) \quad (7-17)$$

For the case of a vertical wall, i.e.,  $\alpha = 90'$ , Equation 7.17 is reduced to the following form:

---

<sup>8</sup>Description of these two states is given in their paper (Reimbert and Reimbert, 1974).

$$P_o = \frac{1}{2} \gamma_L h^2 (1 - \sin\phi) \left( 1 - \frac{2t}{180^\circ} \right) \quad (7-18)$$

The wall friction,  $\phi_w$ , affects the total wall thrust,  $P_o$ , through the amount of friction actually mobilized at the wall surface. This mobilized wall friction is called 'effective wall friction', denoted as  $\phi'_w$  in this thesis. It was anticipated that the relationship between  $\phi_w$  and  $\phi'_w$ , and hence between  $P_o$  and  $\phi_w$ , would take a complicated form as the relationship was expected to not only depend on the geometry but also on the history of the loading. Various functional relationships derived between total wall thrust and wall friction can testify to that. For example, Reimbert and Reimbert's experiments (1974) showed that the wall friction,  $\phi_w$ , had no effect on the magnitude of the wall thrust; while others, i.e., Equations 7.6 and 7.7, give various functional relationships. Limited computational resources prevented an in-depth derivation of  $K''''$ ; however, the DECICE analysis shows that  $K''''$  is approximately equal to 1 suggesting that the wall friction has negligible influence on the total wall thrust.

### 7.3.2 Overview of DECICE Simulations and Analyses

Equation 7.5 suggests that a direct proportionality exists between the total thrust force,  $P_o$ , and the height squared,  $h^2$ , of the fill. This proportionality is independent of the earth pressure coefficient function,  $K$ . Before a comprehensive investigation of the  $K$  function, a number of DECICE simulations were conducted to verify this dependency.

Validation of this proportionality ensured the scalability<sup>9</sup> of the DECICE results to other heights. After that, the four variables,  $t$ ,  $\alpha$ ,  $\phi$  and  $\phi_a$ , were systematically varied, and their effects on the earth pressure coefficient function,  $K$ , and hence the total wall thrust were examined and delineated. The range of variations for each parameter is given in Table 7.5, with  $t$  at 1, 0.75 and 0.5 times the base value of  $22.5^\circ$ ,  $\alpha$  from  $90^\circ$  to  $45^\circ$ ,  $\phi$  at  $24.2^\circ$  and  $33.2^\circ$ , and  $\phi_a$  set at  $0^\circ$ ,  $11.3^\circ$  and  $21.8^\circ$ . The ice friction angle at the base of the rubble,  $\phi_b$ , was set to  $11.3^\circ$ . The bulk weight density/unit width,  $\gamma_b$ , of the material varied from  $6807 \text{ N/m}^2$  to  $6950 \text{ N/m}^2$  (with an average of  $6887 \text{ N/m}^2$ ) depending on the height of rubble sample. The mass density/unit width,  $\gamma$ , of the material used was  $8829 \text{ kg/m}^3$ . These ranges were expected to encompass the ice and structure conditions encountered in the field.

The test configuration and sample geometry for each test conducted in this series are given in Figure 7.18. In the DECICE analysis, the condition with the non-displacing boundary is analogous to the at-rest earth pressure condition in the field. A total of 48 runs were conducted. For each test configuration, the forces exerted on the wall and the base were computed. The results are summarized in Table 7.6. The variables are defined in Figure 7.19.

The linear dependencies of total wall thrust,  $P_o$ , on  $h^2$ , and the assumed  $K''$  are validated in Sections 7.3.3 and 7.3.4, respectively; whereas, the validities of Equations 7.18 and 7.17 in thrust force predictions are assessed in Sections 7.3.5 and 7.3.6. Table 7.7 lists

---

<sup>9</sup>Scalability also implies repeatability, i.e., repeatability of data in different scales.

the computed values of different functions or functional groups used in the analyses conducted in those sections.

### 7.3.3 Validation of Linear Dependency of Thrust Force on Rubble Height Squared, $h^2$

To validate the linear dependency of the thrust force on  $h^2$ , three base cases with different combinations of  $\phi_w$  and  $\alpha$  were selected for DECICE simulation, i.e.,  $\alpha = 90^\circ$  and  $\phi_w = 0^\circ$ ,  $\alpha = 90^\circ$  and  $\phi_w = 11.3^\circ$ , and  $\alpha = 45^\circ$  and  $\phi_w = 21.8^\circ$ ; and the height of the rubble,  $h$ , for each case was then systematically reduced by 1/3 and 2/3 times while keeping the other parameters constant. The rubble angle,  $t$ , and the internal friction angle,  $\phi$ , are kept at  $22.5^\circ$  and  $24.2^\circ$  respectively for all cases. A total of nine simulation runs were conducted, and the results are summarized in Table 7.8. In the table,  $P_o$  is the value for the total wall thrust in the DECICE simulation, and  $P_{o,h=4.8}$  is the scale-up value of  $P_o$  corresponding to  $h = 4.8$  m using the scaling ratios,  $(h/h_{4.8})^2$  and  $(\gamma_b/\gamma_{b,4.8})$ . The second factor was applied to reduce the variation due to varying weight density between cases. If applying this scale-up factor to each simulated wall thrust produces the same thrust as the simulation with  $h = 4.8$  m, this would tend to confirm  $h^2$  dependency for the thrust. This is confirmed by the present simulations. The scaled-up values of the thrust,  $P_{o,h=4.8}$ , all lie within 2.5% of the simulated values at  $h = 4.8$  m for each set.

### 7.3.4 Validation of Linear Dependency of Thrust Force on the Function, $1 - \frac{2t}{180^\circ}$

To validate the linear dependency of the total wall thrust,  $P_o$ , on the assumed  $K''$ , i.e.,  $1 - \frac{2t}{180^\circ}$ , a correlation analysis was performed on all DECICE simulations to establish the degree of correlation between  $P_o$  and  $K''$ , for constant  $\alpha$ ,  $\phi$ , and  $\phi_w$ . Since  $h$  and  $\gamma_b$  differed from case to case, the  $K''$  was multiplied by  $\gamma_b h^2$  before comparison to eliminate the variation due to  $h$  and  $\gamma_b$ . The y-intercept of the unknown regression line was assumed to be zero, i.e.,

$$P_o = m \left[ \gamma_b h^2 \left( 1 - \frac{2t}{180^\circ} \right) \right] \quad (7-19)$$

where  $m$  is the slope. With this assumption, the number of degrees of freedom,  $df$ , can be taken as  $(n-1)$ , since there exist only one independent relationship involving the  $n$  pairs of values of  $P_o$  and  $\gamma_b h^2 \left( 1 - \frac{2t}{180^\circ} \right)$ . This allows the correlation coefficient to be computed for a data set with as few as two data points.

Table 7.9 summarizes the results of the correlation analysis. The test matrix has been given in Section 7.3.2. Data with same  $\alpha$ ,  $\phi$ , and  $\phi_w$  are grouped together resulting into 18 possible data sets. In the table, the coefficient of determination,  $r^2$ , the correlation coefficient,  $r$ , and the degrees of freedom,  $df$ , of each test set are summarized. The minimum values of  $r$  required to establish the confidence level of 90%, 95% and 99% for a given  $df$  are

also listed.<sup>10</sup> If the computed  $r$  value is above the required minimum value, it can be concluded with the corresponding confidence level that a linear relationship exists between the examined variable pair,  $P_o$  and  $\gamma_b h^2 \left(1 - \frac{2t}{180^\circ}\right)$ . The table shows the two variables were highly correlated with all  $r$  values being higher than 0.937. All data sets with more than three data pairs, i.e.,  $df \geq 2$ , has  $r$  values exceeding 99% confidence level. The data set with only two data pairs, i.e.,  $df = 1$ , gives a lower confidence level, the uncertainty of which is a direct result of the small number of data pairs used; however, all of them are either close to or exceed the 90% confidence level. It can be concluded with a high degree of confidence that linear correlation exists between the  $P_o$  -  $K''$  variable pair.

### 7.3.5 Validity of Equation 7.18 for Vertical Walls

In this section, the validity of Equation 7.18 for wall thrust computation associated with vertical walls is assessed. The results from DECICE simulation runs conducted with a frictionless vertical wall and a backfill with a value of  $t$  set at 1, 0.75, and 0.5, times the base value of  $22.5^\circ$  were selected for analysis. The  $\phi$  was  $24.2^\circ$  and  $33.2^\circ$  which correspond to the ice contact coefficient of friction,  $\mu$ , of 0.2 and 0.4, respectively. In addition, the simulation runs with wall friction angle,  $\phi_w$ , equal to  $11.3^\circ$  and  $21.8^\circ$  were also analysed. This was to examine the sensitivity of the above equation to wall friction.

---

<sup>10</sup>The 95% confidence indicates there is only a 5% chance of having  $r$  as large as those in the table when no correlation exists. In order to conclude at a given confidence level that the correlation does exist, the calculated  $r$  should exceed the tabulated value of  $r$ .

The parameters for the base cases and their variations associated with this task are listed in Table 7.10. (Please refer to Table 7.6 for the details of the individual tests and Table 7.7 for the computed values used in this analysis.) Figure 7.20 gives the comparisons of the total wall thrusts computed by Equation 7.18 and the simulated values for the three values of  $\phi_w$ . The data shows a remarkable agreement between the values computed from Equation 7.18 and the values obtained from the simulations. Linear regression conducted on the three individual sets of data give the following results:

$$P_{o,pred} = 0.988 P_{o,simul}; \quad r^2 = 0.996$$

$$P_{o,pred} = 1.025 P_{o,simul}; \quad r^2 = 0.992$$

and

$$P_{o,pred} = 1.073 P_{o,simul}; \quad r^2 = 0.991$$

for the three  $\phi_w$  values of  $0^\circ$ ,  $11.3^\circ$  and  $21.8^\circ$ , respectively.

The data shows a slight dependency of the measured  $P_o$  on the wall friction angle with a decrease of thrust by 3.7% to 8.5% (on average), when the wall friction angle increases from  $0^\circ$  to  $11.3^\circ$  and  $21.8^\circ$ , respectively.

It is concluded that Equation 7.18 is valid for the thrust computation for a vertical wall and a rubble with varying  $t$  and  $\phi$ . Wall friction slightly decreases the measured  $P_o$ ; and

hence the prediction slightly errs on the conservative side by omitting the effect of wall friction. The effect of wall friction will further be explored in Section 7.3.7.

### 7.3.6 Validity of Equation 7.17 for Inclined Walls

Existing earth pressure theories suggest a significant effect of the wall inclination on the thrust exerted upon a retaining wall by the earthfill. For example, for a granular fill, with an internal friction angle,  $\phi = 25^\circ$ , inclined at its angle of repose, i.e.,  $t = \phi = 25^\circ$ , the Coulomb equation (Equation 7.6) predicts an increase of thrust by 67% when a smooth wall changes its incline from  $90^\circ$  to  $45^\circ$ ; while Reimbert and Reimbert's equation (Equation 7.8) gives a 69% increase for the same change.

In this section, the analysis is extended to examine the effects of wall angle on the total wall thrust, and the validity of Equation 7.17 for inclined wall is assessed. Four base cases with a combination of  $t = 22.5^\circ$  and  $17.3^\circ$  and  $\phi = 24.2^\circ$  and  $33.2^\circ$  were selected and tested with  $\alpha$  values  $90^\circ$ ,  $75^\circ$ ,  $60^\circ$  and  $45^\circ$ . The simulations were conducted with  $\phi_w = 11.3^\circ$  and  $21.8^\circ$ . The runs related to this series are listed in Table 7.11. Again, please refer to Tables 7.7 for the computation results.

Figure 7.21 gives a comparison of the  $P_o$  computed from Equation 7.17 and the corresponding simulated wall thrust. The figure clearly shows a substantial over-estimation of the wall thrust by Equation 7.17. The over-estimation increases with the increased deviation of wall angle from the vertical. For example, Equation 7.17 overestimates the thrust by 23%, 20%, and 29% when the wall angle changes from  $90^\circ$  to  $75^\circ$  to  $60^\circ$  to  $45^\circ$ .

respectively.

Despite the discrepancy, the general trend predicted by Equation 7.17 is consistent with the results from the DECICE simulations in which the thrust decreases with the increase of the wall angle, and the rate of decrease is larger for a larger rubble angle, as shown in Figure 7.22. Therefore, the form of the assumed  $K'''$  was retained but modified to fit the test data. It was found by trial that the following function agreed well with the data:

$$K'''(\alpha, \phi) = \left( \frac{180^\circ - \alpha - 2\phi}{90^\circ - 2\phi} \right)^{\frac{1}{3}} \quad (7-20)$$

This gives the following general equation for the thrust:

$$P_o = \frac{1}{2} \gamma_b h^2 (1 - \sin\phi) \left( 1 - \frac{2\phi}{180^\circ} \right) \left( \frac{180^\circ - \alpha - 2\phi}{90^\circ - 2\phi} \right)^{\frac{1}{3}} \quad (7-21)$$

Figure 7.23 shows a comparison of the  $P_o$  computed from Equation 7.21 and the corresponding thrust on the wall in the simulation for the two values of  $\phi_w$ . Linear regression conducted on the two individual sets of data gave the following results:

$$P_{o,pred} = 1.065 P_{o,simul}; \quad r^2 = 0.973$$

and

$$P_{o,pred} = 1.070 P_{o,simul}; \quad r^2 = 0.965$$

for the  $\phi_w$  values of  $11.3^\circ$  and  $21.8^\circ$ , respectively. Equation 7.21 only slightly over-estimates the simulated values in the order of 7% with a  $r^2$  value better than 0.965 for the two values of  $\phi_w$ . Again, the overestimation can be attributed to the omission of the effect of wall friction on  $P_o$ .

### 7.3.7 Derivation of Effective Wall Friction, $\phi'_w$

The angle of wall friction is often assumed to be a material property but this assumption is incorrect. It depends upon the direction of movement, the amount of movement and the properties of the material. Moreover, it may also vary along the wall. Hence it is a response and not a property.

During transportation of the rubble ice up the cone facets, the rubble tends to slide down due to its own weight. Because of friction between the rubble and the ride-up ice, the tendency is to cause a downward frictional force on the ride-up. The magnitude of this force is limited by the friction angle,  $\phi_w$ , between the rubble and the ride-up ice. For ice,  $\phi_w$  typically has a value ranging from  $11.3^\circ$  to  $21.8^\circ$ , and is frequently quoted toward the lower end.

When the relative motion between the rubble and the ride-up is not sufficient to fully mobilize the available frictional resistance at the interface, the amount of friction mobilized is indeterminate. However, the effective wall friction angle,  $\phi'_w$ , can be computed empirically from the data by considering force equilibrium at the interface, and is given by

the following equation:

$$\phi'_w = \tan^{-1} \left( \frac{P_{wv}\sin(\alpha) - P_{wh}\cos(\alpha)}{P_{wv}\cos(\alpha) + P_{wh}\sin(\alpha)} \right) \quad (7-22)$$

The angle,  $\phi'_w$ , together with the wall inclination,  $\alpha$ , determines the direction of the thrust exerted on the wall. In order to maintain equilibrium condition, the thrust always acts upon the wall at an angle:

$$\alpha_p = 90^\circ - (\alpha - \phi'_w) \quad (7-23)$$

measured from the horizontal plane. In order to accurately predict the direction of the thrust, and hence its horizontal and vertical components, this  $\phi'_w$  must be known.

Figures 7.24 and 7.25 show the  $\phi'_w$  computed from Equation 7.22 as a function of  $\alpha$  for  $\phi_w$  equal to  $11.3^\circ$  and  $21.8^\circ$ , respectively. The data set includes tests with  $t = 22.5^\circ$  and  $17.3^\circ$ , and  $\phi = 24.2^\circ$  and  $33.2^\circ$ . The data show a definite dependency of  $\phi'_w$  on the  $\alpha$  and  $\phi_w$ , while the trends with other parameters were of lesser significance. Comparing the two figures, the value of  $\phi'_w$  is substantially higher with the higher value of  $\phi_w$  for the same cone angle. Despite a large scatter in data, the trends are linear with the following two equations fitting the data with  $\alpha$  between  $60^\circ$  to  $90^\circ$ :

$$\phi'_w = -0.2561\alpha + 24.758; \quad r^2 = 0.779 \quad (7-24)$$

for  $\phi_w = 11.3^\circ$ , and

$$\phi'_w = -0.3407\alpha + 39.339; \quad r^2 = 0.842 \quad (7-25)$$

for  $\phi_w = 21.8^\circ$ , respectively; and the value of  $\phi'_w$  is always smaller than or equal to the value of  $\phi_w$ .

In Figures 7.24 and 7.25, the broken lines correspond to  $\phi'_w = \phi_w$ , which is the limiting value corresponding to the condition of full friction mobilisation at the wall. Equations 7.24 and 7.25 predict that such conditions would occur when  $\alpha < 53^\circ$  for  $\phi_w = 11.3^\circ$  and  $\alpha < 44^\circ$  for  $\phi_w = 21.8^\circ$ , respectively. Since wall inclination of most offshore structures are designed within the range of  $40^\circ$  to  $60^\circ$ , as a rule-of-thumb the wall friction will be fully or almost fully mobilized at the wall for the commonly quoted coefficient of ice friction between 0.2 to 0.4, i.e., the friction mobilized on the wall for  $\mu = 0.2$  and 0.4 is 83% and 80% of wall friction, respectively, for  $\alpha = 60^\circ$ . It should be noted that although the frictional resistance is exhausted at the wall, the frictional resistance at the rubble's bottom face may still be sufficient to hold the rubble in static equilibrium.

When the frictional resistance at both the wall and the supporting ice sheet are fully mobilized, i.e.,  $\phi'_w = \phi_w$  and  $\phi'_b = \phi_b$ , the rubble starts to slide down the slope. These conditions are reached for two simulations, i.e., Runs R12W2\_2 and R12W3\_2. Figure 7.26 is a snap-shot of Run R12W3\_2 showing the whole rubble mass sliding down along the wall and the supporting ice surfaces.

### 7.3.8 Summary of the Formulae Derived from Best Fit of DECICE Data

Based on the DECICE simulations, a simple expression was formulated to calculate the thrust exerted on an unyielding wall, from a knowledge of the ice and structural parameters:

$$P_a = \frac{1}{2} \gamma_b h^2 \left(1 - \sin\phi\right) \left(1 - \frac{2\alpha}{180^\circ}\right) \left(\frac{180^\circ - \alpha - 2\phi}{90^\circ - 2\phi}\right)^{\frac{1}{3}} \quad (7-26)$$

with  $P_a$  making an angle:

$$\alpha_p = 90^\circ - (\alpha - \phi'_w) \quad (7-27)$$

from the horizontal, where the effective wall friction angle,  $\phi'_w$ , is the angle of friction mobilised at the wall. This effective wall friction angle was found to be a function of the wall inclination,  $\alpha$ , and the wall friction angle,  $\phi_w$ , with the following empirical relationships:

$$\phi'_w = -0.2561\alpha + 24.758 \quad (7-28)$$

for  $\phi_w = 11.32^\circ$ ; and

$$\phi'_w = -0.3407\alpha + 39.339 \quad (7-29)$$

for  $\phi_w = 21.8^\circ$ , respectively. The  $\phi'_w$  is always smaller than or equal to  $\phi_w$ .

The equation is similar to the universal formula proposed by Reimbert and Reimbert,

i.e., Equations 7.8 and 7.9. The coefficient for maximum thrust,  $(\frac{180^\circ - 2\phi}{180^\circ + 2\phi})^2$ , is replaced by the coefficient at rest,  $K_o = (1 - \phi)$ , of the granular material, which reflects the appropriate at rest stress condition in the ice rubble. The coefficient,  $1 - \frac{2\alpha}{180^\circ}$ , suggested by Reimbert and Reimbert (1974) to account for the effects of backfill's inclinations for the maximum active and the minimum passive state is found to be applicable to the 'at rest' state of stress as well. However, Reimbert and Reimbert's coefficient,  $\frac{180^\circ - \alpha - 2\phi}{90^\circ - \phi}$ , for the effect of wall inclination significantly overestimates the simulated thrust on the wall, specially for a small wall angle. Instead, a coefficient function,  $(\frac{180^\circ - \alpha - 2\phi}{90^\circ - 2\phi})^{\frac{1}{3}}$ , is found to give a much better agreement with the DECICE simulation.

#### 7.4 Load Components Distributed on the Wall and the Supporting Ice Sheet

The weight of the ice rubble is partly supported by the ride-up ice and partly by the supporting ice sheet. The horizontal and vertical components of the thrust exerted on the ride-up ice are given by the following equations:

$$P_{uh} = \frac{1}{2} \gamma_b h^2 (1 - \sin\phi) \left(1 - \frac{2\alpha}{180^\circ}\right) \left(\frac{180^\circ - \alpha - 2\phi}{90^\circ - 2\phi}\right)^{\frac{1}{3}} \cos(90^\circ - (\alpha - \phi_u')) \quad (7-30)$$

$$P_{uv} = \frac{1}{2} \gamma_b h^2 (1 - \sin\phi) \left(1 - \frac{2\alpha}{180^\circ}\right) \left(\frac{180^\circ - \alpha - 2\phi}{90^\circ - 2\phi}\right)^{\frac{1}{3}} \sin(90^\circ - (\alpha - \phi_u')) \quad (7-31)$$

The horizontal and vertical forces exerted on the supporting ice sheet can be computed through a consideration of simple force equilibrium as shown in Figure 7.27; and

are given as the following:

$$P_{bh} = P_{wh} \quad (7-32)$$

$$P_{bv} = W_r - P_{wh} \quad (7-33)$$

while  $W_r$  is the weight of the rubble computed from its known geometry and bulk density.

The contact friction mobilized at the bottom surface of the rubble is equal to:

$$\phi'_b = \tan^{-1} \left( \frac{P_{bh}}{P_{bv}} \right) \quad (7-34)$$

and is limited to  $\phi_b$ , the friction angle at the supporting ice surface.

Table 7.12 summarizes a result of least squares fit of computed force components to corresponding simulated values for the cases with the three wall friction angles, respectively. The analysis shows good overall agreement for the force components.

## 7.5 Application of the New Formula for Walls with Multiple Slopes

Equations 7.30 and 7.31 can be generalized and applied to walls with multiple slope angles. For example, for a multi-sloped wall retaining a rubble, as illustrated in Figure 7.28, the pressure,  $p$ , at a depth  $h_d$  measured from the maximum height of the rubble is given by:

$$P = \gamma_b h_d (1 - \sin\phi) \left(1 - \frac{2i}{180^\circ}\right) \left(\frac{180^\circ - \alpha - 2\phi}{90^\circ - 2\phi}\right)^{\frac{1}{3}} \quad (7-35)$$

and the thrust for an arbitrary section, i:

$$P_{i,i} = \frac{1}{2} \gamma_b (h_{h,i}^2 - h_{t,i}^2) (1 - \sin\phi) \left(1 - \frac{2i}{180^\circ}\right) \left(\frac{180^\circ - \alpha_i - 2\phi}{90^\circ - 2\phi}\right)^{\frac{1}{3}} \quad (7-36)$$

where  $h_{t,i}$  and  $h_{h,i}$  are the vertical distance of the top and bottom level of an arbitrary section i measured from the maximum height of the rubble.

The total horizontal and vertical forces exerted on the wall are, therefore:

$$P_{nh} = \frac{1}{2} \gamma_b (1 - \sin\phi) \left(1 - \frac{2i}{180^\circ}\right) \sum_{i=1,k} (h_{h,i}^2 - h_{t,i}^2) \left(\frac{180^\circ - \alpha_i - 2\phi}{90^\circ - 2\phi}\right)^{\frac{1}{3}} \cos(90^\circ - (\alpha_i - \phi'_{w,i})) \quad (7-37)$$

$$P_{nv} = \frac{1}{2} \gamma_b (1 - \sin\phi) \left(1 - \frac{2i}{180^\circ}\right) \sum_{i=1,k} (h_{t,i}^2 - h_{h,i}^2) \left(\frac{180^\circ - \alpha_i - 2\phi}{90^\circ - 2\phi}\right)^{\frac{1}{3}} \sin(90^\circ - (\alpha_i - \phi'_{w,i})) \quad (7-38)$$

where k is the number of sections covered by the rubble. The effective friction angle for section i,  $\phi'_{w,i}$ , is calculated from Equations 7.24 or 7.25, and is less than or equal to the wall friction angle  $\phi_{w,i}$ .

The weight of the rubble per unit width is given as:

$$W_r = \frac{1}{2} \gamma_b \left[ h_r^2 \left( \frac{1}{\tan \alpha_1} - \frac{1}{\tan \alpha_k} \right) + \sum_{i=1, k+1} h_i^2 \left( \frac{1}{\tan \alpha_i} - \frac{1}{\tan \alpha_{i+1}} \right) \right] \quad (7-39)$$

where  $h_r$  is the rubble height,  $h_i$  is the height of section  $i$ , and  $k$  is the highest section the rubble reaches.

For example, for the retaining wall and backfill of Figure 7.29, simple geometric consideration gives the base lengths,  $b_1$ ,  $b_2$ , and  $b_3$  equal to 4.8562, 1, and 0.57735 m respectively, with the total cross-sectional area of the rubble equal to 8.2842 m<sup>2</sup> and the weight of the rubble equal to 58909 N/m. With  $\phi_u = 11.3^\circ$  common for each section,  $\phi'_u$  is obtained from Equation 7.24 as 1.7°, 9.4°, and 11.3° for the upper, the middle and the lower sections, respectively. Substituting  $\phi'_u$  for the respective section into Equations 7.37 and 7.38,  $P_{uh}$  and  $P_{uv}$  are computed as 10923 and 11384 N/m, respectively. Finally, the normal force,  $P_{hb}$ , and the frictional resistance,  $P_{hv}$  acting on the base are computed from Equations 7.32 and 7.33 as 10923 N/m and 48596 N/m, respectively.

An example calculation for Test MUNCONE3 is given in Appendix C.

## 7.6 Application of the New Formula for Other Loading Conditions

Two other loading conditions are of interest to designers. The first is associated with the basal sliding at the rubble/ice interfaces, and the second one associated with bearing failure of the supporting ice sheet. Both conditions may limit the maximum slope and height that a rubble can attain, and hence, limit the maximum load that a rubble can exert on the

structure. In this section, application of the new model formula to the aforementioned cases is briefly described.

### **7.6.1 Maximum Slope of Rubble with Basal Sliding at the Rubble/Ice Interfaces**

When rubble is pushed up a sloping plane, the free surface slope of the rubble is limited by one of the two failure criteria: slope instability and basal sliding as described in Chapter 5. The first criterion limits the rubble angle to the material's angle of repose; whereas, the second criterion prevents further ride-up of the rubble mass onto the slope. And, hence, the second criterion further limits the maximum angle that the rubble can attain. If the surface slope momentarily increases beyond this limiting value, the whole rubble will slide down the sloping plane to seek for the limited equilibrium state exhibited by Runs R12W2\_2 and R12W3\_2 conducted in the previous section.

The equations presented in Section 7.3 can also be applied to the limiting equilibrium state on the onset of this basal sliding. In this case, the value of slope angle,  $t$ , is unknown which is to be determined by back calculation using the known frictional resistance at both the wall and the supporting ice sheet, i.e.,  $\phi'_w = \phi_w$  and  $\phi'_b = \phi_b$ . It is expected that the angle,  $t$ , will be a function of wall angle, internal friction angle, and ice friction at the interfaces. The corresponding thrust,  $P_o$ , is the maximum load that can be exerted on the structure.

## **7.6.2 Maximum Rubble Height Limited by Bearing Failure of the Supporting Ice**

### **Sheet**

The supporting ice sheet may fail before the full development of the ice rubble, which limits the amount of ice piled up in front of the cone, and the size of the rubble is no longer determined by the mass balance requirement, but is rather limited by the strength of the supporting ice sheet. This type of bearing failure was observed in a number of tests conducted in IME's series when the ice sheets were weak and thin. In this case, the height of the rubble,  $h$ , is unknown. The  $h$  can be determined by back calculation using the equations derived in Section 7.3 with the known bearing resistance, i.e.,  $P_{bh}$ , calculated from bearing analysis of the underlying ice sheet. Again, the corresponding thrust,  $P_o$ , is the maximum load that can be exerted on the structure.

Table 7.1 DECICE parameters for the simulations of rubble mass at the "at-rest" condition

Solution Scheme	Two-dimensional plain-strain explicit time-stepping algorithm
Time Step Length	Program generated default value
Constitutive Model	Perfectly elastic
Element - Ice Blocks	Simply deformable solid
Element - Walls, Top and Base Plates	Rigid
Ice Elastic Modulus (Pa)	0.2E7
Inter-Element Stiffness (Pa)	0.2E8
Ice Density (kg/m <sup>3</sup> )	900
Poison Ratio	0.3
Gravity	No gravity for the oedometer tests, and 1-g for all the other tests

Table 7.2 Summary of the coefficient of lateral earth pressure at rest,  $K_{o,1}$ , estimated by gravity method

Test	$h$ (m)	$b$ (m)	$\mu$	$P_{wh}$ (N)	$P_{bv}$ (N)	$p_{wh}$ (N/m)	$p_{bv}$ (N/m)	$K_{o,1}$	$\phi_i$ (°)
Set 1: Piece Size = 0.16 m x 0.16 m									
P11	5.20	2.75	0	92271	107361	17744	39042	0.909	5.2
P12	5.50	2.75	0.2	63361	107361	11520	39040	0.590	24.2
P13	5.80	2.75	0.4	51257	107361	8837	39040	0.453	33.2
Set 2: Piece Size = 0.16m x 0.32 m									
P21	7.30	3.89	0	163410	214721	22385	55198	0.811	10.9
P22	7.60	3.89	0.2	117610	214721	15475	55198	0.561	26.1
P23	8.10	3.89	0.4	106891	214721	13196	55198	0.478	31.5
Set 3: Piece Size = 0.16m x 0.48 m									
P31	8.70	4.80	0	250528	322082	28796	67100	0.858	8.1
P32	9.60	4.80	0.2	184705	322082	38480	67100	0.573	25.2
P33	10.10	4.80	0.4	139972	322082	13859	67100	0.413	35.9

Table 7.3 Summary of the coefficient of lateral earth pressure at rest,  $K_{o,2}$ , measured from the oedometer tests

Test	Sampling Point	$h$ (m)	$b$ (m)	$\mu$	$P_{sh}$ (N)	$P_{bv}$ (N)	$p_{sh}$ (N/m)	$p_{bv}$ (N/m)	$K_{o,2}$	$\phi_2$ (°)	Extrapolated Values at $P_{sh} = 0$ N
Set 1: Piece Size = 0.16 m x 0.16 m											
Q12	1 <sup>st</sup>	5.44	2.75	0.2	44861	38983	8242	14176	0.581	24.7	$K_{o,2} = 0.593$
	2 <sup>nd</sup>	5.32			114702	105361	21544	38313	0.562	26.0	$\phi_2 = 24.0^\circ$
Q13	1 <sup>st</sup>	5.69	2.75	0.4	27460	31695	4823	11526	0.419	35.6	$K_{o,2} = 0.419$
	2 <sup>nd</sup>	5.57			80137	101877	14377	37046	0.388	37.7	$\phi_2 = 34.5^\circ$
Set 2: Piece Size = 0.16 m x 0.32 m											
Q22	1 <sup>st</sup>	7.84	3.89	0.2	55657	50969	7095	13103	0.542	27.3	$K_{o,2} = 0.566$
	2 <sup>nd</sup>	7.68			140712	142019	18329	36509	0.502	29.9	$\phi_2 = 25.7^\circ$
Q23	1 <sup>st</sup>	8.13	3.89	0.4	2889	3006	355	773	0.460	32.7	$K_{o,2} = 0.460$
	2 <sup>nd</sup>	7.97			67232	72075	8440	18528	0.456	33.0	$\phi_2 = 32.7^\circ$
Set 3: Piece Size = 0.16 m x 0.48 m											
Q32	1 <sup>st</sup>	9.41	4.80	0.2	80011	75039	8502	15633	0.544	27.1	$K_{o,2} = 0.593$
	2 <sup>nd</sup>	9.21			192033	185920	20850	38733	0.538	27.5	$\phi_2 = 26.9^\circ$
Q33	1 <sup>st</sup>	10.16	4.80	0.4	319	252	21	53	0.406	36.4	$K_{o,2} = 0.407$
	2 <sup>nd</sup>	9.96			35892	43992	3604	9165	0.393	37.4	$\phi_2 = 36.4^\circ$

Note: Forces Measured on the two side walls are within 0.46% of each other; whereas, those measured on the top and bottom plates are within 1.1%. The values given are the average values.

Table 7.4 Summary of the angle of repose,  $\phi_r$ , estimated from the rubble's natural slope after slope failure

Test	$\mu$	$\phi_r$ ( $^{\circ}$ )	$\phi_i$ ( $^{\circ}$ )	$\phi_r/\phi_i$ (N)
Set 1: Piece Size = 0.16 m x 0.16 m				
S12	0.2	24	24.2	0.99
S13	0.4	31	33.2	0.93
Set 2: Piece Size = 0.16 m x 0.32 m				
S22	0.2	25	26.1	0.96
S23	0.4	27	31.5	0.86
Set 3: Piece Size = 0.16 m x 0.48 m				
S32	0.2	22	25.2	0.87
S33	0.4	32	35.9	0.89

Table 7.5 Matrix of DECICE simulations of the thrust exerted upon a retaining wall by cohesionless granular materials at "at-rest" state of stress

Parameters	Variation
Height of Rubble, $h$ (m)	from 1.6 to 4.8
Rubble Angle, $t$ ( $^{\circ}$ )	22.5, 17.3, 11.7
Wall Angle, $\alpha$ ( $^{\circ}$ )	45, 60, 75, 90
Internal Friction Angle of Rubble, $\phi$ ( $^{\circ}$ )	24.2, 33.2
Friction Angle at Wall, $\phi_w$ ( $^{\circ}$ )	0, 11.3, 21.8
Friction Angle at Base, $\phi_b$ ( $^{\circ}$ )	11.3
Number of Tests	48

Table 7.6 Summary of DECICE simulations of the thrust exerted upon a retaining wall by cohesionless granular materials at "at-rest" state of stress

Test	h (m)	b (m)	$\alpha$ (°)	$t$ (°)	$\phi$ (°)	$\gamma_b$ (N/m <sup>2</sup> )	$P_{wh} =$ $P_{bh}$ (N)	$P_{wv}$ (N)	$P_{bv}$ (N)	$P_o$ (N)	$\alpha_p$ (°)
Set 1: $\phi_w = 0^\circ$											
R12_1	4.80	11.59	90	22.5	24.2	6940	35139	0	193019	35139	0.0
R12A_1	3.20	7.73	90	22.5	24.2	6839	15355	0	84530	15355	0.0
R12B_1	1.60	3.86	90	22.5	24.2	6876	3805	0	21249	3805	0.0
R13_1	4.80	11.59	90	22.5	33.2	6940	27603	0	193019	27603	0.0
R22_1	3.60	11.59	90	17.3	24.2	6892	21365	0	143747	21365	0.0
R23_1	3.60	11.59	90	17.3	33.2	6892	17485	0	143748	17485	0.0
R32_1	2.40	11.59	90	11.7	24.2	6826	10360	0	94926	10360	0.0
R33_1	2.40	11.59	90	11.7	33.2	6826	8638	0	94926	8638	0.0
Set 2: $\phi_w = 11.3^\circ$											
R12_2	4.80	11.59	90	22.5	24.2	6940	33227	1601	191418	33265	2.8
R12A_2	3.20	7.73	90	22.5	24.2	6837	14407	271	84239	14410	1.1
R12B_2	1.60	3.86	90	22.5	24.2	6873	3644	408	20833	3666	6.4
R13_2	4.80	11.59	90	22.5	33.2	6940	27364	554	192466	27369	1.2
R22_2	3.60	11.59	90	17.3	24.2	6892	20417	538	143209	20425	1.5
R23_2	3.60	11.59	90	17.3	33.2	6892	17039	754	142993	17056	2.5
R32_2	2.40	11.59	90	11.7	24.2	6826	9728	1139	93787	9794	6.7
R33_2	2.40	11.59	90	11.7	33.2	6826	8277	766	94160	8312	5.3
R12W1_2	4.80	10.30	75	22.5	24.2	6950	30967	12927	158917	33557	22.7
R12W2_2	4.80	8.82	60	22.5	24.2				Sliding Failure		
R12W3_2	4.80	6.79	45	22.5	24.2				Sliding Failure		
R13W1_2	4.80	10.30	75	22.5	33.2	6950	27091	8435	163408	28374	17.3
R13W2_2	4.80	8.82	60	22.5	33.2	6928	24685	21594	125005	32797	41.2
R13W3_2	4.80	6.79	45	22.5	33.2	6876	19294	28940	83074	34782	56.3
R22W1_2	3.49	10.30	75	17.3	24.2	6896	18075	6333	117670	19152	19.3
R22W2_2	3.34	8.82	60	17.3	24.2	6854	16428	13160	87687	21049	38.7
R22W3_2	3.06	6.79	45	17.3	24.2	6807	10097	15015	55663	18094	56.1
R23W1_2	3.49	10.30	75	17.3	33.2	6896	16102	6092	117911	17216	20.7
R23W2_2	3.34	8.82	60	17.3	33.2	6854	16153	12396	88452	20361	37.5
R23W3_2	3.06	6.79	45	17.3	33.2	6807	10190	14111	56567	17405	54.2

Table 7.6 Summary of DECICE simulations of the thrust exerted upon a retaining wall by cohesionless granular materials at "at-rest" state of stress (cont'd)

Test	h (m)	b (m)	$\alpha$ (°)	$\iota$ (°)	$\phi$ (°)	$\gamma_b$ (N/m <sup>2</sup> )	$P_{wh} =$ $P_{bh}$ (N)	$P_{wv}$ (N)	$P_{bv}$ (N)	$P_o$ (N)	$\alpha_p$ (°)
Set 3: $\phi_w = 21.8^\circ$											
R12_3	4.80	11.59	90	22.5	24.2	6940	31030	6246	186773	31652	11.4
R13_3	4.80	11.59	90	22.5	33.2	6940	25700	4180	189000	26038	9.2
R22_3	3.60	11.59	90	17.3	24.2	6892	19304	3117	140630	19554	9.2
R23_3	3.60	11.59	90	17.3	33.2	6892	16150	2412	141335	16329	8.5
R32_3	2.40	11.59	90	11.7	24.2	6826	9701	1619	93307	9836	9.5
R33_3	2.40	11.59	90	11.7	33.2	6826	7862	1479	93447	8000	10.7
R12W1_3	4.80	10.30	75	22.5	24.2	6950	29983	16540	155309	34243	28.9
R12W2_3	4.80	8.82	60	22.5	24.2	6929	23407	28376	118235	36784	50.5
R12W3_3	4.80	6.79	45	22.5	24.2	6926	15109	33568	69264	38612	65.8
R12W3A_3	3.20	4.53	45	22.5	24.2	6733	6651	14826	33927	16250	65.8
R12W3B_3	1.60	2.26	45	22.5	24.2	6892	1628	3622	8853	3971	65.8
R13W1_3	4.80	10.30	75	22.5	33.2	6950	24595	13315	158525	27968	28.4
R13W2_3	4.80	8.82	60	22.5	33.2	6904	22900	27100	119000	35480	49.8
R13W3_3	4.80	6.79	45	22.5	33.2	6926	15269	34946	77883	38136	66.4
R22W1_3	3.49	10.30	75	17.3	24.2	6896	17336	7716	116287	18976	24.0
R22W2_3	3.34	8.82	60	17.3	24.2	6854	13908	16660	84188	21702	50.1
R22W3_3	3.06	6.79	45	17.3	24.2	6807	8277	18077	52600	19882	65.4
R23W1_3	3.49	10.30	75	17.3	33.2	6896	14833	7468	116535	16606	26.7
R23W2_3	3.34	8.82	60	17.3	33.2	6854	13274	15130	85717	20128	48.7
R23W3_3	3.06	6.79	45	17.3	33.2	6807	8389	17035	53642	18989	63.8

Table 7.7 Computed values for DECICE Analyses conducted in Sections 7.3.3 to 7.3.6

Test	$P_{o,meas}$ (N)	$\gamma_b h^3(1-2t/180^\circ)$ (N)	$P_{o,pred}$ (EQ. 7.18) (N)	$P_{o,pred}$ (EQ. 7.17) (N)	$P_{o,pred}$ (EQ. 7.21) (N)
Set 1: $\phi_w = 0^\circ$					
R12_1	35139	119928	35383	35383	35383
R12A_1	15355	52523		Not Computed	
R12B_1	3805	13202		Not Computed	
R13_1	27603	119928	27130	27130	27130
R22_1	21365	72188	21298	21298	21298
R23_1	17485	72188	16330	16330	16330
R32_1	10360	34208	10093	10093	10093
R33_1	8638	34208	7739	7739	7739
Set 2: $\phi_w = 11.3^\circ$					
R12_2	33265	119928	35383	35383	35383
R12A_2	14410	52510		Not Computed	
R12B_2	3666	13197		Not Computed	
R13_2	27369	119928	27130	27130	27130
R22_2	20425	72188	21298	21298	21298
R23_2	17056	72188	16330	16330	16330
R32_2	9794	34208	10093	10093	10093
R33_2	8312	34208	7739	7739	7739
R12W1_2	33557	120102	43513	35435	39265
R12W2_2			Sliding Failure		
R12W3_2			Sliding Failure		
R13W1_2	28374	120102	34344	27169	32011
R13W2_2	32797	119716	41386	27082	35598
R13W3_2	34782	118813	48172	26878	38359
R22W1_2	19152	67927	24610	20041	22207
R22W2_2	21049	61713	26509	18208	21821
R22W3_2	18094	51489	25581	15191	19397
R23W1_2	17216	67927	19424	15366	18105
R23W2_2	20361	61713	21334	13961	18351
R23W3_2	17405	51489	20876	11648	16623

Table 7.7 Computed values for DECICE Analyses conducted in Sections 7.3.3 to 7.3.6  
(cont'd)

Test	$P_{o,meas}$ (N)	$\gamma_b h^2(1-2t/180^\circ)$ (N)	$P_{o,pred}$ (EQ. 7.18) (N)	$P_{o,pred}$ (EQ. 7.17) (N)	$P_{o,pred}$ (EQ. 7.21) (N)
Set 3: $\phi_w = 21.8^\circ$					
R12_3	31652	119928	35383	35383	35383
R13_3	26038	120028	27153	27153	27153
R22_3	19554	72188	21298	21298	21298
R23_3	16329	72188	16330	16330	16330
R32_3	9836	34208	10093	10093	10093
R33_3	8000	34208	7739	7739	7739
R12W1_3	34243	120105	43514	35436	39266
R12W2_3	36784	119726	51429	35324	42332
R12W3_3	36812	109073	54189	32181	41090
R12W3A_3	16250	25855		Not Computed	
R12W3B_3	3971	6616		Not Computed	
R13W1_3	27968	120099	34343	27168	32010
R13W2_3	35480	119309	41245	26990	35477
R13W3_3	38136	119676	48522	27073	38637
R22W1_3	18976	67927	24610	20041	22207
R22W2_3	21702	61713	26509	18208	21821
R22W3_3	19882	51489	25581	15191	19397
R23W1_3	16606	67927	19424	15366	18105
R23W2_3	20128	61713	21334	13961	18351
R23W3_3	18989	51489	20876	11648	16623

Table 7.8 Results of simulation runs to validate the direct proportionality between the rubble height squared,  $h^2$ , and the total wall thrust,  $P_o$  ( $t = 22.5^\circ$  and  $\phi = 24.2^\circ$  for all cases)

Test	$h$ (m)	$\gamma_b$ (N/m <sup>3</sup> )	$P_o$ (N)	$(h/h_{4.8})^2$	$(\gamma_b/\gamma_{b=4.8})$	$P_{o,h=4.8}$ (N)	$P_o/P_{o,h=4.8}$
Set 1: $\alpha = 90^\circ$ and $\phi_w = 0^\circ$							
R12_1	4.8	6940	35139	1.000	1.000	35139	1.000
R12A_1	3.2	6838	15355	0.444	0.985	35066	0.998
R12B_1	1.6	6876	3805	0.111	0.991	34758	0.989
Set 2: $\alpha = 90^\circ$ and $\phi_w = 11.3^\circ$							
R12_2	4.8	6940	33265	1.000	1.000	33265	1.000
R12A_2	3.2	6874	14410	0.444	0.990	32734	0.984
R12B_2	1.6	6950	3666	0.111	1.001	32945	0.990
Set 3: $\alpha = 45^\circ$ and $\phi_w = 21.8^\circ$							
R12W_3	4.8	6926	36812	1.000	1.000	36812	1.000
R12W3A_3	3.2	6733	16249	0.444	0.972	37608	1.022
R12W3B_3	1.6	6892	3971	0.111	0.995	35915	0.976

Note:  $P_{o,h=4.8} = P_o / (h/h_{4.8})^2 / (\gamma_b/\gamma_{b=4.8})$

Table 7.9 Results of the correlation analysis of the  $P_o$  -  $K''$  data pairs

$\alpha$	$\phi$	$\phi_w$	$r^2$	$r$	df	90%	95%	99%
90	24.2	0	1.000	1.000	4	0.729	0.811	0.917
		11.3	1.000	1.000	4	0.729	0.811	0.917
		21.8	0.997	0.999	2	0.900	0.950	0.990
	33.2	0	0.995	0.997	2	0.900	0.950	0.990
		11.3	0.998	0.999	2	0.900	0.950	0.990
		21.8	0.997	0.998	2	0.900	0.950	0.990
75	24.2	11.3	1.000	1.000	1	0.988	0.997	1.000
		21.8	1.000	1.000	1	0.988	0.997	1.000
	33.2	11.3	0.983	0.992	1	0.988	0.997	1.000
		21.8	0.993	0.996	1	0.988	0.997	1.000
60	24.2	11.3	NA (too few samples)					
		21.8	0.878	0.937	1	0.988	0.997	1.000
	33.2	11.3	0.948	0.974	1	0.988	0.997	1.000
		21.8	0.979	0.989	1	0.988	0.997	1.000
45	24.2	11.3	NA (too few samples)					
		21.8	0.986	0.993	3	0.805	0.878	0.959
	33.2	11.3	0.964	0.982	1	0.988	0.997	1.000
		21.8	0.969	0.985	1	0.988	0.997	1.000

- Note: 1. Number of sample pairs,  $n = df + 1$ , where df is the number of degrees of freedom  
 2. Minimum values for 90%, 95% and 99% confidence level are taken from Fisher and Yates (1970).

Table 7.10 Base cases and their variations selected to assess the validity of Equation 7.18 for vertical walls

Base Parameters		Test Run (Base Case)	Test Run (Variation)	
$\phi$ ( $^{\circ}$ )	$\phi_w$ ( $^{\circ}$ )	$t = 22.5$ ( $^{\circ}$ )	$t = 17.3$ ( $^{\circ}$ )	$t = 11.3$ ( $^{\circ}$ )
24.2	0	R12_1	R22_1	R32_1
33.2	0	R13_1	R23_1	R33_1
24.2	11.3	R12_2	R22_2	R32_2
33.2	11.3	R13_2	R23_2	R33_2
24.2	21.8	R12_3	R22_3	R32_3
33.2	21.8	R13_3	R23_3	R33_3

Table 7.11 Base cases selected to assess the validity of Equation 7.17 for inclined walls

Test Run	Base Parameters			
Base Case	h (m)	$\iota (^{\circ})$	$\phi (^{\circ})$	$\phi_w (^{\circ})$
R12_2	4.8	22.5	24.2	11.3
R13_2	4.8	22.5	33.2	11.3
R22_2	3.6	17.3	24.2	11.3
R23_2	3.6	17.3	33.2	11.3
R12_3	4.8	22.5	24.2	21.8
R13_3	4.8	22.5	33.2	21.8
R22_3	3.6	17.3	24.2	21.8
R23_3	3.6	17.3	33.2	21.8

Note: For the base case,  $\alpha = 90^{\circ}$ ; the wall angle of each case was varied from  $90^{\circ}$  to  $75^{\circ}$  to  $60^{\circ}$  to  $45^{\circ}$  with the runs bearing the extension W1, W2, and W3 respectively.

Table 7.12 Least squares fit of force components computed from Equations 7.31, 7.32, and 7.34, to values obtained directly from simulation runs assuming  $\phi_w$  equal to  $0^\circ$ ,  $11.3^\circ$  and  $22.5^\circ$

Force Component	$\phi_w$ ( $^\circ$ )	Least Squares Fit ( $P_{pred} = m P_{simul}$ )	
		m	$r^2$
$P_{wh}$	0	0.989	0.997
	11.3	1.062	0.961
	22.5	1.093	0.973
$P_{ws}$	11.3	0.969	0.968
	22.5	1.042	0.982
$P_{hs}$	0	1.000	1.000
	11.3	0.999	0.999
	22.5	0.995	0.999

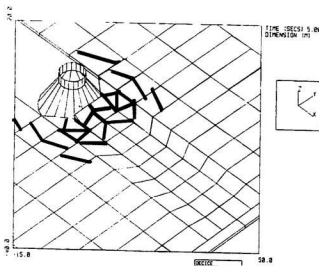


Figure 7.1 Figure showing the interaction of ice blocks, cone and ice sheet from a typical DECICE simulation (after Lau, 1994a)

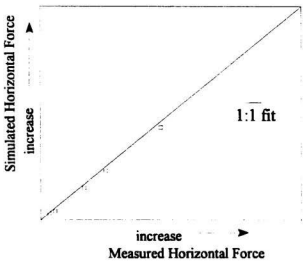


Figure 7.2 Simulated versus measured horizontal peak forces for a 60 degrees cone in level ice (after Lau, 1994a) (Axis scaling is not given due to data propriety)

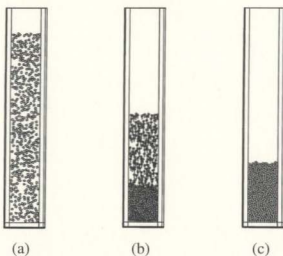


Figure 7.3 Snap-shots showing generation process of rubble sample: (a) random generation of ice blocks; (b) free falling of ice blocks; and (c) final configuration of rubble sample

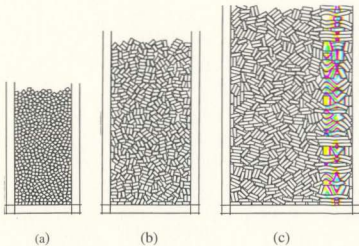


Figure 7.4 Final configuration of rubble samples after initial compaction: ice piece size: (a)  $0.16 \text{ m} \times 0.16 \text{ m}$ ; (b)  $0.16 \text{ m} \times 0.32 \text{ m}$ ; and (c)  $0.16 \text{ m} \times 0.48 \text{ m}$

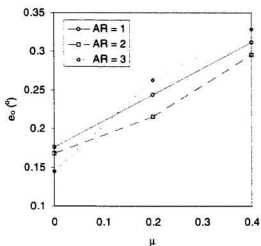


Figure 7.5 Comparison of initial void ratio,  $e_0$ , and the associated contact friction,  $\mu$ , with aspect ratios, AR = 1, 2 and 3

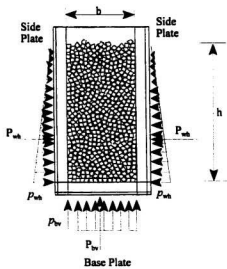


Figure 7.6 Pressure distributions of rubble sample assumed in the gravity test

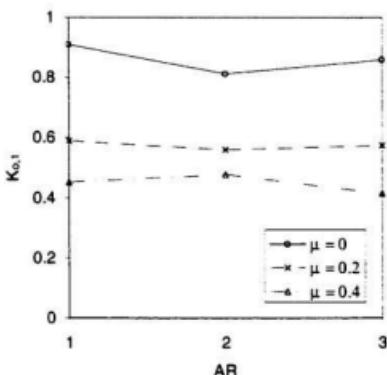


Figure 7.7 Comparison of earth pressure coefficient at-rest,  $K_{o,1}$ , and the associated aspect ratio, AR, for contact friction,  $\mu = 0, 0.2$  and  $0.4$ : gravity method

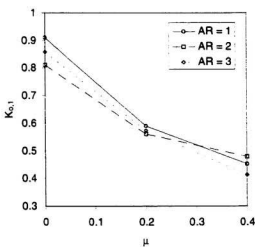


Figure 7.8 Comparison of earth pressure coefficient at rest,  $K_{o,1}$ , and the associated contact friction,  $\mu$ , for aspect ratio, AR = 1, 2 and 3: gravity method

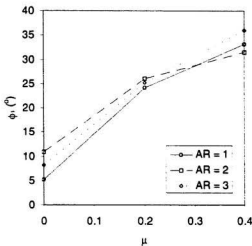


Figure 7.9 Comparison of internal friction angle,  $\bar{\phi}_1$ , and the associated contact friction,  $\mu$ , for aspect ratio, AR = 1, 2 and 3: gravity method

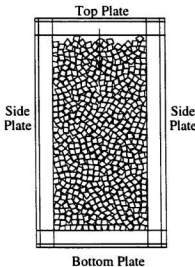


Figure 7.10 Configuration of oedometer tests: side and bottom plates fixed while the top plate moves downward at  $V = 0.4$  m/s

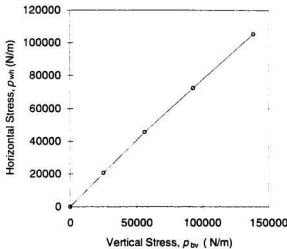


Figure 7.11 Figure showing the increase of horizontal stress,  $p_{wh}$ , with the increase of vertical stress,  $p_{bv}$ , in a typical simulated oedometer test (Run Q12)

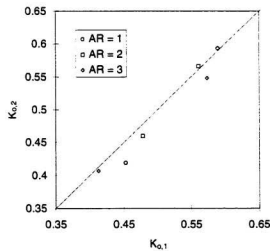


Figure 7.12 Comparison of the at-rest earth pressure coefficient,  $K_{o,2}$ , in simulated oedometer tests and the corresponding coefficient,  $K_{o,1}$ , estimated from gravity test simulations

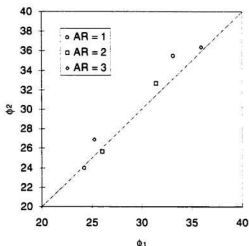


Figure 7.13 Comparison of the internal friction angle,  $\phi_2$ , estimated from oedometer test simulations and the corresponding internal friction angle,  $\phi_1$ , from gravity test simulations

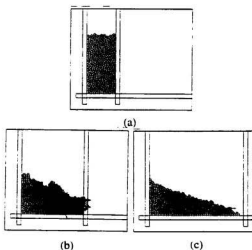


Figure 7.14 Snap shots of Run S12 at (a)  $t = 0$  s, (b)  $t = 15.3$  s and (c)  $t = 30.6$  s showing a typical angle of repose tests

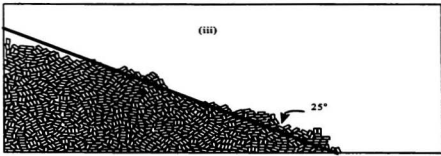
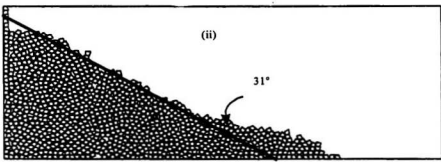
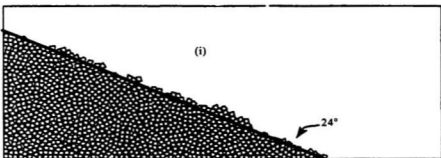


Figure 7.15a Final configuration of rubbles in the angle of repose tests: (i) Test S12; (ii) Test S13; and (iii) Test S22

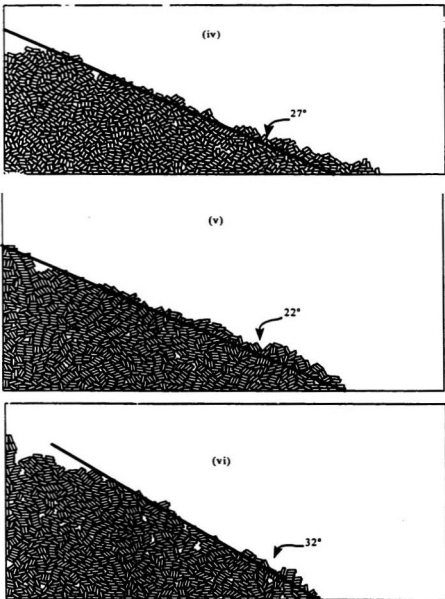


Figure 7.15b Final configuration of rubbles in the angle of repose tests: (iv) Test S23; (v) Test S32; and (vi) Test S33

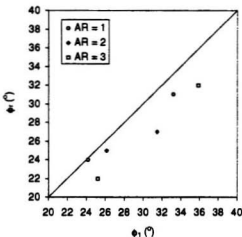


Figure 7.16 Comparison of the angle of repose,  $\phi_r$ , and the associated internal friction angle,  $\phi_1$ , obtained from gravity test simulations

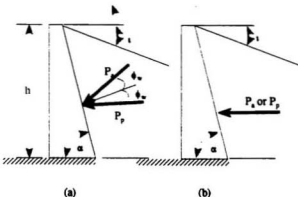


Figure 7.17 Definition of variables commonly used in various earth equations: (a) Coulomb's equation; and (b) Reimbert and Reimbert's equation. (The direction of total wall thrust as defined in Coulomb's equation and Reimbert and Reimbert's equation are different.)

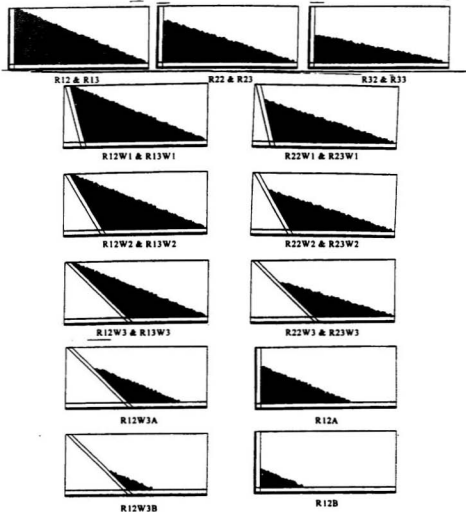


Figure 7.18 Test configuration and sample geometry for each test simulation conducted for the thrust equation formulation. The results are given in Table 7.6.

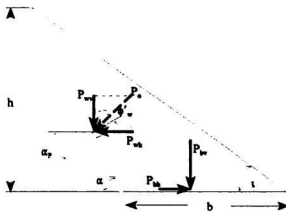


Figure 7.19 Definition of variables used in Table 7.6

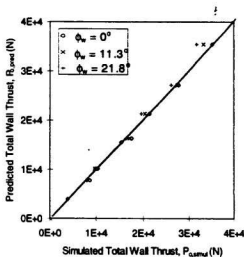


Figure 7.20 Comparison of the predictions from Equation 7.18 and the total thrust measured on the wall for the three values of wall friction,  $\phi_w = 0^\circ$ ,  $11.3^\circ$ , and  $21.8^\circ$ , in DECICE simulations

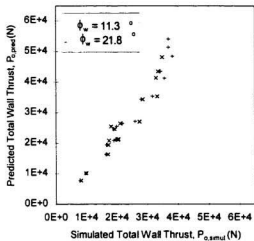


Figure 7.21 Comparison of the predictions from Equation 7.17 and the total thrust measured on the wall for the two values of wall friction,  $\phi_w = 11.3^\circ$  and  $21.8^\circ$ , in the DECICE simulations

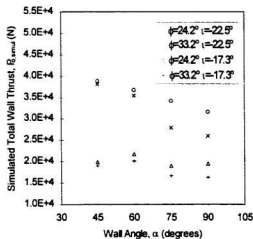


Figure 7.22 Effects of the wall angle on wall thrust for a combination of internal friction angle,  $\phi$ , and rubble angle,  $i$  (wall friction,  $\phi_w = 21.8^\circ$ )

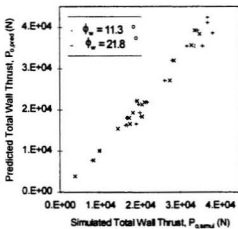


Figure 7.23 Comparison of the predictions from Equation 7.21 and the thrust on the wall in the DECICE simulation

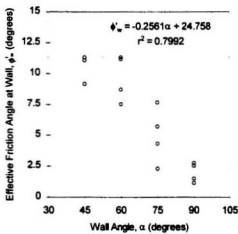


Figure 7.24 Computed effective friction angle at wall,  $\phi'_w$ , versus wall angle,  $\alpha$ , for wall friction angle,  $\phi_w = 11.3^\circ$ . The broken line corresponds to  $\phi'_w = \phi_w = 11.3^\circ$ , and the regression line fits data with  $\alpha$  between  $60^\circ$  to  $90^\circ$ .

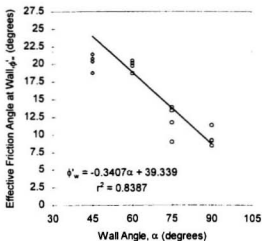


Figure 7.25 Computed effective friction angle at wall,  $\phi'_w$ , versus wall angle,  $\alpha$ , for wall friction angle  $\phi_w = 21.8^\circ$ . The broken line corresponds to  $\phi'_w = \phi_w = 21.8^\circ$ , and the regression line fits data with  $\alpha$  between  $60^\circ$  to  $90^\circ$ .

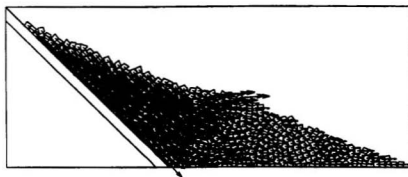


Figure 7.26 Snap-shot of Run R12W3\_2 showing the whole rubble mass sliding down along the wall and the supporting ice surfaces.

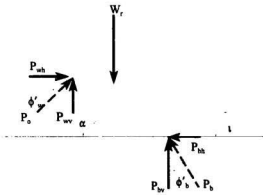


Figure 7.27 Force equilibrium of the rubble body

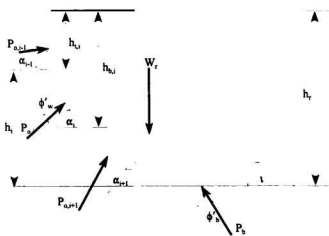


Figure 7.28 Figure of a rubble retained by a multi-sloped wall showing the wall thrust and the wall angle of each section

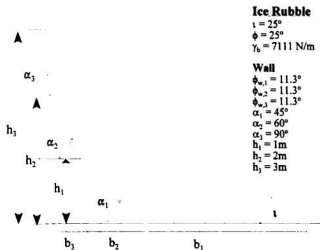


Figure 7.29 Data for sample calculation showing the use of the derived equations

## **Part III      Ice Force Model**

### **Chapter 8   Development of a New Ice Force Model**

In Chapter 6, a new rubble geometry prediction model was formulated from mass balance and interaction geometry considerations. With the geometry of the rubble known, the forces imposed by the rubble on the ride-up ice and the supporting ice sheet can then be computed via the set of equations derived in Chapter 7. These forces, interacting with the ride-up ice and the supporting ice sheet, affect the magnitude of loads acting on the cone.

While the estimation of the load imposed by the ride-up ice is rather simple, the breaking behaviour of ice under the complex geometry imposed by both the rubble and the ride-up ice is complex. Many models have been constructed to predict ice forces on cone for the cases where there is no rubble buildup. In this chapter, those models are examined, and a base model is selected to model the breaking behaviour of intact ice. The new rubble model is then incorporated into the base model to compute the peak ice load exerted on the cone due to the passage of a combined ice sheet/rubble system.

In Section 8.1 the base model is selected from four representative models. The primary criterion for selection is the degree of simplicity and accuracy. The adaptation of the rubble model to the base model is presented in Section 8.2; while, in Section 8.3 the new ice force model is validated by the experimental results presented in Part I of this thesis.

## **8.1 Selection of Base Model for Modelling of Ice Breaking Behaviour of Intact Ice**

In Section 8.1.1 the experimental data and the analytical models used for comparison are briefly described. All data and models are for smooth cones only. In Section 8.1.2, a method to adapt the 2-D model to 3-D cases is presented. This method is incorporated into the Croasdale's model to give a better representation of the 3-D nature of ice load. In Section 8.1.3, accuracy of the existing mathematical models is assessed and discussed.

### **8.1.1 Experimental Data and Ice Force Models for Smooth Cones, with Ride-Up Ice, But No Rubble**

The data set utilizes data from ten test programs done worldwide on smooth conical structures with a total of 226 data points (Afanas'ev et al, 1971; Verity, 1975; Edwards et al, 1975; Edwards and Croasdale, 1976; Manders and Abdelnour, 1978; Hirayama and Akamatsu, 1982; Wessels, 1984; Sodhi et al, 1985; Lau et al, 1988; and Izumiya et al, 1991). The test condition of each program is summarized in Table 8.1. These data encompass most of the data available during the last 25 years which have been widely cited in the open literature. All tests were conducted in model basins where the uniformity of ice properties was highly controlled, and the ice properties and load data were well documented.

Three widely used analytical/mathematical models for smooth cones were chosen as possible candidates for the base model. They are:

- (i) Nevel's elasticity model (1992);
- (ii) Ralston's plasticity model (1977); and

- (iii) Croasdale's 3-D model (1980) with in-plane force adjustment (Croasdale et al, 1994).

In addition, Croasdale's model was modified to give a better representation of the 3-D geometry of ice loading. The modified model is referred to as 'Lau-Croasdale' model in the rest of the section. The modification is described in Section 8.1.2.

These models are representative of the existing major model treatments of ice forces on conical structures. The models and their particular modelling features have been reviewed in Chapter 2.

Ralston's model allows computation of failure load due to two types of failure criteria, i.e., Johansen and Tresca failure criteria. In this work, the Johansen failure criterion was assumed.<sup>1</sup>

For Nevel's model, the computer program supplied by Nevel (1992) was used. Nevel's computer program provides calculations for a combination of selected interaction conditions including: sequential or simultaneous ice breaking, inclusion or exclusion of ice pieces on neck section, and active or passive ice actions, with a total of 8 possible interaction scenarios. Computations for each assumed scenario is given elsewhere (Lau, 1999). In the present comparison, ice load for each individual test was computed for all 8 scenarios and then averaged to give the model prediction for that test.

---

<sup>1</sup>In the present test sets, computation using Tresca failure criterion gives an overall 12.5% higher force values in both the horizontal and the vertical directions than that computed using the Johansen failure criterion.

### 8.1.2 3-D Modification of Croasdale's Model

Croasdale's (1980) provided a method to adapt his 2-D model to a 3-D case, i.e., narrow structures, by considering the length of circumferential cracks to extend beyond the structures. For example, in Croasdale's model, the total horizontal and vertical forces,  $H_{TOT}$  and  $V_{TOT}$ , exerted on the front half of the smooth cone can be expressed in the following simplified form:

$$H_{TOT} = F_\xi V_{TOT} \quad (8-1)$$

$$V_{TOT} = V'_b L_C + W_{ru} \quad (8-2)$$

where  $F_\xi$  is the resolution factor for a sloping plane,  $\xi$ , as defined in Equation 2.2;  $L_C$  is the total length of the circumferential crack;  $W_{ru}$  is the total weight of ride-up ice; and  $V'_b$  is the effective breaking load per unit width of ice beam under combined bending and in-plane compression. As noted already, the concern here is only with a single layer of ice, of thickness,  $t$ , riding up the front half of the cone with no rubble accumulation on top of the ice layer or ice sheet.  $L_C$ ,  $W_{ru}$  and  $V'_b$  are expressed as follows:

$$L_C = D \left( 1 + \frac{\pi^2 l_c}{4D} \right) \quad (8-3)$$

$$W_n = D \left( \frac{z}{\sin \alpha} \right) t \gamma \quad (8-4)$$

$$V_b' = 0.68 \sigma_f' \left( \frac{Y_w t^5}{E} \right)^{\frac{1}{4}} \quad (8-5)$$

where  $\gamma$  the weight density of ice;  $\gamma_w$ , the weight density of water;  $E$ , the elastic modulus of ice;  $t$ , the ice thickness;  $D$ , the waterline width of the structure;  $\alpha$ , the inclination angle;  $z$ , the free-board;  $L_c$ , the characteristic length of ice; and  $\sigma_f'$ , is the effective flexural strength of the ice beam under combined bending and in-plane compression. The method to compute  $\sigma_f'$ , is given by Croasdale et al (1994) and is further discussed in Section 8.2.7.

It has been shown in Chapter 4 that the 3-D distribution of ice loads is important, particularly in a larger scale, and  $F_\xi$  in Equation 8.1 should be approximately equal to  $(2/\pi)\xi$  (see Section 4.4.1). By assuming  $F_\xi$  is equal to  $\xi$ , Croasdale's model tends to overestimate the horizontal force component. Furthermore, while the equations for  $L_c$  and  $W_n$  are derived considering a sloping plane, their application to conical structures omits of the 3-D nature of ice load distribution caused by the cone's curvature.

The following method is proposed by the present author to adapt Croasdale's 2-D model to a 3-D case, which gives a better representation of the 3-D nature of ice loading on

the cone. The method considers the direction of ice force distribution around the cone surface, and gives a better estimation of  $W_n$  and  $L_c$ . It first computes and integrates the distributed ice forces along the front perimeter of the cone to give the net vertical loads, and then calculates the net horizontal force by the appropriate resolution factor for a 3-D case, i.e.,  $(2/\pi)\xi$ .

For modelling purposes, only the loads on the front half of the cone are considered, and full coverage of ride-up ice on this half of the cone is assumed as shown in Figure 8.1. The total weight of ride-up ice,  $W_n$ , is given in the following expression:

$$W_n = \pi \left( \frac{D_n + D}{4} \right) \left( \frac{z}{\sin \alpha} \right) t \gamma \quad (8-6)$$

where  $D$  and  $D_n$  are the waterline and neck diameters of the cone, respectively.

The breaking force is computed by considering simultaneous failure of a series of wedge beams along the cone's front perimeter (see Figure 8.1). Each beam has a breaking length,  $L_L$ , derived from the theory of semi-infinite elastic beam on elastic foundation (Hetenyi, 1946), i.e.,

$$L_L = \frac{\pi}{4} l_c \quad (8-7)$$

The distance of the circumferential crack to the centre of the cone is equal to  $[D/2 + (\pi/4)l_c]$  and the total length of the circumferential crack,  $L_c$ , is given as follows:

$$L_c = \pi \left( \frac{D}{2} + \frac{\pi l_c}{4} \right) \quad (8-8)$$

With the  $W_n$  and  $L_c$  given in Equations 8.6 and 8.8, the vertical load on each wedge beam is computed via Croasdale's 2-D model, i.e., Equation 8.2, and then summed up to give the net vertical breaking load,  $V_{TOT}$ :

$$V_{TOT} = 0.68\sigma'_f \left( \frac{\gamma_w t^5}{E} \right)^{\frac{1}{4}} \pi \left( \frac{D}{2} + \frac{\pi l_c}{4} \right) + \pi \left( \frac{D_n + D}{4} \right) \left( \frac{z}{\sin\alpha} \right) t \gamma \quad (8-9)$$

Since that the vertical load,  $V_{TOT}$ , is uniformly distributed along the front half of the cone, the horizontal load,  $H_{TOT}$ , is related to  $V_{TOT}$ , by  $\xi_{3D}$  (see Section 4.4.1), i.e.,

$$H_{TOT} = \xi_{3D} V_{TOT} = \frac{2}{\pi} \xi V_{TOT} \quad (8-10)$$

The adjustment for the effect of in-plane compression on  $\sigma'_f$  can be performed for each beam in the same manner as suggested by Croasdale et al (1994) (see Section 8.2.7).

### 8.1.3 Result of Model Assessment

Figure 8.2 compares the predicted horizontal force,  $F_{x,pred}$ , computed from Lau-Croasdale's model to the horizontal mean peak force,  $F_{x,meas}$ , measured from each test in the data sets listed in Section 8.1.1, and the comparison for the vertical force is shown in Figure

8.3. Comparisons for the Croasdale's model, the Nevel's model, and the Ralston's model are shown in Figures 8.4 to 8.9. Table 8.2 summarizes the average and standard deviation of the predicted to measured mean peak force ratio,  $F_{\text{pred}}/F_{\text{meas}}$ , associated with each test data set. The data are plotted in Figures 8.10 and 8.11 for two respective directions. Both the Nevel's and the Ralston's models give very high estimates of the horizontal forces measured for the 80° cone model in the Hirayama et al's tests (Series #3), i.e., 13.8 and 12.8 times the measured values, respectively; hence, the statistics were computed without the corresponding runs. Figure 8.12 gives the overall average  $F_{\text{pred}}/F_{\text{meas}}$  ratio for each ice force model, and the associated statistics are summarized in Table 8.3.<sup>2</sup>

Ralston's model over-estimates ice loads by 41% in both the horizontal and vertical directions and is eliminated from further consideration. This over-prediction is a consequence of the plasticity modelling (see Section 2.2.1.3).

Croasdale's and Nevel's models predict well the ice force in the vertical direction with overprediction by merely 4% and 6 %, respectively; however, these models overestimate the horizontal ice force by 37% and 12%, respectively. The over-prediction of ice force in the horizontal direction by the Croasdale's model is due to the 2-D treatment of load distribution; whereas, the source of over-prediction for the Nevel's model is uncertain.

Overall, Lau-Croasdale's model gives the best agreement with test data for both the horizontal and the vertical loads with an average  $F_{\text{pred}}/F_{\text{meas}}$  value of 0.92 and 1.01 for the

---

<sup>2</sup>The values given in Table 8.3 is the arithmetic mean of the statistics calculated for each test set as given in Table 8.2. This gives equal weighting for each test set.

respective directions. The 8% discrepancy between the predicted and the measured horizontal force values is mainly contributed by the discrepancy between the measured and predicted resolution factors associated with tests with smaller ratio of waterline diameter to ice characteristic length, when the measured resolution factor diverges from the assumed value of  $(2/\pi)\xi$  and moves toward  $\xi$  as the ratio decreases (See Figure 4.12).

All the models deal with forces from the ice sheet and ride-up ice, not considering the forces due to rubble. Based on the above assessment, Lau-Croasdale's model is selected as the basis for further model formulation to include the effect of rubble.

## 8.2 Formulation of Ice Force Model with Rubble at a Faceted Cone

The problem of ice rubble loading on cones is essentially a three-dimensional problem. Any satisfactory treatment of the problem would have to account for the three-dimensional nature of the interaction as in the previous section. However, a complete three-dimensional treatment of the problem would lead to complexities too difficult for analysis. Instead, a pseudo-three-dimensional treatment of the interaction was performed by recognizing the two-dimensional nature of the interaction geometry associated with individual facet. This treatment results in a set of simple equations which can be easily incorporated into a probabilistic methodology.

In this model, only the front half of the cone is considered, and the loading on each facet is treated two-dimensionally. The horizontal and vertical forces in the plane perpendicular to each facet are first computed using a two-dimensional model. These forces

are then transformed into their X and Z Cartesian components using the appropriate resolution factors and summed up vectorially to give the net force on the cone.

Section 8.2.1 describes the general features and assumptions of the interaction system. The coordinate system and geometry of the problem are described in Section 8.2.2. The basic governing equations to transform the interactive forces on a particular facet into components acting along the principal axes directions are given in Section 8.2.3. Section 8.2.4 describes the various force components to be considered in the model, followed by detailed derivations of each component in Sections 8.2.5 and 8.2.6. Section 8.2.7 describes the computational procedure to adjust for the effect of in-plane compression on failure load.

### **8.2.1 General Features and Simplifications of the Ice-Structure Interaction**

The interaction processes under investigation are quite complex resulting from the complex interaction geometry existing between the rubble, the ride-up ice and the structure. Simplifications were adopted to generate fairly realistic representations of a range of ice structure interaction conditions while at the same time providing computational simplicity. The general features and the simplifications of the interaction system with regard to the ice breaking pattern, the rubble and ride-up ice geometries and weights, and the load distribution and failure of ice sheet are described in the following section.

#### **8.2.1.1 Characteristic Ice Breaking Pattern**

The characteristic ice crack patterns are depicted schematically in Figure 8.13. Two

radial cracks make an angle,  $\theta_{cr}$ , extending outward from the corners of a facet forming a cantilever beam with the width,  $d_{cr}$ , slightly wider than the structure. The  $d_{cr}$  is related to  $\theta_{cr}$  and the broken beam length,  $L_L$  by the following relationship:

$$d_{cr} = w_f + 2L_L \tan\theta_{cr} \quad (8-11)$$

where  $w_f$  is the width of facet at waterline. In the present model, the values of  $\theta_{cr}$  is assumed to be 30°, and the  $L_L$  can be computed from the empirical equation derived in Section 4.2.2, i.e., Equation 4.5, or from field measurements. As depicted in Figure 8.13, the same value of ice breaking width,  $d_{cr}$ , is assumed for broken wedge in front of the three facets.

The broken ice pieces riding up the central facet are trapezoidal in shape. This train of ride-up ice results in an ice wall with an average width,  $w_{nuc}$ , being:

$$w_{nuc} = \frac{1}{2}(d_{cr} + w_f) = w_f + L_L \tan\theta_{cr} \quad (8-12)$$

As these ice pieces eventually contribute to the ice supply to the rubble,  $w_{nuc}$  should be used to calculate the rubble geometry as the width of the central zone, i.e., by simply replacing  $w_f$  with  $w_{nuc}$  in the equations given in Chapter 6.

### 8.2.1.2 Heights, Width, and Weights of Rubble in Front of the Front Facet

At the front facet, the rubble increases in height from the two edges reaching a maximum value at the centerline. In order to compute total thrust on the facet using the

equations derived in Chapter 7, an average height and width of the rubble in front of the front facet, i.e.,  $h_{r,c}$  and  $w_{r,c}$ , must be estimated.  $h_{r,c}$  is given by the following equation:

$$h_{r,c} = h_{rf} + (h_{rm} - h_{rf}) \left( 1 - \frac{w}{w_{r,c}} \right) \quad (8-13)$$

where  $h_{rf}$  is the rubble height at the edge of the front facet;  $h_{rm}$  is the maximum rubble height at the front facet;  $w$  is the width computed from Equation 6.34 (see Section 6.3.3), and  $w_{r,c}$  is the width of the rubble.  $w_{r,c}$  is equal to  $w_{n.c.}$ , which can be computed via Equation 8.12.

The total weight of the rubble,  $W_{r,c}$ , in front of the front facet is given as:

$$W_{r,c} = \frac{1}{2} \gamma_b w_{r,c} \left[ h_{r,c}^2 \left( \frac{1}{\tan \phi} - \frac{1}{\tan \alpha_k} \right) - \sum_{i=1,k+1} h_i^2 \left( \frac{1}{\tan \alpha_i} - \frac{1}{\tan \alpha_{i+1}} \right) \right] \quad (8-14)$$

where  $\gamma_b$  is the bulk weight density of the rubble;  $\phi$ , the rubble inclination;  $\alpha_i$  and  $h_i$ , the cone angle and height of an arbitrary section  $i$ , respectively; and  $k$  is the highest section the rubble reaches.

### 8.2.1.3 Weights of Ride-Up Ice on Individual Sections on the Front Facet

In the present model, the weight of ride-up ice covering the individual sections is needed. Observation from model tests showed an average extrusion of 5 pieces of ice constantly maintained on the neck beyond the top of the rubble before they fell onto the on-

coming rubble. Therefore, the following ride-up height on the front facet,  $h_{ru,c}$ , is assumed:

$$h_{ru,c} = 5L_L + h_{r,c} \quad (8-15)$$

or

$$h_{ru,c} = 5L_L + h_n \quad (8-16)$$

whichever is greater.  $h_n$  is the base height of the neck section from the waterline.

With ride-up ice reaching the neck, all sections are covered with ice. The weight of ride-up ice,  $W_{ru,c,i}$ , covering an arbitrary section, i, is given as:

$$W_{ru,c,i} = \gamma \cdot i \cdot w_{ru,c} \frac{h_{l,i}}{\sin\alpha_i} \quad (8-17)$$

where  $h_{l,i}$  is the length of ride-up ice of an arbitrary section i as defined in Figure 8.14. For the neck section,  $h_{l,i}$  is equal to  $h_{ru,c}$  minus  $h_n$ ; and for the lower sections,  $h_{l,i}$  is equal to  $h_{i+1}$  minus  $h_i$ .

#### 8.2.1.4 Heights, Width, and Weights of Rubble in Front of the Side Facets

The average rubble height in front of the side facet,  $h_{rs}$ , is taken as the average of the height at the edge of the front facet,  $h_{rf}$ , and the height at the side,  $h_n$ , i.e.,

$$h_{rs} = \frac{1}{2}(h_{rf} + h_n) \quad (8-18)$$

The total weight of rubble,  $W_{rs}$ , in front of the side facet can be estimated by divided the portion of rubble mass in question into two volumes,  $V_I$  and  $V_{II}$ , as shown in Figure 8.15.  $V_I$  is approximately equal to the volume resulting from rotating the cross-section A by 90° about axis  $Z_1$  (see Figure 8.15).  $V_I$  can be computed using the following equation:

$$V_I = \frac{1}{12} \pi \left[ h_{rf}^3 \left( \frac{1}{\tan^2 \phi} - \frac{1}{\tan^2 \alpha_k} \right) + \sum_{i=1, k+1} h_i^3 \left( \frac{1}{\tan^2 \alpha_i} - \frac{1}{\tan^2 \alpha_{i-1}} \right) \right] \quad (8-19)$$

$V_{II}$  is approximately equal to a volume formed by two equal and parallel cross-sections,  $A_{rr}$  and  $A_{rs}$ , with a distance  $d_{II}$  between them. The distance  $d_{II}$  depends on  $h_{rf}$  and is computed by the following expression:

$$d_{II} = \frac{1}{2} D_{k+1} \cos(30^\circ) + \frac{h_k - h_{rf}}{\tan(\alpha_k)} \quad (8-20)$$

where  $k$  is the highest section the rubble reaches at the edge of the front facet, and  $D_{k+1}$  is the diameter of the  $k+1$  section.<sup>3</sup> Therefore,  $V_{II}$  can be computed using the following equation:

$$V_{II} = A_{rr} d_{II} = \left( \frac{w_{rus,I}}{2(1-p)} \right) \left( \frac{1}{2} D_{k+1} \cos(30^\circ) + \frac{h_k - h_{rf}}{\tan(\alpha_k)} \right) \quad (8-21)$$

and the total weight of the rubble,  $W_{rs}$ , in front of the side facet is given as:

<sup>3</sup>If the rubble reaches the neck section,  $D_{k+1}$  is assumed equal to  $D_n$ , the diameter of the neck section.

$$W_{r,s} = (V_I + V_H) \gamma_b \quad (8-22)$$

Again, an average width of the rubble,  $w_{r,s}$ , at the side facet is needed to calculate the total wall thrust due to rubble. This width can be approximated by assuming an equivalent rubble in front of the facet with a constant width  $w_{r,s}$  and a height  $h_{r,s}$ .  $w_{r,s}$  is calculated by dividing the total volume,  $V_I + V_H$ , by the cross-sectional area of the equivalent rubble,  $A_{eq} = W/\gamma_b$ , where  $W$  is the weight of the rubble per unit width computed by Equation 7.40, and  $\gamma_b$  is the bulk weight density of the rubble, i.e.,

$$w_{r,s} = \frac{V_I + V_H}{\frac{1}{2} \left[ h_{r,s}^2 \left( \frac{1}{\tan \alpha_1} - \frac{1}{\tan \alpha_k} \right) - \sum_{i=1,k-1} h_i^2 \left( \frac{1}{\tan \alpha_i} - \frac{1}{\tan \alpha_{i+1}} \right) \right]} \quad (8-23)$$

### 8.2.1.5 Weights of Ride-Up Ice on Individual Sections on the Side Facets

The amount of ice riding-up the side facets can be estimated by considering the amount of ice on the side zone, with width of the side zone,  $d_s = 0.5(D - w_{ns,s})$ , which must be displaced by the cone, i.e., the shaded area, abc, as shown in Figure 8.16, with the total weight of ride-up ice,  $W_{ns,s}$ , displaced being:

$$W_{ns,s} = \gamma \left( \frac{1}{8} \right) \left( \frac{t}{\tan 30^\circ} \right) \left( D - w_{ns,s} \right)^2 \quad (8-24)$$

for a six-faceted cone.

The coverage of ride-up ice on the side facet is not constant which leads to uneven weight distribution along the facet. To simplify the computation, the weight is assumed to be distributed evenly along the lowest section of the facet.

#### **8.2.1.6 Load Distribution and Failure of Ice Sheet**

The base model selected in Section 8.1 computes the breaking load resulting from simultaneous bending failure of a series of wedge beams loaded at their tips. While this loading condition is a good characterization of the contact loads imposed on the supporting ice sheet by the ride-up ice and the cone, the presence of rubble significantly modifies the load distribution the intact ice experiences. In addition to a concentrated load transferred via the ride-up ice to the tip of the ice sheet, the rubble distributes its mass and imposes a triangular load distribution along the supporting ice sheet. The effect of this distributed load on the breaking behaviour of the supporting ice sheet is not examined in this work; instead, the load is assumed to act at the tip of the supporting ice sheet as assumed in previous models. Since the distributed load can be transformed into a point load as well as a moment applied at the tip of the ice beam with the moment tending to facilitate breaking of ice, omission of this moment renders the approximation conservative.

Different failure modes due to a combination of axial, shear, and bending stresses can also occur; however, only ice failure due to bending is modelled in this model. Failure due to other modes should be considered during the design process.

### 8.2.2 Coordinate System and Geometry

Consider a quarter of a faceted conical structure above the waterline which has an inclination of angle  $\alpha$ , with respect to the horizontal, as shown in Figure 8.17. Let (XYZ) be a right handed Cartesian coordinate system. The water surface is the ( $Z=0$ )-plane. The +X-axis is opposite to the motion of the ice; the +Z-axis is directed upward through the center of the cone; and the +Y direction is then toward the viewer when viewing the (X-Z)-plane.

The ice moves from the X direction and the broken ice pieces slide over the cone in planes parallel to the X-Z plane as shown by the path in Figure 8.17. Consider an ice piece on the surface of the cone at position b. At this point there is a force,  $N$ , normal to the surface of the cone and a frictional force,  $\mu N$ , tangential to the surface of the cone where  $\mu$ , is the coefficient of ice friction.

Plane abd is a plane parallel to the X-Z plane with line ab coincident with the ice path. Plane bed is a plane perpendicular to the cone surface. The angle  $\theta$  is the angle between plane bed and plane abd. For the 6-faceted cone,  $\theta$  equal to  $0^\circ$  for the front facet and  $60^\circ$  for the side facets. The angle  $\psi$  is the angle of the frictional force at any point on the cone surface with respect to the X-axis and can be related to  $\theta$  and  $\alpha$ :

$$\tan \psi = \tan \alpha \cos \theta \quad (8-25)$$

### 8.2.3 Normal and Frictional Forces on Each Facet

The equations for the direction cosines,  $\cos(x_N)$  and  $\cos(z_N)$ , of any normal force,  $N$ , on the front half of the cone are given as follows:

$$\cos x_N = -\sin \alpha \cos \theta \quad (8-26)$$

$$\cos z_N = -\cos \alpha \quad (8-27)$$

where  $x_N$  and  $z_N$  are the angle between the normal force and the respective axes, and the angles,  $\alpha$  and  $\theta$ , are between  $0^\circ$  and  $90^\circ$  as shown in Figure 8.17. The scalar quantities,  $|N|\cos(x_N)$  and  $|N|\cos(z_N)$ , are equal to the components of  $N$  in the direction of the respective  $X$  and  $Z$  axes. If the ice path is parallel to  $X-Z$  plane, the equations for the direction cosines of the frictional force,  $\cos(x_F)$  and  $\cos(z_F)$ , on the front half of the cone are given as follows:

$$\cos x_F = -\cos \psi \quad (8-28)$$

$$\cos z_F = \sin \psi \quad (8-29)$$

The components,  $F_x$  and  $F_z$ , along the negative  $X$  and  $Z$  axis of any normal force  $N$  and its frictional force  $\mu_s N$  at any point on front half of the cone surface can be resolved using the direction cosines, i.e.,

$$F_x = N(\cos x_N + \mu_s \cos x_F) = N(\sin \alpha \cos \theta + \mu_s \cos \psi) \quad (8-30)$$

$$F_z = N(\cos z_N + \mu_i \cos z_F) = N(\cos \alpha - \mu_i \sin \psi) \quad (8-31)$$

And, hence,  $F_x$  is related to  $F_z$  through the following ratios:

$$\frac{F_x}{F_z} = \frac{\sin \alpha \cos \theta + \mu_i \cos \psi}{\cos \alpha - \mu_i \sin \psi} \quad (8-32)$$

For the forces acting at the front facet, where  $\psi = \alpha$  and  $\theta = 0$ , Equations 8.30 to 8.32 get reduced to the following familiar form:

$$F_x = N(\sin \alpha + \mu_i \cos \alpha) \quad (8-33)$$

$$F_z = N(\cos \alpha - \mu_i \sin \alpha) \quad (8-34)$$

$$\frac{F_x}{F_z} = \frac{\sin \alpha + \mu_i \cos \alpha}{\cos \alpha - \mu_i \sin \alpha} = \xi \quad (8-35)$$

If we let  $X'$  be the direction perpendicular to the side facet at the waterline as shown in Figure 8.17, then  $F_{x'}$  and  $F_z$  at any point on the surface of the side facet are related by  $\xi$ , and the following relationship between  $F_{x'}$  and  $F_z$  is valid:

$$F_t = \frac{F_{t'}}{\xi} \left( \frac{\sin\alpha \cos\theta + \mu_i \cos\psi}{\cos\alpha - \mu_i \sin\psi} \right) \quad (8-36)$$

By treating the side facet as a simplified two-dimensional system, the total horizontal force,  $F_t$ , on the facet is computed first, and then resolved to  $F_s$  using Equation 8.36.

#### 8.2.4 Overview of Various Force Components

Consider the general interaction between the ice and a sloping wall in a simplified 2-D system as shown in Figure 8.18. The load on the cone is derived from two sources:

- (i) The contact load exerted directly on the cone surface by the ride-up and the rubble as they are being pushed up the slope by the ice sheet, i.e., the reaction forces of  $H_s$  and  $V_s$ ; and,
- (ii) The contact load exerted by the ice sheet at the waterline as it slides up the slope, i.e., the reaction forces of  $H_w$  and  $V_w$ . This load is limited by the ultimate failure of the ice sheet.

The rubble interacts with and imposes loads on the riding-up ice and the supporting ice sheet, i.e.,  $P_o w_r$ ,  $P_{bh} w_r$ , and  $P_{bv} w_r$ , as shown in Figure 8.18 (with  $w_r$  being the width of rubble). These loads are eventually transferred onto the cone as additional loads. Equations to compute these loads have been derived in the Chapter 7.

The total force acting on the cone can be related to the forces acting at the tip of the ice sheet as shown in Figure 8.19 with the forces imposed by the rubble included.  $H_T$  and

$V_T$  are the total horizontal and vertical forces acting at the top edge of the ice sheet, i.e.,

$$H_T = P \cos\alpha + P_{bh} W_r \quad (8-37)$$

$$V_T = P \sin\alpha + P_{bv} W_r \quad (8-38)$$

where  $P$  is the force required to push ice blocks up the slope through ice rubble. Equations to compute  $P$  are derived in Section 8.2.5. The reactions of  $H_T$  and  $V_T$  eventually act on the cone surface through the ride-up ice, i.e.,

$$H_S = H_T \quad (8-39)$$

$$V_S = W_r + W_n - V_T \quad (8-40)$$

where  $H_S$  and  $V_S$  are the total horizontal and vertical forces on the cone surface above waterline; and  $W_r$  and  $W_n$  are the total weights of the ice rubble and the ride-up ice, respectively.

$H_w$  and  $V_w$  in Figure 8.19 are the total horizontal and vertical forces acting at the bottom edge of the ice sheet, i.e.,

$$H_w = V_w \xi \quad (8-41)$$

$$V_w = V_T + V'_b d_{cr} \quad (8-42)$$

Where  $V'_b$  is the effective breaking load per unit width of the ice beam under combined bending and in-plane compression, and  $d_{cr}$  is the crack length. In this model  $V'_b$  is calculated using Equation 8.5 as derived by Croasdale et al (1994). The reactions of  $H_w$  and  $V_w$  give total loads on the cone surface at the waterline.

Therefore, the total horizontal and vertical loads on the cone,  $H_{TOT}$  and  $V_{TOT}$ , are given as follows:

$$H_{TOT} = H_S + H_w = H_T + H_w \quad (8-43)$$

$$V_{TOT} = V_S + V_w = V'_b d_{cr} + W_r + W_n \quad (8-44)$$

$H_T$  and  $H_w$  are derived in Section 8.2.6,  $V'_b$  is computed in Section 8.2.7, and Equations to compute  $W_r$  and  $W_n$  are given in Sections 8.2.1.2 to 8.2.1.5 with a given amount of ride-up and rubble ice for the respective facets.

### 8.2.5 Forces Required to Push Ice Blocks Up the Slope Through Ice Rubble

Figure 8.20 shows the forces acting on a layer of ride-up ice at an arbitrary cone section, i. Force balance at direction parallel to the structure slope gives:

$$P_i = W_{n,i} \sin \alpha_i + N_{s,i} \mu_s + P_{o,i} w_r \sin \phi'_{w,i} + P_{i+1} \cos(\alpha_{i+1} - \alpha_i) \quad (8-45)$$

where  $P_{o,i}$ , and  $\phi'_{w,i}$ , are the rubble thrust force per unit width of rubble and its angle of action exerted on the ride-up ice,  $W_{ru,i}$  is the weight of the ride-up ice, and  $P_{i,i}$  is the total force transferred from the above conical section.  $P_{o,i}$  and  $\phi'_{w,i}$  are computed from the universal equation given in Chapter 7.

Force balance perpendicular to the structure slope gives:

$$N_{s,i} = P_{o,i} w_r \cos\phi'_{w,i} + W_{ru,i} \cos\alpha_i + P_{i,i} \sin(\alpha_{i+1} - \alpha_i) \quad (8-46)$$

By substituting Equations 8.46 into Equation 8.45,  $P_i$  is found:

$$\begin{aligned} P_i &= W_{ru,i} (\sin\alpha_i + \mu_s \cos\alpha_i) + P_{o,i} w_r (\sin\phi'_{w,i} + \mu_s \cos\phi'_{w,i}) \\ &\quad + P_{i-1} [\cos(\alpha_{i+1} - \alpha_i) + \mu_s \sin(\alpha_{i+1} - \alpha_i)] \end{aligned} \quad (8-47)$$

The forces,  $P_i$ , are determined for each section proceeding from the neck to the lowest cone section at the waterline, with the lowest cone being designated as the first section.  $W_{ru,i}$  and  $w_r$  are equal to  $W_{ru,c,i}$  and  $w_{r,c}$ , respectively, for the front facet. Likewise,  $W_{ru,i}$  and  $w_r$  are equal to  $W_{ru,s,i}$  and  $w_{r,s}$  for the side facets.

### 8.2.6 Forces Acting on the Ice Sheet at Waterline

The forces acting on the tips of an ice wedge have been shown in Figure 8.19.  $H_T$  and  $V_T$  are the horizontal and vertical components of the forces necessary to push the ice blocks and the rubble up the slope. The components, which are assumed to act at the top of the

wedge tip, are given as:

$$H_T = P_i \cos \alpha_1 + P_{bh} w_r \quad (8-48)$$

$$V_T = P_i \sin \alpha_1 + P_{bv} w_r \quad (8-49)$$

where  $P_i$  is the total force transferred to the top of the ice sheet from the pushing of the ride-up ice through the ice rubble;  $\alpha_1$  is the cone angle at the waterline; and  $P_{bh}$  and  $P_{bv}$  are the forces per unit width of rubble acting on the ice sheet due to the pushing of the ice sheet under the rubble. The  $P_{bh}$  and  $P_{bv}$  are computed from the rubble model.

The vertical component,  $V_w$ , of the contact load acting on the bottom tip of the ice sheet is given as follows:

$$V_w = V_T + V_b' d_{cr} = P_i \sin \alpha_1 + P_{bv} w_r + 0.68 \sigma_f' \left( \frac{\gamma_w t^5}{E} \right)^{1/4} d_{cr} \quad (8-50)$$

The horizontal component,  $H_w$ , of the contact load acting on the bottom tip of the ice sheet is related to  $V_b$ :

$$H_w = V_w \xi = \left[ P_i \sin \alpha_1 + P_{bv} w_r + 0.68 \sigma_f' \left( \frac{\gamma_w t^5}{E} \right)^{1/4} d_{cr} \right] \xi \quad (8-51)$$

where  $\xi$  is defined by Equation 2.2.

### 8.2.7 Modification of Breaking Load for In-Plane Force (Croasdale et al, 1994)

The horizontal force acting on the ice sheet, i.e.,  $H_{TOT}$ , creates an in-plane compression and an edge moment at the ice edge. The maximum tensile stress per unit width along the bottom surface of the beam due to the combined out-of-plane bending and in-plane compression, equal to the effective flexural strength of ice,  $\sigma'_f$ , i.e.,

$$\sigma'_f = + \frac{(V'_b + V_T)\xi + H_T}{t} - \frac{3[H_T - (V'_b + V_T)\xi]}{t} + \frac{V_b \left( \frac{E}{\gamma t^3} \right)^{\frac{1}{2}}}{0.68} \quad (8-52)$$

The first term on the right hand side of Equation 8.52 is the compressive stress due to the in-plane compression (-ve). The second term is the tensile stress due to the combined edge moment applied at the top and bottom tip of the wedge. The eccentricity is assumed equal to  $\frac{1}{2}$  of ice thickness. The last term is the maximum tensile stress of the ice beam due to transverse load only (Hetenyi, 1946).

The above equation can be written as below:

$$\sigma'_f = + \frac{(V'_b + V_T)\xi + H_T}{t} - \frac{3[H_T - (V'_b + V_T)\xi]}{t} + \sigma_f \quad (8-53)$$

where  $\sigma_f$  is the flexural strength measured by transverse loading only; and  $V'_b$  is given in Equation 8.5. The value of  $\sigma'_f$  can be obtained by trial and error method using  $\sigma_f$  as the initial strength. Several iterations are needed to converge to a new value for  $\sigma'_f$ . In the

following comparison, the decrease of effective strength due to edge moment is ignored, which tends to give a more conservative prediction.

### 8.3 Validation of the New Ice Load Model

The experimental data from the IMD's series and the ERCL's series are chosen for the validation of the new ice force model. The model assumes uniformity of test condition; therefore, mean peak force is compared. Since Metge and Weiss (1989) and Metge and Tucker (1990) reported only the maximum loads,  $F_m$ , on the structure, their data was adjusted by assuming the following relationship between the mean peak load,  $F_{meas}$ , and the maximum load,  $F_m$ , hold:

$$F_{meas} = \frac{F_m}{1.08} \quad (8-54)$$

The relationship is true for the IMD's data. The computed and the measured ice forces, i.e.,  $F_{pred}$  and  $F_{meas}$ , are summarized in Table 8.4. An example computation is given in Appendix C.

Figures 8.21 and 8.22 plot the model predictions against ERCL's and IMD's test data, respectively. Results from linear regression for the two comparisons are given in the respective figures. The comparison shows good agreement between model predictions and test data. On average, the model overpredicted the horizontal ice force by 12.9% for ERCL's data, and underpredicted by 8.9% for the IMD's data; whereas, it underpredicted the vertical

ice force by 1.4% for ERCL's data, and 13.1% for IMD's data.

Despite limited data, the agreement between model predictions and experiment data in the horizontal direction is significant, as the loading in this direction tends to destabilize the structures, and accurate estimation of this force component is important. Nevertheless, the discrepancy of load warrants further refinement of the model.

One source of error may be attributed to the ice breaking model used. The failure mechanism observed from IMD's test series was associated with the ultimate failure of finite cantilever beams (see Section 4.2), while the ice breaking model used in this work is for semi-infinite beams. Models based on failure of a semi-infinite beam may not predict well the ice breaking load with thick ice. This observation is consistent with IMD's data in which the comparison of the load is good for the thinner ice (i.e., the semi-infinite beam formula may be valid), and the degree of underprediction increases with the increasing ice thickness; however, further investigation is needed to verify the above observation.

The underestimation in the vertical direction may also partly due to the omission of ice loading at the back half of the cone. This amount of ice cannot be estimated precisely. However, if we arbitrarily assumed 50% of the ride-up and rubble ice loading on the front side facet would load on the back side facet as well, the model will overestimate ERCL's data by 8.4% and underestimate IMD's data by 2.7% in the vertical direction.

Table 8.1 Summary of test conditions used in the selected test programs

Test Set	Reference	$\alpha$ (°)	D (m)	Ice Type	$\sigma_t^1$ (kPa)	t (cm)	No. of Data Pts.
1	Sodhi et al, 1985	45	1.5	EGADS	20-45 ↑	4.5-9.0	28
2	Izumiayama et al, 1991	60	0.5, 0.6, 0.7	EGADS	24-59 ↓	1.8-4.6	19
3	Hirayama and Akamatsu, 1982	50, 60, 70, 80	0.14, 0.17	fresh-water	1177 ↓	0.6-0.9	46
4	Edwards and Croasdale, 1976	45	0.25, 0.5, 1.0	saline	1-41 ↑	1.9-6.8	20
5	Afanas'ev et al, 1972	30, 45, 60	0.12 - 0.28	saline	40 ↑	3	14
6	Manders and Abdelnour, 1978	45	0.67, 1.5	saline	11-21 ↓	2.2-5.1	23
7	Wessels, 1984	30, 45, 60	1.08, 1.28, 1.48	EGADS	60 ↓	3.0-7.0	14
8	Lau et al, 1988	30, 45, 60	1.08, 1.28, 1.48	EGADS	24-47 ↓	3.0-6.8	54
9	Verity, 1975	45	3.3	saline	210-495 ↑	6.8-23.5	8
10	Edwards et al, 1975	45	0.10, 0.15, 0.31, 0.61	synthetic	20-98 ↓	0.7-8.9	40

Note: ↑ Arrow indicates loading directions.

Table 8.2 Summary of average and standard deviation of the predicted to measured mean peak force ratio,  $F_{\text{pred}}/F_{\text{meas}}$ , in each test data set

Test	Statistics	Lau-	Lau-	Croasdale	Croasdale	Croasdale	Nevel	Nevel	Ralston	Ralston
		Croasdale	Croasdale	$F_x$	$F_z$	$F_x$	$F_z$	$F_x$	$F_z$	$F_x$
1	Average	0.83	0.71	1.58	0.95	1.24	0.89	1.33	0.95	
	StDev	0.17	0.10	0.35	0.15	0.24	0.14	0.27	0.13	
2	Average	1.01	N/A	1.50	N/A	1.36	N/A	1.60	N/A	
	StDev	0.28		0.56		0.45		0.31		
3	Average	0.88	1.29	1.27	1.20	1.19	1.28	2.69	2.21	
	StDev	0.17	0.23	0.25	0.22	0.22	0.77	0.65	0.42	
4	Average	0.65	0.81	1.27	1.19	0.80	1.00	0.97	1.05	
	StDev	0.18	0.13	0.42	0.36	0.27	0.27	0.24	0.12	
5	Average	0.59	N/A	0.83	N/A	0.53	N/A	1.12	N/A	
	StDev	0.13		0.20		0.13		0.28		
6	Average	1.14	N/A	1.56	N/A	1.30	N/A	1.37	N/A	
	StDev	0.50		0.57		0.48		0.50		
7	Average	0.99	0.97	1.29	0.87	1.30	1.02	1.42	1.13	
	StDev	0.33	0.16	0.58	0.23	0.51	0.23	0.50	0.17	
8	Average	1.34	1.15	1.68	0.92	1.39	1.21	1.35	1.13	
	StDev	0.74	0.41	1.11	0.30	0.61	0.52	0.43	0.35	
9	Average	0.96	1.07	1.46	1.10	1.13	1.03	1.91	1.73	
	StDev	0.35	0.39	0.51	0.39	0.38	0.36	0.72	0.66	
10	Average	0.85	1.08	1.21	1.02	0.99	0.99	1.62	1.68	
	StDev	0.22	0.31	0.32	0.27	0.32	0.26	0.37	0.52	

Table 8.3 Summary of average and standard deviation of the predicted to measured mean peak force ratio,  $F_{\text{pred}}/F_{\text{meas}}$ , of all tests for each ice force models

		Lau-Croasdale	Croasdale	Nevel	Ralston
$F_{\text{x,pred}}/F_{\text{x,meas}}$	Average	0.92	1.37	1.12	1.41
	StDev	0.21	0.23	0.26	0.46
$F_{\text{z,pred}}/F_{\text{z,meas}}$	Average	1.01	1.04	1.06	1.41
	StDev	0.19	0.12	0.12	0.43

Table 8.4 Summary of measured loads from IMD's and ERCL's test data and the forces predicted by the new model

Test	Measured Peak Force				Predicted Mean Peak Force, $F_{\text{pred}}$	
	Maximum, $F_m$		Mean, $F_{\text{meas}}$			
(#)	$F_x$ (kN)	$F_z$ (kN)	$F_x$ (kN)	$F_z$ (kN)	$F_x$ (kN)	$F_z$ (kN)
<b>ERCL Test Series (1:10 scale)</b>						
T1_R1	10	11	9.26	10.2	11.4	11.9
T2_R1	19	22	17.6	20.4	16.2	16.4
T2_R2	20	20	18.5	18.5	27.4	28.3
T3_R1	30	38	27.8	35.2	27.6	29.0
T4_R1	30	35	27.8	32.4	32.8	34.2
<b>IMD Test Series (MUNCONE)</b>						
3_001	N/A	N/A	4.29	5.30	4.03	4.04
4_001	N/A	N/A	5.00	4.72	4.28	4.38
5_001	N/A	N/A	1.95	1.98	2.04	2.14
6_003	N/A	N/A	2.81	3.06	2.78	2.93

Note: Test condition for each test is given in Chapter 3.

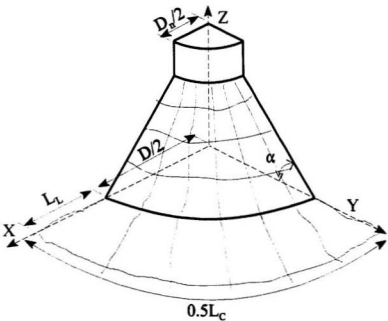


Figure 8.1     Breaking and ride-up patterns assumed in Lau-Croasdale's model (only the front right quarter of the cone is shown)

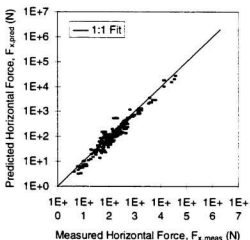


Figure 8.2 Comparison of Lau-Croasdale's model with existing test data for smooth cones: horizontal mean peak force

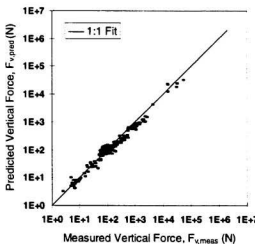


Figure 8.3 Comparison of Lau-Croasdale's model with existing test data for smooth cones: vertical mean peak force

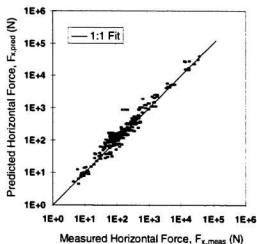


Figure 8.4 Comparison of Croasdale's model with existing test data for smooth cones: horizontal mean peak force

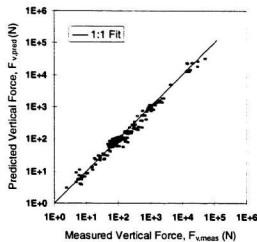


Figure 8.5 Comparison of Croasdale's model with existing test data for smooth cones: vertical mean peak force

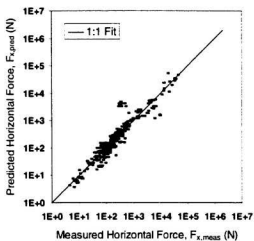


Figure 8.6 Comparison of Nevel's model with existing test data for smooth cones: horizontal mean peak force

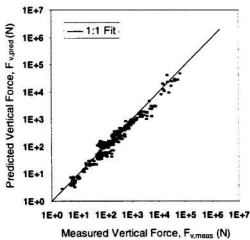


Figure 8.7 Comparison of Nevel's model with existing test data for smooth cones: vertical mean peak force

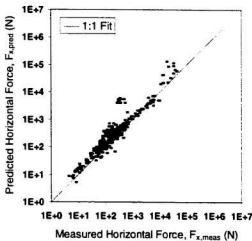


Figure 8.8 Comparison of Ralston's model with existing test data for smooth cones: horizontal mean peak force

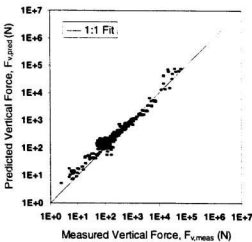


Figure 8.9 Comparison of Ralston's model with existing test data for smooth cones: vertical mean peak force

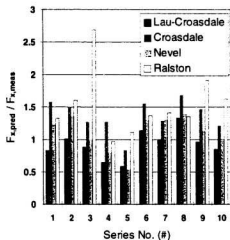


Figure 8.10 Comparison of predicted to measured values for each test series: horizontal mean peak force

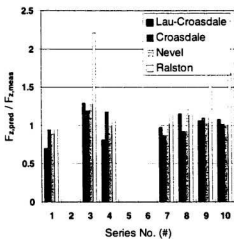


Figure 8.11 Comparison of predicted to measured values for each test series: vertical mean peak force

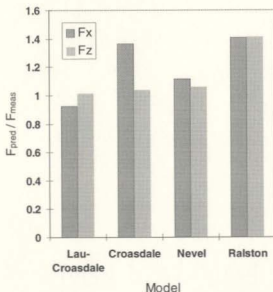


Figure 8.12 Average predicted to measured peak force values for each ice force model

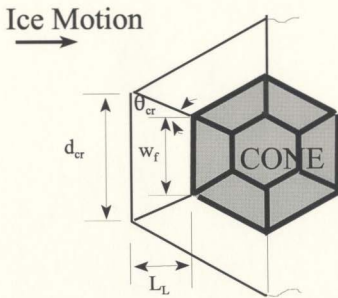


Figure 8.13 Schematic of crack pattern in front of a faceted cone

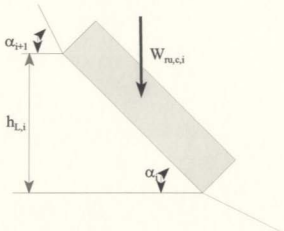


Figure 8.14 Coverage of ride-up ice on an arbitrary section  $i$

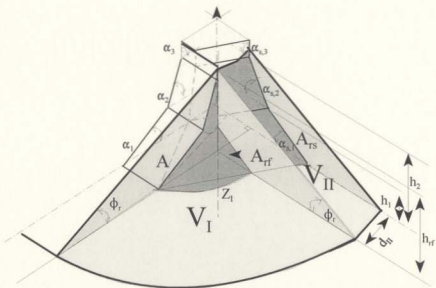


Figure 8.15 Geometry of rubble mass in front of the side facet showing the idealized volumes,  $V_I$  and  $V_{II}$

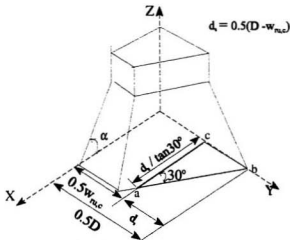


Figure 8.16 Geometry of ice rode up the side facet (only the front right quarter of the cone is shown)

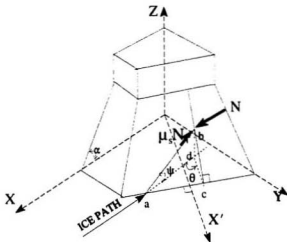


Figure 8.17 Coordinates and geometry (only the front right quarter of the cone is shown)

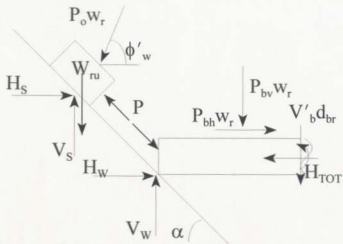


Figure 8.18 General interaction between ice and sloping structure showing ice forces on ride-up ice and the ice sheet

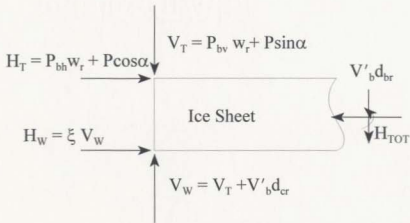


Figure 8.19 Forces acting at the tip of the ice wedge

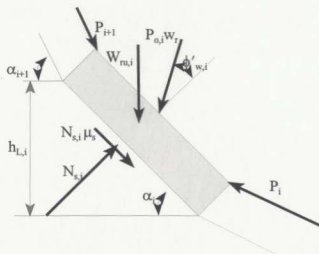


Figure 8.20 Forces acting on a layer of ride-up ice at an arbitrary cone section

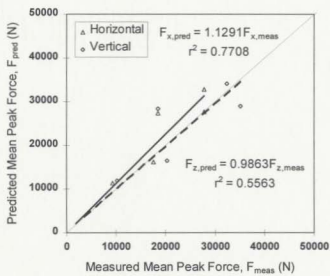


Figure 8.21 Comparison of model prediction and ERCL's test data

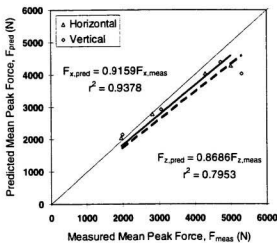


Figure 8.22 Comparison of model prediction and IMD's test data

## **Chapter 9 Conclusions and Recommendations**

This study employed experimental, numerical and analytical methods to study ice forces on a faceted cone due to the passage of a level ice field during continuous ice breaking. The main objectives were to improve our understanding of the interaction and failure processes, and to provide engineers with a set of easy-to-apply formulae for ice load calculation.

Both objectives of the study were reached. First, the experimental investigation provided a clear insight into the interaction processes and the failure mechanisms through relevant observations and interpretation of model test results. The suitability of the existing theories for predicting ice forces on comparable faceted cones was assessed and deficiencies identified. The deficiencies were then addressed and an improved load prediction model was developed in the subsequent numerical and analytical investigations. The model represents the most comprehensive attempt to date to incorporate fundamental processes in the problem treatment and provides a new conceptual framework for future model refinements.

Focus was put on developing a physical sense of the general processes, and a quantitative sense of the magnitude of ice force expected. Simple theories were used, and the mathematical treatment of the topic was kept to minimum. Insofar as possible, the accuracy and range of applicability of the models were evaluated by comparison with experimental data. The model predictions of the rubble geometry, ice movement and the associated forces agreed well with the interaction determined by experiment.

Sections 9.1 to 9.3 highlight the major conclusions drawn regarding the results of the experimental, numerical, and analytical investigations, respectively. Section 9.4 summarizes the main contributions made in the course of this investigation. Recommendations for further work are given in Section 9.5.

## 9.1 Conclusions From the Experimental Investigation (Part I)

In the present study, the results from the multi-faceted cone tests conducted in three ice tanks were consolidated and analyzed. The following conclusions can be drawn for the results of the experiments:

- (i) **Interaction Process:** The interaction process was substantially different from that of a smooth cone and a two-dimensional sloping plane. The flat facet and large neck tended to prevent efficient ice clearing, and rubble building was found to be an essential part of the ice clearing process. An ice clearing component which is as much as 80% of the total load on the structure has been measured. No previously reported work identifies the factors which contribute to the amount of ride-up and rubble formation, and their subsequent effects on the interaction process; this omission can lead to a severe underestimation of the ice forces.
- (ii) **Ice Breaking Mechanism:** Piece size measurements significantly diverged from those predicted by existing classical thin plate theories. This study has shown the important influence of ice thickness on ice breaking. Incorporating the three-dimensional nature of ice behaviour into the problem treatment is essential to

- advance our present understanding of the ice breaking process.
- (iii) **Efficiency of Existing Models in Predicting Ice Forces on Multifaceted Cones:** The analysis of ice sheet loads with a leading ice force predictor revealed that the presently available theory for smooth cones can give sufficiently accurate prediction of ice loads on faceted cones when rubble piling is absent; however, it also indicated that the theory would likely under-predict the clearing component of ice loads. The error in ice load estimation may be quite large when a large rubble field piles in front of the structure, justifying the development of new formulae for the estimation of ice loads on such structures.
- (iv) **Conceptual Model:** A conceptual model was proposed to explain the observed interaction processes between a faceted cone and a level ice sheet during a continuous ice breaking mode. It outlines the three primary interaction processes, i.e., ice breaking, ride-up, and rubble pile-up, where different features dominate, and provides a means of incorporating rubble load theory into existing ice force models.

## **9.2 Conclusions From the Numerical Investigation (Part II)**

In Part II, the unique rubble piling process was further examined with the aid of existing particulate mechanics and a comprehensive numerical analysis. A new rubble model was developed to predict the geometry of the rubble and the forces exerted on the structure and the base support. Based on the result of the rubble modelling, the following conclusions may be drawn regarding the formation process, material properties, stress state, geometry and

associated load of a rubble:

- (i) **Formation Process:** The basic mechanical behaviour and the failure processes of ice rubble under loading conditions typical of the ice-cone interaction process have been examined in Chapter 5. It is concluded that the flow process of ice blocks around the structure can be idealized as quasi-static and steady, and the material as cohesionless coulomb material. The rubble is formed by a natural dumping process, and the clearing of the rubble from the structure is analogous to the bulk material transport on an inclined belt conveyor as the supporting ice sheet and the ride-up ice act as the belt conveyor. Furthermore, the shear strength is fully mobilized at the rubble's free surface.
- (ii) **Stress State:** Based on basic theories of soil mechanics, it is concluded that the cohesionless rubble is in an elastic state throughout its mass during the typical ice-cone interaction process under investigation. Three important phenomenological parameters: the angle of internal friction, the angle of repose, and the 'at rest' earth coefficient function were identified and further explored. These parameters are essential in modelling of rubble behaviour associated with the problem under investigation; yet, measurements associated with ice rubble are scanty.
- (iii) **Model Geometry:** A new model to predict the shape and size of the rubble has been presented based on insights obtained from the experiments and the basic soil mechanics theories. The idealized geometry is uniquely defined by the rubble's angle of repose, and the characteristic rubble heights along the cone perimeter. The amount

of ice piled up was calculated via mass balance considerations. Despite limited data used, the predictions from the derived equations give excellent agreement with the measurements from the experiment.

- (iv) **Rubble Load:** Discrete element analysis using the computer program DECICE has provided a powerful tool for complementing the analytical and experimental work. The analysis helped the development of a semi-empirical equation for the computation of total wall thrust for a variety of ice and structure conditions. The equation is simple to use and yet accounts fully for the discrete nature of the rubble materials. The following conclusions may be drawn regarding the formula that was developed:
- (a) The formula retains the form used in theories of earth pressure on retaining walls, and it represents a best fit of the DECICE results.
  - (b) The proposed equation for rubble load may be applied to design problems; but with caution, since only limited checks have been made.
  - (c) The formula can be adapted to the existing ice breaking model with ease. It substantially reduces the mathematical complexity of the model formulation by allowing the load exerted on the ride-up and supporting ice sheet to be computed via simple semi-empirical equations. The modular nature of the model allows its adoption to future and more advanced ice breaking models with the same degree of ease.

### **9.3 Conclusions From the Ice Force Modelling (Part III)**

In Part III, a base model is first selected from the existing theories to model the breaking behaviour of intact ice, and the new rubble model is then incorporated into the base model to compute the peak ice load exerted on the cone due to the passage of a combined ice sheet/rubble system. The following conclusions may be drawn regarding the model that was developed herein:

- (i) **Base Model:** As it gives the best agreement with experiments, Croasdale's (1980) model, with the 3-D modifications suggested in this thesis, was selected as the base model for ice breaking load.
- (ii) **Ice Load Model:** The model is based on a pseudo-three-dimensional treatment of the interaction, by recognizing the two-dimensional nature of the interaction geometry associated with individual facets. It does so in enough detail to allow exploration of first order effects resulting from changes in the most important design parameters. The expression for ice load has been established in detail. Experimental data affirmed the validity of the developed ice load model and demonstrated its ability to account for the effect of rubble piling.

### **9.4 Contributions of This Work**

The physical experiments reviewed and the numerical experiments performed in this work provide a clear insight into the interaction processes and improves our understanding of the dominant ice-structure interaction processes taking place around faceted cones. They

also provide a set of valuable data useful in confirming and calibrating algorithms for ice loads. A new ice force model has also been developed to compute ice load on the faceted cones. Although the problem was highly idealized, it accurately captured the essential features of a typical interaction and predicted the ice forces well.

The above developments and results are significant, because, for the first time, to the knowledge of the author, an ice load model has been established to account for the effect of rubble in ice loading on a multifaceted cone based on essential features of the interaction. The results provide a useful framework for further model development.

The state-of-the-art is such that it is now possible to incorporate rubble load in the force calculation with higher degree of confidence. The methodology for doing so has been developed and presented herein, and constitutes the main contribution of this work to the state-of-the-art.

## **9.5 Recommendations for Future Work**

While considerable effort has been expended to document the model, no sensitivity analysis has been performed for the model developed in Chapter 6 through 8. Comprehensive sensitivity analyses would help to identify the most important parameters.

Limited experimental data have prevented a comprehensive assessment of the accuracy and limitations of the model, which constitutes a potential weakness of this work. Furthermore, the model was developed from model test data. Some assumptions may be valid in the ideal conditions of the ice tank, but may not be sustainable in the field where the

scale is larger and inhomogeneities more prevalent. Until it is calibrated against full scale data, there will always be uncertainty. A comprehensive assessment of the model results against field measurements (when available) will give a better sense of its accuracy and limitations for different ranges of ice and structure conditions.

The theoretical developments of rubble behaviour draw heavily on soil mechanics. Most of the phenomenological theories and correlations used are empirical, i.e., they are based on observation and results of experimental measurements on soil materials under specific conditions. For example, Jáky's equation for lateral earth pressure at rest, used in the present study to estimate internal friction angle of ice rubble, is known to be valid for normally consolidated soils. Despite the particulate nature of both soils and ice rubble, uncertainty still remains concerning the applicability of the soil mechanics theories to rubble behaviour. Improvements in the theories developed in this study depend crucially upon the availability of accurate field data, i.e., shear strength, rubble geometry and ice load measurements. This would seem to be an area ripe for experimental research.

Due to the pilot nature of this work, there are many aspects of the interaction, which it has not been possible to explore; however, it is evident from the results that a useful modelling framework has been developed. The immediate need is for the incorporation into the theory of some of the more complex aspects of the interaction with respect to rubble piling and ice loads.

### **9.5.1 Refinements of the Rubble Model**

The model is applicable to thick and strong ice impacting on the structure at low to moderate velocity. In order to extend the model to other conditions, the following factors should be considered in further modelling:

- (i) **Dynamic Rubble Piling:** This requires more complicated assumptions for ice block motions within the rubble mass and for ice generation and clearing rates.
- (ii) **Deformation of Rubble Mass:** The possible increase of load on the wall due to deformation of the rubble mass as it is pushed against and up the cone wall should be included as suggested in Section 5.3.2.
- (iii) **Secondary Breaking of Ride-Up Ice:** If the ice in question is thin and weak, i.e., first year ice around a bridge pier, secondary breaking of the ride-up ice may occur which increases the width of the side zones, and the width of the accumulation zone decreases. This will affect the mass balance and profile of the rubble in front of the cone and should be incorporated into further model treatments.
- (iv) **Rubble Cohesion:** If the rubble mass is allowed to stagnate in front of the structure for a period of time, cohesive strength may develop within the pile and increase the rubble load.
- (v) **Effective Wall Friction:** A better picture of the functional relationship between wall friction and ice force awaits the development of a theory to predict the effective friction mobilized at the wall.

It is desirable to develop a purely theoretical rubble model that would, at a future

date, replace the empirical formulations presently adopted in this research. Furthermore, measurements on ice rubble material properties to better define the shear strength in the loose state are needed.

### 9.5.2 Refinements of the Ice Force Model

The present study analysed rubble loading on the basis of the interaction observed in IMD's tests. Other failure modes, and test conditions have not been accounted for; however, the methodology used here can be extended to those cases. A number of areas require further attention. These include:

- (i) **Ice Breaking Component:** The ice breaking is modelled comparatively crudely and much work is needed to improve the model prediction as indicated in Section 4.2.
- (ii) **Further Model and Field Tests:** Improvements in the theory of this study and the development of extensions depends crucially upon the availability of accurate complete field data; therefore, large-scale field tests are strongly recommended.

## REFERENCES

- Abu-Zaid, S., and Ahmadi, G., 1993. Analysis of Rapid Shear Flows of Granular Materials by Kinetic Model Including Frictional Losses, *Power Technology*, Vol. 77, No. 1, Oct., pp. 7-17.
- Afanas'ev, V.P., Dolgopolov, Y.V., and Shvaishstein, Z.I., 1971. Ice Pressure on Individual Marine Structures, in Studies in Ice Physics and Ice Engineering, Edited by G.N. Yakovlev, Published by Israel Program for Scientific Translations, Jerusalem, Israel, pp. 50-68.
- Amontons, G., 1699. De la Résistance Causée Dans les Machines, Tant Par les Frottements des Parties Qui les Composent Que Par la Roideur des Cordes Qu'on y Employe, et la Manière de Calculer L'Un et L'Autre, *Mém. Math. Phys. Hist. Acad. Roy. Sci.*, pp. 206-227.
- Alberta Research Council, 1980. Field Measurements of Ice Forces on Bridge Piers 1973-1979, Report SWE 80-3, Department of Transportation and Surface Water Engineering, Edmonton, Alberta.
- Andrawes, K.Z., and El-Sohby, M.A., 1973. Factors Affecting  $K_o$ , *J. of the Geotechnical Engineering Division, ASCE*, Vol. 99, No. SM7, July, pp. 527-539.
- Applied Mechanics, Inc., 1985. Mechanical Analysis of Spray Ice Platform, Final Report Prepared for Standard Oil Company (Indiana), Amoco Research Center, by Applied Mechanics, Inc., Lakewood, CO.

- Babic, M., Shen, H.T., and Bjedov, G., 1990. Discrete Element Simulations of River Ice Transport, Proc. 10<sup>th</sup> IAHR Ice Symp., Vol. 1, Espoo, Finland, pp. 564-574.
- Baker, W.H., and Krizek, R.J., 1970. Mohr-Coulomb Strength Theory for Anisotropic Soils, J. of the Soil Mechanics and Foundations Division, ASCE 96, Vol. 1, pp. 269-292.
- Balandran, B., and Nemat-Nasser, S., 1993. Double Sliding Model for Cyclic Deformation of Granular Materials, Including Dilatancy Effects, J. of Mechanics and Physics of Solids, Vol. 41, No. 3, pp. 573-612.
- Bashir, Y. M., and Goddard, J.D., 1991. A Novel Simulation Method for the Quasi-Static Mechanics of Granular Assemblages, J. of Rheology, Transactions of the Society of Rheology, Vol. 35, No. 5, pp. 849-885.
- Bazant, Z.P., and Li, Y.N., 1993. Fracture Analysis of Penetration Through Floating Sea Ice Plate and Size Effect, Proc. Ice Mechanics --1993, 1<sup>st</sup> Joint Mechanics Meeting of ASME•ASCE•SES - MEET'N'93, ASCE, Edited by J.P. Dempsey, Charlottesville, VA, p.131-144.
- Been K., and Jefferies, M.G., 1985. A State Parameter for Sands, Geotechnique, Vol. 35, No. 2, 99-112.
- Bercha, F.G., and Danys, J.V., 1975. Prediction of Ice Forces on Conical Offshore Structures, Proc. 3<sup>rd</sup> IAHR Ice Symp., Hanover, NH, pp. 447-458.
- Bishop, A.W., 1955. The Use of Slip Circle in the Stability Analysis of Slopes, Geotechnique, Vol. 5, No. 1, pp. 7-17.
- Bishop, A.W., 1971. Shear Strength Parameters for Undisturbed and Remoulded Soil

- Specimens, Proc. Roscoe Memorial Symp., Foulis & Co., pp. 3-58.
- Boehler, J.P., and Sawzuck, A., 1970. Equilibre Limite des Sols Anisotropes, J. de Mecanique, Vol. 9, No. 1, pp. 5-33.
- Bolton, M.D., 1986. The Strength and Dilatancy of Sands, Geotechnique, Vol. 36, No. 1, pp. 65-78. Discussion: Vol. 37, No. 2, pp. 219-226.
- Boussinesq, J., 1885. Application des Potentiels à L'Étude de L'Équilibre et du Mouvement des Solids Élastiques, Gauthier-Villars, Paris.
- Brooker, E.W., and Ireland, H.O., 1965. Earth Pressures at Rest Related to Stress History, Canadian Geotechnical J., National Research Council, Ottawa, Ontario, Vol. 2, No. 1, Feb., pp. 1-15.
- Brooks, L.D., 1981. Ice Resistance Equation for Fixed Conical Structures, Proc. 6<sup>th</sup> Intl. Conf. on Port and Ocean Engineering under Arctic Conditions, Vol. 1, Quebec City, pp. 90-99.
- Brown, T.G., Croasdale, K.R., Bruce, J.R., and Azarnejad, A., 1998. Observations from the Confederation Bridge Ice Monitoring Program, Proceedings of the 8<sup>th</sup> Intl. Offshore and Polar Engineering Conf., Montreal, Canada, pp. 438-442.
- Bruneau, S.E., 1997. Development of A First-year Ridge Keel Load Model, Thesis (Ph.D.)--Memorial University of Newfoundland, St. John's, Newfoundland, 307p.
- Bruneau, S.E., Croasdale, K.R., Crocker, G.B., McKenna, R.F., Metge, M., Ritch, R., and Weaver, J.S., 1998. Development of Techniques for Measuring *In Situ* Ice Rubble Shear Strength, Proceedings of the 14<sup>th</sup> International IAHR Symposium, Potstam,

NY.

Cammaert, A.B., and Muggeridge, D.B., 1988, Ice Interaction with Offshore Structures, Van Nostrand Reinhold, New York.

Cantelaube-Lebec, F., Limon-Duparcmeur, Y., Bideau, D., and Troadec, J.P., 1995. Equilibrium in a 2-Dimensional Granular Flow, Proc. 10<sup>th</sup> Conf. on Engineering Mechanics, Vol. 1, ASCE, New York, pp. 618-621.

Caquot, A., and Kerisel, J., 1948. Tables for Calculation of Passive Pressure, Active Pressure, and Bearing Capacity of Foundations, Gauthier-Villars, Paris.

Case, P., 1991. A Continued Study of the Frictional and Cohesive-Like Behaviour of Floating Model Ice Rubble, IMD/NRC Report LM-1991-27, National Research Council of Canada, Institute for Marine Dynamics, St. John's, Newfoundland.

Chabot, L., 1985. ODECO Designs Massive Deepwater Rig, Oil and Gas J., June, pp. 59-63.

Chao, J.C., 1992. Comparison of Sheet Ice Load Prediction Methods and Experimental Data for Conical Structures, Proc. 11<sup>th</sup> Intl. Conf. on Offshore Mechanics and Arctic Engineering, Calgary, Vol. 4, pp 183-193.

Chao, J.C., 1993. An Analysis of Ice Rubble Shear Strength Data, Proc. 3<sup>rd</sup> Intl. Offshore and Polar Engineering Conf., Singapore, Vol. 2, pp. 607-612

Cheung, M.S., 1997. Instrumentation and Research Program on Confederation Bridge, Proc. 7<sup>th</sup> Intl. Offshore and Polar Engineering Conf., Hawaii, USA, pp. 10-16.

Chou, C.S., 1994. Studies of Granular Flows Down Inclined Bumpy Surfaces, J. of Wuhan University of Technology, Material Science Edition, Vol. 5, No. 2, pp.152-162.

- Clough, H.F., and Vinson, T.S., 1986. Ice Forces on Fixed Conical Structures, Proc. 5<sup>th</sup> Intl. Conf. on Offshore Mechanics and Arctic Engineering, Vol. 4, Tokyo, pp.507-514.
- Coulomb, C.A., 1773. *Essai sur une Application des Règles des Maximis et Minimis à Quelques Problèmes de Statique, Relatifs à L'Architecture, Mémoires de Mathematique et de Physique, à L'Academie Royale des Sciences*, Paris, Vol. 5, No. 7, pp. 343-382 (published in 1776).
- Croasdale, K.R., 1980. Ice Forces on Fixed, Rigid Structures, A State-of-the-Art Report by IAHR Working Group on Ice Forces on Structures, Edited by T. Carsten, CRREL Special Report 80-26, U.S. Army CRREL, Hanover, N.H., pp. 34-106.
- Croasdale, K.R., Cammaert, A.B., and Metge, M., 1994. A Method for the Calculation of Sheet Ice Loads on Sloping Structures, Proc. 12<sup>th</sup> International Symposium on Ice, IAHR, Trondheim, Norway, Vol. 2, pp. 874-885.
- Croasdale, K.R., and Muggeridge, D.B., 1993. A Collaborative Research Program to Investigate Ice Loads on Multifaceted Conical Structures, Proc. 12<sup>th</sup> Intl. Conf. on Port and Ocean Engineering under Arctic Conditions, Vol. 2, Hamburg, pp. 475-486.
- Danys, J. V., and Bercha, F.G., 1975. Determination of Ice Forces on Conical Offshore Structures, Proc. 3<sup>rd</sup> Intl. Conf. on Port and Ocean Engineering under Arctic Conditions, Vol. 2, Fairbanks, pp. 741-752.
- De Wet, 1961. The Use of the Energy Concept in Soil Mechanics, Proc. 5<sup>th</sup> Intl. Conf. on Soil Mechanics and Foundation Engineering, ICSMFE, Paris, Vol. 1, pp. 403-406.
- Delanges, P., 1788. *Statica e Macinica de Semi-Fluidi*, Mem. de Mat. e Fis. della Soc.

Italiana, 4 (cf. Feld, 1948)

- Derradji-Aouat, A., 1994. Ice Loads on Conical Piers - A Finite Element Investigation, *Intl. J. of Offshore and Polar Engineering*, Vol. 4, No. 1. ISOPE, pp. 53-61.
- Desai, C.S., and Siriwardane, H.J., 1984. Constitutive Laws for Engineering Materials - with Emphasis on Geologic Materials, Englewood Cliffs/N.J., Prentice-Hall, N.J.
- Drucker, D.C., and Prager, W., 1952. Soil Mechanics and Plastic Analysis or Limit Design, *Quarterly of Applied Mathematics*, Vol. 10, pp. 157-165.
- Edwards, R.Y., and Croasdale, K.R., 1976. Model Experiments to Determine Ice Forces on Conical Structures, *Proc. Applied Glaciology Symp.*, Cambridge, U.K.; *J. of Glaciology*, Vol. 19, No. 81, p. 660.
- Edwards, R.Y., Wallace, W.G., and Abdelnour, R., 1975. Model Experiments to Determine the Forces Exerted on Structures by Moving Ice Field (Comparison with the Small Prototype Cone Results), *APOA Project Report APOA 077-01*, Prepared for Arctic Petroleum Operators Association by Arctec Canada Limited, Montreal, P.Q., 51p.
- Ettema, R., Sharifi, M.B., Georgakakos, K.P., and Stern, F., 1991. Chaos in Continuous-Mode Icebreaking, *Cold Regions Science and Technology*, Vol. 19, No. 2, pp. 131-144.
- Ettema, R., and Urroz-Aguirre, G.E., 1989. On Internal Friction and Cohesion in Unconsolidated Ice Rubble, *Cold Regions Science and Technology*, Vol. 16, No. 3, pp. 237-248.
- Ettema, R., and Urroz-Aguirre, G.E., 1991. Friction and Cohesion in Ice Rubble Reviewed.

- Proc. 6<sup>th</sup> Int. Specialty Conf. on Cold Regions Engineering, CRREL, U.S. Army Corps of Engineers, pp. 316-325, Hanover, N.H., U.S.A.
- Evgin, E., and Sun, L.B., 1989. Review of Analytical Modelling of Ice Cover Evolution: Final Report, Dept. of Civil Engineering, University of Ottawa, Ottawa, 185p.
- Evgin, E., Zhan, C., and Timco, G.W., 1993. Distinct Element Modelling of Seabed Ice Rubble Interaction, Proc. 4<sup>th</sup> Canadian Conference on Marine Geotechnical Engineering, Vol. 3, St. John's, Newfoundland, pp. 1164-1180.
- Feda, J., 1982. Mechanics of Particulate Materials - The Principles, Elsevier Scientific Pub. Co., New York.
- Feda, J., Boháć, J., and Herle, I., 1995. K<sub>o</sub>-Compression of Reconstituted Loess and Sand with Stress Perturbation, Soils and Foundations, Japan Geotechnical Society, Vol. 35, No. 3, pp. 97-104.
- Feld, J., 1948. Early History and Bibliography of Soil Mechanics, Proc. 2<sup>nd</sup> Intl. Conf. on Soil Mechanics and Foundation Engineering, ICOSMFE, Rotterdam, Vol. 1, pp. 1-7.
- Fellenius, W., 1936. Calculation of the Stability of Earth Dams, Transactions of the 2<sup>nd</sup> Congress on Large Dams, Washington, D.C., Vol. 4, pp. 445-462.
- Finn, D., 1991 Vertical and Inclined Edge-indentation of Freshwater Ice Sheets, M.Eng. Thesis, Memorial University of Newfoundland, St. John's, NF, 97p.
- Fisher, R.A., and Yates, F., 1970. Statistical Tables for Biological, Agricultural and Medical Research, 6<sup>th</sup> Ed., Hafner Publishing Company, Darien, Conn.
- Fransson, L., and Sandkvist, J., 1985. Brash Ice Shear Properties -- Laboratory Tests, Proc.

- 8<sup>th</sup> Intl. Conf. on Port and Ocean Engineering under Arctic Conditions, Vol. 1, Narssarssuaq, Greenland, pp. 75-87.
- Frederking, R.M.W., Sayed, M., Hodgson, T., and Berthelet, W., 1985. Ice Force Results from the Modified Yamamichi Bend Lightpier, Winter 1983-84, Proc. Can. Coastal Conf., St. John's, pp. 319-331.
- Frederking, R.M.W., Sayed, M., and Penney, G., 1992. Ice Forces on Light Piers in St. Lawrence Seaway. International Journal of Offshore and Polar Engineering, ISOPE, Vol. 2, San Francisco, No. 1, pp. 67-72.
- Frederking, R.M.W., and Timco, G.W., 1985. Quantitative Analysis of Ice Sheet Failure Against an Inclined Plane. Proc. 4<sup>th</sup> Intl. Conf. on Offshore Mechanics and Arctic Engineering, Vol. 2, Dallas, pp. 160-169.
- Fukagawa, R., and Ohta, H., 1988. Effect of Some Factors on  $K_o$ -Value of a Sand. Soils and Foundations, Vol. 28, No. 4, pp. 93-106.
- Gale, A.D., Sego, D.C., and Morgenstern, N.R., 1985. Geotechnical Properties of Ice Rubble, Report I, Report submitted to the Natural Sciences and Engineering Research Council.
- Goddard, J.D., 1992. New Theoretical Estimates for Dilatancy in Granular Materials, In Theoretical and Applied Rheology, Proc. 11<sup>th</sup> Intl. Congr. of Rheology, Edited by P. Moldenaers and R. Keuning, Elsevier, Amsterdam.
- Goddard, J.D., and Bashir, Y.M., 1990. On Reynolds Dilatancy, In Recent Developments in Structured Continua, Vol. 2, Edited by D. De Kee and P. N. Kaloni, Longman

- Scientific and Technical, London, pp. 23-35.
- Haynes, F.D., Sodhi, D.S., Kato, K., Hirayama, K., 1983. Ice Forces on Model Bridge Piers, CRREL Report 83-19, U.S. Army CRREL, Hanover, N.H..
- Hellman, J.H., 1984. Basic Investigations of Mush Ice, Proc. 7<sup>th</sup> IAHR Ice Symp., Hamburg, Vol. 3, pp. 37-55.
- Hetenyi, M., 1946. Beam on Elastic Foundations, University of Michigan Studies, Scientific Series, Vol. XVI, The University of Michigan Press.
- Hill, R., 1950. The Mathematical Theory of Plasticity, Oxford University Press, London, England.
- Hirayama, K., and Akamatsu, H., 1982. Experimental Study of Ice Forces on Conical Structures. Technical Report: 21-45, IWATE University, Morioka, Japan.
- Hirayama, K., and Obara, I., 1986. Ice Forces on Inclined Structures, Proc. 5<sup>th</sup> Intl. Conf. on Offshore Mechanics and Arctic Engineering, Vol. 4, Tokyo, pp. 515-520.
- Hocking, G., Mustoe, G.G.W., and Williams, J.R., 1985a. Influence of Artificial Island Side-Slopes on Ice Ride-Up and Pile-Up, Proc. ARCTIC '85 Conf., ASCE, San Francisco, pp. 185-192.
- Hocking, G., Mustoe, G.G.W., and Williams, J.R., 1985b. Dynamic Global Forces on an Offshore Structure from Multi-Year Ice Floe Impact, Proc. ARCTIC '85 Conf., ASCE, San Francisco, pp. 202-210.
- Hocking, G., Mustoe, G.G.W., and Williams, J.R., 1985c. Validation of the CICE Code for Ice Ride-Up and Ice Ridge Cone Interaction, Proc. ARCTIC '85 Conf., ASCE, San

- Francisco, pp. 962-970.
- Hoek, E. and Bray, J., 1981. Rock Slope Engineering, The Institution of Mining and Metallurgy, London.
- Hoikkanen, J., 1985. Measurements and Analysis of Ice Force Against a Conical Structure, Proc. 8<sup>th</sup> Intl. Conf. on Port and Ocean Engineering under Arctic Conditions, Vol. 3, Narssarssuaq, Greenland, pp. 1203-1220.
- Holtz, W.G., and Gibbs, H.J., 1956. Shear Strength of Previous Gravelly Soils, Proc. ASCE, Vol. 82, Paper No. 867.
- Hopkins, M.A., 1992. Numerical Simulation of Systems of Multitudinous Polygonal Blocks, U.S. Army CRREL Report 92-22, U.S. Army Cold Regions Research and Engineering Laboratory (CRREL), Hanover, NH, 74p.
- Hopkins, M.A., 1995. Numerical Simulation of Arctic Pressure Ridging, Proc. Sea Ice Mechanics and Arctic Modeling Workshop, Vol.1, Anchorage, AK, pp.199-208.
- Hopkins, M.A., and Hibler, W.D., III, 1991. On the Shear Strength of Geophysical Scale Ice Rubble, Cold Regions Science and Technology, Vol. 19, No. 2, pp. 201-212
- Houlby, G.T., 1991. How the Dilatancy of Soils Affects Their Behavior, Proc. 10<sup>th</sup> European Conf. on Soil Mechanics and Foundation Engineering, Florence, Italy, Vol. 4, pp. 1189-1202.
- Howard, D., and Abdelnour, R., 1987. The Testing of the 1:8 Scale Model of the R-Class in Level Ice, Transportation Development Centre Report TP8828E, submitted by Artec Newfoundland Limited, Transportation Development Centre, Quebec.

- Huang, Y.H., 1983. Stability Analysis of Earth Slopes, Van Nostrand Reinhold Company Inc., New York, N.Y.
- Intera Technologies, Inc., 1986a. Quantification of First-Year and Multi-Year Ice Ridge Properties, Final Report for Alaskan Oil and Gas Association Joint Industry Study, AOGA #305, Lakewood, Colorado.
- Intera Technologies, Inc., 1986b. Ice Sheet Ridging Loads for Limit Force Design, Final Report for Alaskan Oil and Gas Association Joint Industry Study, Lakewood, Colorado.
- Intera Technologies, Inc., 1986c. DECICE Theoretical Manual, Lakewood, Colorado.
- Irani, M.B., and Timco, G.W., 1993. Ice Loading on a Multifaceted Conical Structure, Proc. 3<sup>rd</sup> Intl. Offshore and Polar Engineering Conf., Singapore, Vol. 2, pp. 520-558.
- Irani, M.B., Timco, G.W., and Muggeridge, D.B., 1992. Ice Loading on a Multifaceted Conical Structure, Technical Report IME-CRE-TR-005, National Research Council of Canada, Institute for Mechanical Engineering, Cold Regions Engineering, Ottawa, Ontario.
- Izumiya, K., Irani, M.B., and Timco, G.W., 1993. Computation of Sheet Ice Forces on a Faceted Conical Structure, Proc. 12<sup>th</sup> Intl. Conf. on Port and Ocean Engineering under Arctic Conditions, Vol. 2, Hamburg, pp. 517-526.
- Izumiya, K., Irani, M.B., and Timco, G.W., 1994. Influence of a Rubble Field in Front of a Conical Structure, Proc. 4<sup>th</sup> Intl. Offshore and Polar Engineering Conf., Osaka, Vol. 2, pp. 553-558.

- Izumiya, K., Kitagawa, H., Koyama, K., and Uto, S., 1991. On the Interaction Between a Conical Structure and Ice Sheet, Proc. 11<sup>th</sup> Intl. Conf. on Port and Ocean Engineering under Arctic Conditions, Vol. 1, St. John's, pp. 155-166.
- Jáky, J., 1944. The Coefficient of Earth Pressure at Rest, J. of the Society of Hungarian Architects and Engineers, Vol. 78, No. 22, pp. 355-358.
- Jáky, J., 1948. Pressure in Silo, Proc. 2<sup>nd</sup> Int. Conf. on Soil Mechanics and Foundation Engineering I, Rotterdam.
- James, R.G., and Bransby, P.L., 1971. A Velocity Field for Some Passive Earth Pressure Problems, Geotechnique, London, England, Vol. 21, No. 1, pp. 61-84.
- Jan, C.D., Shen, H.W., Lang, C.H. and Chen, C.L., 1992. Sphere Moving Down an Inclined Bumpy Surface, Proc. 9<sup>th</sup> Conf. on Engineering Mechanics, ASCE, New York, pp. 768-771.
- Janbu, N., 1973. Slope Stability Computation, Embankment-Dam Engineering, Casagrande Volume, Edited by R.C. Hirschfeld and S.J. Poulos, John Wiley and Sons, New York, pp. 47-86.
- Jebaraj, C., Swamidas, A.S.J., Shih, L.Y., and Munaswamy, K., 1992. Finite Element Analysis of Ship/Ice Interaction, Computers and Structures, Vol. 43, No. 2, pp. 205-221.
- Jones, S.J., 1993. Ice Tank Test Procedures at the Institute for Marine Dynamics, Institute for Marine Dynamics Report LM-AVR-20, National Research Council of Canada, Institute for Marine Dynamics, St. John's, Newfoundland.

- Jumikis, A.R., 1962. Soil Mechanics, University Series in Civil Engineering and Applied Mechanics, Edited by S.F. Borg, D. Van Nostrand Company, Inc., Princeton, New Jersey.
- Jürgenson, L., 1934. The Application of Theories of Elasticity and Plasticity to Foundation Problem, in p. 184 of Contribution to Soil Mechanics, 1925-1940, J. Boston Soc. Civil Engineers, BSCE, (published in 1940).
- Kato, K., 1986. Experimental Studies of Ice Forces on Conical Structures, Proc. 8<sup>th</sup> IAHR Ice Symp., Vol. 1, Iowa City, pp. 185-196.
- Katsuragi, K., Ochi, M., Seto, H., and Kawasaki, T., 1997. Distinct Element Simulation of Ice Sheet Failure Against Offshore Structures, Proc. 7<sup>th</sup> Intl. Offshore and Polar Engineering Conf., ISOPE, Hawaii, USA, pp. 356-359.
- Keinonen, A., 1983. Major Scaling Problems with Ice Model Testing of Ships, Proc. 20th American Towing Tank Conf., Davidson Laboratory, Stevens Institute of Technology, Hoboken, N.J., Vol. 2, pp. 595-612.
- Keinonen, A.J., Browne, R., and Reynolds, A., 1993. Model/Full Scale Ice Analysis -- Volume I, Transportation Development Centre Report TP11545E, Transport Canada, Prepared by Arno Keinonen Arctic Consulting Inc., 137p.
- Keinonen, A., and Nyman, T., 1978. An Experimental Model-Scale Study on the Compressible, Frictional and Cohesive Behaviour of Broken Ice Mass, Proc. 5<sup>th</sup> IAHR Ice Symp., Lulea, Part 2, pp. 335-353.
- Lambe, T.W., and Whitman, R.V., 1979. Soil Mechanics SI Version, MIT, John Wiley &

- Sons, New York.
- Lau, M., 1994a. A Three Dimensional 'DECICE' Simulation of Ice Sheet Impacting a 60-Degree Conical Structure, NRC/IMD Report CR-1994-16, National Research Council of Canada, Institute for Marine Dynamics, St. John's, Newfoundland.
- Lau, M., 1994b. Pack Ice Jamming Simulation: DECICE2D, Contract Report to NRC/IMD, National Research Council of Canada, Institute for Marine Dynamics, St. John's, Newfoundland.
- Lau, M., Jones, S.J., Tucker, J.R., and Muggeridge, D.B., 1993a. Model Ice Ridge Forces on a Multi-Faceted Cone, Proc. 12<sup>th</sup> Intl. Conf. on Port and Ocean Engineering under Arctic Conditions, Vol. 2, Hamburg, pp. 537-546.
- Lau, M., Muggeridge, D.B., and Williams, F.M., 1988. Model Tests of Fixed and Free Floating Downward Breaking Cones in Ice, Proc. 7<sup>th</sup> Intl. Conf. on Offshore Mechanics and Arctic Engineering, Houston, pp. 239-247.
- Lau, M., Tucker, J.R., Jones, S.J., and Muggeridge, D.B., 1993b. Model Ice Forces on an Upward Breaking Multi-Faceted Cone, NRC/IMD Report TR-1993-07, National Research Council of Canada, Institute for Marine Dynamics, St. John's, Newfoundland.
- Lau, M., and Williams, F.M., 1991. Model Ice Forces on a Downward Breaking Cone, Proc. 11<sup>th</sup> Intl. Conf. on Port and Ocean Engineering under Arctic Conditions, Vol. 1, St. John's, pp. 167-184.
- Linoya, K., Gotoh, K., and Higashitani, K., 1990. Power Technology Handbook; Marcel

Dekker Inc., New York.

- Liu, C., and Evett, J.B., 1987. Soils and Foundations, 2<sup>nd</sup> Edition, Prentice-Hall, Inc., Englewood Cliffs, N.J.
- Løset, S., 1994a. Discrete element modelling of a broken ice field - Part II: simulation of ice loads on a boom, *Cold Regions Science and Technology*, Vol.22, No.4, pp. 349-360.
- Løset, S., 1994b. Discrete Element Modelling of A Broken Ice Field - Part I: Model Development, *Cold Regions Science and Technology*, Vol.22, No.4, pp. 339-347.
- Løset, S., and Sayed, M., 1993. Proportional Strain Tests of Freshwater Ice Rubble, *J. of Cold Regions Engineering*, Vol. 7, No. 2, pp. 44-61
- Maattanen, M., 1986. Ice Sheet Failure Against an Inclined Wall, Proc. 8<sup>th</sup> IAHR Ice Symp., Vol. 1, Iowa City, pp. 149-158.
- Maattanen, M., 1994. Ice Force Design and Measurement of a Conical Structure, Proc. 12th IAHR Ice Symposium, Trondheim, pp. 401-410.
- Maattanen, M., and Hoikkanen, J., 1990. The Effect of Ice Pile-Up on the Ice Force of a Conical Structure, Proc. 10<sup>th</sup> Intl. Symp. on Ice, Vol. 2, Espoo, Finland, pp. 1010-1021.
- Maattanen, M., and Mustamaki, E.O., 1985. Ice Forces Exerted on a Conical Structure on the Gulf of Bothnia, Proc. 17th Offshore Technology Conference, Vol. 4, Paper No. 5054, Houston, pp. 313-320.
- Macmillan, N.N., 1972. Review: The Theoretical Strength of Solids, *J. of Material Science*, Vol. 7, No. 2, pp. 239-254.

- Manders, C., and Abdelnour, R., 1978. A Series of Model Tests of Down Breaking Cones in Level and Multi-Year Ridged Ice Fields, Arctec Canada Limited, Report submitted to Gulf Oil Canada.
- Marcellus, R.W., Morrison, T.B., Allyn, N.F.B., Croasdale, K.R., Iyer, H.S., and Tseng, J., 1988. Ice Forces on Marine Structures: Volume 2 -- Discussion, Department of Public Works Canada Report AES/SAG 1-2:88-5v2, Public Works Canada, Ottawa, ON, submitted by C.M.E.L. Enterprises Ltd.
- Matsu, M., Kenmochi, S., and Yagi, H., 1978. Experimental Study on Earth Pressure of Retaining Wall by Field Tests, Soil and Foundations, Vol. 18, No. 3, pp. 27-41.
- Matsuoka, H., and Sakakibara, K., 1987. A Constitutive Model for Sands and Clays Evaluating Principal Stress Rotation, Soils and Foundations, Vol. 27, No. 4, pp. 73-88.
- Mayne, P.W., and Kulhawy, F.H., 1982.  $K_0$ -OCR Relationships in Soil. J. of the Geotechnical Engineering Division, ASCE, Vol. 108, No. GT6, June, pp. 851-872.
- McKenna, R.F., and Bruneau, S.E., 1997. Ice Rubble Build-Up on Conical Structures During Ridge Interactions, Proc. 16<sup>th</sup> Intl. Conf. on Offshore Mechanics and Arctic Engineering, Vol. 4, Yokohama, Japan, p. 355-364.
- McKenna, R.F., Walker, D., Lau, M., and Daley, C., 1997. Ice Loads on CALM Buoy at Butinge Oil Terminal, Contract Report Prepared for SOFEC, Inc., by the Center for Cold Oceans Resources and Engineering and Marineering Ltd., St. John's, Newfoundland.

- Melkote, R.S., 1977. Design Pressures for Retaining Walls with Triangular Fills, Proc. 3<sup>rd</sup> Intl. Symp. on Soil Structure Interaction, Vol. 2, U. of Roorkee, India, pp. 31-35.
- Mesri, G., and Hayat, T.M., 1993. The Coefficient of Earth Pressure at Rest, Can. Geotech. J., Vol. 30, No. 4, pp. 647-666.
- Metge, M., and Tucker, J.R., 1990. Multifaceted Cone Tests -- Year Two, 1989-1990, Technical Report, Esso Resources Canada Limited, Calgary, Alberta.
- Metge, M., and Weiss, R.T., 1989. Multifaceted Cone Tests 1988-1989, Technical Report, Esso Resources Canada Limited, Calgary, Alberta.
- Michel, B., 1978, Ice Mechanics, Les Presses de l'Universite' Laval, Quebec.
- Michel, B., and Picard, F., 1989. Major Differences in the Failure Modes of an Ice Sheet on an Inclined Plane: Laboratory Tests, Proc. 10<sup>th</sup> Intl. Conf. on Port and Ocean Engineering under Arctic Conditions, Vol. 1, Lulea, pp. 235-248.
- Mitchell, J.K., 1976. Fundamentals of Soil Behavior, John Wiley and Sons, New York.
- Mohr, O., 1882. Ueber die Darstellung des Spannungszustandes und des Deformationszustandes eines Körperelementes und über die Anwendung derselben in der Festigkeitslehre, Civilingenieur, Vol. 28, pp. 113-156
- Morgenstern, N., and Price, V.E., 1965. The Analysis of the Stability of General Slip Surfaces, Geotechnique, Vol. 15, No. 1, pp. 79-93.
- Myslivec, A., 1972. Pressure at Rest of Cohesive Soil, in Structures Subjected to Lateral Forces, Proc. 5<sup>th</sup> European Conf. on Soil Mechanics and Foundation Engineering, Madrid.

- Natural Resources Canada, 1993. Canada's Energy Outlook, 1992-2020: Working Paper, Prepared by Energy and Fiscal Analysis Division, Economic and Financial Analysis Branch, Energy Sector, Ottawa, 96p.
- Nevel, D.E., 1965. A Semi-Infinite Plate on an Elastic Foundation, CRREL Research Report No. 136, U.S. Army CRREL, Hanover, NH.
- Nevel, D.E., 1972. The Ultimate Failure of a Floating Ice Sheet, Proc 2<sup>nd</sup> IAHR Ice Symp., Part I, Leningrad, U.S.S.R., pp. 23-27.
- Nevel, D.E., 1980. Bending and Buckling of a Wedge on an Elastic Foundation, Proc. IUTAM Symp. on Physics and Mechanics of Ice, Copenhagen, Edited by P. Tryde, Springer-Verlag, Berlin, pp.278-288.
- Nevel, D.E., 1992. Ice Forces on Cones from Floes, Proc. 11<sup>th</sup> IAHR Ice Symp., Vol. 3. Banff, pp. 1391-1401.
- Nova, R., and Sacchi, G., 1979. A Generalized Failure Condition for Orthotropic Solids, Proc. Euromech Colloquium 115, Villard-de-Lans, pp. 623-641.
- Oshima, M., Narita, H., Yashima, N., and Tabuchi, H., 1980. Model and Field Experiments for Development of ACE Resistant Offshore Structures, Proc. 12th Offshore Technology Conference, Vol. 4, Paper No. 3885, Houston, pp. 307-314.
- Packshaw, S., 1969. Earth Pressure and Earth Resistance, A Century of Soil Mechanics, The Institution of Engineers, London, England, pp. 409-434.
- Patton, F.D., 1966. Multiple Modes of Shear Failure in Rock and Related Materials, Ph.D. Thesis, University of Illinois, Illinois.

- Pearce, J.C., and Strickland, G.E., 1979. Ice Forces on Conical Structures, Proc. 11<sup>th</sup> Offshore Technology Conf., Vol. 4, Paper No. 3635, Houston, pp. 2407-2414.
- Poncelet, J.V., 1840. Memoire Sur la Stabilite des Revetments et de Leurs Fondation, Note Additionnelle Sur les Relations Analytiques Qui Lient Entre Elles la Poussee et la Butee de la Terre, Memorial de L'Officier du Genie, Paris, Vol. 13.
- Pouliquen, O., and Renaut, N., 1996. Onset of Granular Flows on an Inclined Rough Surface: Dilatancy Effect, J. de Physique, II, Vol. 6, No. 6, pp. 923-935.
- Prodanovic, A., 1979. Model Tests of Ice Rubble Strength, Proc. 5<sup>th</sup> Intl. Conf. on Port and Ocean Engineering under Arctic Conditions, Vol. 1, Trondheim, pp.667-678.
- Pruška, L., 1972. Basic Equations of Pressure at Rest of Granular Materials, in Structures Subjected to Lateral Forces, Proc. 5<sup>th</sup> European Conf. on Soil Mechanics and Foundation Engineering, Madrid.
- Ralston, T.D., 1977. Ice Force Design Considerations for Conical Structures, Proc. 4<sup>th</sup> Intl. Conf. on Port and Ocean Engineering under Arctic Conditions, Vol. 2, St John's, pp. 741-752.
- Rankine, W.J. M., 1858. A Manual of Applied Mechanics, Griffin, London.
- Reimbert, M.L., and Reimbert, A.M., 1974. Retaining Walls, Anchorage and Sheet Piling -- Theory and Practice -- Volume I, Tran Tech Publications, Clausthal, Germany.
- Reynolds, O., 1885. On the Dilation of Media Composed of Rigid Particles in Contact, with Experimental Illustrations, Philos. Mag., Vol. 20, pp. 469-481.
- Rowe, P.W., 1962. The Stress-Dilatancy Relation for Static Equilibrium of an Assembly of

- Particles in Contact, Proc. Royal Society, A269, pp. 500-527.
- Rymsza, B., 1979. Earth Pressure At Rest in Design of Retaining Structure, Proc. 7<sup>th</sup> European Conf. on Soil Mechanics and Foundation Engineering, Vol. I, Brighton.
- Saada, A.S., Bianchini, G.F., and Puccini, P., 1983. The Mechanical Properties of Anisotropic Granular Soils, Colloque Intl. du C. N. R. S. No. 351, Villard, Villard-de-Lans.
- Sanderson, T.J.O., 1988. Ice Mechanics, Risks to Offshore Structures, Graham Trotman, London.
- Savage, S.B., and Nohguchi, Y., 1988. Similarity Solutions for Avalanches of Granular Materials Down Curved Beds, ATCA Mechanica, Vol. 75, pp. 153-174.
- Sayed, M., 1987. Mechanical Properties of Model Ice Rubble, In Material and Member Behaviour, Proc. Structures Congress '87, Orlando, FL, American Society of Civil Engineers, New York, pp. 647-659.
- Sayed, M., 1995. Numerical Simulation of the Interaction Between Ice Ridges and Bridge Piers, Technical Report TR-1995-10, National Research Council of Canada, Ottawa, Ontario.
- Sayed, M., 1997. Discrete and Lattice Models of Floating Ice Covers, Proc. 7<sup>th</sup> Intl. Offshore and Polar Engineering Conf., ISOPE, Hawaii, USA, pp. 428-433.
- Sayed, M., and Timco, G.W., 1998. A Lattice Model of Ice Failure, ERD/CHC Report 9-77, Technical Report HYD-TR-035, NRC, Ottawa.
- Sayed, M., Timco, G.W., and Sun, L., 1992. Testing Model Ice Rubble under Proportional

- Strains, Proc. 11<sup>th</sup> Intl. Conf. on Offshore Mechanics and Arctic Engineering, Vol. 4, Calgary, pp. 335-341.
- Schanz, T., and Vermeer, P.A., 1996. Angles of Friction and Dilatancy of Sand, Geotechnique, Vol. 46, No. 1, pp. 145-151.
- Seed, H.B., and Sultan, H.A., 1967. Stability Analysis for a Sloping Core Embankment, J. of the Soil Mechanics and Foundations Division, ASCE, Vol. 93, No. SM4, pp. 69-84.
- Sepehr, K., Selvadurai, A.P.S., and Comfort, G., 1997. Discrete Element Modelling of the Local Interaction Between a Stationary Structure and a Moving Ice Pack, Proc. 7<sup>th</sup> Intl. Offshore and Polar Engineering Conf., ISOPE, Hawaii, USA, pp. 480-486.
- Shields, D.H., and Tolunay, A.Z., 1973. Passive Pressure by Method of Slices, J. of the Soil Mechanics and Foundations Division, ASCE, Vol. 99, No. SM12, pp. 1043-1053.
- Simons, N., 1958. Contribution to discussion, Proc. Brussels Conf. on Earth Pressure Problem, Vol. 3, pp. 50-53.
- Sodhi, D.S., 1987. Flexural and Buckling Failure of Floating Ice Sheets Against Structures. 3<sup>rd</sup> State-of-the-Art Report, IAHR Working Group on Ice Forces, Edited by T.J.O. Sanderson, CRREL Special Report 87-17, U.S. Army CRREL, Hanover, N.H., pp. 53-73
- Sodhi, D.S., Kato, K., and Haynes, F.D., 1982. Determining the Characteristic Length of Model Ice Sheets, Cold Regions Science and Technology, Vol. 6, No. 2, pp. 99-104.
- Sodhi, D.S., Morris, C.E., and Cox, G.F., 1985. Sheet Ice Forces on a Conical Structure - An

- Experimental Study, Proc. 8<sup>th</sup> Intl. Conf. on Port and Ocean Engineering under Arctic Conditions, Vol. 2, Narssarssuaq, pp. 643-655.
- Sorensen, C., 1978. Interaction Between Floating Ice Sheets and Sloping Structures, Series Paper 19, Technical University of Denmark, Institute of Hydrodynamics and Hydraulic Engineering, Denmark, 175p.
- Spencer, D., McKenna , R., and Lau, M., 1993. Ice Model Tests of a 60° Upward Breaking Bridge Pier for the Northumberland Strait Crossing, NRC/IMD Report TR-1993-05 (Protected), National Research Council of Canada, Institute for Marine Dynamics, St. John's, Newfoundland.
- Spencer, E., 1967. A Method of Analysis of the Stability of Embankments Assuming Parallel Inter-Slice Forces, Geotechnique, Vol. 17, No. 1, pp. 11-26.
- Szepesházi, R.. 1994. On the K<sub>o</sub> Factor, Periodica Polytechnica Ser. Civil Eng., Vol. 38, No. 1, pp. 127-135.
- Tatinclaux, J.C., 1986. Ice Floe Distribution in the Wake of a Simple Wedge, Proc. 5<sup>th</sup> Intl. Conf. on Offshore Mechanics and Arctic Engineering, Vol. 4, Tokyo, pp. 622-629.
- Terzaghi, K., 1955. The Influence of Geological Factors in the Engineering Properties of Sediments, Econ. Geol., 50<sup>th</sup> Ann. Vol., pp. 557-618.
- Terzaghi, K., and Peck, R.B., 1976. Soil Mechanics in Engineering Practice, Wiley, New York.
- Timco, G.W. 1984a. Ice Forces on Structures, Proc. 7<sup>th</sup> IAHR Ice Symp., Vol. 4, Hamburg, pp. 117-150.

- Timco, G.W. 1984b. Model Tests of Ice Forces on a Wide Inclined Structure, Proc. 7<sup>th</sup> IAHR Ice Symp., Vol. 2, Hamburg, pp. 89-96.
- Timco, G.W., 1986. EG/AD/S: A New Type of Model Ice for Refrigerated Towing Tanks, Cold Regions Science and Technology, Vol. 12, No. 2, pp. 175-195.
- Timco, G.W., Irani, M.B., English, L.A., Carroll, L.B., and Arambarri, E., 1993. Ice Loads Distribution on a Faceted Conical Structure, Proc. 12<sup>th</sup> Intl. Conf. on Port and Ocean Engineering under Arctic Conditions, Vol. 2, Hamburg, pp. 607-616.
- Tsai, S.W., and Wu, E.M., 1971. A General Theory of Strength for Anisotropic Materials, J. of Composite Materials, Vol. 5, pp. 58-80.
- Tschebotarioff, G.P., 1951. Soil Mechanics, Foundations, and Earth Structures, New York, McGraw-Hill.
- Urroz-Aguirre, G.E., and Ettema, R., 1987. Simple Shear Box Experiments with Floating Ice Rubble, Cold Regions Science and Technology, Vol. 14, No. 2, pp. 185-199.
- Valanto, P., 1989. Experimental Study of the Ice Breaking Cycle in 2-D, Proc. 8<sup>th</sup> Intl. Conf. on Offshore Mechanics and Arctic Engineering, Vol. 4, The Hague, pp. 343-349.
- Valanto, P., 1992. The Icebreaking Problem in Two Dimensions: Experiments and Theory, J. of Ship Research, Vol. 36, No. 4, pp. 229-316.
- Valanto, P., 1993. Investigation of Icebreaking Pattern at the Bow of The IB Kapitan Sorokin on the Yenisei River Estuary in May 1991, Proc. 12<sup>th</sup> Intl. Conf. on Offshore Mechanics and Arctic Engineering, Vol. 4, pp. 127-134.
- Varsta, P., 1983. On the Mechanics of Ice Load on Ships in Level Ice in the Baltic,

Technical Research Centre of Finland, Publication No. 11, Espoo.

- Verity, P.H., 1975. Small Prototype Cone Tests, Winter '73 - '74, APOA Project No. 65 Report, Imperial Oil Ltd., Distributed by Pallister Resource Management Ltd., Calgary, Alberta.
- Wang, F.D., Sun, M.C., and Ropchan, D.M., 1972. Computer Program for Pit Slope Stability Analysis by the Finite Element Stress Analysis and Limiting Equilibrium Method, RI 7685, Bureau of Mines.
- Wang, Z.G., Muggeridge, D.B., and Crosdale, K.R., 1997. Ridge Ice Loads On Proposed Faceted Conical Structure, Proc. 7<sup>th</sup> Intl. Offshore and Polar Engineering Conf., Vol. 2, Hawaii, USA, pp. 449-456.
- Weiss, R.T., Prodanovic, A., and Wood, K.N., 1981. Determination of Ice Rubble Shear Properties, Proc. Intl. Association for Hydraulics Research Ice Symp., Quebec City, pp. 861-872.
- Wessels, E., 1984. Model Test Investigation of Ice Forces on Fixed and Floating Conical Structures, Proc. 7<sup>th</sup> Ice Symp., IAHR, Vol. 3, Hamburg, pp. 203-220.
- Wessels, E., and Kato, K., 1989. Ice Forces on Fixed and Floating Conical Structures, IAHR Working Group on Ice Forces, 4<sup>th</sup> State-of-the-Art Report, CRREL Special Report 89-5, U.S. Army CRREL, Hanover, N.H., pp. 231-258.
- Wong, T.T., Gale, A.D., Sego, D.C., and Morgenstern, N.R., 1987. Shear Box Tests on Broken Ice, Proc. 9<sup>th</sup> Intl. Conf. on Port and Ocean Engineering under Arctic Conditions, Vol. 3, pp. 97-107.

- Wroth, C.P., 1972. General Theories of Earth Pressures and Deformations, Proc. 5<sup>th</sup> European Conf. on Soil Mechanics and Foundation Engineering, Vol. 2, Madrid, pp. 33-52.
- Wu, E.M., 1974. Phenomenological Anisotropic Failure Criterion, in Mechanics of Composite Materials, Edited by G.P. Sendeckyj, Academic Press, N.Y., Vol. 2, pp. 353-432.
- Zabilansky, L.J., Nevel, D.E., and Haynes, F.D., 1975. Ice Forces on Model Structures, Canadian J. of Civil Engineering, Vol. 2, pp. 400-417.

## **Appendix A**

### **Summary of Test Conditions, Configurations, and Results of ERCL's and IME's Test Series:**

#### **Level Ice**

The measured ice properties, configurations and results associated with each test for the individual test series in the "MUN/ERCL/NRC Multi-Faceted Cone Study" are extracted from respective data report and reproduced here for quick reference.

The measured ice properties along with the configuration of the test condition in each test for the two test series are given in Tables A1 and A2; whereas, the results of each test series are consolidated and summarized in Tables A3 and A4.

Tables A3 summarizes the mean, maximum, and peak values of the global and neck forces measured in the IME's level ice tests. The force statistics are computed only for the steady state portion of the force records. Table A4, on the other hand, gives only the maximum loads measured in the ERCL's level ice tests since most of the runs were stopped before a quasi-steady-state interaction was achieved.

Peak force analysis was not carried out on IME's tests; instead, the peak forces were calculated as suggested by Irani and Timco (1993) as the sum of the mean plus one and a half times the standard deviation of the force record. It should be noticed that after publishing their data report, Irani and Timco (1993) have since revised and published their global load measurements. The data given in Tables A3 are the revised values.

Table A1 Matrix for level ice tests: NRC-IME series

Test	Model Orient. (°)	V (cm/s)	t (cm)	LEVEL ICE PROPERTIES	
				$\sigma_{fu}$ (kPa)	$\sigma_{fd}$ (kPa)
C_001	15	2.6	2.6	46	73
C_002	15	9.8	2.3	46	73
C_003	15	4.8	2.3	46	73
C_004	15	2.2	3.3	104	166
C_005	15	3.8	3.7	104	166
C_006	15	6.2	3.7	104	166
C_007	15	2	2.4	24	29
C_008	15	4	2.3	24	29
C_009	15	6	2.2	24	29
C_010	15	2.2	4	58	67
C_011	15	4.1	3.8	58	67
C_012	15	6.1	4.1	58	67
C_013	15	2	1.7	42	67
C_014	15	4.3	1.6	42	67
C_015	15	6	1.8	42	67
C_016	0	6	3.4	96	72
C_017	0	6	2.4	73	122
C_018	0	6.1	2.1	37	59
C_019	0	6.2	2.3	13	21
C_020	0	5.9	5.7	23	37
C_021	0	5.8	5.7	11	17
C_022	0	5.9	3.4	84	134
C_023	0	6	3.3	29	47
C_024	0	5.8	3.4	16	25
C_025	0	6	4.5	78	125
C_026	0	6	4.6	64	102
C_027	0	6	4.7	51	82
C_028	0	5.7	4.4	63	81
C_029	0	5.7	4.2	28	45
C_030	0	5.7	4.5	16	26
C_031	30	5.7	2.4	22	56
C_032	30	5.7	2	9	27
C_033	30	5.7	1.8	3	17
C_034	30	5.7	3.5	71	112

Table A1 Matrix for level ice tests: NRC-IME series (continued)

Test	Model Orient. ( $^{\circ}$ )	V (cm/s)	LEVEL ICE PROPERTIES		
			t (cm)	$\sigma_{fu}$ (kPa)	$\sigma_{fd}$ (kPa)
C_035	30	5.7	3.4	64	44
C_036	30	5.8	3.4	13	25
C_037	30	6.2	5.6	41	60
C_038	30	5.9	5.6	40	40
C_039	30	6.2	4.9	39	44
C_040	30	6.2	5.1	30	15
C_041	30	5.9	5.4	14	12
C_042	0	6	3.3	40	41
C_043	15	6.1	3	40	41
C_044	30	6	3.3	40	41
C_050	0	6.2	2.8	11	21
C_054	0	6.1	4.2	40	80
C_055	0	5.8	3.6	27	76
C_056	0	5.9	3.5	24	49
C_057	0	5.9	3.6	10	25
C_060	0	6	3	9	36
C_061	15	5.9	3.1	9	36
C_062	30	6	3.1	9	36

Note:  $\sigma_{fu}$  = upward breaking flexural strength;  $\sigma_{fd}$  = downward breaking flexural strength  
Structure orientation:  $0^{\circ}$  = face-on;  $15^{\circ}$  = intermediate;  $30^{\circ}$  = edge-on  
A friction coefficient of 0 is associated with runs 1 to 38, and a friction coefficient of 0.1 is associated with runs 39 to 66.

Table A2 Matrix for level ice tests: ERCL series

Test	V (cm/s)	t (cm)	$\sigma_f$ (kPa)	E (MPa)
Year One: 1988-89; 1:10S				
T1_R1	6	33	165	1136
Year One: 1988-89; 1:10L				
T2_R2	6	34	183	836
T3_R2	6	27	249	1129
T4_R1	6	12	159	1590
Year Two: 1989-90; 1:20L				
T1_R1	6	25	50	203
T1_R2	6	25	50	203
T2_R1	6	32	35	288
T2_R2	6	36	141	1154
T3_R1	6	38.5	125	569
T3_R2	6	38.5	125	569
T4_R1	6	41	141	853
T4_R1	6	41	141	853
T5_R1	6	5	na	na
T5_R2	6	5	na	na

Table A.3

Summary of level ice test results: NRC-IME series (Irani and Timco, 1992; and Irani et al., 1992)

Test	GLOBAL * HORIZONTAL FORCE (kN)			GLOBAL * VERTICAL FORCE (kN)			NECK * HORIZONTAL FORCE (kN)		
	Mean	Max.	Peak	Mean	Max.	Peak	Mean	Max.	Peak
1	0.132	0.219	0.164	0.176	0.262	0.221	0.00	0.03	0.007
2	0.117	0.214	0.161	0.173	0.261	0.227	0.00	0.04	0.006
3	0.122	0.188	0.153	0.162	0.233	0.207	0.00	0.03	0.010
4	0.189	0.335	0.269	0.244	0.417	0.337	0.01	0.04	0.019
5	0.161	0.288	0.227	0.222	0.369	0.320	0.01	0.03	0.011
6	0.160	0.236	0.218	0.218	0.334	0.307	0.01	0.03	0.014
7	0.113	0.143	0.134	0.152	0.192	0.182	0.00	0.01	0.006
8	0.108	0.150	0.129	0.151	0.206	0.179	0.00	0.01	0.005
9	0.115	0.175	0.140	0.157	0.208	0.193	0.00	0.01	0.005
10	0.284	0.438	0.366	0.374	0.541	0.463	0.01	0.04	0.002
11	0.280	1.420	0.430	0.320	0.470	0.410	0.01	0.10	0.029
12	0.295	0.465	0.410	0.404	0.633	0.554	0.00	0.00	0.014
13	0.074	0.105	0.097	0.111	0.159	0.144	0.00	0.01	0.004
14	0.060	0.086	0.081	0.089	0.128	0.115	0.00	0.00	0.002
15	0.064	0.093	0.087	0.095	0.129	0.123	0.00	0.01	0.002
16	0.210	0.690	0.300	0.281	0.609	0.381	0.01	0.12	0.003
17	0.113	0.183	0.152	0.125	0.203	0.174	0.00	0.04	0.010
18	0.110	0.160	0.140	0.140	0.190	0.170	0.00	0.01	0.005
19	0.115	0.160	0.146	0.149	0.210	0.191	0.00	0.01	0.006
20	0.390	0.630	0.500	0.510	0.710	0.630	0.01	0.10	0.034
21	0.360	0.600	0.450	0.470	0.620	0.550	0.01	0.10	0.034
22	0.199	0.324	0.266	0.280	0.484	0.375	0.01	0.03	0.013
23	0.190	0.345	0.250	0.265	0.414	0.345	0.01	0.04	0.014
24	0.176	0.382	0.233	0.230	0.386	0.288	0.01	0.08	0.024
25	0.386	1.593	0.649	0.510	1.396	0.772	0.01	0.28	0.043
26	0.398	0.887	0.578	0.534	0.890	0.742	0.01	0.05	0.026
27	0.426	0.811	0.619	0.563	0.940	0.795	0.01	0.05	0.030
28	0.300	0.540	0.420	0.360	0.058	0.500	0.01	0.05	0.025
29	0.333	0.650	0.428	0.432	0.652	0.540	0.01	0.04	0.026
30	0.254	0.339	0.306	0.353	0.469	0.419	0.01	0.03	0.018
31	0.077	0.097	0.090	0.124	0.155	0.144	0.00	0.00	0.002

Table A.3

Summary of level ice test results: NRC-IME series (Irani and Timco, 1992; and Irani et al, 1992) (cont'd)

Test	GLOBAL * HORIZONTAL FORCE (kN)			GLOBAL * VERTICAL FORCE (kN)			NECK * HORIZONTAL FORCE (kN)		
	Mean	Max.	Peak	Mean	Max.	Peak	Mean	Max.	Peak
32	0.069	0.088	0.079	0.109	0.133	0.122	0.00	0.00	0.00
33	0.056	0.08	0.072	0.088	0.135	0.114	0.00	0.00	0.00
34	0.15	0.225	0.197	0.238	0.354	0.305	0.00	0.02	0.01
35	0.157	0.22	0.196	0.243	0.314	0.290	0.00	0.02	0.01
36	0.113	0.161	0.137	0.181	0.246	0.215	0.00	0.01	0.00
37	0.355	0.606	0.489	0.527	0.802	0.691	0.01	0.05	0.02
38	0.348	0.595	0.482	0.499	0.823	0.662	0.01	0.07	0.02
39	0.253	0.37	0.328	0.382	0.516	0.482	0.00	0.03	0.01
40	0.193	0.291	0.246	0.308	0.4	0.370	0.00	0.02	0.01
41	0.18	0.24	0.211	0.294	0.362	0.332	0.00	0.02	0.01
42	0.149	0.226	0.198	0.16	0.212	0.199	0.00	0.01	0.01
43	0.132	0.253	0.199	0.147	0.259	0.213	0.00	0.01	0.01
44	0.123	0.161	0.143	0.134	0.173	0.159	0.00	0.01	0.00
50	0.164	0.313	0.226	0.167	0.243	0.196	0.00	0.01	0.00
54	0.428	0.707	0.577	0.353	0.554	0.470	0.01	0.05	0.02
55	0.237	0.421	0.317	0.202	0.331	0.260	0.00	0.02	0.01
56	0.248	0.429	0.334	0.21	0.331	0.272	0.00	0.02	0.01
57	0.268	0.426	0.358	0.242	0.35	0.299	0.00	0.02	0.01
60	0.166	0.314	0.238	0.167	0.261	0.214	0.00	0.01	0.00
61	0.168	0.285	0.23	0.158	0.235	0.206	0.00	0.01	0.00
62	0.145	0.199	0.176	0.145	0.196	0.177	0.00	0.01	0.00

Note: Global forces are taken from Irani and Timco (1993). Neck forces are estimated from time-history given in Irani et al (1992).

\*Horizontal - (+) toward the model; Vertical - (+) downward

Table A4 Summary of level ice test results: ERCL series

	GLOBAL * HORIZONTAL FORCE (kN)	GLOBAL * VERTICAL FORCE (kN)	NECK * HORIZONTAL FORCE (kN)
Test	Max	Max	Max
Year One: 1988-89; 1:10			
T1_R1	40	48**	1.5
T2_R2	10	8	0.8
T3_R2	17	19	NA
T4_R1	12	15	0
Year Two: 1989-90; 1:20			
T1_R1	10	11	0.7
T1_R2	1.5	4	0.8
T2_R1	19	22	5
T2_R2	20	20	8
T3_R1	30	38	2.5
T4_R1	30	35	5
T5_R1	2	4	0

Note: \* Horizontal - (+) toward the model; Vertical - (+) downward

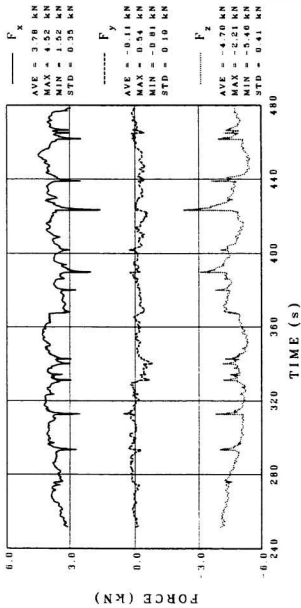
\*\*Typo error in original report

## **APPENDIX B**

**Load Time History of Tests Conducted in  
IMD's Test Series**

## FORCE ON STRUCTURE IN X, Y, Z DIRECTIONS

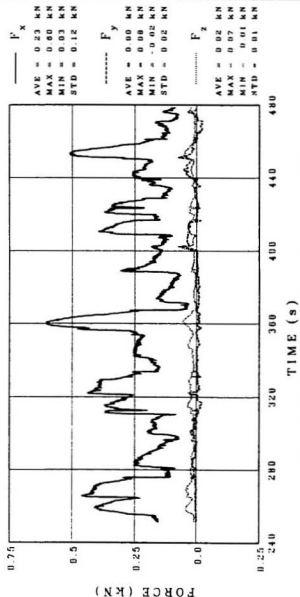
MUNLINE 3\_001



NECK SIZE -- SMALL	ICE THICKNESS = 15.8 cm	NO RIDGE
FRICTION -- 0.11	FLEX STR (down) = 916 kN/cm <sup>-3</sup>	STEADY STATE PORTION ONLY
DIRECTION -- BROAD ON	FLEX STR (up) = 79.8 kPa	
SPEED = 1. um/s	FLEX STR (up) = 44.4 kPa	

**MULTIFACETED CONE TESTS       $\lambda = 25.00$ , NRC/IMD**

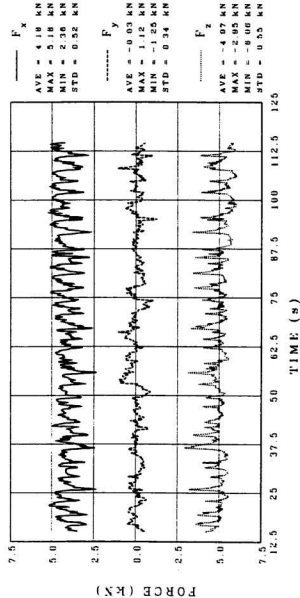
FORCE ON NECK IN X, Y, Z DIRECTIONS      MUNICONE 3\_001



NECK SIZE -- SMALL	ICE THICKNESS = 15.0 cm	NO RIDGE
FRICTION -- 0.11	ICE DENSITY = 916. kg/m <sup>3</sup>	STEADY STATE PORTION ONLY
DIRECTION -- BROAD ON	FLEX STR (down) = 70.6 kPa	
SPEED = 1. cm/s	FLEX STR (up) = 44.4 kPa	

MULTIFACETED CONE TESTS       $\lambda = 25.00$ , NRC / IMD

## FORCE ON STRUCTURE IN X, Y, Z DIRECTIONS MUNCONE3\_002



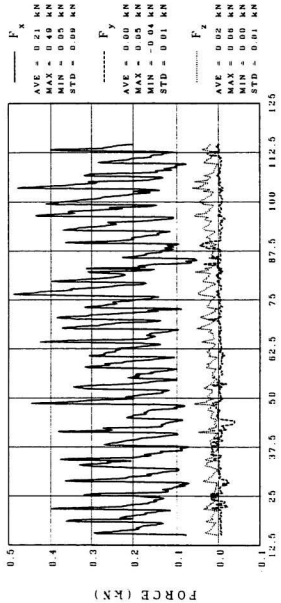
NECK SIZE = SMALL  
FRICTION = 0.11  
DIRECTION = BROAD ON  
SPEED = 0. cm/s

ICE THICKNESS = 15.0 cm  
ICE DENSITY = 916. kg/m<sup>3</sup>  
FLEX STR (down) = 70.4 kPa  
FLEX STR (up) = 44.1 kPa

NO RIDGE  
STEADY STATE PORTION ONLY

MULTIFACETED CONE TESTS  $\lambda = 25.00$ , NRC / IMD

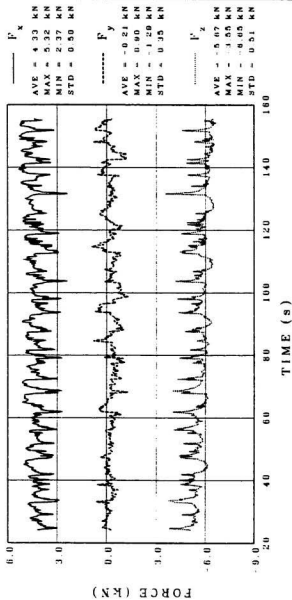
FORCE ON NECK IN X, Y, Z DIRECTIONS      MUNCONE 3\_002



NECK SIZE = SMALL	ICE THICKNESS = 15.6 cm	NO RIDGE STEADY STATE PORTION ONLY
FRACTION = 0.11	ICE DENSITY = 916 kg/m <sup>3</sup>	
DIRECTION = BROAD ON	FLEX STR (down) = 78.4 kPa	
SPEED = 0.0 m/s	FLEX STR (up) = 44.1 kPa	

MULTIFACETED CONE TESTS       $\lambda = 25.00$ , NRC/IMD

## FORCE ON STRUCTURE IN X, Y, Z DIRECTIONS MUNCONE 3\_003



NECK SIZE = SMALL  
 FRICTION = 0.11  
 DIRECTION -- BROAD ON  
 SPEED = 4. cm/s

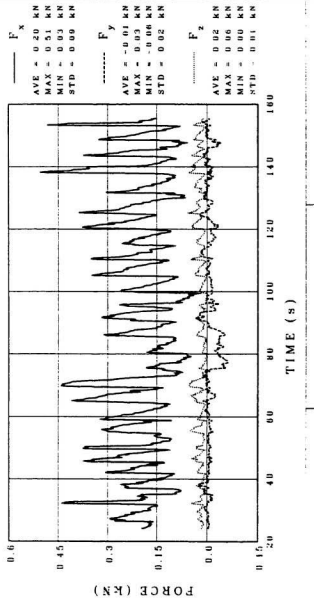
ICE THICKNESS = 15.0 cm  
 ICE DENSITY = 916. kg/m<sup>3</sup>  
 FLEX STR (down) = 78.7 kPa  
 FLEX STR (up) = 43.6 kPa

NO RIDGE  
 STEADY STATE PORTION ONLY

MULTIFACETED CONE TESTS       $\lambda = 25.00$ , NRC / IMD

## FORCE ON NECK IN X, Y, Z DIRECTIONS

MUNICINF 3\_003



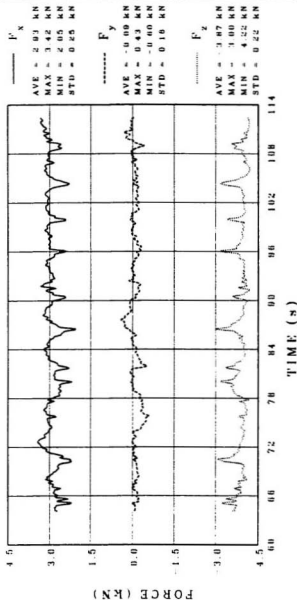
NECK SIZE = SMALL	ICE THICKNESS = 15.8 cm
FRICTION = 0.11	ICE DENSITY = 916 kg/m <sup>3</sup>
DIRECTION = BROAD ON	PLEX STR (down) = 78.7 kPa
SPEED = 4 cm/s	PLEX STR (up) = 43.6 kPa

NO RIDGE  
STEADY STATE PORTION ONLY

MULTIFACETED CONE TESTS       $\lambda = 25.00$ , NRC / IMD

## FORCE ON STRUCTURE IN X, Y, Z DIRECTIONS

MUNICONE 3, 005,



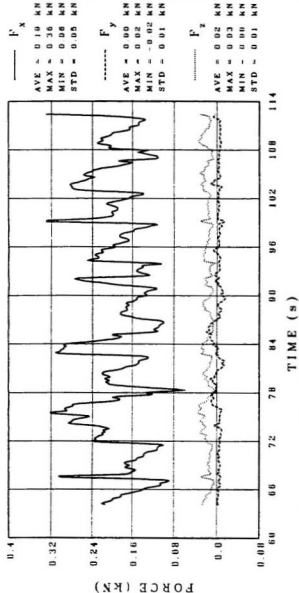
NECK SIZE -- SMALL  
FRACTION -- 0.09  
DIRECTION -- BROAD ON  
SPEED = 4. cm/s

ICE THICKNESS = 1.4 cm  
ICE DENSITY = 921 kg/m<sup>3</sup>  
FLEX STR (down) = 42.3 kPa  
FLEX STR (up) = 29.3 kPa

NO RIDGE  
STEADY STATE PORTION ONLY

MULTIFACETED CONE TESTS       $\lambda = 25.00$ , NRC/IMD

MUNICONE 5\_005  
FORCE ON NECK IN X, Y, Z DIRECTIONS



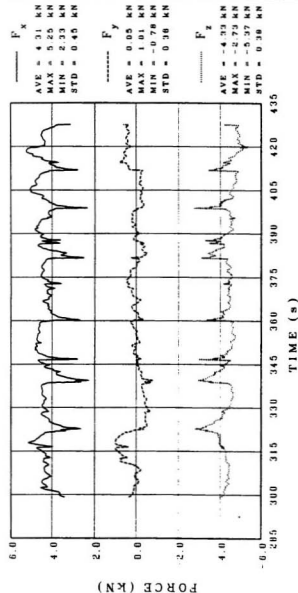
NECK SIZE = SMALL  
FRACTION = 0.09  
DIRECTION = BROAD ON  
SPEED = 4. cm/s

ICE THICKNESS = 14.8 cm  
ICE DENSITY = 921 kg/m<sup>3</sup>  
FLEX STR (down) = 42.3 kPa  
FLEX STR (up) = 26.3 kPa

NO RIDGE  
STEADY STATE PORTION ONLY

MULTIFACETED CONE TESTS       $\lambda = 25.00$ , NRC / IMD

FORCE ON STRUCTURE IN X, Y, Z DIRECTIONS      MUNCONE 4\_001



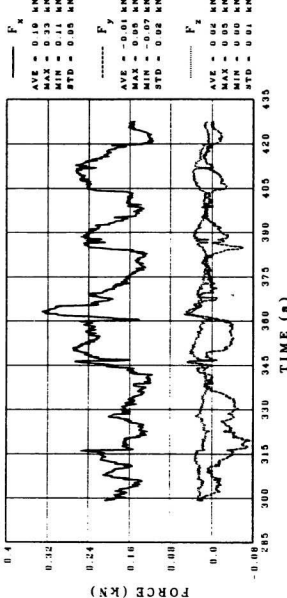
NECK SIZE -- LARGE	ICE THICKNESS = 16.0 cm
FRICTION -- 0.09	ICE DENSITY = 916 kg/m <sup>3</sup>
DIRECTION -- BROAD ON	PLEX STR (down) = 74.7 kPa
SPEED = 1. cm/s	PLEX STR (up) = 41.1 kPa

NO RIDGE  
STEADY STATE PORTION ONLY

MULTIFACETED CONE TESTS       $\lambda = 25.00$ , NRC / IMD

## FORCE ON NECK IN X, Y, Z DIRECTIONS

MUNCONE 4\_001



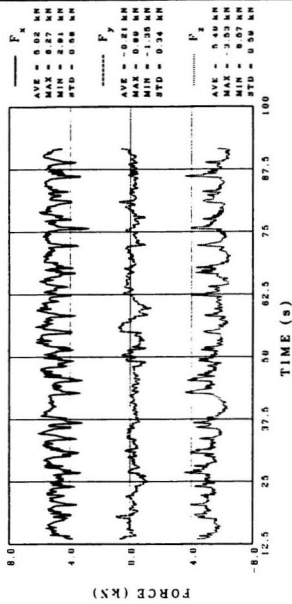
NECK SIZE = LARGE  
 FRICTION = 0.08  
 DIRECTION = BROAD ON  
 SPEED = 1. um/s

ICE THICKNESS = 10.0 cm  
 ICE DENSITY = 914. kg/m<sup>3</sup>  
 FLEX STR (down) = 74.7 kPa  
 FLEX STR (up) = 41.1 kPa

NO RIDGE  
 STEADY STATE PORTION ONLY

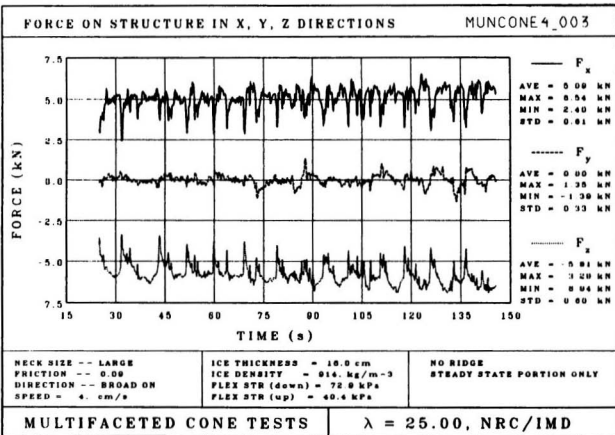
**MULTIFACETED CONE TESTS       $\lambda = 25.00$ , NRC/IMD**

FORCE ON STRUCTURE IN X, Y, Z DIRECTIONS      MUNICONE 4\_002



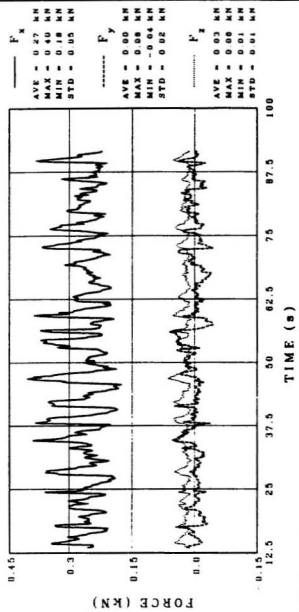
NECK SIZE -- LARGE	ICE THICKNESS = 16.0 cm	NO RIDGE
FRICITION -- 0.08	ICE DENSITY = 914. kg/m <sup>3</sup>	STEADY STATE PORTION ONLY
DIRECTION -- BROAD ON	FLX STR (down) = 73.5 kPa	
SPEED -- 0. cm/s	FLX STR (up) = 40.0 kPa	

MULTIFACETED CONE TESTS       $\lambda = 25.00$ , NRC/IMD



## FORCE ON NECK IN X, Y, Z DIRECTIONS

MUNCONE 4\_002

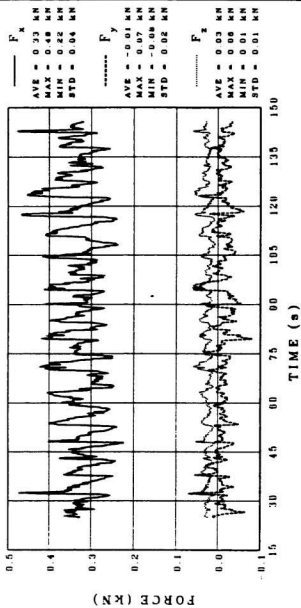


NECK SIZE -- LARGE	ICE THICKNESS = 16.0 cm	NO RIDGE STEADY STATE PORTION ONLY
FRICITION -- 0.09	ICE DENSITY = 914. kg/m <sup>3</sup>	
DIRECTION -- BROAD ON	PLEX STR (down) = 72.5 kPa	
SPEED = 6. cm/s	PLEX STR (up) = 40.6 kPa	

MULTIFACETED CONE TESTS       $\lambda = 25.00$ , NRC/IMD

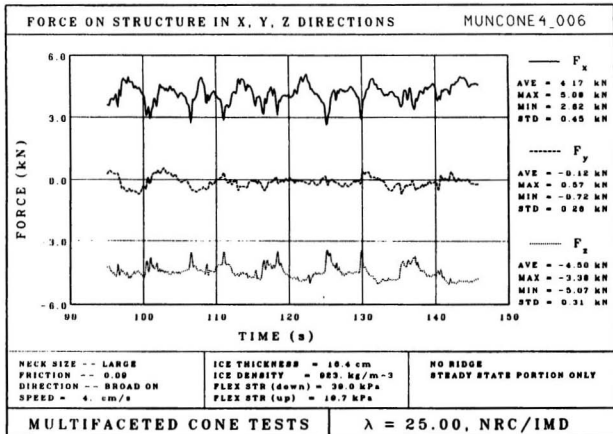
FORCE ON NECK IN X, Y, Z DIRECTIONS

MUNICONE 4.003

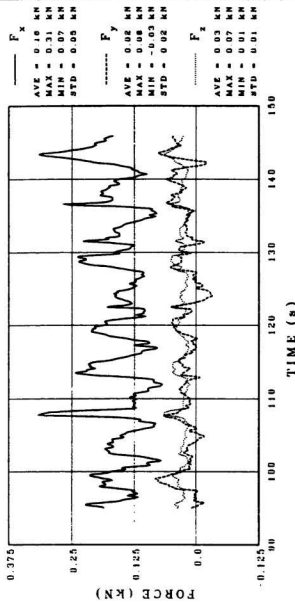


NECK SIZE = 1A1H	ICE THICKNESS = 18.0 cm	NO RIDGE
FRICITION = 0.09	ICE DENSITY = 914. kg/m <sup>3</sup>	STEADY STATE PORTION ONLY
DIRECTION = BROAD ON	PLEX STR (DOWN) = 72.0 kPa	
SPEED = 4. cm/s	PLEX STR (UP) = 40.4 kPa	

**MULTIFACETED CONE TESTS       $\lambda = 25.00$ , NRC / IMD**



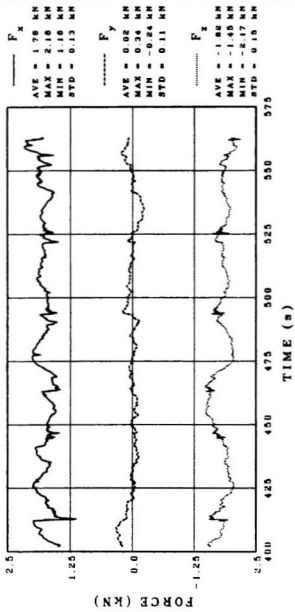
## FORCE ON NECK IN X, Y, Z DIRECTIONS MUNCONE 4\_006



NECK SIZE -- LARGE	ICE THICKNESS = 18.4 cm	NO RIDGE STEADY STATE PORTION ONLY
FRICITION -- 0.60	ICE DENSITY = 923 kg/m <sup>3</sup>	
DIRECTION -- BROAD ON	FLX STR (down) = 39.0 kPa	
SPEED = 4. cm/s	FLX STR (up) = 19.7 kPa	

**MULTIFACETED CONE TESTS       $\lambda = 25.00$ , NRC/IMD**

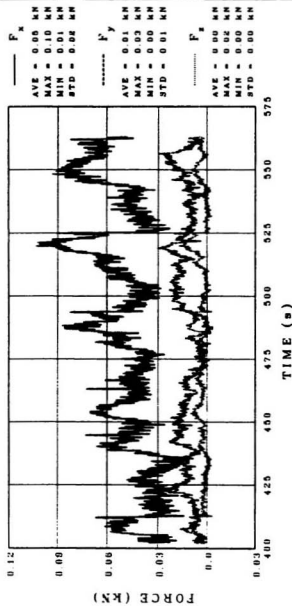
## FORCE ON STRUCTURE IN X, Y, Z DIRECTIONS MUNCONES\_001



NECK SIZE -- LARG	ICE THICKNESS = 8.4 cm	NO RIDGE STEADY STATE PORTION ONLY
FRICITION -- 0.08	ICE DENSITY = 920 kg/m <sup>3</sup>	
DIRECTION -- BROAD ON	FLEX STR (down) = 43.4 kPa	
SPEED = 1. cm/s	FLEX STR (up) = 30.7 kPa	

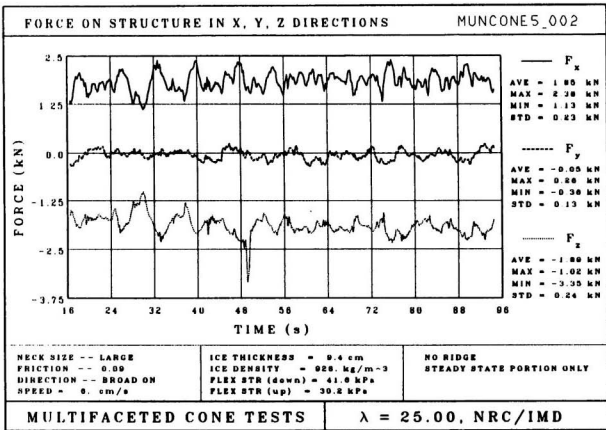
**MULTIFACETED CONE TESTS**       $\lambda = 25.00$ , NRC/IMD

FORCE ON NECK IN X, Y, Z DIRECTIONS      MUNCONE5\_001



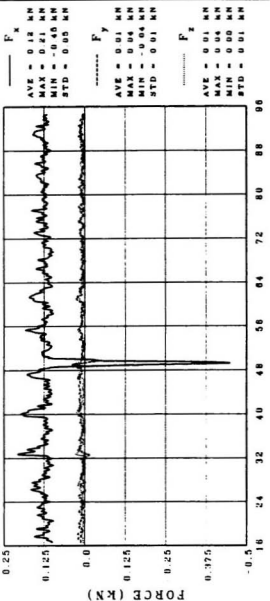
NECK SIZE -- LARGE	ICE THICKNESS = 0.4 cm	NO RIDGE
FRICITION -- 0.09	ICE DENSITY = 926. kg/m <sup>3</sup>	STEADY STATE PORTION ONLY
DIRECTION -- BROAD ON	PLEX STR (down) = 43.4 kPa	
SPEED = 1. cm/s	PLEX STR (up) = 30.7 kPa	

MULTIFACETED CONE TESTS       $\lambda = 25.00$ , NRC/IMD



## FORCE ON NECK IN X, Y, Z DIRECTIONS

MUNCONE5.002



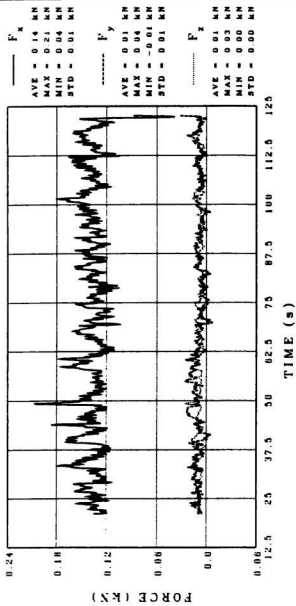
NECK SIZE -- LARGE	ICE THICKNESS = 0.4 m
FRICITION -- 0.09	ICE DENSITY = 920 kg/m <sup>3</sup>
DIRECTION -- BROAD ON	FLX STR (down) = 41.6 kPa
SPEED = 8. cm/s	FLX STR (up) = 30.8 kPa

NO RIDGE  
STEADY STATE PORTION ONLY

MULTIFACETED CONE TESTS     $\lambda = 25.00$ , NRC / IMD

## FORCE ON NECK IN X, Y, Z DIRECTIONS

MUNCONE5\_003



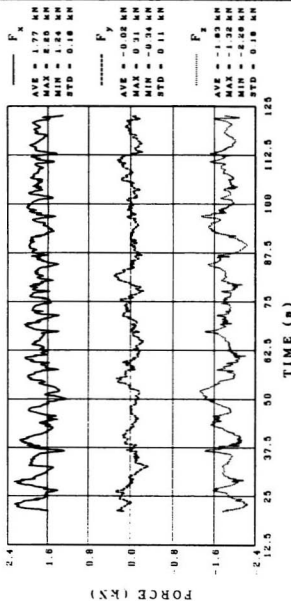
NECK SIZE -- LARGE  
 FRICTION -- 0.09  
 DIRECTION -- BROAD ON  
 SPEED = 4. cm/s

ICE THICKNESS = 0.4 cm  
 ICE DENSITY = 920. kg/m<sup>3</sup>  
 FLEX STR (down) = 40.6 kPa  
 FLEX STR (up) = 28.9 kPa

NO RIDGE  
 STEADY STATE POSITION ONLY

MULTIFACETED CONE TESTS       $\lambda = 25.00$ , NRC / IMD

## FORCE ON STRUCTURE IN X, Y, Z DIRECTIONS MUNICONE 5\_003

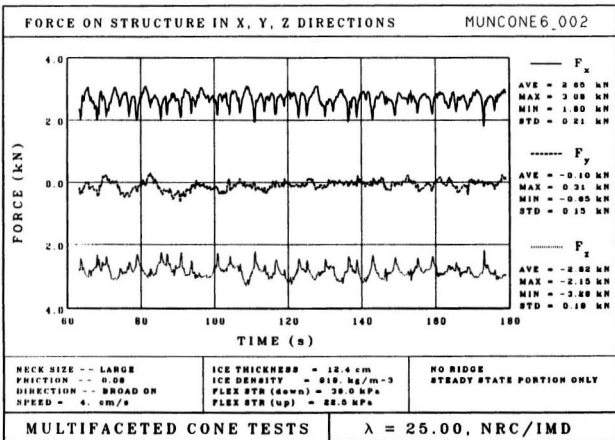


NECK SIZE -- LARGE  
 FRICTION -- 0.08  
 DIRECTION -- BROAD ON  
 SPEED -- 4. cm/s

ICE THICKNESS = 0.4 cm  
 ICE DENSITY = 918 kg/m<sup>3</sup>  
 FLEX STR (Down) = 40.8 kPa  
 FLEX STR (Up) = 29.9 kPa

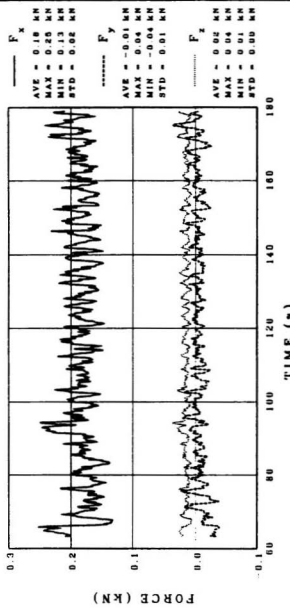
NO RIDGE  
 STEADY STATE PORTION ONLY

MULTIFACETED CONE TESTS       $\lambda = 25.00$ , NRC/IMD



## FORCE ON NECK IN X, Y, Z DIRECTIONS

MUNCONE 6\_002



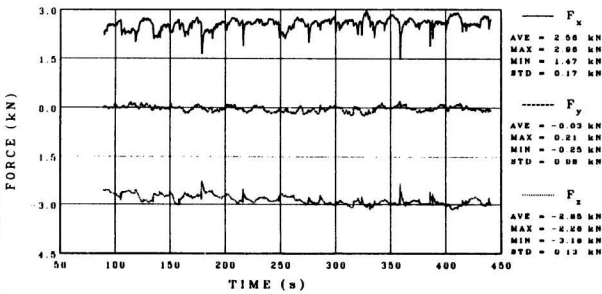
NECK SIZE	TAHUK	ICE THICKNESS = 12.4 cm	NO RIDGE
FRICITION	0.08	ICE DENSITY = 916 kg/m <sup>3</sup>	STEADY STATE PORTION ONLY
DIRECTION -- BROAD ON		FLUX STR (down) = 28.0 kPa	
SPEED =	4 cm/s	FLUX STR (up) = 88.0 kPa	

MULTIFACETED CONE TESTS       $\lambda = 25.00$ , NRC / IMD



## FORCE ON STRUCTURE IN X, Y, Z DIRECTIONS

MUNCONE 6 003



NECK SIZE -- LARGE  
FRICTION -- 0.08  
DIRECTION -- BROAD ON  
SPEED = 1. cm/s

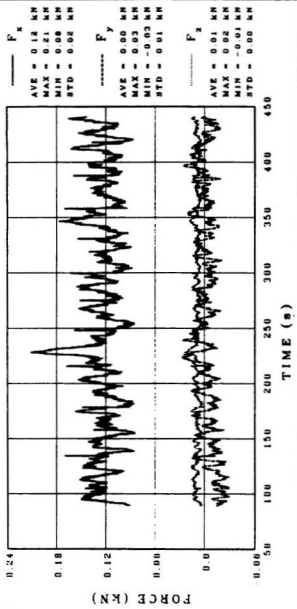
**ICE THICKNESS** = 12.4 cm  
**ICE DENSITY** = 918. kg/m<sup>3</sup>  
**FLEX STR (down)** = 35.4 kPa  
**FLEX STR (up)** = 22.5 kPa

**NO RIDGE  
STEADY STATE PORTION ONLY**

## MULTIFACETED CONE TESTS

$\lambda = 25.00$ , NRC/IMD

## FORCE ON NECK IN X, Y, Z DIRECTIONS MUNCONE6\_003



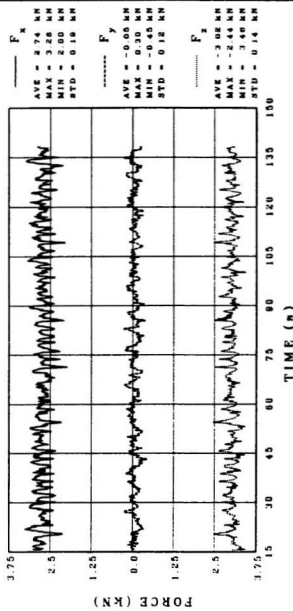
NECK SIZE -- LARGE  
 FRICTION -- 0.08  
 DIRECTION -- SHADON  
 SPEED = 1. cm/s

ICE THICKNESS = 12.4 cm  
 ICE DENSITY = 918 kg/m<sup>3</sup>  
 FLEX STR (down) = 36.4 kPa  
 FLEX STR (up) = 42.0 kPa

NO RIDGE  
 STEADY STATE PORTION ONLY

MULTIFACETED CONE TESTS       $\lambda = 25.00$ , NRC / IMD

## FORCE ON STRUCTURE IN X, Y, Z DIRECTIONS      MUNCONE 6\_004



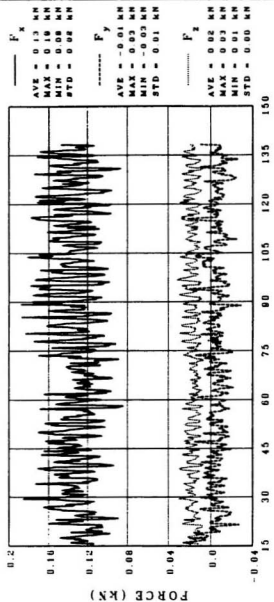
NECK SIZE -- LARGE  
 FRICTION -- 0.08  
 DIRECTION -- BROAD ON  
 SPEED = 6. cm/s

ICE THICKNESS = 12.4 cm  
 ICE DENSITY = 919. kg/m<sup>3</sup>  
 FLEX STR (down) = 35.1 kPa  
 FLEX STR (up) = 48.6 kPa

NO RIDGE  
 STEADY STATE PORTION ONLY

MULTIFACETED CONE TESTS       $\lambda = 25.00$ , NRC/IMD

## FORCE ON NECK IN X, Y, Z DIRECTIONS MUNNONE 6\_004

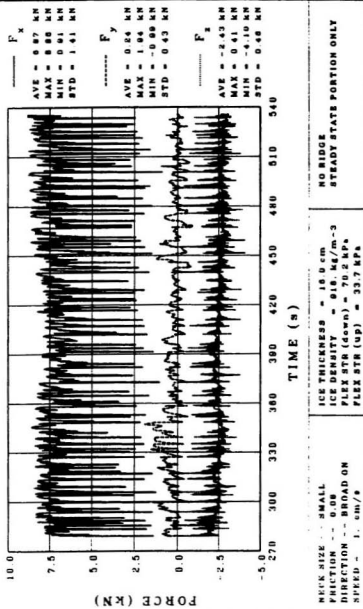


NECK SIZE	LARGE	ICE THICKNESS = 12.4 cm	NO RIDGE
FRICITION	0.08	ICE DENSITY = 910 kg/m <sup>3</sup>	STEADY STATE PORTION ONLY
DIRECTION -- BROAD ON		FLEX STR (down) = 25.1 kPa	
SPEED = 0. cm/s		FLEX STR (up) = 22.0 kPa	

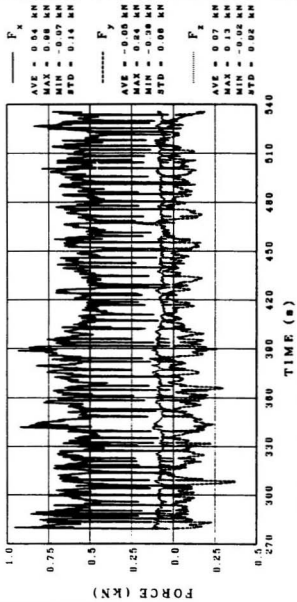
MULTIFACETED CONE TESTS       $\lambda = 25.00$ , NRC/IMD

## FORCE ON STRUCTURE IN X, Y, Z DIRECTIONS

MUNCONE 7\_001

MULTIFACETED CONE TESTS     $\lambda = 50.00$ , NRC/IMD

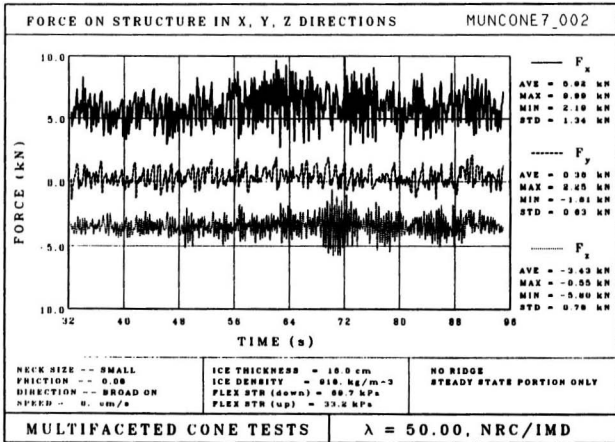
FORCE ON NECK IN X, Y, Z DIRECTIONS      MUNCONE 7\_001

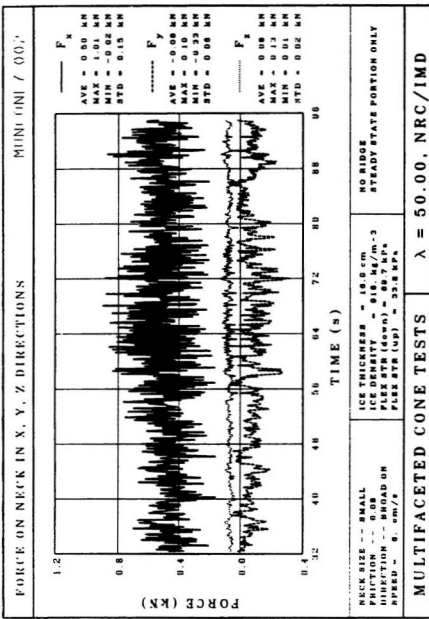


NECK SIZE -- SMALL	ICE THICKNESS = 16.0 cm
FRICITION -- 0.08	ICE DENSITY = 916 kg/m <sup>3</sup>
DIRECTION -- BROAD ON	FLEX STR (down) = 70.2 kPa
SPEED = 1. cm/s	FLEX STR (up) = 33.7 kPa

NO RIDGE  
STEADY STATE PORTION ONLY

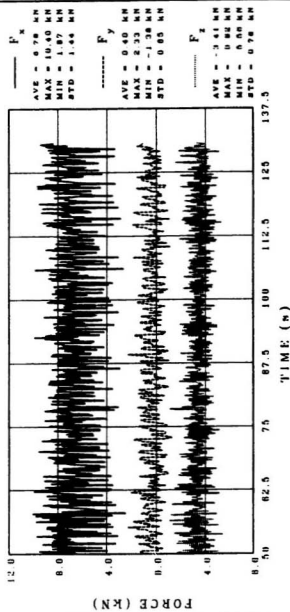
MULTIFACETED CONE TESTS       $\lambda = 50.00$ , NRC/1MD





## FORCE ON STRUCTURE IN X, Y, Z DIRECTIONS

MUNICONE 7\_003

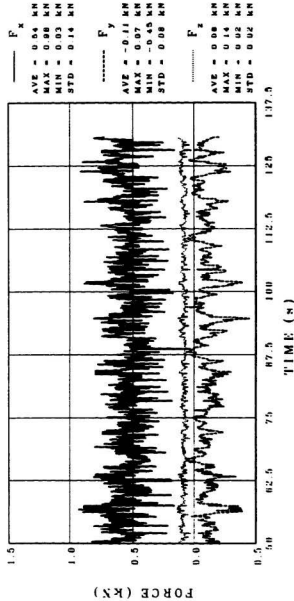


NECK SIZE	SMALL	ICE THICKNESS = 18.0 cm	NO RIDGE
FRICITION	= 0.08	ICE DENSITY = 916 kg/m <sup>3</sup>	STEADY STATE PORTION ONLY
DIRECTION	- BROAD ON	FLX STR (down) = 89.3 kPa	
SPEED	- 4 cm/s	FLX STR (up) = 38.8 kPa	

MULTIFACETED CONE TESTS       $\lambda = 50.00$ , NRC/IMD

## FORCE ON NECK IN X, Y, Z DIRECTIONS

MUNCONE 7\_003

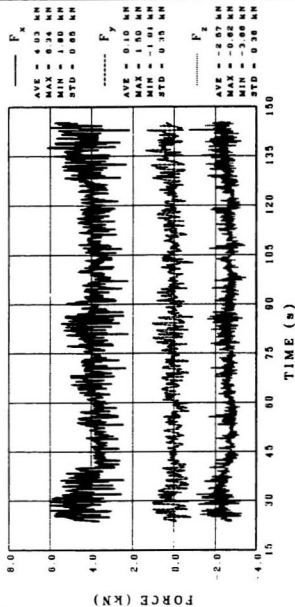


NECK SIZE --- SMALL  
 FRACTION --- 0.06  
 DIRECTION --- BROAD ON  
 SPEED --- 4. cm/s

ICE THICKNESS = 16.0 cm	NO RIDGE
ICE FLEX STR (down) = 66.3 kPa	STEADY STATE PORTION ONLY
ICE FLEX STR (up) = 38.8 kPa	

MULTIFACETED CONE TESTS       $\lambda = 50.00$ , NRC/IMD

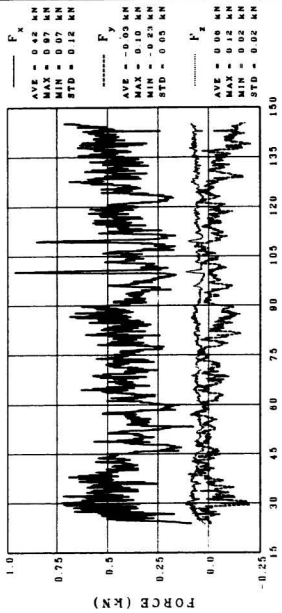
FORCE ON STRUCTURE IN X, Y, Z DIRECTIONS      MUNCONE 7\_006



NECK SIZE -- SMALL	ICE THICKNESS = 18.3 cm	NO RIDGE STEADY STATE PORTION ONLY
FRICITION -- 0.08	ICE DENSITY = 920 kg/m <sup>3</sup>	
DIRECTION -- BROAD ON	FLX STR (down) = 48.8 kPa	
SPEED -- 4.0 m/s	FLX STR (up) = 16.7 kPa	

MULTIFACETED CONE TESTS       $\lambda = 50.00$ , NRC/IMD

FORCE ON NECK IN X, Y, Z DIRECTIONS      MUNC (ON / 00)



NECK SIZE = SMALL  
FRACTION = 0.08  
DIRECTION = BROAD ON  
SPEED = 4. cm/s  
ICE THICKNESS = 16.3 cm  
ICE DENSITY = 920. kg/m<sup>3</sup>  
FLEX STR (down) = 42.8 kPa  
FLEX STR (up) = 18.7 kPa

NO RIDGE  
STEADY STATE PORTION ONLY

MULTIFACETED CONE TESTS       $\lambda = 50.00$ , NRC/IMD

## **APPENDIX C**

**Example Calculation to Illustrate the Application  
of Equations Developed in Chapters 7 to 9**

An example calculation for Test MUNCONE3\_001 is shown here to illustrate the usage of equations developed in Chapters 6 to 8 for the computation of ice loads on faceted cones. Values of the relevant parameters are given as follows:

- (i) **Ice Properties**: Thickness,  $t = 0.1583$  m; flexural strength,  $\sigma_f = 44.38$  kPa; elastic modulus,  $E = 362.2$  MPa; ice-structure friction coefficient,  $\mu_s = 0.1$ ; and weight density,  $\gamma = 8985$  N/m<sup>3</sup>.
- (ii) **Rubble Properties**: Rubble angle,  $\tau = 35^\circ$ ; internal friction angle,  $\phi = 35^\circ$ ; wall friction angle,  $\phi_w = 11.3^\circ$ ; bulk weight density,  $\gamma_b = 6290$  N/m<sup>3</sup>; and porosity,  $p = 0.3$ .
- (iii) **Water Foundation**: Weight density,  $\gamma_w = 9839$  N/m<sup>3</sup>.
- (iv) **Structure Dimensions**: Height of cone section,  $h_1 = 0.233$  m; height of collar section,  $h_2 = 0.473$  m; facet width at waterline,  $w_r = 0.693$  m; cone angle,  $\alpha_1 = 39.8^\circ$ ; collar angle,  $\alpha_2 = 63.4^\circ$ ; neck angle;  $\alpha_3 = 90^\circ$ ; cone angle at side,  $\alpha_{s,1} = 35.8^\circ$ ; collar angle at side,  $\alpha_{s,2} = 60^\circ$ ; neck angle at side,  $\alpha_{s,3} = 90^\circ$ ; and average cone angle,  $\alpha_{ave} = 49.8^\circ$ .
- (v) **Ice Breaking Pattern**: Angle between radial crack and x-axis;  $\theta_{cr} = 30^\circ$ ; and measured broken piece size,  $L_L = 0.1511$  m.

### C.1 Rubble Height Calculation(Chapter 6)

The width of ride-up ice wall at front facet,  $w_{nuc}$ , is equal to 0.7802 m, computed by

Equation 8.12.

### C.1.1 Rubble Height at Side of Front Facet: $h_{rf}$

The cross-section of rubble at both side of cone, A, is equal to  $0.08822 \text{ m}^2$ , computed from Equation 6.5. The rubble height at side of the front facet,  $h_{rf}$ , and the corresponding value of  $B_o$  can be computed using Equations 6.12 and 6.16, respectively, via a trial and error procedure, by arbitrarily assuming a value of n and  $h_{rf}$ :

First trial: n = 1 with an initial value of  $h_{rf} = h_1 = 0.233 \text{ m}$

$B_o = 0.2798 \text{ m}$  and  $h_{rf} = 0.4039 \text{ m}$

Since  $h_{rf} > h_1$ , then n must be greater than 1.

Second trial: n = 2 with an initial value of  $h_{rf} = h_2 = 0.473 \text{ m}$

$B_o = 0.2039 \text{ m}$  and  $h_{rf} = 0.3802 \text{ m}$

Since  $h_{rf} < h_2$ , then n must be equal to 2.

Therefore, the rubble reaches the collar section with  $h_{rf}$  being equal to 0.380 m.

### C.1.2 Rubble Height at Side of Cone: $h_{ns}$

The rubble height at side of the cone,  $h_{ns}$ , can be computed using Equation 6.22 via a similar trial and error procedure:

First trial: for n = 1,  $h_{ns} = 2.0347 \text{ m}$

Since  $h_{ns} > h_1$ , then n must be greater than 1.

Second trial: for n = 2,  $h_{ns} = 0.5087 \text{ m}$

Since  $h_n > h_2$ , then n must be greater than 2.

Third trial: for  $n = 3$ ,  $h_n = 0.4947 \text{ m}$

Therefore, the rubble reaches the neck section with  $h_n$  being equal to 0.495 m.

### C.1.3 Maximum Rubble Height at Front Facet: $h_{rm}$

The maximum rubble height at the front facet,  $h_{rm}$ , is computed as the following:

$B_1 = 0.4507 \text{ m}$  (Equation 6.30);  $\alpha_r = 53.7^\circ$  (Equation 6.33 with  $\alpha = \alpha_{ave}$ );  $A_3 = 0.1705 \text{ r}^2$  (Equation 6.31);  $A_4 = 0.06809 \text{ r}^2$  (Equation 6.32);  $(A_3 + A_4) / A_3 = 1.3994$ ;  $w = 0.3154 \text{ m}$  (Equation 6.34);  $w/w_r = 0.4042$  (implies a trapezoidal profile); and  $h_{rm} = 0.7126 \text{ m}$  (Equation 6.35 with  $h_{rf} = 0.3802 \text{ m}$ ).

Therefore, the rubble has a trapezoidal profile along the front facet with  $h_{rm}$  being equal to 0.713 m.

## C.2 Rubble Load Calculation(Chapter 7)

Rubble loads for the center and the side facets are calculated separately for the respective equivalent rubble heights,  $h_{rc}$  and  $h_{rs}$ .

### C.2.1 Rubble Load Per Unit Width on Center Facet

$h_{rc} = 0.5783 \text{ m}$  (Equation 8.13)

(i) Load per unit width on individual sections:

(a) Lower cone section,  $i = 1$ :  $\phi'_{w,1} = 11.3^\circ$  (Equation 7.29);  $\alpha_{p,1} = 61.49^\circ$  (Equation

- 7.28);  $P_{o,1} = 268.0 \text{ N/m}$  (Equation 7.37);  $P_{wh,1} = 127.9 \text{ N/m}$  (Equation 7.38); and  $P_{vv,1} = 235.5 \text{ N/m}$  (Equation 7.39)
- (b) **Collar section, i=2:**  $\phi'_{w,2} = 8.51^\circ$ ;  $\alpha_{p,2} = 35.0^\circ$ ;  $P_{o,2} = 117.5 \text{ N/m}$ ;  $P_{wh,2} = 96.1 \text{ N/m}$ ; and  $P_{vv,2} = 67.5 \text{ N/m}$
- (c) **Neck section, i=3:**  $\phi'_{w,3} = 1.709^\circ$ ;  $\alpha_{p,3} = 1.709^\circ$ ;  $P_{o,3} = 9.1 \text{ N/m}$ ;  $P_{wh,3} = 9.1 \text{ N/m}$ ; and  $P_{vv,3} = 0.3 \text{ N/m}$
- (ii) **Total rubble load:**  
 $P_{wh} = 233.1 \text{ N/m}$  (Equation 7.38);  $P_{vv} = 303.3 \text{ N/m}$  (Equation 7.39);  $P_{bh} = 233.1 \text{ N/m}$  (Equation 7.33);  $P_{gv} = 727.4 \text{ N/m}$  (Equation 7.34); and  $W_{rc} = W_r = 1030.6 \text{ N/m}$  (Equation 8.14)
- (iii) **Equivalent rubble width:**  
 $w_{rc} = w_{nrc} = 0.7802 \text{ m}$  (Equation 8.12)

### C.2.2 Rubble Load Per Unit Width on Side Facet

- $h_{r,s} = 0.4375 \text{ m}$  (Equation 8.18)
- (i) **Load per unit width on individual sections:**
- (a) **Lower cone section, i=1:**  $\phi'_{w,1} = 11.3^\circ$ ;  $\alpha_{p,1} = 61.49^\circ$ ;  $P_{o,1} = 186.2 \text{ N/m}$ ;  $P_{wh,1} = 88.9 \text{ N/m}$ ; and  $P_{vv,1} = 163.7 \text{ N/m}$
- (b) **Collar section, i=2:**  $\phi'_{w,2} = 8.51^\circ$ ;  $\alpha_{p,2} = 35.0^\circ$ ;  $P_{o,2} = 45.4 \text{ N/m}$ ;  $P_{wh,2} = 37.1 \text{ N/m}$ ; and  $P_{vv,2} = 26.1 \text{ N/m}$

(c) Neck section,  $i = 3$ :  $\phi'_{w,3} = 1.709^\circ$ ;  $\alpha_{g,3} = 1.709^\circ$ ;  $P_{o,3} = 0 \text{ N/m}$ ;  $P_{sh,3} = 0 \text{ N/m}$ ; and

$$P_{vv,3} = 0 \text{ N/m}$$

(ii) Total load:

$P_{sh} = 126.1 \text{ N/m}$ ;  $P_{vv} = 189.8 \text{ N/m}$ ;  $P_{sh} = 126.1 \text{ N/m}$ ;  $P_{bv} = 249.3 \text{ N/m}$ ; and  $W_{r,s} = 439.0 \text{ N/m}$  (Equation 8.14 with  $V_f = 0.02181 \text{ m}^3$  [Equation 8.19] and  $V_B = 0.02175 \text{ m}^3$  [Equation 8.21])

(iii) Equivalent rubble width:

$$w_{r,s} = 0.559 \text{ m} \text{ (Equation 8.23 with } A_{eq} = 0.0698 \text{ m}^2\text{)}$$

### C.3 Ice Load Calculation (Chapter 9)

Ice loads for the center and the side facets are calculated separately.

#### C.3.1 Ice Load on Center Facet

(i) Beam cracking length:

Assuming the ice cracking pattern as shown in Figure 8.13, Equation 8.11 gives a value of 0.1511 m for the beam cracking length,  $d_{cr}$ .

(ii) Ride-up and rubble heights,  $h_{nu,c}$  and  $h_{r,c}$ :

$$h_{r,c} = 0.5783 \text{ m} \text{ (from Section C.2.1)}$$

Since  $h_{r,c} > (h_n = h_2 = 0.473 \text{ m})$ , then  $h_{nu,c} = 1.334 \text{ m}$  (Equation 8.15), and  $h_{L,1} = h_2 - h_1 = 0.233 \text{ m}$ ,  $h_{L,2} = h_3 - h_2 = 0.240 \text{ m}$ , and  $h_{L,3} = h_{nu,c} - h_n = 0.861 \text{ m}$ .

(iii) Weight of ride-up ice,  $W_{nu,c}$ :

$w_{n.c}$  is equal to 0.7802 m (from Section C.1).

- (a) Weight on individual sections:  $W_{n.c.1} = 404.7 \text{ N}$ ;  $W_{n.c.2} = 297.3 \text{ N}$ ; and  $W_{n.c.3} = 955.2 \text{ N}$  (Equation 8.17)
- (b) Total weight:  $W_{n.c.} = W_{n.c.1} + W_{n.c.2} + W_{n.c.3} = 1657.1 \text{ N}$
- (iv) Forces required to push ice blocks up the slope through ice rubble, P:  
Let  $P_4 = 0 \text{ N}$  and  $\alpha_4 = \alpha_3 = 90^\circ$ ;
- (a) Neck section, i = 3:  $P_3 = 956.2 \text{ N}$  (Equation 8.45)
- (b) Collar section, i = 2:  $P_2 = 1207.7 \text{ N}$
- (c) Lower cone section, i = 1:  $P_1 = 1519.2 \text{ N}$
- (v) Force components at waterline,  $H_T, V_T, H_w, V_w$ :  
Assume initial value of  $\sigma'_f = \sigma_f = 44.38 \text{ kPa}$ ;
- (a) 1<sup>st</sup> iteration:  $V'_b = 217.5 \text{ N/m}$  (Equation 8.5);  $H_T = 1350 \text{ N}$  (Equation 8.48);  $V_T = 1540 \text{ N}$  (Equation 8.49);  $V_w = 1729 \text{ N}$  (Equation 8.50);  $\xi = 1.0435$  (Equation 2.2);  $H_w = 1804 \text{ N}$  (Equation 8.51);  $H_{TOT} = 3153 \text{ N}$  (Equation 8.43); and  $V_{TOT} = 2650 \text{ N}$  (Equation 8.44).
- (b) Update the effect flexural strength for in-plane force: Substitute the old value of  $\sigma'_f$ , into  $\sigma_f$ , and calculate the new value of  $\sigma'_f$ , using Equation 8.53. Repeat the above Steps (a) and (b) until  $\sigma'_f$  converges.
- (c) Final results:  $\sigma'_f = 68.11 \text{ kPa}$ ;  $V'_b = 333.9 \text{ N/m}$ ;  $H_T = 1349 \text{ N}$ ;  $V_T = 1540 \text{ N}$ ;  $V_w = 1830 \text{ N}$ ;  $H_w = 1902 \text{ N}$ ;  $H_{TOT} = 3258 \text{ N}$ ; and  $V_{TOT} = 2751 \text{ N}$ .

### C.3.2 Ice Load on Side Facet

- (i) Beam cracking length:

Assuming the ice cracking pattern as shown in Figure 8.13, Equation 8.1 gives a value of 0.86744 m for the beam cracking length,  $d_{cr}$ .

- (ii) Rubble height,  $h_{rs}$ :

$$h_{rs} = 0.4375 \text{ m (from Section C.2.2)}$$

- (iii) Weight of ride-up ice,  $W_{ru,s}$ :

$$\text{Total weight: } W_{ru,s} = 187.5 \text{ N (Equation 8.24)}$$

Distributing the total weight of ride-up ice on the lowest section gives:  $W_{ru,3} = W_{ru,2} = 0 \text{ N}$  and  $W_{ru,1} = W_{ru,s} = 187.5 \text{ N}$ .

- (iv) forces along X' - Z axes required to push ice blocks up the slope through ice rubble,

P<sub>i</sub>:

$$w_{rs} = 0.559 \text{ m (from Section C.2.2.iii)}$$

Let  $P_4 = 0 \text{ N}$  and  $\alpha_4 = \alpha_3 = 90^\circ$ ;

- (a) Neck section, i = 3:  $P_3 = 0 \text{ N}$  (Equation 8.45)

- (b) Collar section, i = 2:  $P_2 = 6.6 \text{ N}$

- (c) Lower cone section, i = 1:  $P_1 = 174.4 \text{ N}$

- (v) Force components along X'-Z axes at waterline:  $H_T, V_T, H_W, V_W$ :

Assume initial value of  $\sigma'_f = \sigma_f = 44.38 \text{ kPa}$ ;

- (a) 1<sup>st</sup> iteration:  $V'_b = 217.5 \text{ N/m}$  (Equation 8.5);  $H_T = 204.5 \text{ N}$  (Equation 8.48);  $V_T =$

$251.0 \text{ N}$  (Equation 8.49);  $V_w = 439.7 \text{ N}$  (Equation 8.50);  $\xi = 1.0435$  (Equation 2.2);  $H_w = 458.8 \text{ N}$  (Equation 8.51);  $H_{TOT} = 663.3 \text{ N}$  (Equation 8.43); and  $V_{TOT} = 621.6 \text{ N}$  (Equation 8.44).

- (b) Update the effect flexural strength for in-plane force: Substitute the old value of  $\sigma'_f$  into  $\sigma_f$ , and calculate the new value of  $\sigma'_f$  using Equation 8.53. Repeat the above Steps (a) and (b) until  $\sigma'_f$  converges.
- (c) Final results:  $\sigma'_f = 49.37 \text{ kPa}$ ;  $V'_{b} = 242.0 \text{ N/m}$ ;  $H_T = 204.5 \text{ N}$ ;  $V_T = 251.0 \text{ N}$ ;  $V_w = 460.9 \text{ N}$ ;  $H_w = 481.0 \text{ N}$ ;  $H_{TOT} = 685.5 \text{ N}$ ; and  $V_{TOT} = 642.8 \text{ N}$ .
- (vi) Force component of  $H_{TOT}$  Along X-Z Axes:  
 $H_{TOT \text{ (along X axis)}} = 383.8 \text{ N}$  (Equation 8.36)

### C.3.3 Total Ice Load on Cone

$$V_{TOT \text{ (total)}} = V_{TOT \text{ (front)}} + 2V_{TOT \text{ (side)}} = 4051 \text{ N}$$

$$H_{TOT \text{ (total)}} = H_{TOT \text{ (front)}} + 2H_{TOT \text{ (side, along X axis)}} = 4041.5 \text{ N}$$







